

Measurement of the Neutron Electromagnetic Form Factor Ratio at High Momentum Transfer

Sean Patrick Jeffas
Secaucus, NJ, USA

B.S. Physics, B.S Mathematics, Stony Brook University, 2018

*A Dissertation presented to the Graduate Faculty of the University of Virginia
in Candidacy for the degree of Doctor of Philosophy*

Department of Physics

UNIVERSITY OF VIRGINIA

July, 2024

Abstract

The inner structure of the nucleon (proton and neutron) remains a topic of great interest in nuclear and particle physics, after many decades of study. For example, understanding the quark-gluon dynamics inside the nucleon would shed light on how 99% of the nucleon mass is created. The neutron electromagnetic form factors, G_E^n and G_M^n , give important insights into the neutron structure. The Super BigBite Spectrometer (SBS) program at Jefferson Lab (JLab) seeks to extend the form factor measurements for both the proton and the neutron. The neutron electric form factor, G_E^n , has been historically difficult to measure due to the short lifetime of the free neutron and the small value of G_E^n .

The GEN-II experiment is part of the SBS program and seeks to measure G_E^n , significantly increasing the high momentum transfer coverage. A newly designed polarized ^3He target increased the figure of merit by three times compared to previous measurements. The analysis of this data is especially challenging due to the unprecedented high-rate environment caused by the open nature of the spectrometer with a direct line of sight to the target. This required developing new Gas Electron Multiplier (GEM) particle trackers which can cover large areas demanded by this setup and handle particle rates up to 500 kHz/cm². Rates this high over a large area is unprecedented in particle tracking systems and came with a number of challenges. Data taken in the SBS program was critical to understanding hardware and software solutions that improved the track reconstruction efficiency to be >97% with a position resolution of 70 μm .

In previous experiments the proton electromagnetic form factors, G_E^p and G_M^p were measured up to $Q^2 = 8.5 \text{ GeV}^2$ and $Q^2 = 30 \text{ GeV}^2$, respectively, while G_E^n has only been measured up to $Q^2 = 3.4 \text{ GeV}^2$. The GEN-II experiment has measured the neutron form factor ratio, G_E^n/G_M^n , at Q^2 values of 2.90, 6.50, and 9.47 GeV^2 by scattering a polarized electron beam with a polarized ^3He target, used here as an effective polarized neutron target, and measuring the double spin asymmetry of the cross section. Previous G_E^n measurements do not extend above $Q^2 = 3.4 \text{ GeV}^2$, and therefore this analysis has extended the world data by almost three times. The background correction is especially difficult at the higher Q^2 settings leading to large systematic errors. As very exploratory results from this early analysis of the data, we find for $Q^2 = 2.90 \text{ GeV}^2$, $G_E^n = 0.0157 \pm_{\text{stat}} 0.0016 \pm_{\text{sys}} 0.0011$, for $Q^2 = 6.50 \text{ GeV}^2$, $G_E^n = 0.0067 \pm_{\text{stat}} 0.0019 \pm_{\text{sys}} 0.0005$,

and for $Q^2 = 9.46 \text{ GeV}^2$, $G_E^n = 0.0046 \pm_{\text{stat}} 0.0023 \pm_{\text{sys}} 0.0005$. These results are compared to predictions from the Dyson-Schwinger Equations (DSE) model and a Relativistic Constituent Quark Model (RCQM).

Acknowledgements

The work presented here was made possible through the efforts of many individuals that have helped and guided me throughout my physics career and personal life. Firstly I must give my heartfelt thanks to my parents, Gary and Jean, who started this all by fostering my curiosity and always supporting my interest in science. You have always instilled in me a belief that all my goals are achievable with enough effort. Your constant love is the single biggest factor that has made me the person I am today.

I must next thank my advisor, Nilanga Liyanage. You have provided to me almost all of the opportunities in my graduate career and were always quick to answer "yes" whenever I asked to try something new. You have been incredibly supportive of my unorthodox graduate career, moving to JLab later than originally planned, and then moving back to Charlottesville during the experiment because of delays. I am grateful to have found such a caring and understanding advisor, who helped improve my independence as a scientist and as a professional.

Next I would like to thank my colleagues at UVA that I worked with daily over the course of these past years. Specifically Kondo Gnanvo, Huong Nguyen, and Xinzhan Bai, who set the foundation for me with hands on scientific principles and analyses. You have generously offered your time and patience to me throughout the years. And I would like to thank my fellow graduate students John Boyd and Anuruddha Rathnayake. John and I worked together for a year in the lab, partially during the pandemic with just the two of us, constructing and testing detectors. No greater bonds are built in science than working daily in the lab, and I thank John for the many good conversations and distractions during the often tedious work. For Anu, we similarly spent years together beating our heads against the wall at JLab, and I am also grateful for your friendship and conversation during that time. You are the best roommate I had in grad school, besides my wife of course! As for the other students at UVA, I appreciate all the time we have had together, whether it be at a conference, at the lab, or in the office: Vimukthi Gamage, Bhashitha Dharmasena, and Jacob McMurtry.

Next I would like to thank my colleagues at JLab, who poured their efforts out with me running experiments. First to the GEM group, who had the greatest complexity and time spent fixing issues in the counting house of any group in the SBS experiments: Zeke Wertz, Holly Szumila-Vance, Thir Gautam, Malinga Rathnayake, Manjukrishna Suresh, and Saru Dhital. I am not sure if we will ever go through an experience again quite like running the GEMs for SBS and I thank you all for your time

and support. Also a big thanks to Ben Raydo and Bryan Moffit with their technical assistance and guidance through this time.

I must also express my gratitude to all the other graduate students that worked at JLab with me. There is no bonding experience in the world like what we went through with the SBS experiments, and I am eternally grateful to have gone through it with all of you: Provakar Datta, Sebastian Seeds, Maria Satnik, Hunter Presley, Gary Penman, Kate Evans, Jack Jackson, and Faraz Chahili. The time we have spent together in and out of JLab have been the some of the best memories of grad school, and definitely kept me going during my time there. I would also like to thank other colleagues at JLab that offered their assistance and guidance, without which I would not have finished this work: Andrew Puckett, Arun Tadepalli, Eric Fuchey, and Bogdan Wojtsekhowski.

I must also thank more friends that have made graduate school a good time whenever possible. For Thomas Krahulik, Matthew Wampler, Jacob Higgins, Anna Hall, Miller Eaton, Adrian Gutierrez, and Arthur Conover; the board game parties, dinners, hiking adventures, and more have been a highlight of these last years.

And for my darling wife, Marybeth, I am eternally grateful. This thesis comes second to you for my greatest achievement in graduate school. I am very thankful to have had you to lean on throughout the years and to share this experience with. These grad school years have been the best of my life with you, and I look forward to many more to come.

Contents

Abstract	ii
Acknowledgements	iv
1 Introduction	1
1.1 Elastic Electron-Nucleon Scattering	2
1.2 Nucleon Structure	4
1.3 Electromagnetic Form Factors	6
1.4 Sachs Form Factors	7
1.4.1 Quark Flavor Decomposition	8
1.5 Previous G_E^n Measurements	9
1.5.1 Rosenbluth Separation	10
1.5.2 Polarization Method	10
1.5.3 GEN-I Experiment	11
1.6 Nucleon Models	12
1.6.1 pQCD	13
1.6.2 Relativistic Constituent Quark Model	13
1.6.3 Dyson-Schwinger Equations	13
1.6.4 Generalized Parton Distributions	14
1.7 Parameterizations	15
1.7.1 Dipole	15
1.7.2 Glaster	15

1.7.3	Kelly	16
1.7.4	Global Fits	16
2	SBS Program	18
2.1	GMn Experiment	19
2.2	GEn-II Experiment	19
2.3	GEp-V Experiment	20
3	GEn-II Experiment Overview	21
3.1	Kinematic Notes	22
3.2	Double Polarization Method	22
3.3	CEBAF Accelerator	24
3.4	Experimental Setup	25
3.5	Coordinate Systems	26
3.6	Electron Arm Detectors	27
3.6.1	GEM Trackers	27
3.6.2	BigBite Calorimeter	28
3.6.3	GRINCH	30
3.6.4	Hodoscope	30
3.7	Hadron Arm Detectors	31
3.7.1	Hadron Calorimeter	32
3.8	Beamline	33
3.8.1	Beam Position	33
3.8.2	Beam Helicity	35
3.8.3	Beam Polarization	37
3.9	Magnets and Optics	38
3.10	Targets	41
3.10.1	Carbon Foil Target	41

3.10.2	Hydrogen Target	41
3.10.3	Polarized ^3He as a Neutron Target	42
3.10.4	Polarization Measurements	45
	NMR Measurements	45
	EPR Measurements	46
3.11	Data Acquisition	47
3.11.1	Triggers	48
4	GEM Detectors	53
4.1	Working Principles	53
4.1.1	GEM Foil	55
4.1.2	Readout	56
4.2	GEM Types	57
4.3	Design and Construction	58
4.3.1	High Voltage	61
4.3.2	Shielding	63
4.4	DAQ	64
4.4.1	APV	64
4.4.2	MPD	64
4.4.3	VTP	65
4.5	Analysis	65
4.5.1	Raw Signal	65
4.5.2	Pedestal Calculation	66
4.5.3	Common Mode	66
4.5.4	Sorting Method	67
4.5.5	Danning Method	67
4.5.6	Histogramming Method	69

4.5.7	Zero Suppression	70
4.5.8	Clustering	70
	1D Clustering	73
	2D Clustering	75
4.5.9	Track Finding	75
4.5.10	Spatial Resolution and Efficiency	76
5	GEM Analysis	77
5.1	Common Mode	77
	5.1.1 Rolling Common Mode	79
5.2	Common Mode Algorithm Studies	79
5.3	Shielding Results	83
5.4	Negative Signal Study	83
5.5	High Voltage Study	86
5.6	Spatial Resolution and Efficiency	89
6	Calibrations	93
6.1	Kinematic Notes	93
6.2	GEM Trackers	94
	6.2.1 Alignment	94
	6.2.2 Gain Matching	96
	6.2.3 ADC Thresholds	97
	6.2.4 Timing	99
6.3	Beam Position	100
6.4	Optics	101
6.5	Momentum	105
6.6	BigBite Calorimeter	106
6.7	Hodoscope	108

6.8	GRINCH	109
6.9	Hadron Calorimeter	110
7	Analysis	112
7.1	Analysis Software	112
7.2	Monte Carlo Simulation	113
7.3	Good Run Selection	114
7.4	Quasielastic Event Selection	115
7.4.1	Track Vertex	115
7.4.2	Preshower Energy	116
7.4.3	Invariant Mass	117
7.4.4	Coincidence Time	119
7.4.5	Hadron Particle Identification	120
7.4.6	Chosen Cuts	123
7.5	Simulation Fitting	124
7.6	Polarizations	126
7.7	Helicity Calculation	129
7.8	Asymmetry Formalism	130
7.8.1	Accidental Contamination	132
7.8.2	Nitrogen Contamination	134
7.8.3	Pion Contamination	136
7.8.4	Inelastic Contamination	140
7.8.5	Proton Contamination	146
7.8.6	Nuclear Effects and Final State Interactions	147
7.9	Run Summation	148
7.10	Finite Acceptance	149
7.11	G_E^n Extraction	150

8	Results and Outlook	152
8.1	Error Calculations	152
8.1.1	Asymmetry and Fractional Errors	152
8.1.2	Pion Errors	153
8.1.3	Proton Asymmetry	153
8.1.4	Nitrogen Fraction	154
8.1.5	Inelastic Fraction	154
8.1.6	Physical Asymmetry Error	155
8.1.7	G_E^n Error	157
8.2	Contamination Values	158
8.2.1	Accidentals	158
8.2.2	Nitrogen	159
8.2.3	Pion	160
8.2.4	Inelastic	160
8.2.5	Proton	161
8.2.6	FSI	162
8.3	Exploratory G_E^n Result	162
8.4	Variable Cuts	167
8.5	Conclusions and Future	168

Chapter 1

Introduction

On July 4th 2012 the world tuned in to the announcement of the Higgs particle discovery at CERN. This made international news and was widely celebrated as a great achievement in physics. With the Higgs confirmed we now know how elementary particles obtain their mass. However we must also keep in mind that most of the mass in the universe is not in elementary particles but in composite particles. Only about 1% of nucleon (proton and neutron) mass can be attributed to the Higgs mechanism, while the rest is due to the strong force and quark-gluon dynamics. Therefore understanding the nucleon dynamics is pivotal to understanding the world around us.

The proton and neutron, discovered in 1917 by Rutherford and 1932 by Chadwick, respectively, were originally thought to be elementary particles. Point particles of spin 1/2 are known to have magnetic moment

$$\mu = g \left(\frac{e}{2m} \right) \frac{\hbar}{2} \quad (1.1)$$

where g is the g -factor, e is the electron charge, m is the particle mass, and \hbar is Planck's constant. Let us denote the expected proton magnetic moment, μ_N , meanwhile the neutron is zero due to being uncharged. It came as a surprise in 1933 when Otto Stern measured the proton $\mu = 2.79\mu_N$ and then in 1940 Alvarez and Bloch measured the neutron $\mu = -1.91\mu_N$. These measurements were the first sign that that nucleons were composite particles.

In the 1950's Robert Hofstadter pioneered electron scattering off nucleons to determine their structure. His experiments were the first conclusive measurement that the scattering cross section deviated from point like behavior and he reported the first values of the proton's finite size [1]. This has laid the foundation for decades of elastic electron-nucleon scattering to probe the nucleon inner structure. As detector and

accelerator technologies have improved significantly the resolutions on the nucleon structure has been refined over time, but more work needs to be done. Jefferson lab has been on the forefront of elastic electron-nucleon scattering measurements for 30 years and now continues to push for even greater precision.

1.1 Elastic Electron-Nucleon Scattering

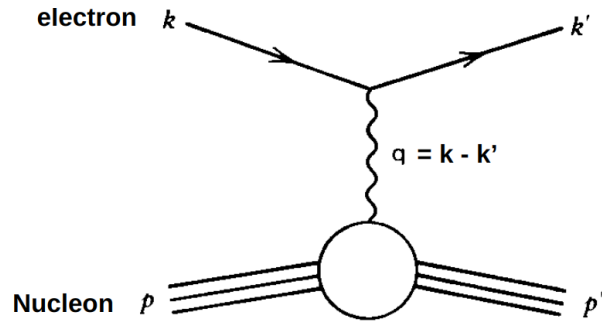


FIGURE 1.1: Feynman diagram of one photon exchange electron-nucleon scattering.

TABLE 1.1: Table of kinematic variables for electron-nucleon scattering.

Variable	Expression	Definition
k		Four-momentum of incoming electron
k'		Four-momentum of outgoing electron
p		Four-momentum of incoming nucleon
p'		Four-momentum of outgoing nucleon
θ		Electron Scattering angle
q	$q = k - k'$	Four-momentum exchange
ν	$E - E'$	Energy exchange
Q^2	$-q^2$	Virtuality of exchanged photon
W^2	$M^2 + 2\nu M - Q^2$	Invariant mass of the recoiled baryon
x	$Q^2/2p \cdot q$	Bjorken variable
ξ	$x/(2 - x)$	Skewness parameter
y	$(q \cdot p)/(k \cdot p)$	Fraction of electron energy lost
b_T		Transverse position of the parton scattered

The electromagnetic interaction is well understood to extreme experimental precision. It is then beneficial to use the well known electromagnetic interaction to investigate the structure of the lesser known nucleon. Figure 1.1 shows the one photon exchange Feynman diagram for electron scattering. In this first order approximation

the electron exchanges a singular virtual photon with the nucleon. This process has been well studied and therefore a common list of variables has been developed to help explain the scattering process. These variables are shown in table 1.1.

For scattering off a point like, spin 1/2 particle, with no other interactions except electromagnetic, the Dirac formula can be used

$$(i\gamma^\mu\delta_\mu - m)\psi = 0 \quad (1.2)$$

where m is the particle mass, ψ is the wave function, μ sums from 0 to 3, and γ^μ are the Dirac matrices [2]. Following the Feynman rules for QED we obtain the amplitude for the elastic scattering in figure 1.1

$$\mathcal{M} = e^2 [\bar{u}(k')\gamma^\mu u(k)] \frac{g_{\mu\nu}}{q^2} [\bar{u}(p')\gamma^\nu u(p)] \quad (1.3)$$

where e is the electron charge, $g_{\mu\nu}$ is the Minkowski metric, and u and \bar{u} are the spinor and adjoint solutions to the free Dirac equation.

The reaction rate for scattering off a point-like spin 1/2 particle can then be found using Fermi's golden rule

$$W = 2\pi|\mathcal{M}|^2\rho \quad (1.4)$$

where ρ is the density of states. From this we can calculate the differential cross section

$$\frac{d\sigma}{d\Omega} = \frac{W}{\Phi} \quad (1.5)$$

where Φ is the particle flux. The scattering cross section from a spinless point particle can be shown to be

$$\left(\frac{d\sigma}{d\Omega}\right)_{\text{Mott}} = \frac{\alpha^2 \cos^2(\theta/2)}{4E^2 \sin^4(\theta/2)} \quad (1.6)$$

and scattering off a 1/2 spin point particle will be

$$\frac{d\sigma}{d\Omega} = \left(\frac{d\sigma}{d\Omega}\right)_{\text{Mott}} \frac{E'}{E} \left(1 - \frac{q^2}{2M} \tan^2(\theta/2)\right) \quad (1.7)$$

where $\alpha = \frac{e^2}{4\pi}$ is the fine structure constant, θ is the electron scattering angle, and E is the incoming electron energy, E' is the outgoing electron energy, and M is the nucleon mass. The elastic scattering off of a spinless point particle is referred to as "Mott" scattering, hence the subscript in equation 1.6, and will be used in future sections.

1.2 Nucleon Structure

For a nucleon with structure the formalism presented in section 1.1 must be modified. The Feynman currents used for the amplitude calculation in equation 1.3 are modified to include information about the structure

$$\begin{aligned} j^\mu &= \bar{u}(k')\gamma^\mu u(k) \\ J^\mu &= \bar{u}(p')\Gamma^\mu u(p) \end{aligned} \quad (1.8)$$

where j^μ is the electron current and J^μ is the hadronic current from a nucleon with structure. The Γ^μ tensor holds the information about the nucleon structure. The amplitude then follows from equation 1.3 with the currents modified.

$$\mathcal{M} = e^2 j^\mu \frac{g^{\mu\nu}}{q^2} J^\nu \quad (1.9)$$

All possible linearly independent matrices that fit the interaction current may be candidates for Γ^μ . The full list of matrices is then

$$I, \gamma^\mu, \sigma^{\mu\nu}, \gamma^5, \gamma^\mu \gamma^5 \quad (1.10)$$

where I is the identity matrix and the other objects are further defined

$$\sigma^{\mu\nu} = \frac{1}{2}(\gamma^\mu \gamma^\nu - \gamma^\nu \gamma^\mu) \quad (1.11)$$

$$\gamma^5 = i\gamma^0 \gamma^1 \gamma^2 \gamma^3 \quad (1.12)$$

γ^5 anticommutes with parity operator and since the electromagnetic interaction conserves parity, the terms including γ^5 can be neglected. Equation 1.9 can be expanded to

$$\begin{aligned} J^\mu &= \bar{u}(p') \left[K_1(q^2)\gamma^\mu + iK_2(q^2)\sigma^{\mu\nu}(p - p')_\nu + iK_3(q^2)\sigma^{\mu\nu}(p + p')_\nu \right. \\ &\quad \left. + K_4(q^2)(p' - p)^\mu + K_5(q^2)(p + p')^\mu \right] u(p) \end{aligned} \quad (1.13)$$

where all K variables are real valued numbers and only dependent on Q^2 . Equation 1.13 can be reduced further using some identities. We first take advantage of the Gordon identity

$$\begin{aligned} \bar{u}\gamma^\mu u &= \frac{1}{2M}\bar{u}((p + p')^\mu + i\sigma^{\mu\nu}(p' - p)_\nu)u \Rightarrow \\ \bar{u}(p + p')^\mu u &= 2M\bar{u}(\gamma^\mu - i\sigma^{\mu\nu}(p' - p)_\nu)u \end{aligned} \quad (1.14)$$

This identity implies that the K_3 and K_5 term in equation 1.13 containing $(p + p')^\mu$ can be absorbed into other terms. Also we can enforce current conservation, $\delta_\mu J^\mu = 0$, so that any terms that do not vanish must have $K = 0$. For equation 1.13 this applies to terms with $(p - p')^\mu$ and therefore the K_4 term must be zero. Rearranging the terms in equation 1.13 and combining like factors we arrive at the final hadronic current

$$J^\mu = \bar{u}(p') \left[F_1(q^2) \gamma^\mu + \frac{i\kappa}{2M} F_2(q^2) \sigma^{\mu\nu} q_\nu \right] u(p) \quad (1.15)$$

where κ is the anomalous magnetic moment and $q_\nu = (p' - p)_\nu$ has been used.

F_1 and F_2 are independent functions of only Q^2 and hold the information of the nucleon structure. F_1 and F_2 are respectively referred to as the Pauli and Dirac form factors. As $Q^2 \rightarrow 0$ the F_1 and F_2 should reduce to values such that the scattering becomes point-like again. From this the cross section can be found

$$\frac{d\sigma}{d\Omega} = \left(\frac{d\sigma}{d\Omega} \right)_{\text{Mott}} \frac{E'}{E} \left[\left(F_1^2 - \frac{\kappa^2 q^2}{4M^2} F_2^2 \right) \cos^2 \frac{\theta}{2} - \frac{q^2}{2M^2} (F_1 + \kappa F_2)^2 \sin^2 \frac{\theta}{2} \right] \quad (1.16)$$

where $(d\sigma/d\Omega)_{\text{Mott}}$ comes from equation 1.6. This is known as the Rosenbluth formula [3] and it is the cross section for an electron scattering of a 1/2 spin particle with structure.

1.3 Electromagnetic Form Factors

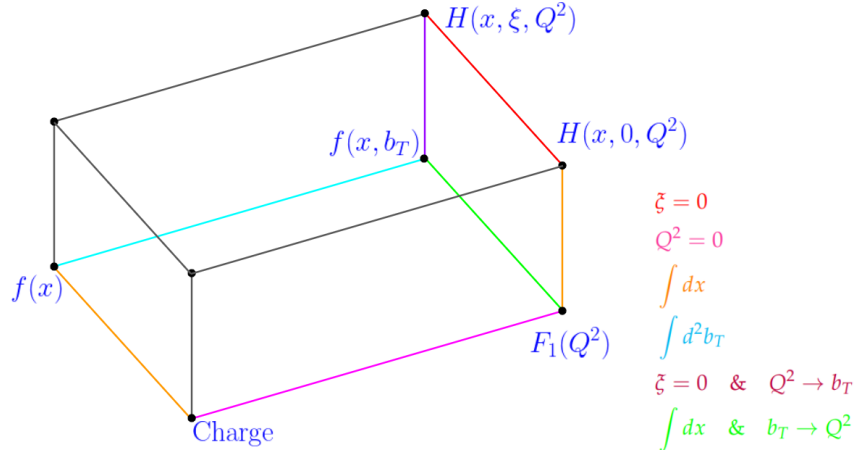


FIGURE 1.2: Diagram of different distribution functions and their relations, modified from [4]. The colors denote the variable integration or setting to convert between distributions. Note that $Q^2 \leftrightarrow b_T$ is a Fourier transform.

Figure 1.2 shows the many different distribution functions which describe the parton structure inside the nucleon. The distributions are listed below with increasing complexity:

- Parton distribution function (PDF), $f(x)$, describes the number density as a function of Bjorken x .
- Impact parameter distribution, $f(x, b_T)$, describes the number density as a function of both Bjorken x and the impact parameter.
- Generalized parton distribution (GPD), $H(x, \xi, Q^2)$, describes the number density as a function of Bjorken x , ξ , and Q^2 .

These distributions will not be discussed in detail in this work but they give important insights into the full parton picture of the nucleon. Figure 1.2 shows how the form factors are related to other distributions through parameter conversions. Theoretical models would like to encapsulate the entire parton picture, and therefore make predictions on the higher order distributions, like GPDs. The form factor data are simpler to measure compared to the higher order distributions and so more form factor data is currently available. The first moments of GPDs yield electromagnetic form factors,

and as such, high Q^2 form factor measurements anchor GPD models. Therefore, high resolution form factor results are critical for GPD theories to be compared against.

1.4 Sachs Form Factors

Sachs realized a certain linear combination of F_1 and F_2 is more convenient for measurement and interpretation purposes [5]. First we define some helpful new variables to reduce the number of terms.

$$\tau = \frac{Q^2}{4M^2} \quad (1.17)$$

$$\epsilon = \frac{1}{1 + 2(1 + \tau) \tan^2(\theta/2)} \quad (1.18)$$

ϵ is referred to as the polarization of the virtual photon. Sachs form factors are then defined as a linear combination of F_1 and F_2 .

$$G_E = F_1 - \kappa\tau F_2 \quad (1.19)$$

$$G_M = F_1 + \kappa F_2 \quad (1.20)$$

The cross section from equation 1.16 then reduces to the following simple formula utilizing these new definitions.

$$\frac{d\sigma}{d\Omega} = \left(\frac{d\sigma}{d\Omega} \right)_{\text{Mott}} \frac{\epsilon G_E^2 + \tau G_M^2}{\epsilon(1 + \tau)} \quad (1.21)$$

G_E and G_M are related to the Fourier transform of the electric charge and magnetic moment distribution in the infinite momentum frame. So far we have described scattering off "a nucleon", and now we can specifically describe the nucleon type using superscripts. $G_{E/M}^n$ is the neutron form factors and $G_{E/M}^p$ is the proton form factors. In the low energy limit, $Q^2 \rightarrow 0$, the form factors reduce to the point particle result for the neutron and proton.

$$\begin{aligned} G_E^p(0) &= 1 & G_M^p(0) &= \mu_p \\ G_E^n(0) &= 0 & G_M^n(0) &= \mu_n \end{aligned} \quad (1.22)$$

$\mu_p = 2.79$ and $\mu_n = -1.91$ are the anomalous magnetic moment factors for the proton and neutron respectively, referenced in equation 1.1. Similar subscripts for the proton

and neutron can be used for F_1 and F_2 .

1.4.1 Quark Flavor Decomposition

The elastic form factors have been presented for the nucleons, proton and neutron. We can combine the form factors to disentangle the individual quark flavor form factors for the proton, assuming iso-spin symmetry and the contributions from the heavier quarks to the nucleon form factors are negligible [6]

$$F_{1(2)}^u = 2F_{1(2)}^p + 2F_{1(2)}^n \quad F_{1(2)}^d = 2F_{1(2)}^n + 2F_{1(2)}^p \quad (1.23)$$

were $F_{1(2)}^u$ are the form factors for the up quark and $F_{1(2)}^d$ are the form factors for the down quark. This gives information about the up and down quark content inside the proton. The decomposition requires all elastic electric and magnetic form factors for the proton and neutron to be known at each Q^2 . The neutron electric form factor, G_E^n , is currently the limiting value, since it has historically been the most difficult to measure. G_M^p has been measured up to $Q^2 = 30 \text{ GeV}^2$, G_E^p has been measured up to $Q^2 = 8.5 \text{ GeV}^2$, and G_M^n has been measured up to $Q^2 = 19.5 \text{ GeV}^2$, while G_E^n has only been measured to $Q^2 = 3.4 \text{ GeV}^2$. Therefore the flavor decomposition can only be calculated up to $Q^2 = 3.4$.

Figure 1.3 shows the current world data for the quark flavor decomposition. It was found that the down quark contribution was suppressed in both form factors for the proton. This difference in scaling is possible evidence of diquark degrees of freedom [7]. A simple explanation of this is shown in figure 1.4. Any scattering off the down quark must have two gluon contributions, adding a $1/Q^4$ factor, while scattering off the up quark may only have one gluon contribution, adding a $1/Q^2$ factor. Extensions of the G_E^n data will further illuminate the quark flavor scaling and their individual contributions. This will give an important glimpse into the internal makeup of the proton and neutron.

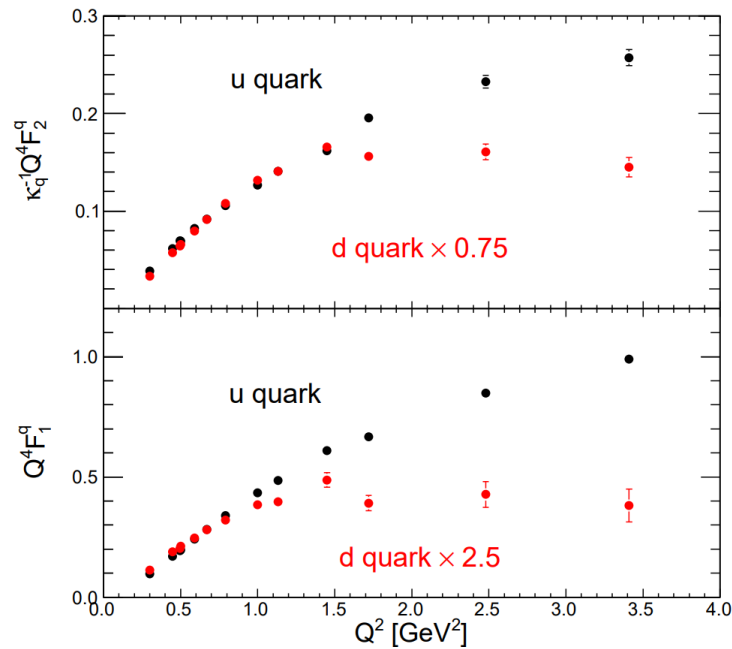


FIGURE 1.3: The Q^2 -dependence for the u and d contributions to the proton form factors [6].

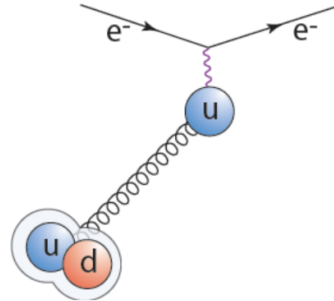


FIGURE 1.4: Simple picture of diquark correlations in the proton. Note that the down quark must be part of the diquark here.

1.5 Previous G_E^n Measurements

The form factors have been measured for decades, with improving energy ranges and resolution over time. The proton form factors have been measured to higher Q^2 values than the neutron, as has been previously described, because of the simplicity of proton targets compared to neutron targets. The proton does have a rich history of innovative experimental methods used to improve resolutions and push boundaries, however this work will focus on the neutron and not detail the proton data. The neutron has been historically more difficult to measure with high resolution since it must be part of a

composite nucleon. All experimental techniques seek to best isolate the neutron scattering events. Here we will overview the history of G_E^n measurements to date.

1.5.1 Rosenbluth Separation

A nucleus with some proton content must be studied to measure scattering off a neutron. The simplest such nucleus is the deuteron, which has one proton and one neutron. Using the Rosenbluth formulation we can define the reduced cross section of scattering off the nucleon with structure to the nucleon without structure

$$\sigma_R = \frac{\frac{d\sigma}{d\Omega}}{\left(\frac{d\sigma}{d\Omega}\right)_{\text{Mott}}} \frac{\epsilon(1+\tau)}{\tau} = \frac{\epsilon}{\tau} G_E^2 + G_M^2 \quad (1.24)$$

where $d\sigma/d\Omega$ is the cross section given by equation 1.21. Experiments can carefully choose scattering kinematics varying the beam energy, E , and scattering angle, θ , such that τ remains constant while varying ϵ . σ_R can then be measured at multiple ϵ points and a linear fit can be applied using $\frac{1}{\tau} G_E^2$ as the slope and G_M^2 as the y-intercept. This extracts G_E and G_M for a single Q^2 point.

These type of measurements were done in the 60's up to $Q^2 = 0.12$ [8][9] GeV^2 and in 1971 the DESY experiment with Glaser [10] measured this up to $Q^2 = 0.6$ GeV^2 . Rosenbluth separation is inherently difficult for measuring G_E^n due to it being a small value compared to G_M^n which would simultaneously be measured using this method. Small deviations on the linear fit would lead to large errors on a small y-intercept extraction. This extraction requires theoretical knowledge of the deuteron wave function which comes with significant systematic effects. This and other higher order effects make it a challenge, even more so at higher Q^2 .

1.5.2 Polarization Method

Using polarized electron beams and polarized targets has been found to be a more accurate method for measuring G_E^n than the Rosenbluth method. Polarization observables can be measured for scattering a polarized beam off an unpolarized target with

the following observables [11]

$$\begin{aligned}
 I_0 P_t &= -2\sqrt{\tau(1+\tau)}G_E G_M \tan(\theta/2) \\
 I_0 P_l &= \frac{E_e + E_{e'}}{M} \sqrt{\tau(1+\tau)}G_M^2 \tan^2(\theta/2) \\
 I_0 &= G_E^2 + \frac{\tau}{\epsilon}G_M^2
 \end{aligned} \tag{1.25}$$

where P_t is the polarization component transverse to the momentum transfer and P_l is the component parallel to the momentum transfer. Combining this together one can extract the form factors from the polarization components.

$$\frac{G_E}{G_M} = -\frac{P_t}{P_l} \frac{E_e + E_{e'}}{2M} \tan(\theta/2) \tag{1.26}$$

For ^2H targets measurements have been achieved up to $Q^2 = 1.45 \text{ GeV}^2$ by 2003 [12][13].

Polarized beams scattering off polarized targets were further proposed as a method to enhance the measurement sensitivity to the neutron. This method is called double polarization. For polarized ^2H targets measurements have been achieved up to $Q^2 = 1.0 \text{ GeV}^2$ by 2004 [14][15]. Polarized ^3He targets were proposed to further enhance G_E^n extractions in 1984 [16]. The cross sectional asymmetry can be used to obtain the G_E^n when G_M^n is already known [17]. This method has been used in several experiments to measure G_E^n up to $Q^2 = 3.41 \text{ GeV}^2$ by 2010 [18][19][20][21]. We will go over this method in detail in the following chapters.

1.5.3 GEN-I Experiment

The experimental method used in this work was previously used in the GEN-I experiment at Jefferson Lab [20]. This experiment collided a polarized electron beam on a polarized ^3He target and extracted G_E^n values up to $Q^2 = 3.41 \text{ GeV}^2$. The results can be seen on figure 1.5 compared to selected world data. This method was able to achieve a 17% relative error at the highest Q^2 value. It's main limitations were the available beam energy and the detector technology to handle the experimental needs. These have improved since the measurement in 2008 and we can now extend this same procedure to even higher Q^2 .

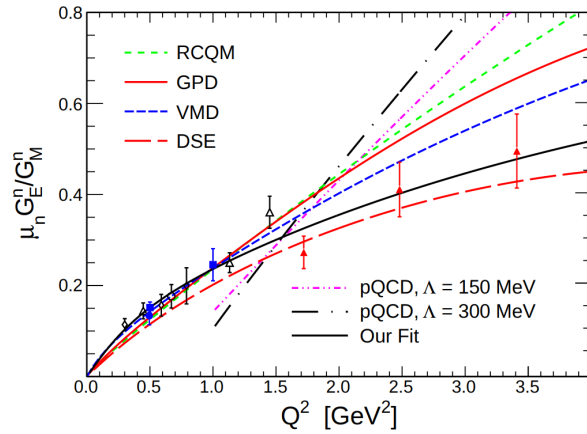


FIGURE 1.5: Result of GEN-I measurement, taken from [20]. The red triangles show the GEN-I double polarization results while the points below $Q^2 = 1.72 \text{ GeV}^2$ are selected world data from a variety of experiments.

1.6 Nucleon Models

Nucleon form factor models seek to match the existing data and predict new data. Validating or excluding these models yields valuable insight into the nucleon structure given the assumptions each model is based on. Since no data currently exists above $Q^2 = 3.4 \text{ GeV}^2$, extending this region can provide a strong constraints for selecting models. The theory curves for various models described in this section are shown in figure 1.6 along with selected world data.

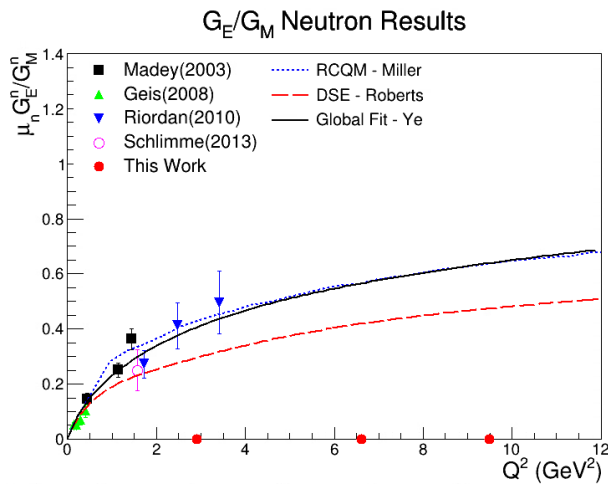


FIGURE 1.6: Selected G_E^n world data with proposed Q^2 points from this work on the horizontal axis. Selected theory curves are also drawn.

1.6.1 pQCD

One important property of QCD is that adequately above $Q^2 \sim 1 \text{ GeV}^2$ the strong coupling constant, α_s , becomes small enough that perturbation theory (pQCD) may become applicable. pQCD inspired models with quark angular momentum included predict the form factors to be [22]

$$\frac{F_2(Q^2)}{F_1(Q^2)} \propto \frac{\log^2(\frac{Q^2}{\Lambda^2})}{Q^2} \Rightarrow \frac{G_E}{G_M} = \frac{Q^2 - \kappa\tau\alpha \log^2(\frac{Q^2}{\Lambda^2})}{Q^2 + \kappa\alpha \log^2(\frac{Q^2}{\Lambda^2})} \quad (1.27)$$

where $\Lambda = 300 \text{ MeV}$ and α is a constant. The GEN-I results indicated a disagreement with with pQCD model (figure 1.5). It is possible that Q^2 of 3.4 GeV^2 was not large enough for pQCD to take effect. There is a strong theoretical basis that pQCD must take effect at a sufficiently large Q^2 . It will be interesting to see as the Q^2 range is extended if results begin to agree with this pQCD based prediction.

1.6.2 Relativistic Constituent Quark Model

Jerry Miller and Ian Clöet have proposed an updated relativistic constituent quark model (RCQM) [23] for nucleon form factors based on quark and di-quark degrees of freedom. This model assumes quark-diquark valence quarks immersed in a pion cloud. Note that the prediction from Miller's earlier version of RCQM shown in figure 1.5 is significantly different from the GEN-I results. However, the model was updated in the years after the GEN-I results to include diquark degrees of freedom instead of assuming three valence quarks and the theory parameters have been updated. The most recent theory prediction is seen in figure 1.6.

1.6.3 Dyson-Schwinger Equations

The Dyson-Schwinger equations (DSE) based models are used to calculate an explicit symmetry-preserving truncation of all quantum field equations for the nucleon bound state system. This methodology is able to provide parameter free predictions for all of the elastic form factors. Previous algorithms have limited these calculations to $Q^2 < 4 \text{ GeV}^2$ but recent DSE methods have employed a statistical Schlessinger point method (SPM) [24] to extend calculations to 12 GeV^2 [25]. Notably previous DSE predictions

had found a zero crossing of G_E^n/G_M^n around 10 GeV² but new results find a zero crossing not expected before 20 GeV². The most recent theory prediction is seen in figure 1.6

1.6.4 Generalized Parton Distributions

Generalized parton distributions (GPDs) are used to describe the hadron structure in the perturbative and non-perturbative regions. GPDs can describe the multivariable parton distribution. These variables can be obtained through Deeply Virtual Compton Scattering (DVCS) processes. Factorization can separate the perturbative part and the non-perturbative part can be extracted, which is also universal and process independent [26]. From DVCS the $H^q(x, \xi, Q^2)$ and $E^q(x, \xi, Q^2)$ GPDs can be extracted. Here ξ is the asymmetry in the quark momentum. From these the form factors can then be found as the first moment of the GPDs

$$\begin{aligned} F_1^q(Q^2) &= \int_{-1}^1 dx H^q(x, 0, Q^2) \\ F_2^q(Q^2) &= \int_{-1}^1 dx E^q(x, 0, Q^2) \end{aligned} \quad (1.28)$$

where q is the quark flavor. From the quark form factors above the nucleon form factors can be calculated [27]

$$\begin{aligned} F_i^p(Q^2) &= \frac{2}{3}F_i^u - \frac{1}{3}F_i^d - \frac{1}{3}F_i^s \\ F_i^n(Q^2) &= -\frac{1}{3}F_i^u + \frac{2}{3}F_i^d - \frac{1}{3}F_i^s \end{aligned} \quad (1.29)$$

where $i = 1, 2$.

Therefore, in principle, theories with GPD predictions can be used to calculate the elastic form factors. This can be used to test the theories. However, there is currently a very limited amount of GPD world data. It is then more useful to take the form factor measurements and work backwards and constrain GPDs and theory predictions until more GPD data is collected.

1.7 Parameterizations

It is desirable to have a functional form from which to evaluate the form factors as a function of Q^2 . Here we will describe some of the most common parameterizations used.

1.7.1 Dipole

The dipole form factor comes from the interpretation of the Sachs form factors as the Fourier transform of the electric and magnetic moment distributions. Assuming a spherically symmetrical charge distribution the form factor is as follows.

$$G_D(Q^2) = \left(1 + \frac{Q^2}{0.71\text{GeV}^2}\right)^{-2} = \frac{G_M^p}{\mu_p} = \frac{G_M^n}{\mu_n} \quad (1.30)$$

Therefore results of $G_M^{n/p}$ measurements are usually compared to $\mu_{n/p}G_D$. It has been found that G_E^p drops off rapidly from G_D after $Q^2 = 1 \text{ GeV}^2$ while G_E^n has never fit this parameterization since $G_E^n(0) = 0$ while $G_D(0) = 1$.

1.7.2 Glaster

An alternative to the dipole parameterization to calculate G_E^n was presented by Glaster in 1971 [10] and takes the form

$$G_E^n(Q^2) = -\frac{\mu_n\tau}{1 + 5.6\tau}G_D(Q^2) \quad (1.31)$$

where G_D comes from equation 1.30 and τ come from equation 1.17. This form matches the necessary condition $G_E^n(0) = 0$. This simple functional form had fit new data well for 30 years after its inception. However a more accurate model can be developed.

1.7.3 Kelly

In 2004 Kelly [28] provided new fits motivated by pQCD scaling rules to parameterize G_E^p , G_M^p , and G_M^n . This follows the form

$$G(Q^2) \propto \frac{\sum_{k=0}^n a_k \tau^k}{1 + \sum_{k=1}^{n+2} b_k \tau^k} \quad (1.32)$$

with limits such that as $Q^2 \rightarrow 0$ then $G_E^p \rightarrow 1$ and the G_M values go to their respective magnetic moments. The Glaser form then remains for the G_E^n function

$$G_E^n(Q^2) = \frac{A\tau}{1 + B\tau} G_D(Q^2) \quad (1.33)$$

where current world data fits use $A = 1.70$ and $B = 2.00$ [20].

1.7.4 Global Fits

Recent global fitting to the world data has been performed by Zhihong Ye et al in 2018 [29]. This uses a polynomial expansion for all form factors.

$$G(Q^2) = \sum_{k=0}^{\max} z = \frac{\sqrt{t_{\text{cut}} + Q^2} - \sqrt{t_{\text{cut}} + t_0}}{\sqrt{t_{\text{cut}} + Q^2} + \sqrt{t_{\text{cut}} + t_0}} \quad (1.34)$$

where $t_{\text{cut}} = 4m_\pi^2$ and $t_0 = -0.7$. These fit results are the most up to date and the most accurate available. The world data and resulting fits are shown in figure 1.7. Throughout this work when a form factor value is needed at a specific Q^2 the value and error is taken from this fit parameterization.

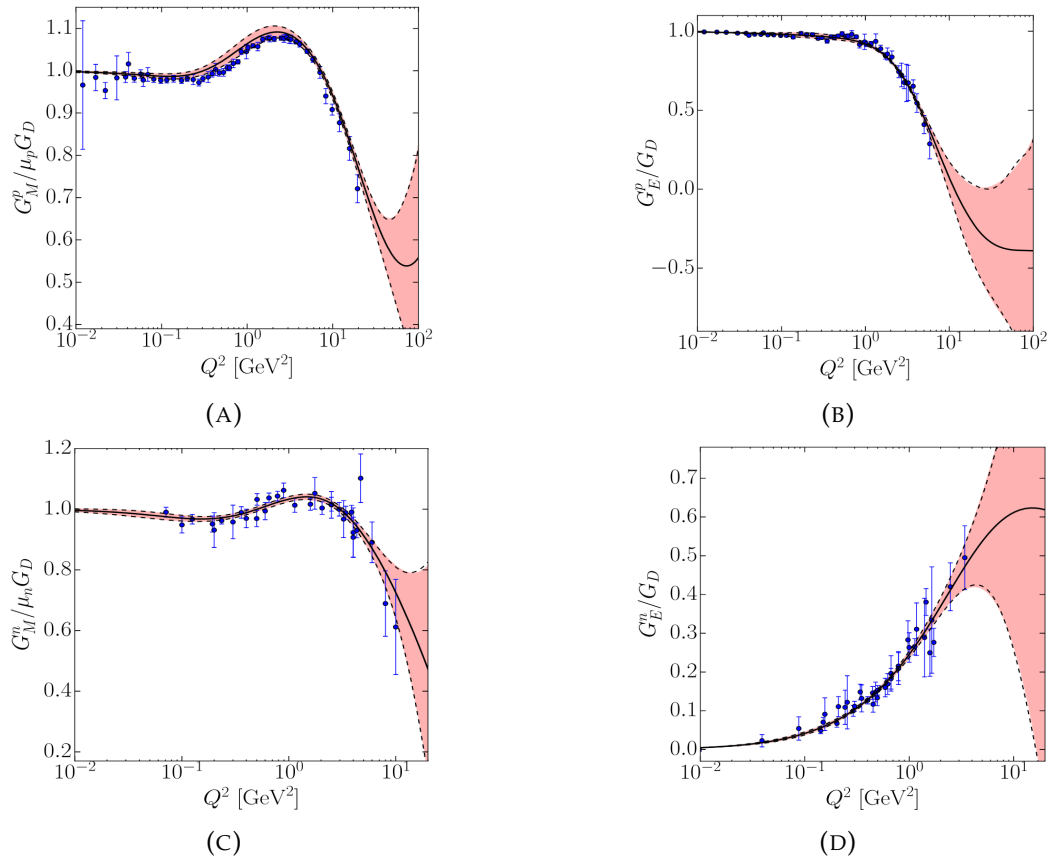


FIGURE 1.7: World data with the Ye parameterization fits (solid curves) and error bands (red curves). Data points represent selected world data used in the fitting procedure [29].

Chapter 2

SBS Program

Jefferson Lab (JLab) has been at the forefront of elastic form factor measurements for decades. In 2017 the accelerator beam energy was upgraded from 6 GeV to 12 GeV. This will be described in more detail later in section 3.3. With higher beam energies and detector technology improvements all form factors could now be measured at higher Q^2 . The Super BigBite (SBS) program at JLab seeks to extend the measurements for G_E^p , G_M^n , and G_E^n to the highest Q^2 so far. These experimental programs will be referred to as GEp-V, GMn, and GEN-II. This thesis will focus on the G_E^n measurement (GEN-II) but the equipment is similar for all experiments and commissioning data from other experiments will be relevant.

Detailed explanation of all parts of the experimental setup will be provided in chapter 3. Here we will go over a few differences between the three experiments. All experiments will collide a electron beam onto a fixed target and will investigate elastic scattering. GEN-II and GEp-V make use of the polarized electron beam while GMn does not require polarized electrons. The typical detector packages are shown in figure 2.1. All measurements have an electron arm and a hadron arm. All detectors systems were newly installed for the SBS program, therefore significant efforts went into understanding and calibrating the detector response for the first time.

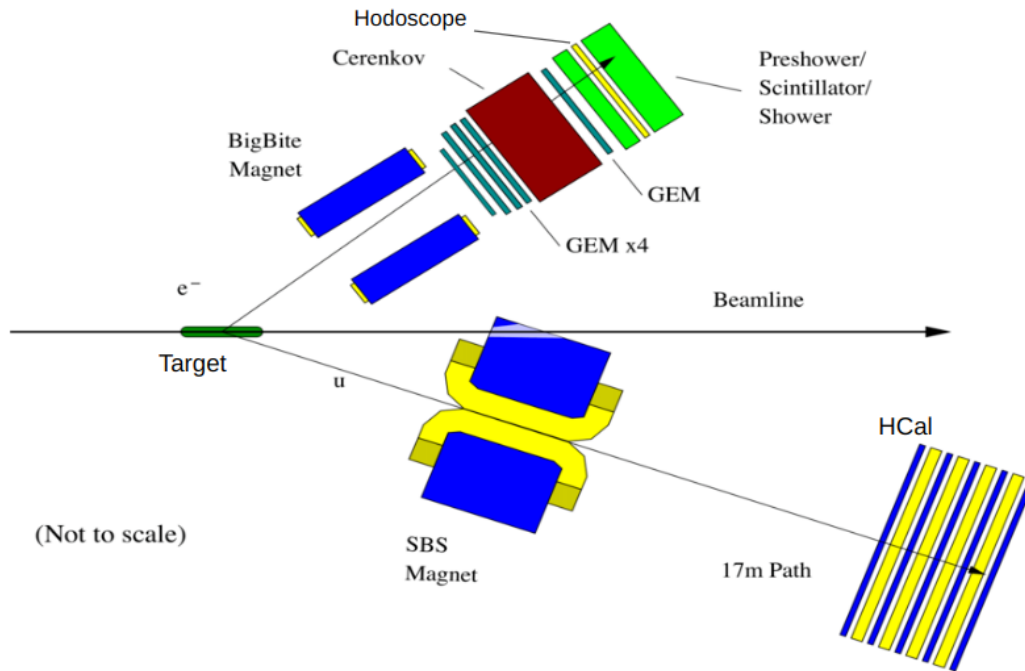


FIGURE 2.1: Experimental setup used for both GMn and GEN-II. Elastic electrons scatter beam left (top of picture) into a detector package and hadrons scatter beam right (bottom of picture) into a separate detector package.

2.1 GMn Experiment

The GMn experiment [30] was completed in 2022 and was the first experiment in the SBS program and the first experiment to use the newly built detector packages. The target was liquid deuterium and the luminosity was $\sim 10^{38} \text{ cm}^{-2}/\text{s}$. This experiment was important to calibrate all the detectors systems and to check gas electron multiplier (GEM) tracker performance. The GEM trackers had not been operated at exposure rates this high before, integrated over the detector area, and therefore some changes were found to be necessary for the hardware and software in preparation for future higher luminosity experiments. We will go into more detail on this in chapter 5.

2.2 GEN-II Experiment

The GEN-II [31][32] experiment was completed in 2023 and had the exact same setup as GMn except for a polarized ^3He target. The occupancies found in GEN-II were 20%

of the GMn data set and therefore the tracking was much more manageable. However several important GEM tracker changes were implemented during GMn, which were then tested for improved performance during GEN-II.

2.3 GEp-V Experiment

The GEp-V experiment [33][34] will start running at the end of 2024 and has a few detector changes from the previous experiments. We will not go into detail here since it is outside of the scope of this work. This experiment is notable here because the luminosities are significantly higher than for GMn or GEN-II. Therefore the high luminosity studies on the GEM trackers done during GMn and GEN-II were for the ultimate purpose of ensuring that the extreme rates of GEp-V can be handled in the future.

Chapter 3

GEN-II Experiment Overview

The JLab designation for this experiment is E12-09-016. It ran from October 2022 - March 2023 and took data at $Q^2 = 2.90, 6.50, \text{ and } 9.47 \text{ GeV}^2$ in hall A. The experiment kinematics are labeled in table 3.1. Notably Kin1 was used for detector and target commissioning and therefore will not be mentioned much in this analysis. Kin2, Kin3, and Kin4 represent all the production data. There was an extension to collect more data at Kin4, which ran again from September - October 2023.

The measurement was done by colliding a polarized electron beam on a polarized ^3He target using the double polarization method. This method allows the extraction of the electron scattering asymmetry between the two beam helicity states. The asymmetry is used to obtain the G_E^n / G_M^n ratio. GEN-II is an extension of the GEN-I data taken in 2008 but with improved equipment and beam energy. On the electron arm side, the spectrometer, called BigBite (BB), was installed with all new equipment. Most notably, the GEM trackers, which can handle higher rates than the old drift chambers could. These will be described in detail in chapter 4. On the hadron arm the Super BigBite (SBS) magnet was used to magnetically separate protons and neutrons and the hadron calorimeter (HCal) was used to measure timing and position. Furthermore a new ^3He target was designed to improve luminosity and polarization yields. This chapter will overview detector systems and the analysis method.

TABLE 3.1: Table of kinematic settings for GEN-II run.

Kin	Q^2 (GeV ²)	E_{beam} (GeV)	θ_{BB} (deg)	θ_{SBS} (deg)	run time (days)
1	1.79	2.206	29.5	34.7	1
2	3.00	4.291	29.5	34.7	13
3	6.83	6.373	36.5	22.1	33
4	9.82	8.448	35	18	86

3.1 Kinematic Notes

It will be beneficial to now list some nuances of the data collection which will be important for calibrations and data analysis discussions. Most important is the extension the the GEN-II run in September - October of 2023. This extra time was granted to collect more data at Kin4 and so the October 2022 - March 2023 data taken at Kin4 is referred to as Kin4a and the September - October 2023 data is referred to as Kin4b. However the Kin4b data was taken very recently relative to the writing of this work and has not had the time to go through all the calibrations that Kin4a has. Therefore we have no choice but to leave this data out of the analysis for a future study to include it into the formalism that will be described here. Throughout this work we will now use Kin4 to mean Kin4a, but it is important to remember that Kin4b will eventually double the statistics of the entire Kin4 data set.

3.2 Double Polarization Method

We have already shown the scattering cross section for an unpolarized electron on an unpolarized target in equation 1.21. With a polarized electron beam the differential cross section can be defined for each helicity state as

$$\sigma_h = \Sigma + h\Delta \quad (3.1)$$

where $h = \pm 1$ depending on the electron polarization parallel for anti-parallel to the beam direction, Σ is the unpolarized cross section, and Δ is the polarized cross section.

Figure 3.1 shows the kinematics for electron scattering off a polarized target. The Σ is simply the unpolarized cross section which we have already shown

$$\Sigma = \left(\frac{d\sigma}{d\Omega} \right)_{\text{Mott}} \frac{\epsilon G_E^2 + \tau G_M^2}{\epsilon(1 + \tau)} \quad (3.2)$$

The polarized cross section can then be calculated for a specific helicity state [35]

$$\Delta = -2 \left(\frac{d\sigma}{d\Omega} \right)_{\text{Mott}} \sqrt{\frac{\tau}{1 + \tau}} \tan(\theta/2) \left[\sqrt{\tau(1 + (1 + \tau) \tan^2(\theta/2))} G_M^2 \cos \theta^* \right. \\ \left. + G_M G_E \sin \theta^* \cos \phi^* \right] \quad (3.3)$$

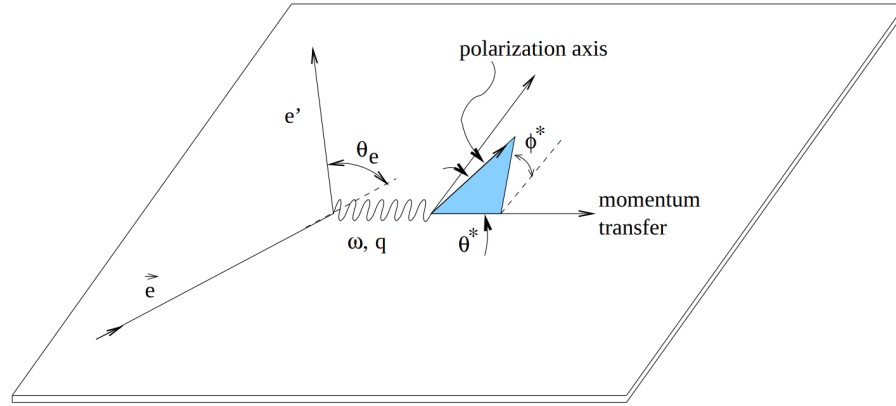


FIGURE 3.1: Kinematics of elastic electron scattering from polarized target.

where θ is the electron scattering angle, θ^* and ϕ^* are the polar and azimuthal angles between the q vector and the target polarization vector, and τ was previously defined in equation 1.17.

We can now form the physics asymmetry for different beam helicities

$$A_{\text{phys}} = \frac{\sigma_+ - \sigma_-}{\sigma_+ + \sigma_-} = \frac{\Delta}{\Sigma} = -\Lambda \frac{2\sqrt{\tau(\tau+1)} \tan(\theta/2) \sin \theta^* \cos \phi^*}{\Lambda^2 + (\tau + 2\tau(1+\tau) \tan^2(\theta/2))} - \frac{2\tau\sqrt{1+\tau + (1+\tau)^2 \tan^2(\theta/2)} \tan(\theta/2) \cos \theta^*}{\Lambda^2 + (\tau + 2\tau(1+\tau) \tan^2(\theta/2))} \quad (3.4)$$

where we introduce $\Lambda = G_E/G_M$, which is convenient since this ratio will come up many times in this work and is our measurement result. If the asymmetry and the scattered electron kinematics are measured then equation 3.4 leaves only the form factor ratio, Λ , as an unknown. G_M^n has been separately measured in companion experiments [30] and can be combined with Λ to extract G_E^n at each Q^2 value.

The polarization angles give a fraction of polarization in relation to the q vector. It is convenient to rewrite this as

$$P_x = \sin \theta^* \cos \phi^* \quad (3.5)$$

$$P_z = \cos \theta^* \quad (3.6)$$

where P_x is the polarization along x-direction and P_z is the polarization along the z-direction in the Target Coordinate System for the hadron, which will be explained in section 3.5. One can also think of P_x as the polarization perpendicular to the q vector

and P_z as the polarization parallel to the q vector. We find that equation 3.4 can be re-written in terms of two asymmetries, perpendicular and parallel polarization components.

$$A_{\perp} = -\Lambda \frac{2\sqrt{\tau(\tau+1)} \tan(\theta/2)}{\Lambda^2 + (\tau + 2\tau(1 + \tau) \tan^2(\theta/2))} \quad (3.7)$$

$$A_{\parallel} = -\frac{2\tau\sqrt{1 + \tau + (1 + \tau)^2 \tan^2(\theta/2)} \tan(\theta/2)}{\Lambda^2 + (\tau + 2\tau(1 + \tau) \tan^2(\theta/2))} \quad (3.8)$$

$$A_{\text{phys}} = A_{\perp} P_x + A_{\parallel} P_z \quad (3.9)$$

Λ is small for the neutron, therefore the denominator, which is the same for both equation directions, is not largely affected by Λ . This means that A_{\perp} is more sensitive to Λ since it there is an extra Λ factor in the numerator. Therefore it is better to choose the target polarization axis as perpendicular as possible to the average q vector direction to enhance the A_{\perp} , and therefore overall A_{phys} , measurement. The asymmetry in equation 3.4 can be further simplified by rewriting it in terms of P_x , P_z , ϵ , and τ .

$$A_{\text{phys}} = -\frac{1}{1 + \frac{\epsilon}{\tau}\Lambda^2} \left[\Lambda \sqrt{\frac{2\epsilon(1 - \epsilon)}{\tau}} P_x + \sqrt{1 - \epsilon^2} P_z \right] \quad (3.10)$$

This outlines the method for extracting G_E^n which will be used in this analysis. The formalism presented here assumes 100% beam polarization and 100% polarized neutron target. In reality these polarization's will be lower and need to be accounted for. Also nuclear corrections will need to be accounted for to extract the exact neutron component from the ^3He asymmetry.

3.3 CEBAF Accelerator

The continuous electron beam accelerator facility (CEBAF) at JLab can deliver continuous electrons at a high polarization ($\sim 86\%$) with beam energies up to 12 GeV and currents up to 150 μA [36]. The beam can then be provided to 4 separate halls simultaneously, A, B, C, D. The new CEBAF has been upgraded from an older 6 GeV CEBAF [37] which was used in GEn-I. The 12 GeV beam has made higher Q^2 measurements possible. Figure 3.2 shows the accelerator design and lists some of the changes implemented to increase to 12 GeV. The two linear accelerators (linac) shown added 0.6 GeV

per pass around the accelerator after the upgrade to a total of 2.2 GeV per pass.

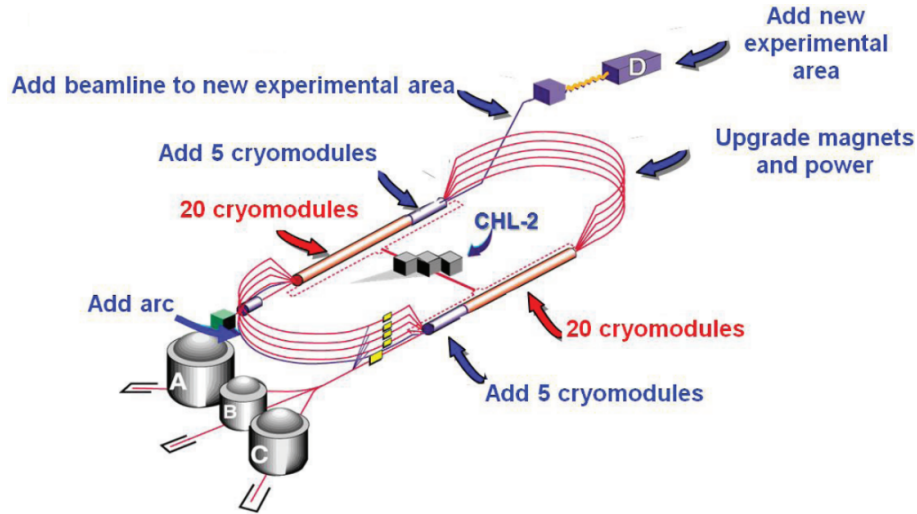


FIGURE 3.2: Schematic of the CEBAF accelerator at JLab after the 12 GeV upgrade.

The injector creates the beam for the main accelerator using a strained GaAs photocathode that produces polarized electrons with energies of 100 keV. Diode laser light passes through an RTP crystal which determines the light polarization and in turn polarizes the electrons. This will be explained in more detail in section 3.8.2

3.4 Experimental Setup

The experimental setup for GEn-II is shown in figure 3.3. All of the equipment shown, except for the polarized ^3He target, were used during the GMn experiment the year before, in 2021. The electron beam collides with the polarized ^3He target on the left and the BigBite (BB) and Super BigBite (SBS) magnets were positioned to match the elastic electron-nucleon scattering kinematics for each Q^2 point. BB and SBS are both large acceptance spectrometers and can handle high rates expected in GEn-II.

The BB arm will measure the electrons track, momentum, energy, and timing, all with great precision. This will be elaborated on in section 3.6. Meanwhile, the SBS arm only has the hadron calorimeter (HCal) so its strength is deflecting charged particles away through the magnet. The HCal will then measure the particle position, energy, and timing for the scattered nucleons. The position and timing resolution will be good,

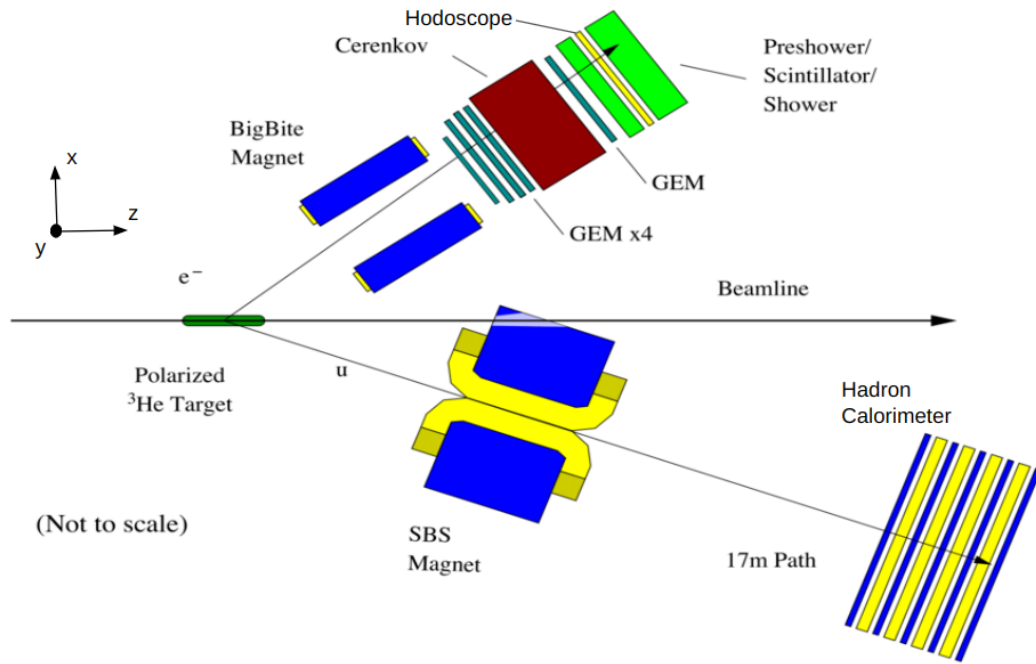


FIGURE 3.3: GEn-II experimental setup.

meanwhile the energy resolution is only 40%, but is not critical for this analysis. We will detail this in section 3.7.

3.5 Coordinate Systems

There are three main coordinate systems used in Hall A. There is the hall coordinate system, which describes the absolute position of everything in the hall, and the target coordinate system for each detector arm, which describes the scattered particle position as it travels from the target to the detector. This means that the BB and SBS arms each have a different target coordinate system.

- **Hall Coordinate System (HCS):** The origin of the system is right at the middle of the target. This is also seen in figure 3.3. \hat{z} points down the beamline in the direction the electrons are traveling. \hat{y} points straight up at the ceiling. \hat{x} then forms a right handed system ($\hat{x} = \hat{y} \times \hat{z}$) and points the left of the beamline, facing down the directions the beam travels.
- **Target Coordinate System (TCS):** The origin of the system is also at the middle of the target. \hat{z} points down at the center of the spectrometer arm. \hat{x} points down

at the ground in the positive dispersion direction. \hat{y} then forms a right handed system $\hat{y} = \hat{z} \times \hat{x}$. Given the \hat{z} for each BB and SBS the detector TCS are not the same. Also notably for BB \hat{y} points away from the beamline while for SBS \hat{y} points towards the beamline.

3.6 Electron Arm Detectors

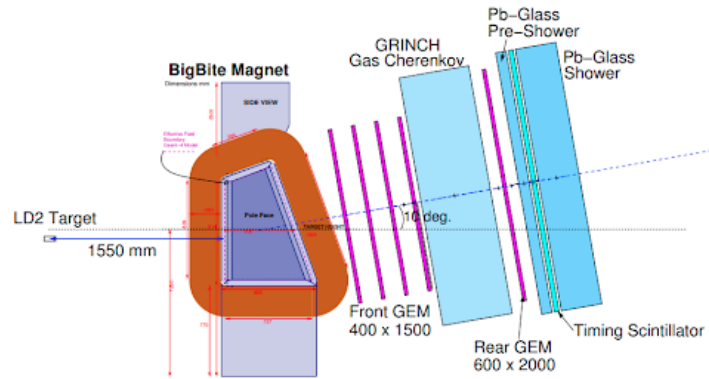


FIGURE 3.4: Schematic of components that make up the BB arm.

All pieces of the BB arm can be seen in figure 3.4. The package of detectors is used to measure everything about the scattered electron. Its design was such that it covers ~ 70 msr acceptance and has good vertex and momentum resolutions. The BB magnet is used to bend electrons for good momentum resolution. For tracking it achieved $70 \mu\text{m}$ position resolution and a momentum resolution of $\sigma_p/p \sim 1.5\%$. The energy resolution is approximately 6.5% and timing resolution could be achieved at 750 ps. We will now detail the subsystems.

3.6.1 GEM Trackers

There are five layers of gas electron multiplier (GEM) trackers which are used to reconstruct the particle track. The GEM layer positions can be seen in figure 3.4 while the layer makeup is shown in figure 3.5. The first four GEM modules are large single modules of $40 \text{ cm} \times 150 \text{ cm}$ while the fifth and last layer is $50 \text{ cm} \times 200 \text{ cm}$ but comprised of four smaller modules stacked side by side. These detectors replaced the older drift chambers, which were previously used for tracking in the BB spectrometer for the GEN-I experiment, and can operate at higher rates. After bending through the BB magnet

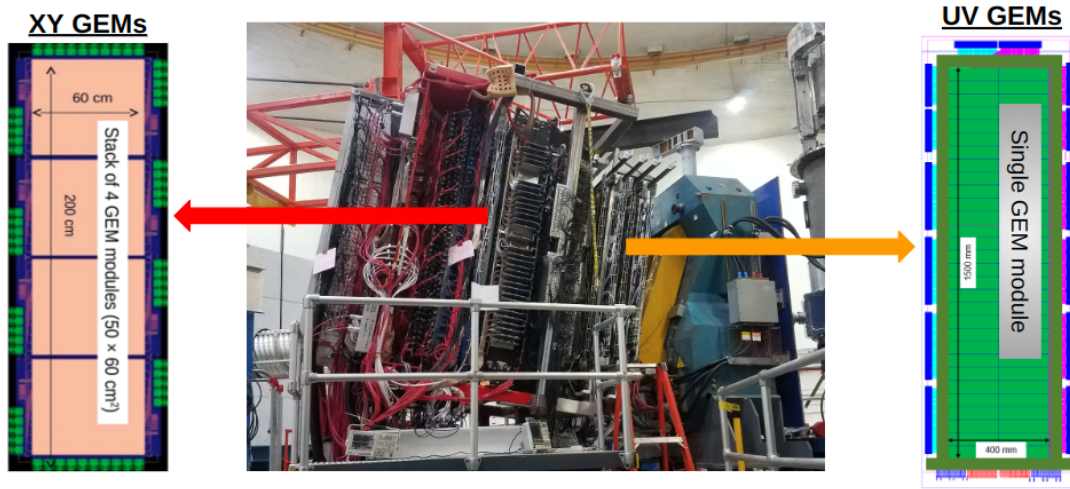


FIGURE 3.5: GEM detectors in the BB apparatus. The front four layers are single UV GEMs. The back layer consists of four XY GEMs combined.

the particle travels again in a straight line through the rest of the detector stack. Each layer forms a point on the track and so multiple layers are needed to reconstruct the full track. The fifth GEM layer is placed further back in the stack, after the Gas Cerenkov detector, to improve tracking results based on its increased distance from the rest of the layers. These detectors will be a specific focus of this work and will be described in thorough detail in chapter 4.

3.6.2 BigBite Calorimeter

The BigBite calorimeter (BBCal) mainly provides the energy measurement for the electron arm. BBCal is made of lead-glass blocks, which can provide energy resolution of $\sim 6\%$ and timing resolution of 2.5 ns [39]. The lead-glass blocks are connected to photomultiplier tubes (PMTs) which read out the signal ADC and TDC. The BBCal energy is used as a trigger for GEN-II. For each kinematic the energy thresholds are set for elastically scattered electrons, and so any energy measurement in BBCal above this threshold triggers an event. BBCal is separated into two main sections, the preshower and shower, as shown in figure 3.6. Although electrons lose $\sim 97\%$ of their energy in the preshower blocks, this energy creates an electromagnetic shower which continues on out of the preshower, since it is only 9 cm thick. The majority of the energy is then deposited in the shower blocks behind the preshower.

Preshower

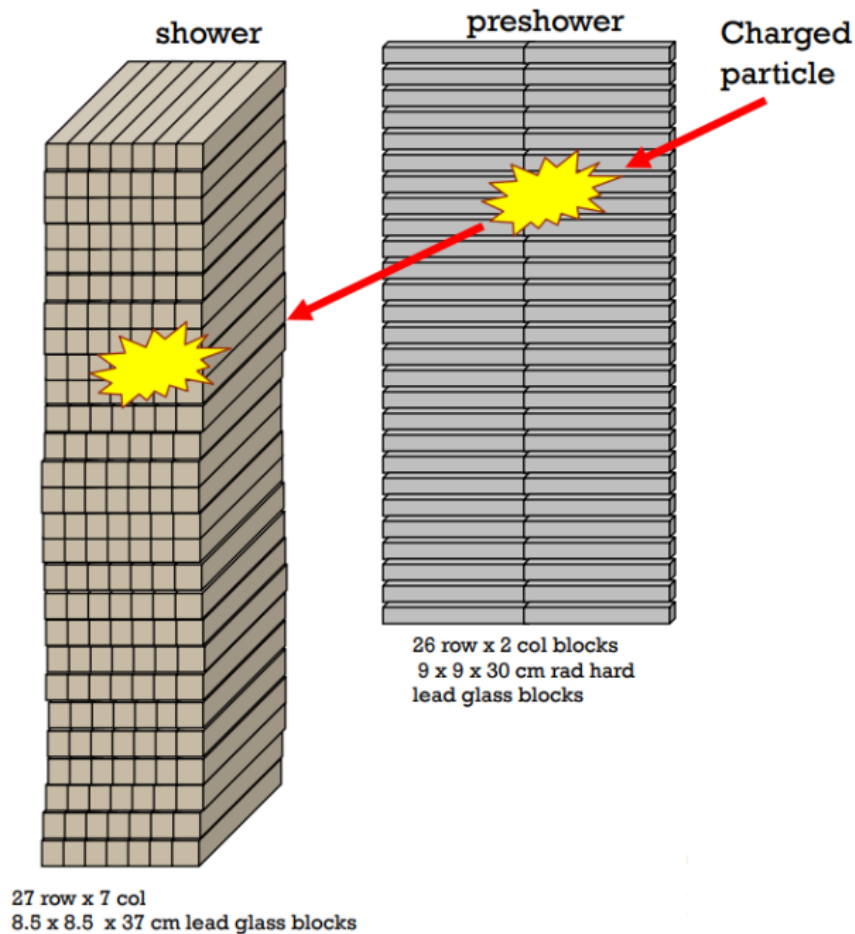


FIGURE 3.6: Schematic of the BBCal preshower and shower. Particles first pass through the preshower and then the shower, depositing energy in each. Image from [38]

The preshower is one layer of BBCal blocks which are stacked such that the PMTs are facing the left and right of the BB apparatus and the particles traverse the shortest length of the block. Each block is $9 \times 9 \times 30$ cm. The electron only travels through the width of the block, 9 cm, and therefore deposits about 30% of its total energy, on average, in the preshower. This is useful for removing pion signals because pions have a different energy deposition mechanism in lead-glass. The probability of pion nuclear interactions is much lower in the 9 cm thickness, and so the pions deposit a much lower energy in the preshower. The preshower will then provide a clear energy difference to cut out the pion background, which appears as a large peak at low energies.

Shower

The shower section is an array of bars stacked such that the PMTs are facing out

the back of BB so the particles have to travel through the full length, 37 cm. Each block is $8.5 \times 8.5 \times 37$ cm. This block length is long enough to capture the full energy of the scattered electron. On average the electrons deposit 70% of their total energy in the shower. Therefore the preshower and shower energy combined can be used to resolve the full energy of a an electron.

3.6.3 GRINCH

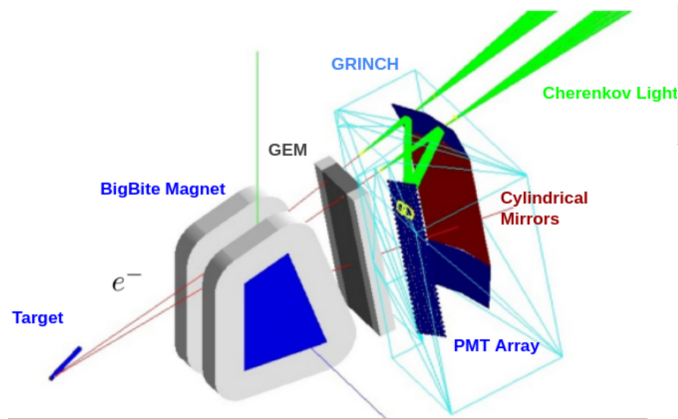


FIGURE 3.7: Diagram of Cherenkov radiation as particles pass through the GRINCH, from [40].

The Gas Ring ImagiNg CHerenkov (GRINCH) detector is used for particle identification. The detector is made of four highly reflective cylindrical mirrors, which reflect Cherenkov light onto 510 PMTs which read out the signal. It is well understood that particles traveling faster than the speed of light in a medium emit Cherenkov radiation. An electron's velocity is larger than pion's velocity at a given momentum. Therefore a medium can be carefully selected such that electron produce Cherenkov radiation while pions do not. For this purpose C_4F_8O heavy gas was used. For pion momentum less than 2.7 GeV pions should not produce radiation. The GRINCH then provides an excellent handle on pion and electron separation.

3.6.4 Hodoscope

The purpose of the hodoscope is to provide precise timing measurements. It is an array of 89 plastic scintillator bars vertically stacked. Each bar has a PMT on both sides to read out the signal traveling both left and right. This signal is then sent to a ADC for

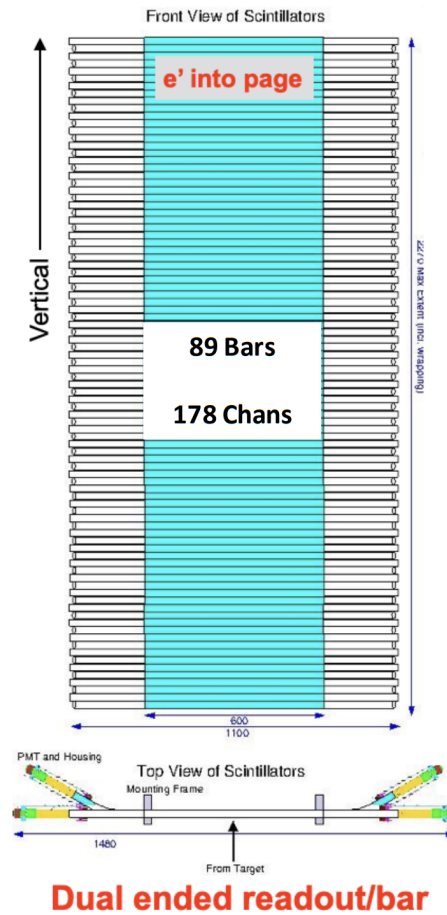


FIGURE 3.8: Schematic of the hodoscope from [41].

signal amplitude and a TDC to record the timing information. The hodoscope was able to achieve timing resolution ~ 600 ps. The difference in signal arrival times at left and right scintillators can also be used to calculate horizontal positions along the hodoscope.

3.7 Hadron Arm Detectors

The hadron arm similarly has acceptance of ~ 70 msr to match BB. It only consists of the Super BigBite (SBS) magnet and the hadron calorimeter (HCal). The purpose here is to maximize the neutron detection efficiency while also separating scattered proton and inelastics events. Other experiments in the SBS program, such as GMn, need to measure the proton data to form the ratio of proton and neutron quasi-elastic cross sections; therefore, the HCal distance from the SBS magnet was decreased and the SBS



FIGURE 3.9: Picture of the hadron arm in hall A. On the left is the SBS magnet and the right is HCal, located 17 m away.

magnetic field was decreased to ensure that the full quasi-elastic proton distribution was captured in HCal in those experiments. In GEN-II we are only interested in the neutron data and so the SBS magnetic field and the HCal distance are maximized to sweep charged particles as far away as possible.

3.7.1 Hadron Calorimeter

The hadron calorimeter (HCal) is a sampling, segmented calorimeter. Each block is alternating iron absorbers and scintillators, as seen in figure 3.11. The iron increases the probability of a hadronic shower from a nuclear interaction caused by the incoming proton and neutrons. The wavelength shifting fiber runs between blocks and captures light generated in the hadronic showers from the scintillators which finally goes to the PMT where the signal ADC and TDC is measured. The blocks are placed in an array seen in figure 3.10. This segmentation method yields >95% detection efficiency for protons and neutrons but comes at the cost of worse energy resolution, which is found to be $\sim 40\%$. The timing resolution is ~ 1.6 ns and position resolution ~ 5 cm. The position resolution is critical since it is used to detect the amount of particle deflection through the SBS magnet. This deflection will be used as particle identification later on.

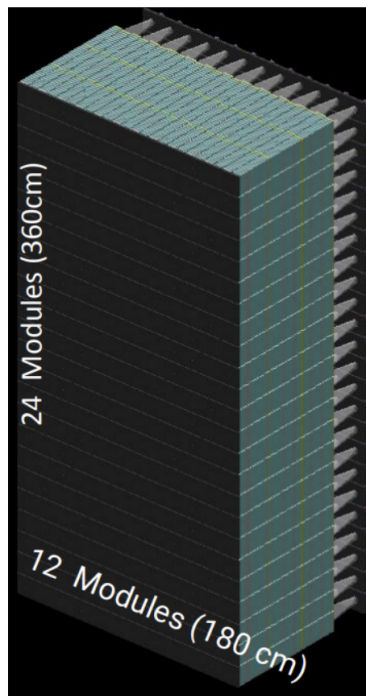


FIGURE 3.10: Schematic of HCal.

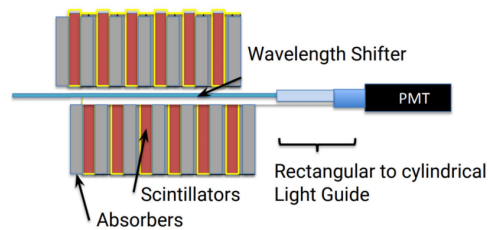


FIGURE 3.11: Schematic of one HCal block.

3.8 Beamline

The hall A beamline gives critical information about the beam properties before it reaches the target. This allows us to know the initial electron kinematics with high accuracy before collision with the target.

3.8.1 Beam Position

Beam position monitors (BPMs) use wire antennas to non-intrusively measure the transverse position of the beam as it travels through. In hall A there are two BPMs, referred



FIGURE 3.12: Diagram of the beam going through the BPMs and reaching the target.

to as upstream and downstream of the beam, which are located 7.53 m and 2.38 m upstream of the hall origin. The BPMs give the beam x and y position at two places along the z direction, from which the beam can be projected to its position at the target. It is important to spread out the beam energy deposition over the surface of the target or else the sensitive glass cell may wear down over time and break. This is done by two pairs of raster magnets upstream of the target which use magnetic fields that slightly deflect the beam. The rasters were set to spread the beam into a circle of diameter 5 mm.

The upstream and downstream BPMs are referred to as BPM A and B. The x and y positions for both BPMs are recorded. The two raster magnets are referred to as raster 1 and raster 2. The x and y currents are recorded for each raster. These values are used to reconstruct the beam position at the target. The electronics that record the BPM is delayed and not accurate on an event by event basis, meanwhile the raster current is accurate to the event. Therefore the BPM information is used to calculate the center position of the raster circle over the course of a many events. The raster currents are then used for each event to calculate offset from the center.

From the two BPMs we can calculate the position at the target as

$$\text{BPM}_{\text{tgt}} = (\text{BPM}_B - \text{BPM}_A) \frac{\text{BPM}_{A,\text{pos}}}{\text{BPM}_L} + \text{BPM}_A \quad (3.11)$$

where BPM_A and BPM_B are the upstream and downstream BPMs, $\text{BPM}_{A,\text{pos}}$ is the upstream BPM distance to the target center, and BPM_L is the distance between BPMA and BPMB. Formula 3.11 is valid for both x and y directions. The raster readback gives a measure of the current, but the absolute value is not relevant. Instead we obtain the

raster current minimum and maximum values. The middle value is then taken to be the beam at the center, while the minimum moves the beam to the negative radius and the maximum moves the beam to the positive radius. This is done for both x and y directions to make a circle. There is a further complication that some kinematic settings used only the upstream raster and some used both rasters. For two rasters, the total raster is the difference between the upstream raster and the downstream raster. We define the raster value as follows, for one raster

$$\text{Rast} = \text{Rast}_{\text{up}} \quad (3.12)$$

where Rast_{up} is the upstream raster reading. Then for two rasters we define the raster as follows

$$\text{Rast} = \text{Rast}_{\text{up}} - \text{Rast}_{\text{dn}} \quad (3.13)$$

where Rast_{dn} is the downstream raster reading. We can then define some useful variables for the raster

$$\begin{aligned} \text{Rast}_{\text{cen}} &= \frac{\text{Rast}_{\text{min}} + \text{Rast}_{\text{max}}}{2} \\ \text{Rast}_{\text{scale}} &= \frac{D_{\text{rast}}}{\text{Rast}_{\text{max}} + \text{Rast}_{\text{min}}} \end{aligned} \quad (3.14)$$

where D_{rast} is the raster diameter, Rast_{min} is the minimum raster value, and Rast_{max} is the maximum raster value. Recall that all the raster values have an x and y current value. In this equation the raster minimum or maximum comes from equation 3.12 or 3.13 depending if one or both rasters, respectively, were used. From equations 3.14 we can now combine the raster with the BPM value from equation 3.11 to get the position at an event

$$x/y_{\text{beam}} = \text{BPM}_{x/y,\text{tgt}} + (\text{Rast}_{x/y} - \text{Rast}_{\text{cen},x/y})\text{Rast}_{\text{scale},x/y} \quad (3.15)$$

where x/y_{beam} is the beam position at the target in the hall coordinate system.

3.8.2 Beam Helicity

The beam helicity is flipped ± 1 to achieve our asymmetry measurement. In simple terms, a laser light is used on a GaAs photocathode and through a photoelectric-like effect produces electrons for the beam. The laser is circularly polarized left and right to induce a +1 or -1 helicity outgoing electron. The entire process can be seen in figure

inserted it would flip the laser polarization and therefore the final electron polarization. This is used to check that there are no asymmetry systematic offsets from the laser electronics. We made sure to evenly distribute out statistics with IHWP set in or out so that the systematics should cancel. The IHWP state (in or out) is also recorded to determine the helicity state. This combined with the pattern determination above provides the absolute helicity value on an event by event basis.

It is also important that the helicity generated by the beam is distributed between +1 and -1 states as evenly as possible in order not to bias the asymmetry reading in our experiment. This can be achieved by monitoring the beam charge asymmetry. To do this we calculate the pattern asymmetry

$$A_{\text{patt}} = \text{Pol}_{\text{true}} \frac{Y_1 + Y_4 - Y_2 - Y_3}{Y_1 + Y_2 + Y_3 + Y_4} \quad (3.16)$$

where Pol_{true} , is the true polarity of the first event in the window, Y_1 to Y_4 is the total yield for event 1 to 4 in the helicity window. The Pockels cell voltages can then be tweaked to reduce A_{patt} as low as possible. For GEN-II the charge asymmetry was kept around 100 ppm on average and never above 500 ppm. These asymmetry levels are significantly lower than the several % physics asymmetry measured in GEN-II experiment and therefore it was decided not to use an active asymmetry correction and instead to check the values a few times a day and correct the Pockels cell voltages as needed.

3.8.3 Beam Polarization

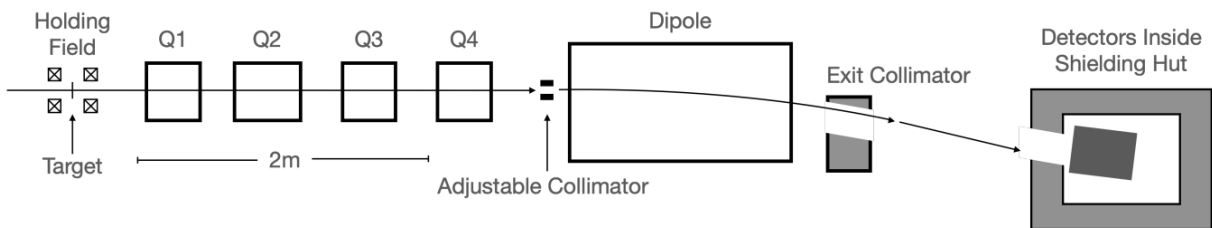


FIGURE 3.14: Diagram of the Møller measurement used in hall A [43].

The physics asymmetry measured in GEN-II depends directly on the beam polarization. As such, the beam polarization must be measured with great accuracy. Møller scattering is a high precision method of measuring the polarization and has been performed at hall A for years [43]. Møller scattering of polarized electrons scattering off a

polarized target, $\vec{e}^- + \vec{e}^- \rightarrow e^- + e^-$, is well understood in QED and a helicity driven asymmetry arises. The measured asymmetry is then

$$A_{\text{meas}} = -P_{\text{beam}}P_{\text{target}}\langle A_{zz} \rangle \quad (3.17)$$

where P_{target} is the polarization of the Møller target and $\langle A_{zz} \rangle$ is the average longitudinal analyzing power of the process. Following first order QED calculation

$$A_{zz}(\theta) = \frac{(7 + \cos^2(\theta)) \sin^2(\theta)}{(3 + \cos^2(\theta))^2} \quad (3.18)$$

where θ is the scattering angle in the center of mass frame. The detector is placed at $\theta = \pi/2$ which maximizes A_{zz} to 7/9. This large analyzing power is what makes Møller scattering so useful for polarization measurement. The Møller target is a pure iron foil target, polarized perpendicular to the beam by magnetic fields in excess of 2 T. This greatly reduces the systematic errors from the P_{target} term down to 0.24%. This method has proven to produce beam polarization measurements with better than 1% precision in hall A [43].

This process is completely destructive to the beam and so dedicated time on the Møller measurement must take away from the ^3He running. Statistics are easily acquired for Møller scattering so only a few hours of data must be collected to calculate the polarization with 1% precision. Therefore a few times each accelerator setting the measurement is performed briefly and the result is assumed to be the same during production running as long as the accelerator settings are unchanged. If any of the accelerator settings are changed a new Møller measurement must be performed or else the beam polarization is unknown.

3.9 Magnets and Optics

Charged particles are deflected through the BB and SBS magnets on their way to the electron arm and hadron arm detector packages. It is then necessary to have a thorough understanding of how the particle position in the spectrometers translates backwards through the magnet to a position at the target interaction point. This is called magnetic optics. In case of the electron spectrometer, BigBite, this is done by placing a "sieve" in front of the magnet which allows particles to pass through holes at known positions

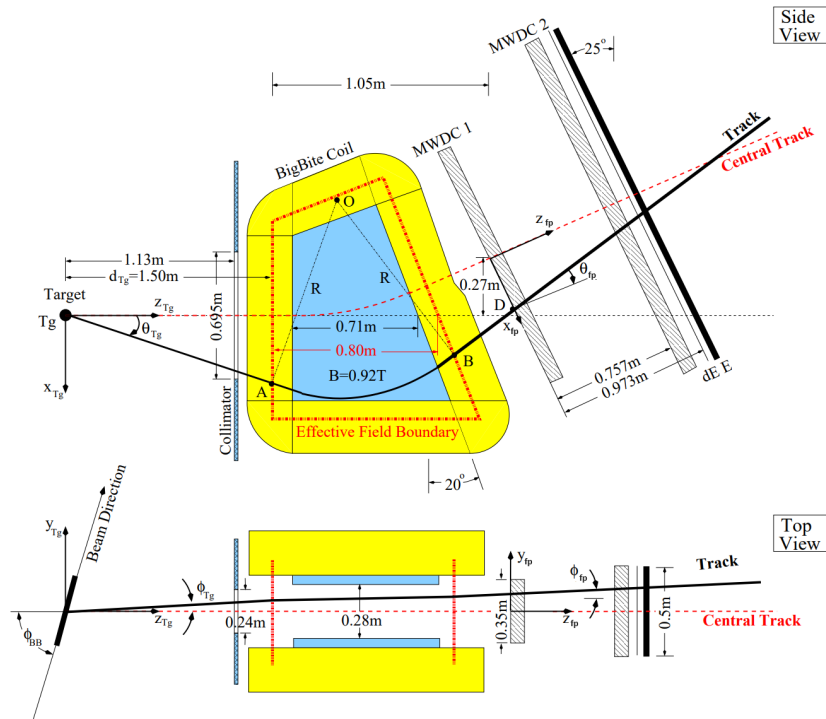
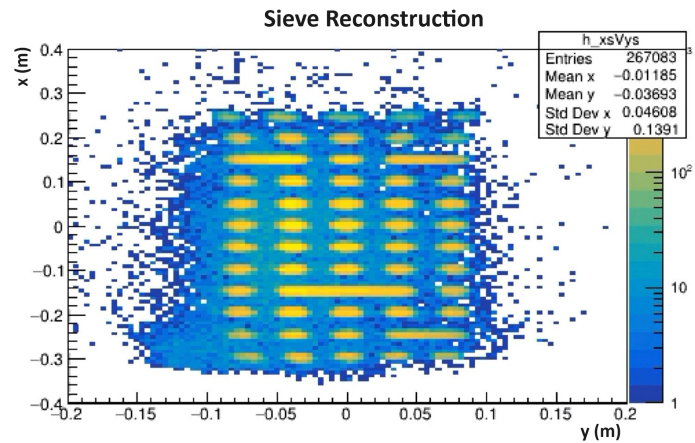


FIGURE 3.15: Coordinate system of a charged particle passing through the BB magnet, from [44]. Note that the detectors referenced (Collimator, and MWDCs) are for an old setup and not relevant to this experiment.



(A)



(B)

FIGURE 3.16: (A) Picture of the sieve plate. (B) Reconstructed events with the sieve plate in front of BB. The hole pattern can clearly be seen.

and blocks mostly anything else, see figures 3.16. The known positions of the sieve holes can then be used to calculate how the particles can be projected backwards to the

target. This procedure is only in place for the BB spectrometer since we need to determine the scattered electron kinematics with high resolution. The SBS magnet does not have a sieve and therefore tracks cannot be projected through the magnet. However, excellent resolution on the scattered electron allows for an elastic kinematic calculation of the scattered hadron. This will be discussed more in chapter 7.

The spectrometer measures the track position and angle at the “focal plane”, meaning at the detectors. This will be referred to as $x_{fp}, y_{fp}, \theta_{fp}, \phi_{fp}$. The variables must be translated back to the “target” coordinates, $y_{tg}, \theta_{tg}, \phi_{tg}$ at the vertex, which are in the TCS. See figure 3.15 for definitions of the optics coordinates. An expansion is done around the focal plane variables to reconstruct the target variables

$$y/\theta/\phi_{tg} = \sum_{i=0}^{i=N} \sum_{j=0}^{j=N-i} \sum_{k=0}^{k=N-i-j} \sum_{l=0}^{l=N-i-j-k} \sum_{m=0}^{m=N-i-j-k-l} C_{ijkl}^{Y/T/P} x_{fp}^m y_{fp}^l \theta_{fp}^k \phi_{fp}^j x_{tg}^i \quad (3.19)$$

where N is the order of the expansion and $C^{Y/T/P}$ is a set of coefficients where Y correlates to y_{tg} , T correlates to θ_{tg} , and P correlates to ϕ_{tg} . For this experiment the BB and SBS magnets are simple dipoles and therefore the expansion order is set to $N = 2$ as to not overfit the results. From the other target variables z_{tg} and x_{tg} can also be calculated using the relations

$$z_{tg} = \frac{-y_{tg}}{\sin(\theta_{BB}) + \cos(\theta_{BB})\phi_{tg}} \quad x_{tg} = -\cos(\theta_{BB})z_{tg}\theta_{tg} - y_{beam} \quad (3.20)$$

where θ_{BB} is the BB spectrometer angle, available from the spectrometer survey, and y_{beam} is from equation 3.15. We note here the complication that z_{tg} is calculated using x_{tg} and x_{tg} is calculated using z_{tg} . Therefore an iterative process is used for z_{tg} and x_{tg} to converge to final values.

The momentum must also be reconstructed. Since the magnet is primarily a dipole, the complicated expansion above would over fit any momentum reconstruction. The bend angle based on momentum is known to be

$$p\theta_{bend} \propto \int B \cdot dl \quad (3.21)$$

where p is the particle momentum and θ_{bend} is the angle of deflection through the magnet. It is then natural that $p\theta_{bend}$ should depend on the incoming angle, θ_{tg} . Data from BB elastic scattering off H_2 is shown in figure 3.17. It is clear that it is a linear relation

and therefore the momentum relationship is defined as

$$p = A(1 + B\theta_{\text{tg}})/\theta_{\text{bend}} \quad (3.22)$$

where the A and B are constant coefficients.

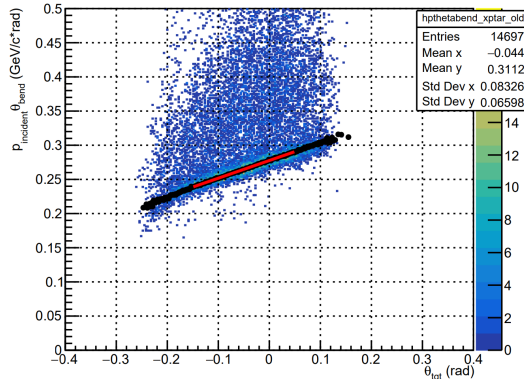


FIGURE 3.17: Elastic data from scattering off H_2 in the BB magnet shows that $p\theta_{\text{bend}}$ is linear with θ_{tg} .

3.10 Targets

3.10.1 Carbon Foil Target

Carbon foil targets are used for a variety of calibrations purposes. Figure 3.18 shows the carbon target schematic. The carbon foils are each 0.01 inch thick [45]. The single foil target is used for accurately calibrating the positions of the detectors. The carbon hole targets were used to ensure that the beam is at the expected position and the beam angle is within acceptable limits, otherwise it could damage the glass cell. Both carbon hole sizes are 2mm in diameter. All eight carbon foils are used for magnetic optics calibrations.

3.10.2 Hydrogen Target

Since hydrogen is a singular proton nucleus its physics signals are extremely clean. For this reason the H_2 target is used for calibrations purposes. The glass cell is the same dimensions of the ^3He target chamber shown in figure 3.19, but instead filled with hydrogen gas. It is mainly used for BB momentum and detector calibration.

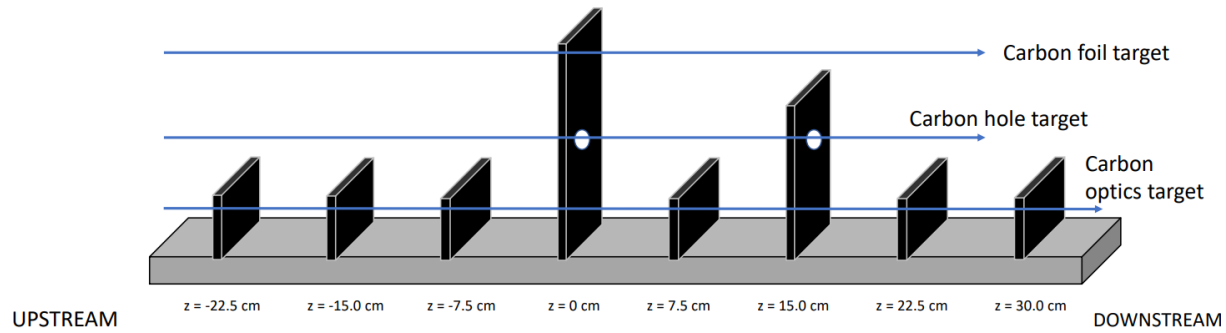


FIGURE 3.18: Optics target used in the GEN-II experiment, taken from [45].

3.10.3 Polarized ^3He as a Neutron Target

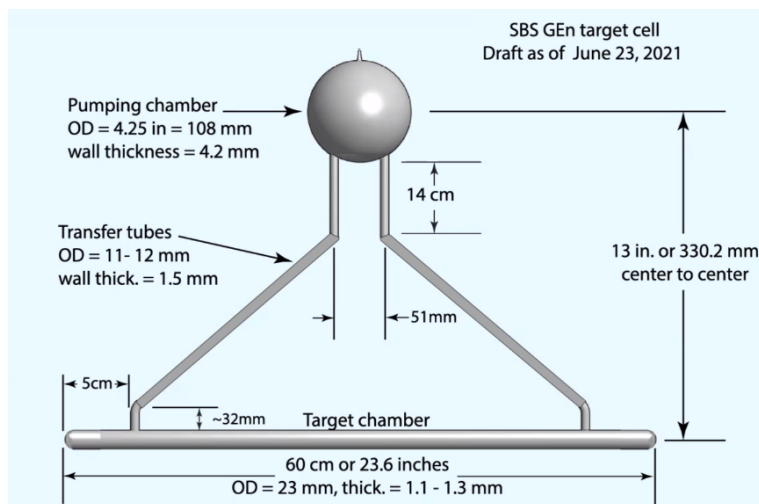


FIGURE 3.19: Schematic of the ^3He target used in GEN-II.

A new ^3He target was developed for this experiment with many improvements over the past designs. The main improvements were increasing the target length while simultaneously increasing the total polarization. This target was developed by Gordon Cates' group at the University of Virginia, improving upon previous designs by their group. The target uses spin exchange optical pumping (SEOP) technique to polarize the ^3He . The final target design can be seen in figure 3.19. The target is made of three main parts

- **Pumping Chamber:** This part contains an alkali mixture of Rb and K with the ^3He gas. This sphere was also inside a heater and had laser trained on it for optical pumping.

- **Transfer Tubes:** The transfer tubes' purpose is for the polarized gas from the pumping chamber to flow down the the target chamber. Convection is used for the gas flow which increases polarization efficiency. One side of the transfer tubes is heated to induce convective flow so the gas continuously flows around the system. This ensures that the newly polarized ^3He in the pumping chamber is constantly circulated into the target chamber.
- **Target Chamber:** This is where the beam travels through and interacts with the ^3He . The beam depolarizes the atoms but newly polarized ^3He is constantly being introduced through the transfer tubes. We will discuss later how effectively the polarization transfers from the pumping chamber to the target chamber.

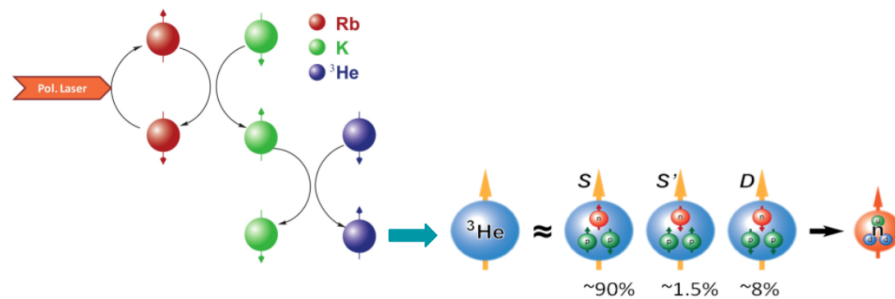


FIGURE 3.20: SEOP process to polarize the neutron. Laser polarize Rb atoms which through collisions pass on the polarization to K atoms and then ^3He .

Polarized ^3He , which contains one neutron and two protons, is well known to act as an effective neutron target. Due to the possible states in the ^3He nucleus with one neutron and two protons, it has been found that the neutron holds $\sim 87\%$ of the total polarization [46]. There is $\sim 3\%$ polarization on the proton, which we will need to account for in the proton contamination in our final calculations.

Figure 3.20 shows the entire process of how the polarization is transferred to the neutron. Spin exchange optical pumping (SEOP) is a well understood process and is utilized here to polarize ^3He . A rubidium and potassium alkali mix used to transfer polarization to ^3He . The whole system is also inside a magnetic field.

- **Optical Pumping:** The Zeeman splitting for ^{85}Rb is shown in figure 3.21. Circularly polarized laser light at 795 nm excites the D1 transition. The transition must follow the selection rule $\Delta m_F = \pm 1$ for right (+) and left (-) circularly polarized light. Therefore since no $m_F = 4$ state exists in the $P_{\frac{1}{2}}$ level the $m_F = 3$ state

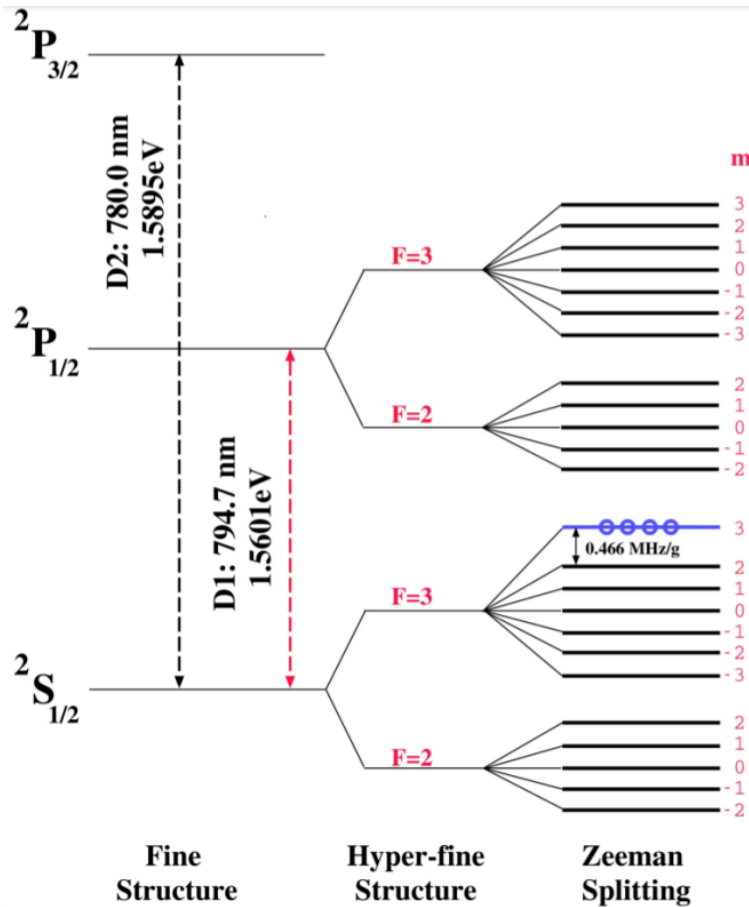


FIGURE 3.21: Zeeman splitting of ^{85}Rb .

exists in the $S_{1/2}$ level are stuck there. Simultaneously other $P_{1/2}$ levels decay via stimulated emission down to $S_{1/2}$, $m_F = 3$ state. A similar process happens for left polarized light which leaves us with the $S_{1/2}$, $m_F = \pm 3$ states populated in the end. Photons emitted may depopulate these states so a small amount of nitrogen gas is added as a quencher to the target to provide a channel for electrons to move to the ground state without emitting photons.

- **Spin Exchange:** It has been found that K- ^3He spin exchange rates are much more favorable than those for Rb- ^3He [47], however lasers for potassium are not as available as they are for rubidium. Also it has been found that K-Rb spin exchange cross section is much larger than Rb-Rb [48]. Taking advantage of all of this, we use a combination of low density Rb that is optically pumped with a higher density K which gets polarized through hyperfine collision interactions with Rb. K- ^3He collisions then exchange this polarization to the ^3He .

3.10.4 Polarization Measurements

The ^3He polarization was measured routinely during GEN-II to correct for the absolute polarization in our final results. Two methods of polarization measurements were used, nuclear magnetic resonance (NMR) and electron paramagnetic resonance (EPR). NMRs were performed routinely every few hours during the experiment running and provided a relative polarization value. EPRs were performed only occasionally and provided an absolute polarization which is used to calibrate the NMRs. The target schematic is seen in figure 3.22. The large Helmholtz coils in both axes provide the holding magnetic field direction for the polarization of the ^3He atoms and are called the “holding coils”. Another pair of coils is used to induce a radio-frequency (RF) field used for NMR measurements. The pickup coils measure the magnetic fields from the ^3He atoms during NMR measurements. We will now detail the background for each technique.

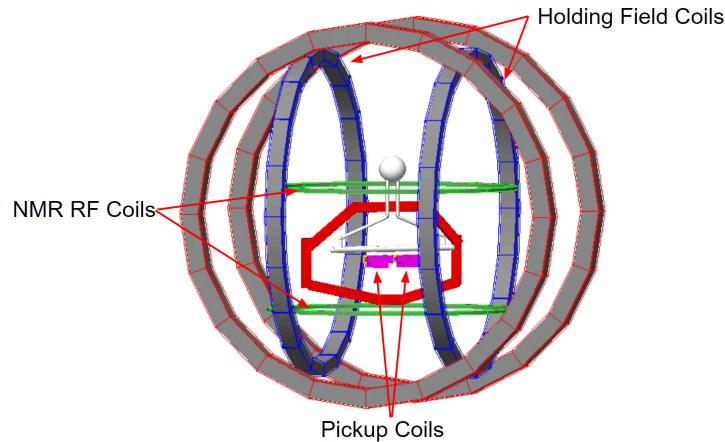


FIGURE 3.22: Schematic of the target and magnetic coils used for polarization measurements. Red and blue coils create the holding fields. Green coils are used for NMR RF measurements.

NMR Measurements

A constant holding field, \vec{B}_0 , and a radio frequency rotating field, \vec{B}_1 , is applied perpendicular to \vec{B}_0 and with frequency ω . The magnetic moment of nuclei will then precess around this field as

$$\frac{d\vec{M}}{dt} = \gamma\vec{M} \times \vec{B}_e \quad (3.23)$$

where γ is the gyromagnetic ratio and \vec{B}_e is the effective field. We can then transform to a rotating frame with the frequency $-\omega$.

$$\vec{B}_e = \left(\vec{B}_0 - \frac{\omega}{\gamma} \right) \hat{z} + \vec{B}_1 \quad (3.24)$$

The holding field strength can then be varied around the B_0 value. For this method to hold we must ensure the Adiabatic Fast Passage (AFP) condition is met

$$\frac{1}{T_2} \ll \frac{1}{B_1} \left| \frac{dB_1}{dt} \right| \ll \omega \quad (3.25)$$

where T_2 is the ^3He spin relaxation time. The AFP condition means that the field sweep must be fast enough such that the nuclear spins do not have time to relax, but also slow enough that the spins still follow the sweep.

The oscillating magnetic field induces a current in the pickup coils which is then read out as the NMR signal. The signal peak is then proportional to the ^3He polarization as follows

$$s \propto \frac{P_{He3} \mu_{He3} B_1}{\sqrt{\left(B_0 - \frac{\omega}{\gamma} \right)^2 + B_1^2}} \quad (3.26)$$

where P_{He3} is the ^3He polarization and μ_{He3} is the ^3He magnetic moment. From the signal peak, s , then P_{He3} can be extracted if a proper factor is found that can convert between two. This is what the EPR is for.

EPR Measurements

EPR measurements are performed occasionally as calibrations to find the NMR calibration factor. As discussed in section 3.10.3 the Rb atoms are all in the $m_F = \pm 3$ state of level $S_{\frac{1}{2}}$ from the Zeeman splitting. The transition from the $m_F = \pm 3$ to $m_F = \pm 2$ state has a frequency dependent on the magnetic field, B_0 , the spin exchange collisions, and the ^3He polarization.

$$\Delta v_{EPR} = \Delta v_{B_0} + \Delta v_{SE} + \Delta v_{He3} \quad (3.27)$$

The EPR measurement flips the ^3He polarization parallel and antiparallel to the holding field, B_0 . The two measurements are then compared

$$\begin{aligned}\Delta v_{EPR}^+ &= \Delta v_{B_0} + \Delta v_{SE} + \Delta v_{He3} \\ \Delta v_{EPR}^- &= \Delta v_{B_0} + \Delta v_{SE} - \Delta v_{He3} \\ \Delta v_{He3} &= \frac{\Delta v_{EPR}^+ - \Delta v_{EPR}^-}{2}\end{aligned}\quad (3.28)$$

It has been shown that the frequency splitting can be related to the polarization as [49]

$$\Delta v_{EPR} = \frac{dv_{EPR}}{dB_0} C n_{He3} \mu_{He3} P_{He3} \quad (3.29)$$

Where C is a constant related to the cell geometry and $\frac{dv_{EPR}}{dB_0}$ is well known and can be calculated from the Breit-Rabi equation. Finally we have the EPR frequency

$$\Delta v_{EPR} = \frac{8\pi}{3} \frac{dv_{EPR}}{dB_0} \kappa_0 \mu_{He3} P_{He3} \quad (3.30)$$

where κ_0 is a dimensionless constant that is dependent on temperature and measured experimentally. From equation 3.30 the absolute polarization is found. NMR measurements were performed before and after each EPR measurement to determine the NMR calibration factor.

3.11 Data Acquisition

The CEBAF online data acquisition (CODA) system is the standard data collection software for all JLab experiments [50]. It was developed by the JLab DAQ group for JLab use. It is configurable to accept many readout controllers (ROC) which write the data as 32 bit words and send to CODA. Therefore any number of detectors can be connected to ROCs and all read out by CODA simultaneously. CODA then writes out the data into event IO (EVIO) files which are subsequently decoded for physics analysis, which we discuss in detail later.

The Experimental Physics and Industrial Control System (EPICS) [51] is also used to record information about the accelerator and hall status. This software is open sourced and used by a number of accelerators around the world as a way of recording data. A wide variety of hardware (HV, gas, beam diagnostics) can be plugged into

the EPICS systems to record information on a slower time scale than the event time scale. This is usually over the course of seconds, and is only used for data that is not needed on an event by event basis, like beam energy or the IHWP state. This data is also inserted into the CODA data stream to be written to the EVIO file.

3.11.1 Triggers

TABLE 3.2: List of triggers used in GEN-II.

Trigger	Description
1	BBCal Trigger
2	HCal Trigger
3	BBCal & HCal Coincidence
4	GRINCH LED Pulser

CODA is triggered to read out an event only when certain thresholds are passed. The DAQ equipment can not handle more than about 5 kHz rate or else it would saturate. Due to the large acceptance of the spectrometers in this experiment there is a very high rate of low energy particle triggers for each detector arm. This must be appropriately handled to ensure that the final trigger rate remains below the 5 kHz threshold. The main triggers used for the GEN-II experiment are listed in table 3.2.

- **Trigger 1:** The diagram for each BBCal block leading to the final trigger signal is shown in figure 3.23. The raw BB trigger signal is in mV. A rough but reasonable conversion between mV and GeV is needed before accurate calibrations are made. For each kinematic the trigger is set at a certain mV threshold which removes almost no quasielastic electrons.
- **Trigger 2:** The diagram for each HCal block leading to the final trigger signal is shown in figure 3.24. The raw HCal trigger is also in mV. Since HCal has a poorer energy resolution the threshold is set to a low value which causes a very high trigger rate, in the MHz range for HCal. This trigger is never used by itself since the rates would overload the DAQ limit.
- **Trigger 3:** This is the logical combination of trigger BBCal and HCal trigger times. The diagram for HCal and BBCal trigger leading to the final coincidence trigger signal is shown in figure 3.25. This is the main physics trigger for GEN-II since there is no need to record a hit if it is not measured in coincidence in both arms.

The coincidence time window was set to 150 ns. This guarantees the hit happens inside the window since an actual coincidence should only have about a 10 ns range at the largest, accounting for hardware time jitters in the two arms.

- **Trigger 4:** The GRINCH is equipped with a LED pulser used for testing. Setting this trigger would pulse light to trigger the GRINCH detector and record events. This was used in GEN-II as a random trigger to keep the event rate above zero, because if the beam goes away and the DAQ stays at 0 Hz for too long some data could get corrupted.

Each trigger also comes with a prescale setting, which tells the DAQ how often to trigger on an event. A prescale of 10 would mean that the DAQ would only trigger on 1 out of every 10 events. This is useful because some of the triggers above are helpful for diagnostics but not for physics. For GEN-II, trigger 3 is the main physics trigger, but the rates are relatively low, given this all trigger 3 events were accepted, while the other trigger types were pre-scaled such that a few hundred Hz of trigger 1 were kept for diagnostics and also 1-2 Hz of trigger 4 were kept to keep the DAQ running even if there is no beam available.

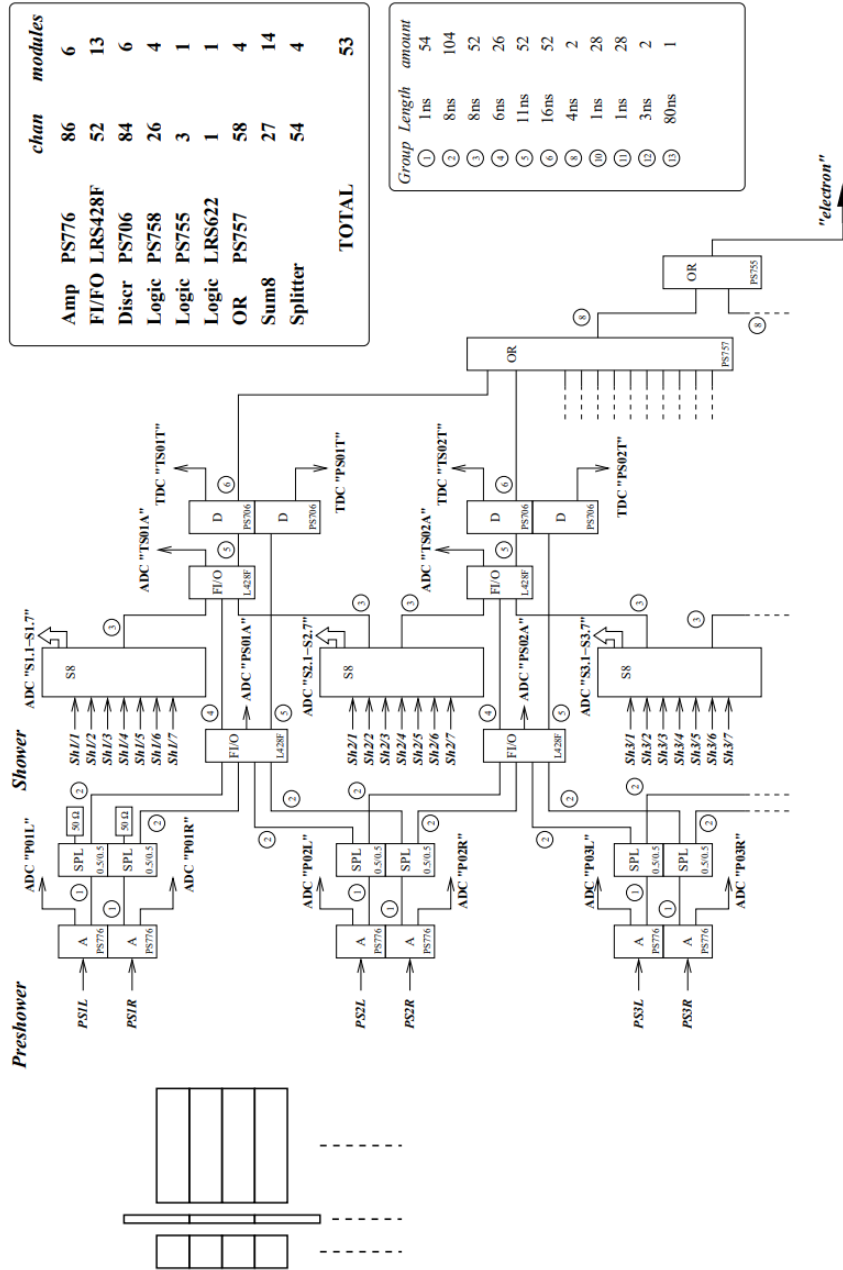


FIGURE 3.23: Schematic of BBcal trigger.

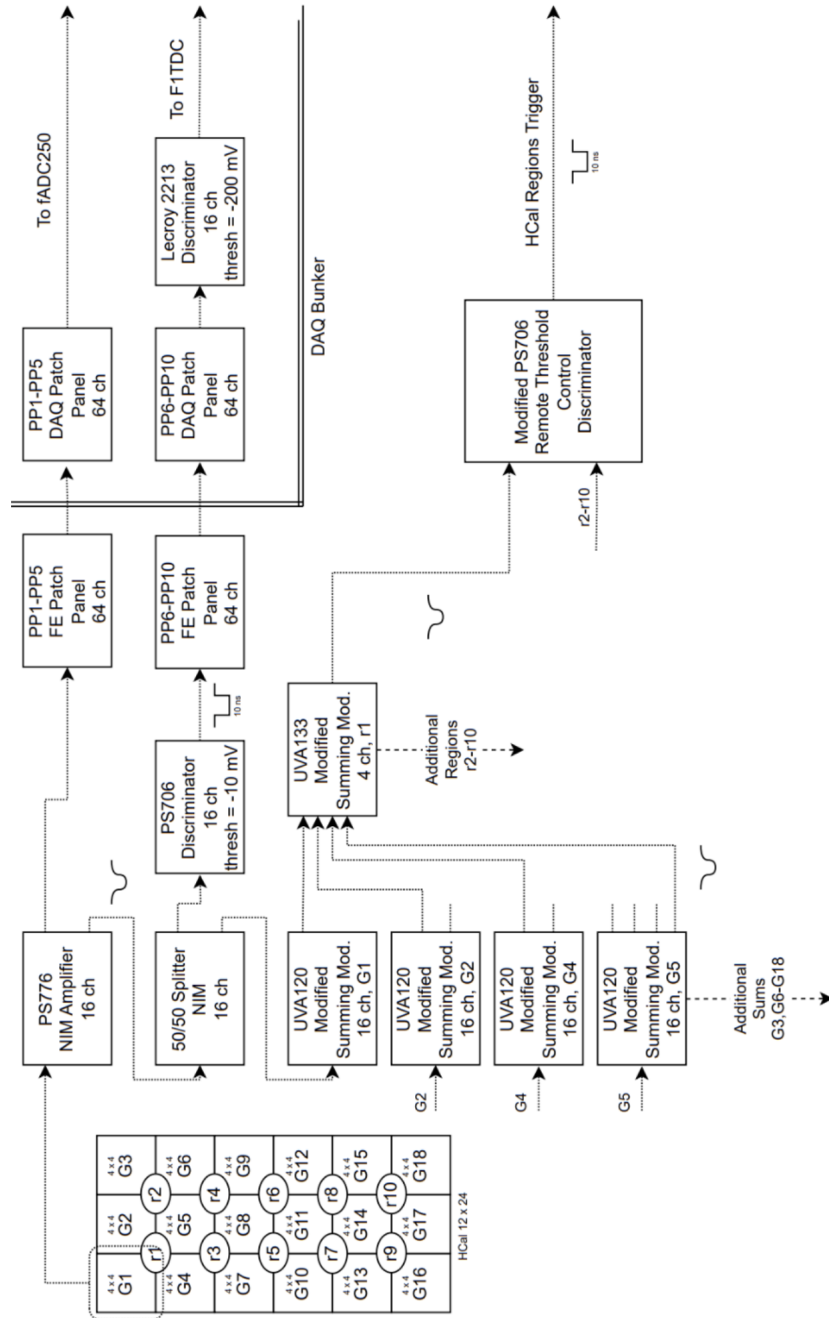


FIGURE 3.24: Schematic of HCal trigger.

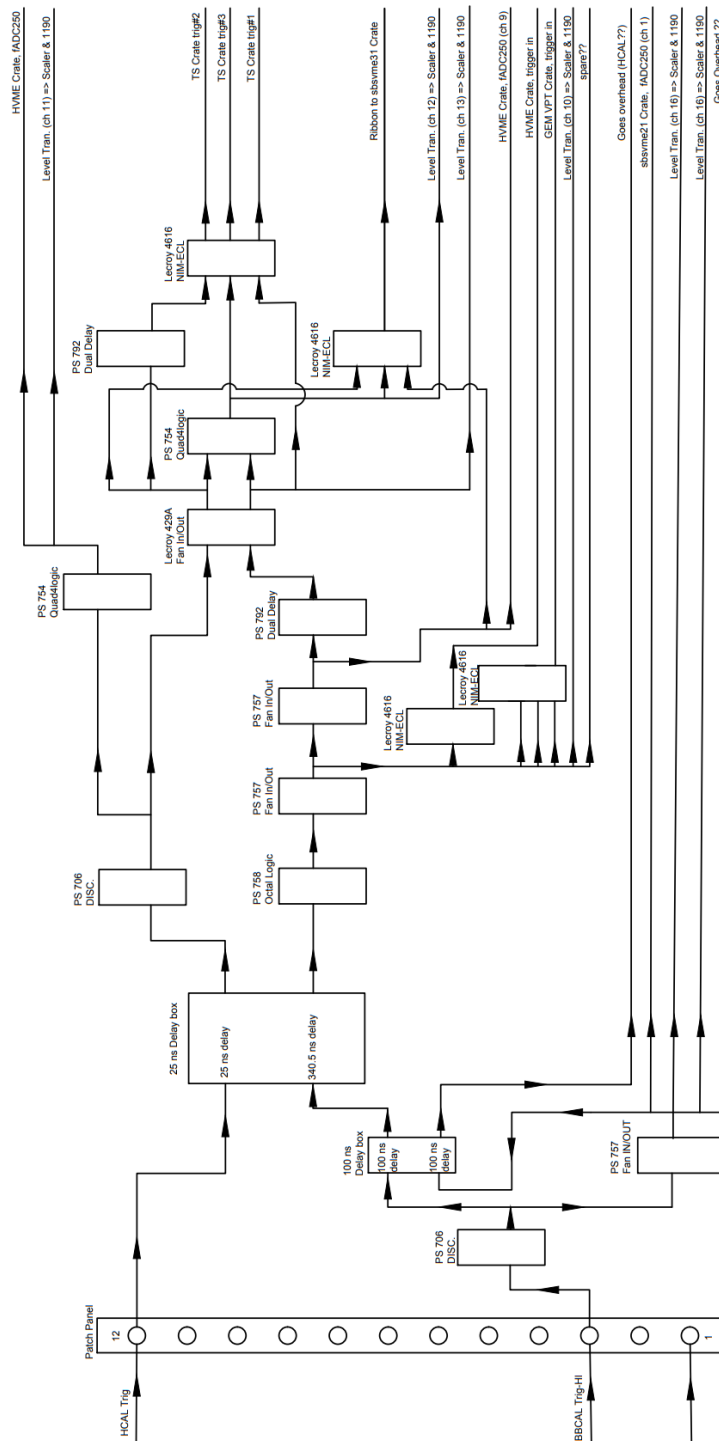


FIGURE 3.25: Schematic of coincidence trigger.

Chapter 4

GEM Detectors

Particle physics experiments require some method of reconstructing the particle trajectories. There is a wide variety of detector concepts and a long history that can be discussed around particle trackers. Suffice it to say that all trackers try to solve the issue of reading out enough data points along a particle's path so that real tracks can be found amongst random background signals. Previously JLab has mainly used multi-wire drift chambers as the main method of particle tracking. However wire chambers are generally limited by their high rate capability. The wire chambers previously used with BB spectrometer were limited to about 10 kHz/cm² incoming charged particle rates due to space charge and occupancy issues.

For high rate experiments, like the SBS program, new trackers were developed. Gas Electron Multiplier (GEM) detectors were developed in 1997 by Sauli [52] and have proven to handle higher rates. The Micro-Pattern Gas Detector group at the University of Virginia (UVA) worked with GEM detector technology and designed and built new trackers to use at JLab. These detectors have a spatial resolution of 70 μm and can handle rates up to 500 kHz/cm², while large covering areas. Here we will detail GEM detector principles and the design and construction at UVA.

4.1 Working Principles

The components of a GEM detector consist of an enclosed chamber with a cathode foil, several layers of GEM foils, and a layer of readout strips at the bottom, see figure 4.1. Our chamber design uses three GEM foils, but two and four GEM foil configurations have also been used in other cases. We will detail these components in the following sections, but for now will go through the overview how the GEM works. The chamber

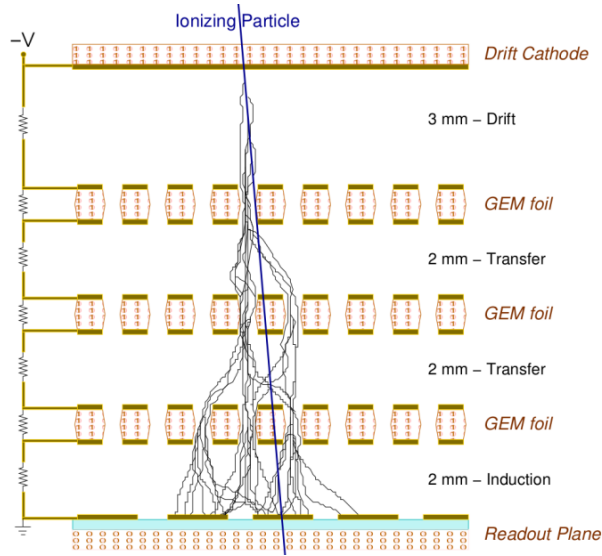


FIGURE 4.1: Single particle causing a shower cascading through the GEM holes and ending on the readout strips.

is filled with an ionizable gas, Ar/CO₂ mixture in our case. A charged particle entering the chamber will ionize the gas and create a shower of electrons. A voltage will drift the electrons down to the nearest GEM foil, which has small holes with extremely high electric fields. These fields cause the electrons to accelerate with sufficient energies within a mean free path to ionize gas atoms again causing an avalanche effect. The electrons then drift down to the next GEM foil. Each foil provides a amplification of ~ 20 and three foils together amplify the original particle by a factor of ~ 8000 . This process is outlined in figure 4.1.

The energy loss rate of a particle traveling through material is described by the Bethe-Block equation [53]

$$\left\langle -\frac{dE}{dx} \right\rangle = Kz^2 \frac{Z}{A} \frac{1}{\beta^2} \left[\ln \frac{2m_e c^2 \beta^2 \gamma^2 W_{\max}}{I^2} - 2\beta^2 - \delta(\beta\gamma) \right] \quad (4.1)$$

where A is the atomic mass, z is the charge number of the incident particle, Z is the charge number, I is the mean excitation energy, and $K = 4\pi N_A r_e^2 m_e c^2$ with $r_e = \frac{e^2}{4\pi\epsilon_0 m_e c^2}$, $\delta(\beta\gamma)$ is a density effect correction due to polarization, and finally $W_{\max} = \frac{2m_e c^2 \beta^2 \gamma^2}{1+2\gamma_e/M+(m_e/M)^2}$ is the maximum energy transfer in one collision. The minimum energy loss for this equation can be found at $\beta\gamma \approx 3$, which are called minimally ionizing particles (MIP) and lose approximately $1.4 \text{ MeV g}^{-1} \text{ cm}^2$ in matter. The main energy loss mechanism for several GeV electrons detected in GEn-II is Bremsstrahlung; as such

the total energy loss for such electrons is much larger than for heavier particles, with the same momentum. However, signal in a thin gaseous detector arises mainly due to the ionization losses. These losses for several GeV electrons is only about a factor of 1.5 times the losses of MIPs, or roughly about $2 \text{ MeV g}^{-1}\text{cm}^2$.

The total energy lost of all materials would then be the following [54].

$$\left\langle \frac{dE}{dx} \right\rangle = \sum_i w_i \left\langle \frac{dE}{dx} \right\rangle_i \quad (4.2)$$

For GEN-II we are using an Ar/CO₂ mixture of 80% and 20% respectively. For the electron energies in this experiment (see table 3.1) we expect energy depositions ~ 1 keV. Secondary photons created during avalanche ionization process lead to secondary avalanches and some times discharges in the detector. The probability for these events increases with high detector gain or with large signals due to highly ionizing particles. This could damage the GEM detector and so CO₂ is added to the gas mixture because it absorbs some photons and reduces the avalanche ionization process.

4.1.1 GEM Foil

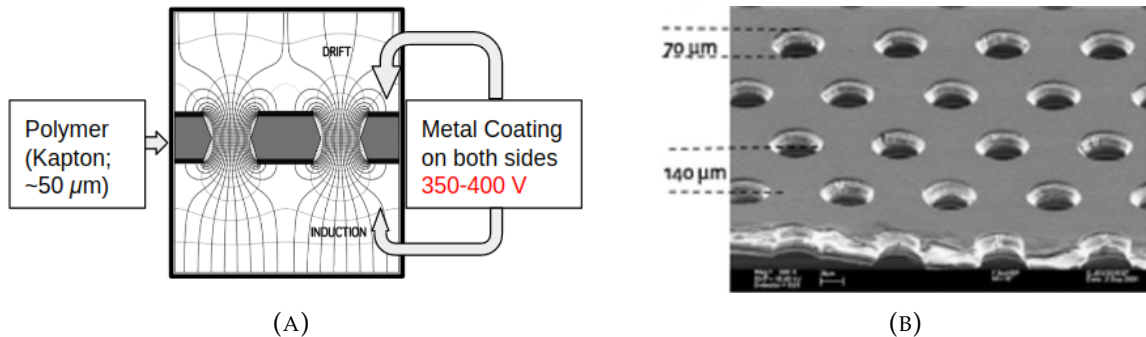


FIGURE 4.2: (A) Schematic slice of a GEM layer. It is $50 \mu\text{m}$ of kapton-like poly-amide with $5 \mu\text{m}$ copper coating on both sides. (B) Electron microscope image of the top of a GEM foil with many $70 \mu\text{m}$ diameter holes.

A GEM foil is $50 \mu\text{m}$ thick of poly-amide with a $5 \mu\text{m}$ coating of copper on both sides, as seen in figure 4.2a. The top and bottom copper coating of a GEM foil have a voltage, typically $\sim 400 \text{ V}$, which produces a large electric field inside the hole region. This has two main benefits, first it pulls all the drifting electrons above from the initial particle into a small area, and second, the electric field gives enough energy for these

electrons to cause avalanche multiplication and amplify the signal. The foil's surface is covered with $70\ \mu\text{m}$ diameter holes, as seen in figure 4.2b. They must be small so that electron shower gets pulled into a small area and the initial particle position does not spread out significantly. As the shower increases in subsequent foils it transversely diffuses, see figure 4.1, but it stays around the first few holes of the initial particle, which overall keeps a good position resolution.

4.1.2 Readout

The electron shower gets deposited on the bottom of the detector and must be measured. The ideal readout would be a pixelated detector bottom that can measure charge deposition in a square of some micrometer size. In other experiments doped silicon pixels are used for this but they are extremely expensive [55]. These are typically used in small areas so the total cost is not limiting. However the number of pixels scales with the area and so the cost of pixels needed to cover $60,000\ \text{cm}^2$ needed in this experiment would be prohibitively large. A cheaper alternative is to use copper strips along the vertical and horizontal direction. This gives one dimensional information but both dimensions can be combined to get the 2D position. This can cause combinatorics issues at high luminosity conditions with many hits on the strips within the readout time window. But for the SBS experiments simulations have shown that rate should be manageable. We will detail how this is done further in section 4.5.9. For generality we will call these strips U and V direction, since U and V do not need to be perpendicular

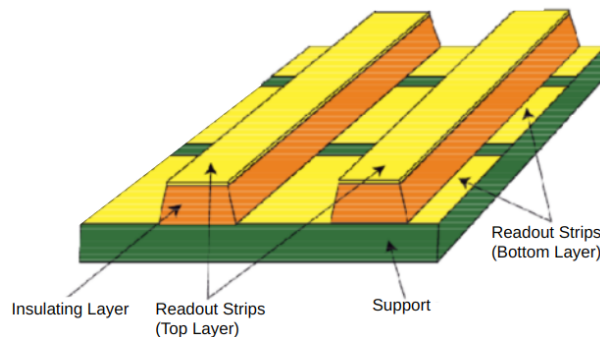


FIGURE 4.3: View of the readout strip configuration. The top strips are electrically insulated via poly-amide from the bottom strips. The top strips are $80\ \mu\text{m}$ wide and the bottom strips are $340\ \mu\text{m}$ wide to make up for the area covered by the top strips.

Figure 4.3 shows how the readout strips sit on top of each other for charge measurement in both directions. The top strip widths are $80\ \mu\text{m}$ and the bottom strips are $340\ \mu\text{m}$ to account for the area covered by the top strip. Charge deposited on a strip creates a small voltage which is measured at the end of the copper strip by readout electronics. The longer the strips are the larger the capacitance which causes larger electric noise fluctuations, so it is preferable to keep the strip lengths as short as possible.

4.2 GEM Types

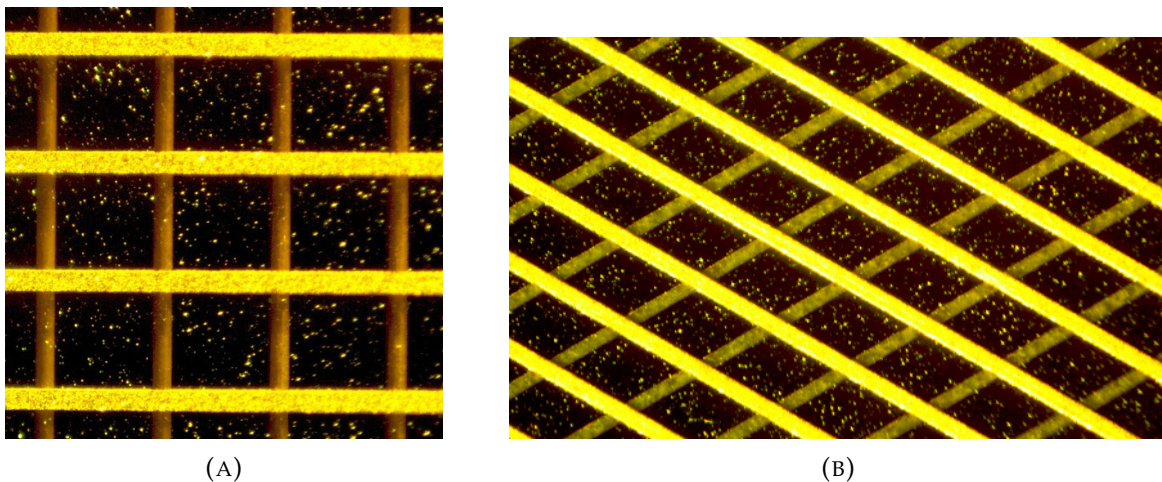


FIGURE 4.4: Microscope images of GEM readout boards. (A) XY GEM readout strips, perpendicular to each other. (B) UV GEM readout strips, at a 60° angle.

The SBS experiments required GEMs to cover an area of $40\ \text{cm} \times 150\ \text{cm}$ at the front of the spectrometer and $60\ \text{cm} \times 200\ \text{cm}$ at the back. Originally it was planned to use smaller GEM chambers of $40\ \text{cm} \times 50\ \text{cm}$ side by side to cover the front area. These modules have readout strips perpendicular to each other in the standard X-Y direction, as seen in figure 4.4a, so we will refer to them as XY chambers. Technological advancements allowed to produce larger GEM foils, which made it possible to cover the $40\ \text{cm} \times 150\ \text{cm}$ area with a single module. To keep the strip length for these modules acceptably small the U and V strips are at a 60° to each other, see figure 4.4b. We will refer to these as the UV chambers. For the SBS experiments both XY and UV GEMs are used, and in GMn and GEn-II experiments only the fifth layer (see figure 3.4) is XY and the rest are UV.

4.3 Design and Construction

The SBS GEMs were constructed in a cleanroom at the University of Virginia, since any contaminant particles inside a GEM hole could create an electrical breakdown under the high electric fields in the holes, leading to damage of the poly-amide layer and causing a short in the foil. The foils were provided by CERN and frames manufactured by a private company, Resarm Engineering Plastics, in Belgium. UVa had previously built 50 XY GEMs by 2019 for the SBS project [56]. In 2020 the components for four UV GEMs arrived at UVa and we will focus on their construction.

Each GEM foil is divided in to 100 cm^2 electrically isolated sectors. For the XY GEMs there are 30 sectors which are only sectored on the top of the foil, while the foil bottom remains a single sheet. This was found to be a problematic design since any GEM sector short circuits would cause the voltage between the common bottom copper layer and the top layers of other sectors to drop and therefore the whole chamber would stop working. This can be fixed by disconnecting the shorted sector, but it then required the detector to be physically worked on which can be difficult while running an experiment. For the UV GEMs the sectors are isolated on both the top and bottom of the foils so a short would only affect one sector. The UV foils contain 60 sectors in total.

Each GEM sector must be tested thoroughly for any shorts during the construction process. To do this we place the foils in a box filled with filtered dry nitrogen gas, see figure 4.5a. The gas constantly flows into the box to minimize the possibility of contamination due to dust particles. When a voltage is applied to a sector there should be no current flow between the top and bottom, as they are isolated from each other. The test involves applying 550 V to a sector for one minutes. If there is no more than $\sim 5 \text{ nA}$ of current the sector is deemed to be in working order. It is possible to have current spikes when the voltage is first applied due to particulates burning away in the foil, but it should settle down within a few seconds and stabilize over the minute. Figure 4.5b shows an example of one sector test, where the current is very stable and we confirmed that this sector is working well.

Three GEM foils are stacked together in each detector using frames to separate them. The frames are fiberglass-reinforced epoxy material Permaglas. After receiving them from the manufacturer we sand them and wash them in an ultrasonic bath to remove any protruding ends that could affect the uniformity of the foils. Finally the foils

are hand brushed with a Nuvovern LW and hardener to prevent any sharp edges. The foils are each stretched in order ensure they are as flat as possible, since any bending would distort the electric field and possibly destroy the detector. Figure 4.6 shows a foil in the stretcher with tension gauges around all sides. The tensions are all set to 0.5 kg/cm and adjusted slightly as needed remove any visible wrinkles in the foil. A thin layer of resin epoxy (Araldite AY103+HD991 Hardener) is applied to the frames and is glued onto the foil. A plexiglass plate is put on top of the frame and weights are applied to ensure a strong bond while the epoxy takes 24 hours to cure. One finished foil, with the frame, is seen in figure 4.6. Note that there is a built in spacer grid across the middle of the frame. This grid is to ensure that the adjacent foils do not come into contact. These pieces are 300 μm wide and do not have a significant impact on the particles traveling through the middle of the chamber.

The sectors are voltage tested again after gluing to check that none have been lost in the process. The frame thickness make up the space for the drift/transfer regions, seen in figure 4.1. Each completed foil with the frame is glued on top of each other as seen in figure 4.7. With all foils glued together it is now air tight except for holes left for gas flow, see figure 4.8. It is critical that the only gas that enters the detectors is sufficiently clean, since any particulates could cause shorts. Therefore the gas input and output are sealed when the chambers are not in use, and when in use only research grade purified gas mixtures are used with a 10 micron particle filter on all input gas lines.

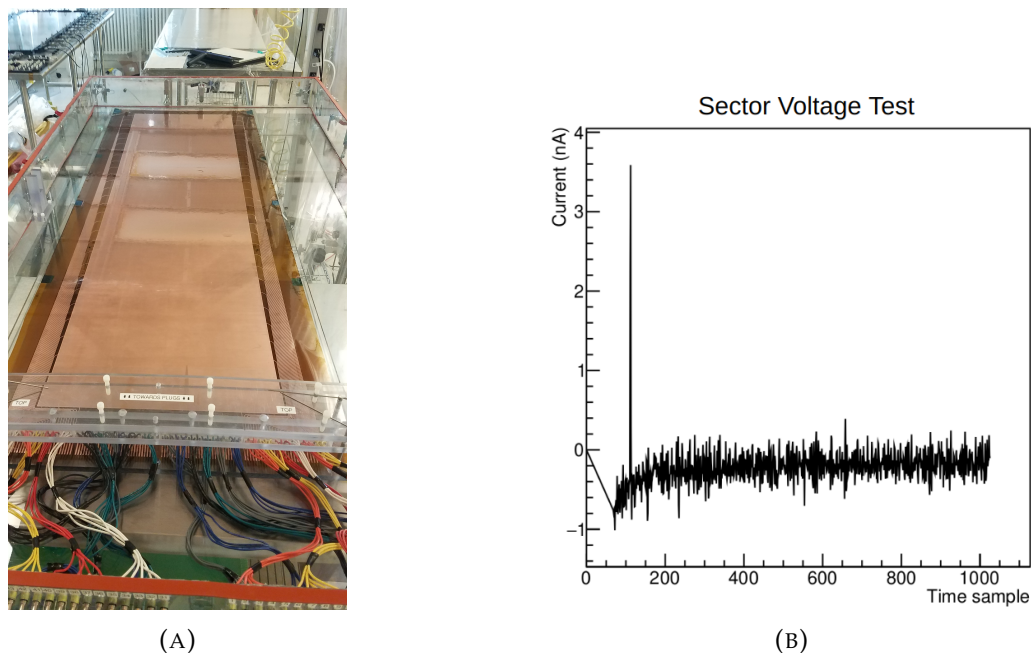


FIGURE 4.5: (A) Sealed box for voltage testing a GEM foil. At the bottom of the picture is the wires connecting the voltage to each individual sector. (B) Example of one sector test. Over the course of a few minutes we see the current is stably less than 5 nA.

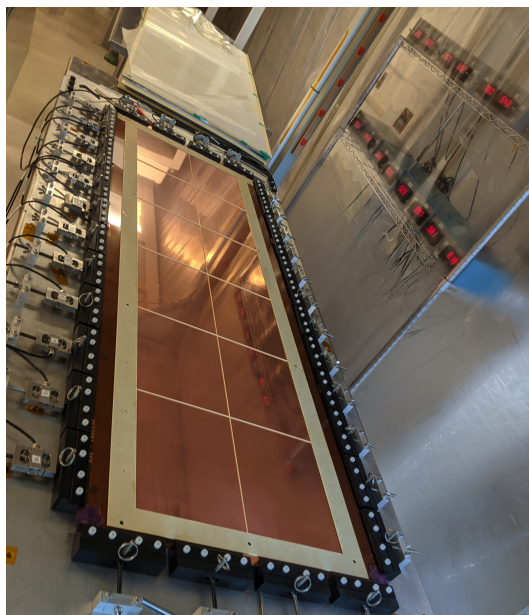


FIGURE 4.6: Stretcher used for flattening GEM foils. Black clamps can be seen around the edges pulling the foil. Tension meters are on the right wall. A frame can be seen on top of the foil after gluing.

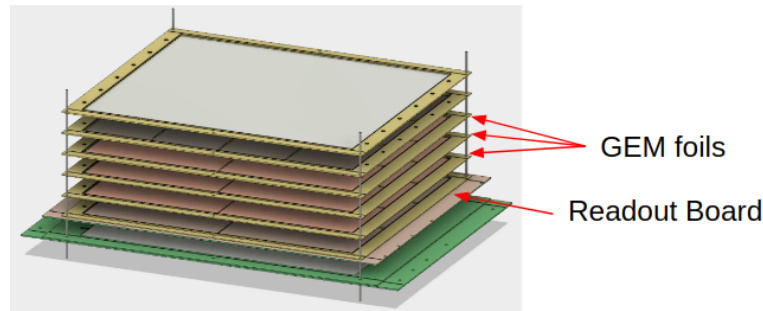


FIGURE 4.7: layers of the readout board, GEM foils, cathode, and window cover are stacked and glued together to make one GEM chamber.

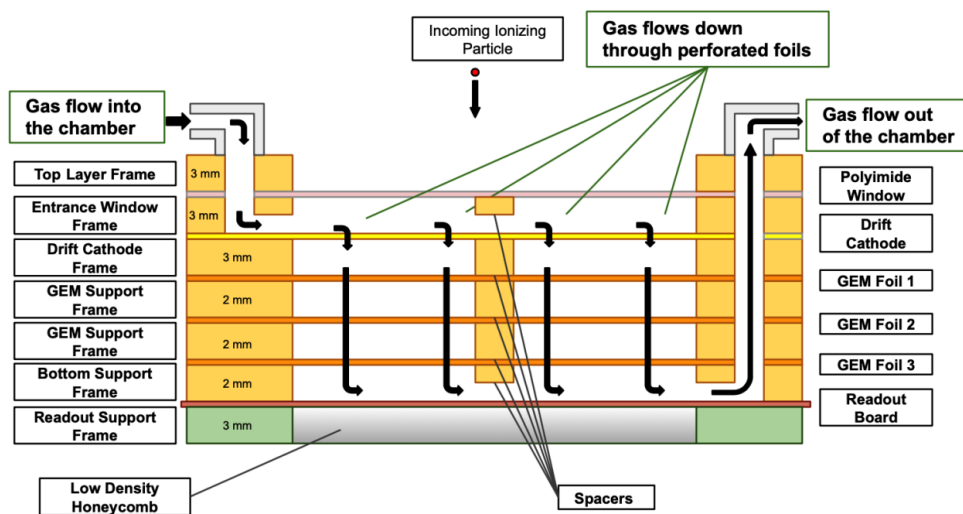


FIGURE 4.8: Schematic of the gas flow through a GEM chamber. Gas flows in through the top left and spreads out evenly in the chamber before flowing out in the bottom right. Figure taken from [57].

4.3.1 High Voltage

The standard power supply for a GEM uses a voltage divider to power the different layers, as seen in figure 4.9a. This is cost effective because one voltage channel is needed to supply the different voltages for each part of the GEM. The GEMs also have “protective” resistors which are 10 M Ω on each sector. If a sector does discharge or short then the protective resistor limits the current to minimize damage to the foils and ensures that the divider chain remains relatively unaffected.

This HV divider has a downside when high particle rates start depositing charge

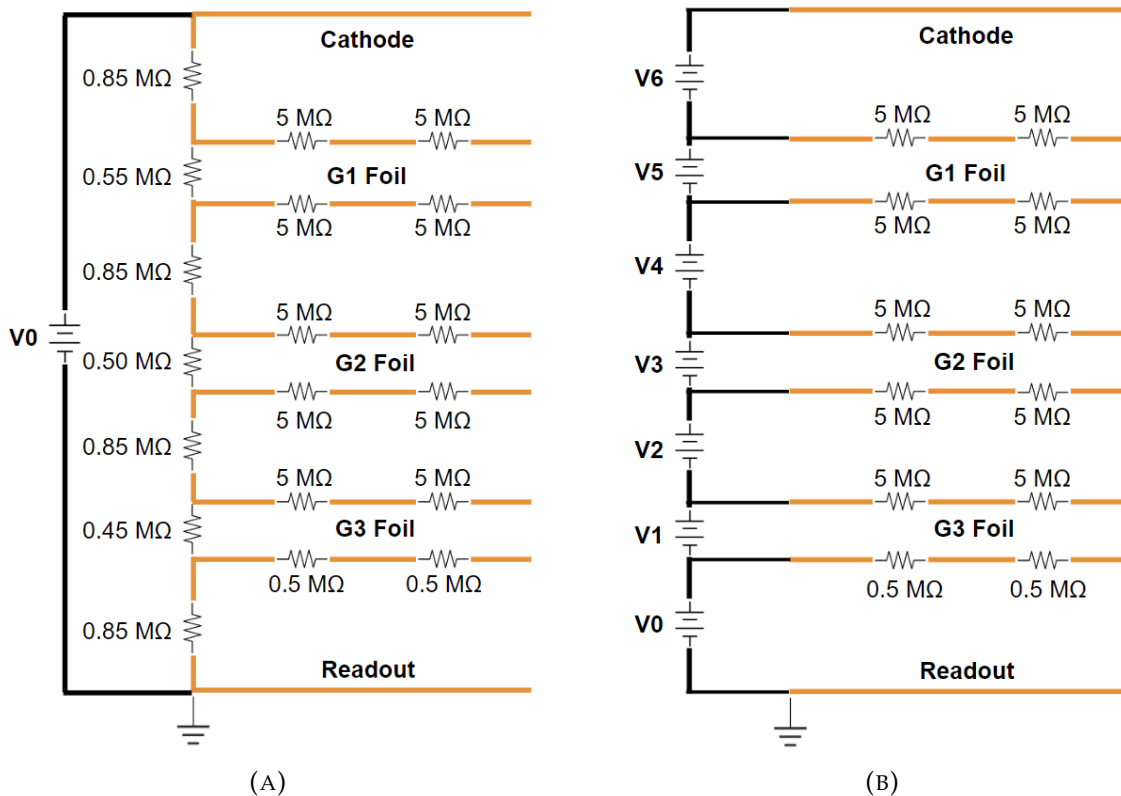


FIGURE 4.9: HV designs used in the SBS experiment. (A) Voltage divider which uses one voltage channel and resistors to supply different voltages for each section of the module. (B) Parallel voltage supply uses one voltage channel for each section of the module in parallel. Note that the $\text{M}\Omega$ protective resistors are still used.

on the foils in sufficient amounts to change the currents which affects the effective voltages. This will be discussed in detail in section 5.5. To counteract this situation a "parallel" power supply is utilized, as shown in figure 4.9b. This HV setup supplies a voltage channel for each GEM region separately. This supply is more expensive since it requires seven HV channels for a single module, however the voltages are then stable and unaffected by any charge deposition, except for the relatively minor drop across the protective resistors.

For modules using the voltage divider the W-IE-NE-R MPOD EHS 8060n power supplies are used. These HV channels can supply up to 6 kV and currents of 1 mA, which is sufficient for operating the GEM modules at 3.6 kV with currents of $745\ \mu\text{A}$. For the parallel HV the CAEN HiVolta DT1415ET power supply are used. Each channel can supply 1 kV floating voltage and currents of 1 mA. This is sufficient as the GEM sections need no more than 600 V. The floating voltages are stacked, biased with respect

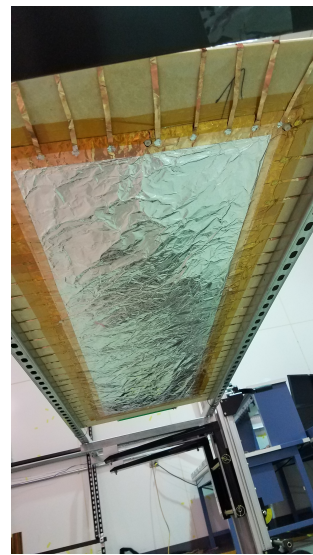
to each other from the ground voltage at the readout place to the maximum voltage at the cathode.

4.3.2 Shielding

During testing in Hall A it was discovered that the detectors' noise level increased as they were installed into the tracker systems in the hall. We installed a Faraday cage-like shield around to detector to protect it from any electrical interference. This was a 50 μm thick aluminum foil which covered the top and bottom of the chamber, as seen in figure 4.10. Three centimeters of space is left between the aluminum and the nearest GEM foil so electrostatic forces do not pull the two together. The aluminum foil is attached using copper tape to a aluminum frame around the GEM frames. Copper strips are then soldered along the chamber connecting the bottom and top aluminum sheets. The copper strips can be seen clearly in the picture in figure 4.10. The affects of this cage on the detector signal will be discussed more in section 5.3. This aluminum shielding was applied to each module in the experiment.



(A)



(B)

FIGURE 4.10: (A) Aluminum shielding covering the top of the GEM. Notice the metal strips wrapping around the edges. (B) Aluminum shielding covering the bottom of the GEM, with the metal strips attaching the top and bottom parts.

4.4 DAQ

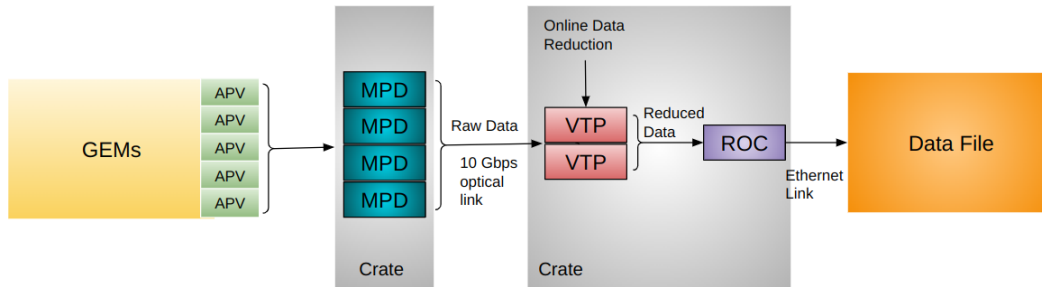


FIGURE 4.11: Data flow for a GEM. The APV cards attached to the GEM send the raw signal to the MPDs which digitize the data. The data is then sent to the VTPs which perform zero suppression and reduce the data which is then recorded in the data file. The number of APVs/MPDs/VTPs is not accurate, just a representation that there are multiple

The data acquisition (DAQ) system for the GEMs is complex and made of many parts. The overview of the data stream is shown in figure 4.11. The GEMs have 7680 strips/channels for UV GEMs and 2816 for XY GEMs. The strips attach to connectors which have 128 channels each, called APVs, so that the UV GEMs have 60 APVs and XY GEMs have 22 APVs. The total raw readout of the GEMs can be as high as 1 Gb/s for the GEN-II experiment. We will now outline the DAQ system.

4.4.1 APV

The APV-25 is a 128 channel chip with low power consumption and low noise [58]. The chip has a 40 MHz clock and there is a synchronization pulse every 35 clock cycles. When the chip receives a trigger it waits for the next 35 cycles to send the data. The data consists of a digital header, digital address, error bit, and analog reading of the signal from each of the 128 channels. The APVs are attached directly to the detectors and send the data through HDMI cables to the Multi-Purpose Digitizer boards (MPDs), which are 10 m away in a radiation bunker.

4.4.2 MPD

The Multi-Purpose Digitizer (MPDs) is a FPGA board designed by Istituto Nazionale di Fisica Nucleare (INFN) [59]. The MPDs are housed in VXS or VME 64x crates. HDMI

cables from APVs are plugged into the MPD which can have up to 16 APVs in one module. The MPD configures and receives the data stream from the APV and transmits these signals. This means that the MPD tells the APVs what their address and position is and records this information for later decoding.

4.4.3 VTP

The VXS Trigger Processor (VTP) was developed at JLab to handle fast and large data processing [60]. It has four QSFP fiber transceivers for a total of 34 Gbps data input. It can also transmit 40 Gbps through the ethernet connection to the the readout controller (ROC). The ROC manages collecting and organizing all data from all detectors and writing it to a single data file. The VTP has capability to preprocess data from the MPD before sending the data forward to be saved. This is extremely useful for us since there are so many GEM channels, the raw data needs significant reduction. The VTP does this by applying zero suppression to remove channels that do not contain signal and can reduce the size of data output by a factor of 10. This reduction will be discussed further in section 5.1. From here the data goes to the ROC which formats the data and sends it to CODA to be saved in the final data file.

4.5 Analysis

The GEM data requires many steps to fully analyze. In a brief overview, the raw data is processed to remove noise, form clusters of strips, form 2D hit combinations, and finally find tracks from multiple layers. Here we will detail all steps to get from raw GEM signals to final particle tracks.

4.5.1 Raw Signal

For one event the signal from one APV is given as six time samples. Each time sample is 25 ns so the total window for one event is 150 ns. This way the signal shape can be recorded along with the amplitude. An example of one APV event can be seen in figure 4.12. The channel amplitude is in ADC units. For a single time sample the baseline has a pedestal offset from the 0 ADC value, which we refer to as the common mode (CM). The CM value does change for each time sample and in an event. Therefore for each

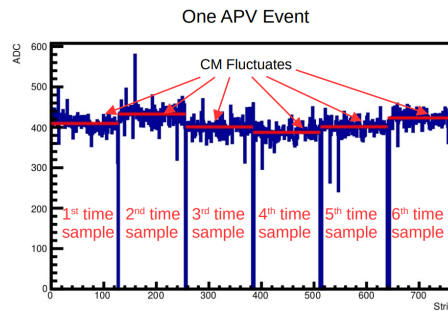


FIGURE 4.12: Example of one APV event. There are six time samples recorded, separated by the vertical bars. Each sample has slight changes in the common mode value.

event the CM needs to be calculated and subtracted to get this offset. Each channel also has random electronic noise fluctuation around the CM value, which also needs to be calculated. This is referred to as the pedestal. A common term we will use here is the "occupancy" of the APV or detector, which means the fraction of total strips that contains a signal.

4.5.2 Pedestal Calculation

A readout channels pedestal is unique to the specific electronics. This means if a GEM/APV/MPD/VTP is replaced then a new pedestal must be calculated. For this, 5000 events are recorded with the GEM HV off so there should be no real signal and only noise fluctuations should remain. This is called a "pedestal run". For each channel the ADC value from all six time samples were averaged. The mean, μ_{ped} , and standard deviation, σ_{ped} , of this value is calculated. These pedestal values are uploaded to the VTP. As data is recorded, the VTP will subtract the pedestal mean in real time. From here the common mode can then be calculated.

4.5.3 Common Mode

The common mode (CM) is also calculated from a pedestal run. As seen in figure 4.12, the CM fluctuates for each time sample. Therefore the CM needs to be reliably calculated for each event and time sample. The common mode algorithm is programmed into the VTP to actively calculate the CM in real time. There are a few different methods to do this.

4.5.4 Sorting Method

The sorting method takes all 128 channels in a time sample and sorts them from lowest to highest ADC values. Then some number of the lowest and highest ADC strips are removed. For this experiment we used the 28 lowest strips and the 28 highest strips since the occupancy levels were low enough that there should be no signals in these extremes. The CM is then calculated as the mean value of the remaining strips. After removing the extreme low and high values the remaining strips should not have signals and be near the true baseline. This method has a drawback when operating under high occupancies as some of the actual signal ADC values would be included in the CM average and bias it to be too high.

This method is generally robust since it does not require the user to set algorithm values for each APV. However sorting 128 channels requires saving the information for all channels and the VTP FPGA did not have enough memory for this. Therefore this method could not be used during data collection, but it remains useful in offline calculations of the CM for testing.

4.5.5 Danning Method

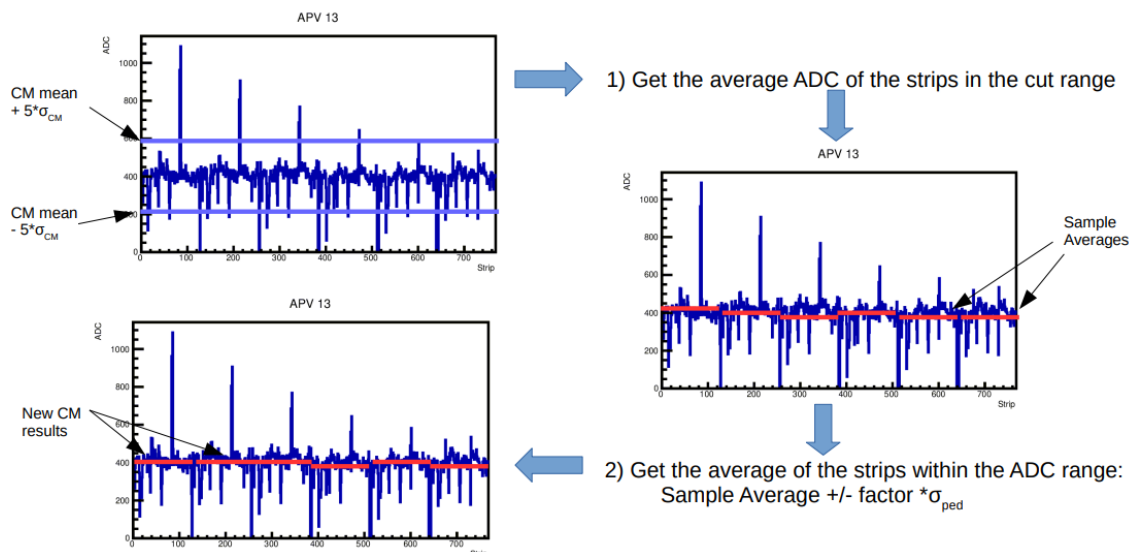


FIGURE 4.13: Process of the Danning algorithm. The red lines show the CM results. Step 2 can be iterated multiple times to refine the CM result.

Danning Di developed an algorithm that can be used online for the VTP, which is now called the Danning method. The algorithm process is outlined in figure 4.13. First the pedestal run has the CM calculated using the sorting method for each APV. See section 4.5.2 for reference on what a pedestal run is. The CM mean, μ_{CM} , and standard deviation, σ_{CM} , are recorded and uploaded to the VTP for online use. For a single APV event during online data processing, the Danning CM is calculated as follows

1. Take all the strips inside the range $\mu_{CM} \pm 5\sigma_{CM}$ and calculate the average value for each time sample. Let us call the CM result CM_i for each time sample i .
2. For each time sample we now refine the calculation. Each strip is checked if it is within the range $CM_i \pm f\sigma_{ped}$. Here the f factor is $3\sqrt{6}$. This is because we use a 3 sigma cut and $\sqrt{6}$ comes from the fact that σ_{ped} is calculated by averaging all 6 time samples. Each strip passing this cut are averaged and this is now our new CM_i .
3. Step 2 can then be repeated multiple times to remove any possible outliers and move the average towards the true result. We use 3 iterations here.

This algorithm does not require the strip information to be saved and therefore it can be utilized by the VTP in real time. This method however may be more susceptible to bias if low ADC signals make it inside the cut ranges, or if the CM value shifts over time from when it was first calculated by the pedestal run. This is the method that was utilized by the VTPs during the GMn and GEn-II experiments.

4.5.6 Histogramming Method

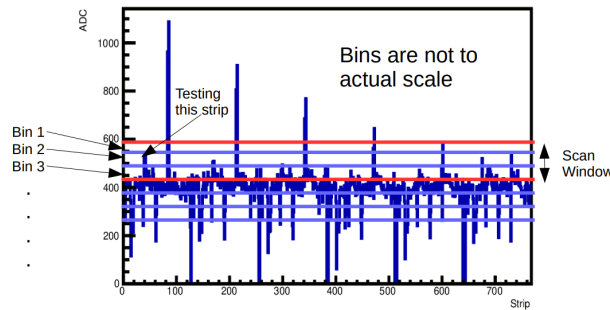


FIGURE 4.14: Process of the Histogramming algorithm. Bins are drawn large for explanation but actual bin sizes are much smaller, ~ 2 ADC.

This method has been originally developed by Andrew Puckett and improved upon in this work. First the ADC range is sliced into many bins, as seen in figure 4.14. The input settings for this method are called the "bin size" and the "scan window". The bin size is set to $0.2\sigma_{CM}$ which is typically ~ 2 ADC channels and the window size is set to $2\sigma_{CM}$ which is typically ~ 20 ADC channels. The method follows this process:

1. Starting at the bottom of the ADC range the scan window is formed and all strips with the ADC values in the window are added to every bin in the window. For example, the strip in figure 4.14 is added to bin 1,2 and 3.
2. The scan window is then moved upward one bin size and step 1 is repeated for all strips in the window. This repeats until all bins have been counted.
3. At the end we are left with the strip count inside each ADC bin. The bin with the largest strip count is selected as the CM and the ADC values in this bin are averaged to give a final CM result.

Step 2 above is the crux of this method. The scan window is necessary because if we tried to count each strip in each bin by itself there would not be enough counts since the bins are only 2 ADC channels wide. Therefore summing the total scan window into each bin increases the counts and helps to average the result. This method is experimental and was developed during GEN-II running but was not used. We will discuss later possible implementations for future experiments.

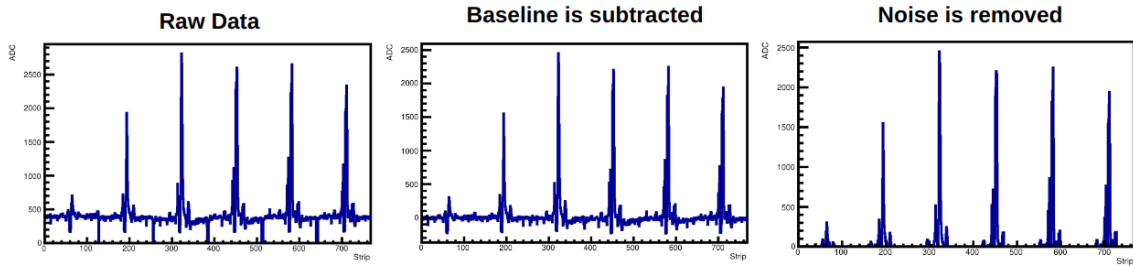


FIGURE 4.15: (Left) Raw APV data with a hit. (Middle) After CM subtraction the baseline is not reduced to near 0. (Right) After zero suppression all the low ADC signals are removed and only the hit data is saved to data.

4.5.7 Zero Suppression

Now the data is pedestal and CM subtracted, the baseline ADC values should reduce down to near zero. Figure 4.15 shows the process of one event after CM subtraction. The next step is to remove all the low ADC channels so they are not saved to data as they have no use. This is called zero suppression (ZS). All strips are now checked if they pass the cut $ADC_i > 5\sigma_{ped}$, where ADC_i is the sum of all six time samples for one channel, i . Only the strips passing the cut are saved to data, and the rest are discarded. This essentially means that strips within 5 sigma of the pedestal noise are discarded.

As previously mentioned, the remaining strips are counted as real signal and we can compute our occupancy here. The occupancy is simply the fraction of strips with a signal that passes the ZS. The example in figure 4.15 is relatively low occupancy, with only ~ 10 strips left over, or $\sim 8\%$ occupancy.

4.5.8 Clustering

The GEMs have two strip axes as described in section 4.1.2. Therefore the clustering must first be done on each axis separately and then 2D clusters are formed later. Production runs have high rates and large number of strips firing on the GEMs. Therefore many cuts can be applied to improve reconstruction of true tracks. Using runs with lower beam currents and lower occupancies make the combinatorics manageable and are used to set parameters for the GEM algorithms to add cuts and improve the algorithm speed. A list of parameters are shown in table 4.1. We will also often make use

of correlation coefficients between two signals. The correlation coefficient is defined as

$$C_{\text{corr}} = \frac{\sum_i U_i V_i - N \frac{\sum_i U_i \sum_i V_i}{N^2}}{N \sqrt{\frac{\sum_i U_i^2}{N} - \left(\frac{\sum_i U_i}{N}\right)^2} \sqrt{\frac{\sum_i V_i^2}{N} - \left(\frac{\sum_i V_i}{N}\right)^2}} \quad (4.3)$$

where U is signal one, V is signal two, N is the number of time samples, and i index is summed from 0 to N . This correlation is used in multiple situations, for example the ADC strip correlation, $ADC_{\text{strip}}^{\text{corr}}$, the two signals are the ADC signal U from one strip and V from a different strip and the sum is over the six time samples.

Another important parameter will be the "calorimeter constraint". The calorimeter constraint is defined by $|x/y_{\text{clust}} - x/y_0^{\text{cal}}| < x/y_w^{\text{cal}}$. This means that GEM cluster or strip must be within some width, x/y_w^{cal} , from the cluster position of BBCal, x/y_0^{cal} . This effectively forms a square constraint on the GEM layers, as shown in figure 4.16. This reduces the clustering and tracking region to the size of this constraint, which is significantly smaller than the entire GEM active area. This constraint is extremely important, as it significantly reduces the combinatorics in the tracking algorithm.

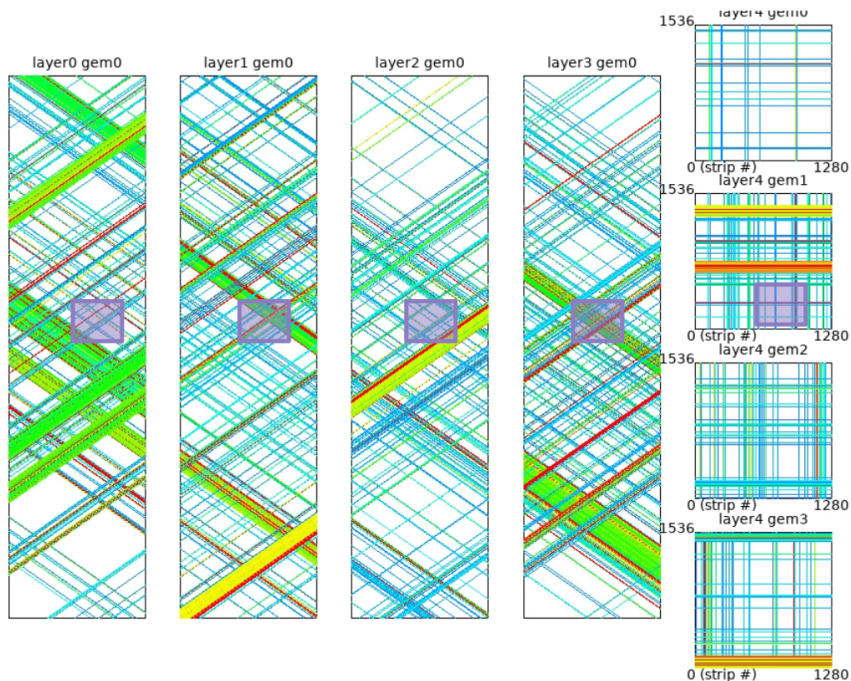


FIGURE 4.16: Illustrative example of the calorimeter constraint (not to scale). Each GEM layer with all strips with signals is shown with the BBCal cluster square block overlaid. Only strips inside the cluster region are considered in the tracking algorithm.

TABLE 4.1: Parameters for GEM clustering algorithm.

Parameter	Definition
$ADC_{\text{Sum}} = \sum_{i=0}^{N_{\text{Samp}}} ADC_i$	ADC sum of all time samples.
$ADC_{\text{Sum}}^{\text{Cut}}$	ADC sum cut, found from calibrations.
$t_{\text{strip}} = \sum_{i=0}^{N_{\text{Samp}}} ADC_i t_i / ADC_{\text{Sum}}$	ADC weighted strip time.
t_0, σ_t	Mean and standard deviation of strip times samples from calibrations
$t_{\text{add strip}}^{\text{Cut}}$	Time cuts used for clustering found from calibrations.
$ADC_{\text{strip}}^{\text{corr}}$	ADC correlation between the peak and other strips in a cluster.
$ADC_{\text{strip}}^{\text{corr, cut}}$	ADC strip correlation cut found from calibrations.
$ADC_{\text{clust}} = \sum_{i=0}^{N_{\text{Strips}}} ADC_{\text{Sum},i}$	ADC cluster is the sum of all time samples for all strips in the cluster.
$ADC_{\text{clust}}^{\text{Cut}}$	Cut for cluster ADC found from calibrations.
$t_{\text{clust}} = \sum_{i=0}^{N_{\text{Strips}}} ADC_{\text{Sum},i} t_{\text{strip},i} / ADC_{\text{clust}}$	Cluster time is the ADC weighted time from all strips in the cluster.
$x_{\text{clust}} = \sum_{i=0}^{N_{\text{Strips}}} x_i^{\text{strip}} ADC_i$	x cluster position, weighted average from x strip positions.
$y_{\text{clust}} = \sum_{i=0}^{N_{\text{Strips}}} y_i^{\text{strip}} ADC_i$	y cluster position, weighted average from y strip positions.
$x_0^{\text{cal}}, x_w^{\text{cal}}, y_0^{\text{cal}}, y_w^{\text{cal}}$	Mid point and width of the calorimeter constraint x and y value.
$\Delta t_{\text{hit}} = t_{\text{clust},u} - t_{\text{clust},v} - (t_{\text{clust},v}^{\mu} - t_{\text{clust},v}^{\mu})$	Time difference cut between two clusters in the 2D hit combination.
Δt^{cut}	Time difference cut from calibration.
$ADC_{\text{hit}} = 0.5(ADC_{\text{clust},u} + ADC_{\text{clust},v})$	2D hit ADC.
$ADC_{\text{asym}} = \frac{ADC_{\text{clust},u} - ADC_{\text{clust},v}}{2ADC_{\text{hit}}}$	ADC asymmetry between two clusters.
$ADC_{\text{asym}}^{\text{Cut}}$	ADC asymmetry cut from calibration.
$ADC_{\text{hit}}^{\text{corr}}$	ADC correlation between two clusters.
$ADC_{\text{hit}}^{\text{corr,Cut}}$	ADC correlation cut from calibration.

1D Clustering

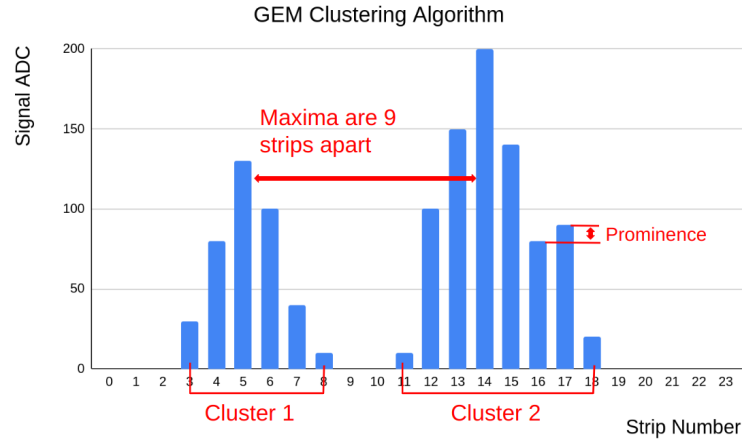


FIGURE 4.17: An illustrative example of the clustering algorithm. The data is not realistic and only used for visual purposes. In this example the algorithm first starts with three clusters at the three local maxima of strip number 5, 14, and 17. However after checking nearby clusters it finds that the cluster at 5 and 14 are too far away, but cluster 14 and 17 are close by and the prominence of 17 is very small. 14 and 17 are then combined into one cluster.

The 1D clustering iterates through all strips with signal found on that axis. Figure 4.17 shows a qualitative picture to reference while going through these steps. Here we will use ADC_{sum} and t_{strip} whose definitions can be found in table 4.1. Starting with the first strip in the list these steps are followed:

1. Check if the current strip ADC_{sum} is larger than the ADC_{sum} of both adjacent strips, left and right. Also check the ADC threshold, $ADC_{\text{sum}} > ADC_{\text{sum}}^{\text{Cut}}$, and check the strip time threshold is close to the expected good mean times, $|t_{\text{strip}} - t_0| < \sigma_t$. If all of these are true then the strip is labeled as a local maximum.
2. Loop through the list of all local maxima. Check the closest local maxima to the right and the left of this peak that is larger. Then check if this peak is within 8 strips of the original maximum. If not then the maxima stay as two separate clusters. If they are close together then follow this next step (a)
 - (a) Look at all strips between these two peaks and find the smallest ADC_{sum} strip. This minimum strip is referred to as the “valley”.
 - (b) Calculate the “prominence” of the current peak, which is the difference in ADC_{sum} between it and the valley. The noise of the ADC_{sum} is $\sigma_{\text{sum}} =$

$N \text{ samples} \cdot \sigma_{\text{ped}}$. Then check to see if the prominence is small enough that the current maximum should not be considered as its own cluster.

$$\text{prominence} < \text{nsigma} \cdot \sigma_{\text{sum}} \text{ or } \frac{\text{prominence}}{\text{ADC}_{\text{max}}} < \text{max fraction} \quad (4.4)$$

The set values for nsigma is 2.5 and max fraction is 0.1. The first condition above, $\text{nsigma} \cdot \sigma_{\text{sum}}$, means the prominence is below the pedestal fluctuations. The second condition means that the prominence is small compared to the peak so it is considered a small bump. If either of the conditions above are true then the peak is not a separate cluster because it is too small of a difference.

3. Loop over the new list of local maxima. For each maximum check each strip to the left of it.
 - (a) Check the first strip to the left, going up to a maximum of four strip distances.
 - (b) Check that the timing on this strip is close to the timing of the maximum strip. Specifically check if $|t_{\text{strip}} - t_{\text{max}}| < t_{\text{add strip}}^{\text{Cut}}$ where t_{max} is the time of the local maxima.
 - (c) Calculate that the correlation coefficient is within the cut $|\text{ADC}_{\text{strip}}^{\text{corr}}| > \text{ADC}_{\text{strip}}^{\text{corr, cut}}$.
 - (d) If the strip passes all these cuts then add it to the cluster and move on to the next strip to the left.

After this is done for the left, repeat the same process for the strips to the right.

4. Create a 1D cluster using the strips that passed all the steps above. It will consist of the local maximum and all strips to the left and right.
5. Check if the cluster position is within the calorimeter constraint region, $|x_{\text{clust}} - x_0^{\text{cal}}| < x_w^{\text{cal}}$ (same for y cluster). If not then the cluster is not saved.
6. Remove clusters that do not pass a cluster ADC sum threshold or do not have at least 2 strips.

The clusters are then formed from all the strips around the local maximum. We will briefly discuss the parameters of a 1D cluster, which are also listed in table 4.1. The cluster variables comprise of the combined values from the strips that form the cluster. The cluster ADC is the sum of all strip ADC sums inside the cluster. The cluster time

is the ADC weighted time of all the strips inside the cluster. The cluster position is the ADC weighted strip positions.

2D Clustering

First all 2D hit combinations are formed for all clusters passing the 1D clustering phase. These 2D clusters will be referred to as "hits". When looking at every possible 2D combination the following conditions are checked.

1. Check if cluster position is within the calorimeter constraint region $|x_{\text{clust}} - x_0^{\text{cal}}| < x_w^{\text{cal}}$ **and** $|y_{\text{clust}} - y_0^{\text{cal}}| < y_w^{\text{cal}}$.
2. Check if the time difference between the two clusters passed the cut $|\Delta t_{\text{hit}}| < \Delta t_{\text{Cut}}$.
3. Check that the correlation coefficient is within the cut $|\text{ADC}_{\text{hit}}^{\text{corr}}| > \text{ADC}_{\text{hit}}^{\text{corr, cut}}$.
4. Check that the ADC asymmetry between the two axes is within $|\text{ADC}_{\text{hit}}^{\text{asym}}| < \text{ADC}_{\text{hit}}^{\text{asym, cut}}$.

After all these cuts are passed then we have a list of 2D hit candidates for each module. Tracking must now be performed to figure out which hits are real and follow a straight line track.

4.5.9 Track Finding

Now we have a list of 2D hits for each layer that are possibly on a track. With multiple GEM layers we can search for a combination of hits that form a straight line between them. This is how the track finding is done:

1. Check that there are enough layers with hits to form a track. For GMn/Gen this number is three, but with higher rate and more layers it should be increased.
2. Loop over all possible combinations of hits from the two outer most layers and form a track between them.
 - (a) Also check that the line projects back to the target and also projects forward to the calorimeter constraint.

3. Loop over all tracks formed and check the every hit on the intermediate layers near these tracks.
4. For each combination fit a line and check that the χ^2 is within some cut.
 - (a) Also check that the line projects back to the target and also projects forward to the calorimeter constraint.

After this we finally are left with a list of good tracks passing all the cuts above. These final tracks are used in the physics analysis.

4.5.10 Spatial Resolution and Efficiency

Each GEM module will have some spatial resolution. Given a track from section 4.5.9 the x/y position at each layer can be calculated, x/y_{track} . The hit position, x/y_{hit} , which formed the track is used for the residual of this hit. The residual is then

$$x/y_{\text{res}} = x/y_{\text{hit}} - x/y_{\text{track}} \quad (4.5)$$

After many events are collected the standard deviation of this variable would give the resolution $\sigma_{x/y}$ for this GEM module.

When a charged particle passes through a GEM it may or may not deposit enough energy to form a hit. We can determine the efficiency of module from a statistically large sample of tracks. The number of tracks that pass through a module can be counted, $N_{\text{should hit}}$. The number of tracks with hits on the module, $N_{\text{did hit}}$, can also be counted. The efficiency is simply the ratio, $Eff = N_{\text{did hit}}/N_{\text{should hit}}$. Ideally $N_{\text{should hit}}$ should be known with a large certainty independent of the GEMs, however the GEM modules were the only trackers in the SBS experiment and so they had to be used to determine their own efficiency. If at least 3 layers do not record a hit then the track is never found which artificially increases the efficiency because $N_{\text{should hit}}$ is decreased. However the change in efficiency would be small and with large GEM efficiencies and the effect is almost negligible. Overall this method is adequate for our purposes.

Chapter 5

GEM Analysis

5.1 Common Mode

The different common mode (CM) algorithm has been explained in detail in section 4.5.3. Since the zero suppression is applied online there would be no way to recover all the information to determine if the CM was calculated correctly. Thus, for diagnostic purposes we set 1% of events to have no CM subtraction or zero suppression online so that it can be fully studied with offline algorithms. We call these events “full readout”. This data was used for the studies that will be subsequently discussed.

The common mode (CM) has a number of intricate issues that go into understanding how analysis of it works. See the example in figure 5.1, which shows an one APV event with a large signal with high occupancy and the CM results for the different algorithms. The question here is which CM is “correct”? The only way to tell is to look at the event display by eye and determine which result is closest to the baseline. Another complication is that μ_{CM} and σ_{CM} is calculated from a pedestal run (section 4.3) and assumes that the baseline is the same during beam conditions as during the pedestal conditions. If the baseline shifts then the search window will be in the wrong area, and will bias the result to incorrect values. Moreover, the experimental data is zero suppressed, as discussed in section 4.5.7, and so the data could be lost and there would be no way to recover where the correct CM was.

During the GMn experiment we discovered that the CM does in fact change under beam conditions. This phenomenon can be seen in figure 5.2. Evidently the beam CM tends to be lower than the pedestal CM. This is due to the nature of the RC circuit in the APV, which decreases the baseline at higher rates [61]. This effect must also be accounted for when determining which CM value is “correct”.

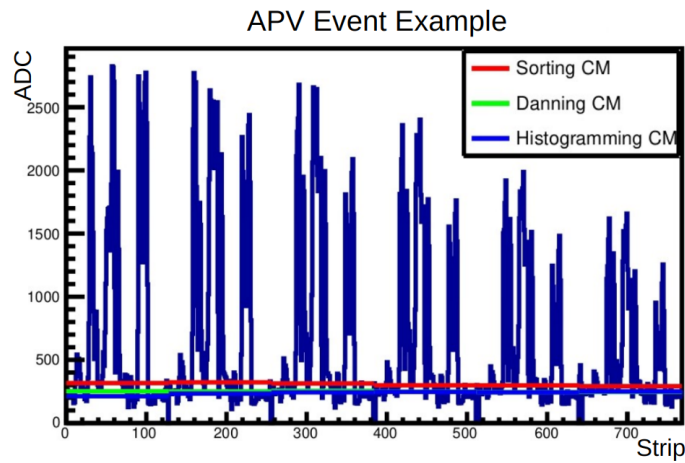


FIGURE 5.1: Example of one APV event with the CM results. Notice how the different common modes give slightly different results in a high occupancy event.

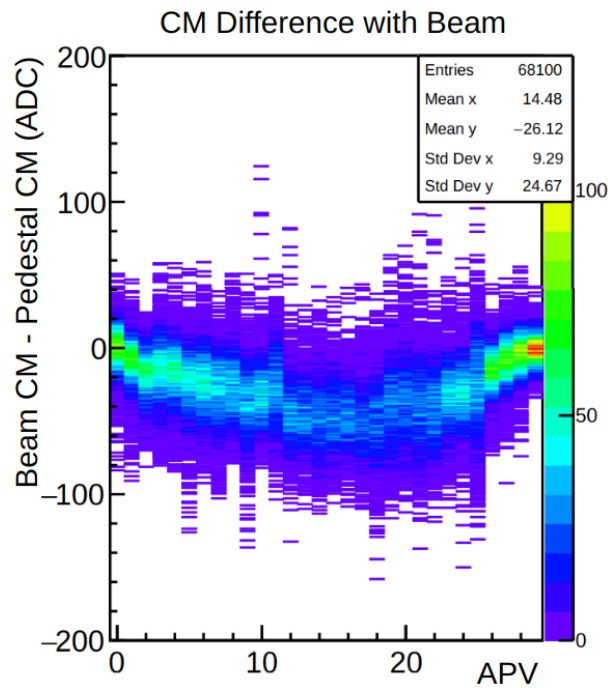


FIGURE 5.2: Example of CM calculated for a few thousand events for one GEM under beam conditions during GMn compared to pedestal conditions. Note that the APV cards in the middle have the largest negative difference, due to higher occupancies.

5.1.1 Rolling Common Mode

To better understand the common mode shift under beam we implemented a “rolling average” of the CM. Recall from section 4.5.5 that the μ_{CM} and σ_{CM} from the pedestal run determine the search window for the Danning method during beam conditions. We can improve this situation by instead taking μ_{CM} and σ_{CM} from the last 100 calculated events under beam conditions to obtain more accurate values. The procedure is as follows:

1. Before collecting 100 full readout events use μ_{CM} and σ_{CM} from the pedestal run.
2. With 100 events collected the μ_{CM} and σ_{CM} is now calculated from those events and used for the search window for the Danning method for the next event.
3. The next event has its CM calculated and it is now added to the end of the 100 event list, while the first event in the list is removed. The μ_{CM} and σ_{CM} is now calculated with the new list of 100 events.
4. Continue step 3 for every event now where the list of 100 events is constantly updating, or “rolling”.

The idea here is that the beginning CM values are slightly incorrect and so we keep updating a list of only the previous 100 events. But as the list of 100 events keeps getting updated the Danning method search window becomes a very good estimate for the beam data CM.

IMPORTANT NOTE: The online DAQ does not have the FPGA resources to perform this rolling average described above. Therefore this averaging is only done with offline data to refine CM calculations and make better estimates of how well the online algorithms are performing.

5.2 Common Mode Algorithm Studies

A study of the different CM algorithms was performed to determine which has the best performance. The goal was to scan from low to high luminosities to see how the algorithm performs. This study was performed during GEN-II on the optics target (figure 3.18), to maximize luminosity, at beam currents of $5 \mu\text{A}$, $15 \mu\text{A}$, $30 \mu\text{A}$, $45 \mu\text{A}$. For each beam current 5000 events were analyzed to obtain a good statistical sample.

Looking at event displays by eye we determine that the histogramming method with a rolling average gives the most accurate CM result. Therefore this will be labeled as the “correct CM” for the purposes of this study. Figure 5.3 shows an example of how the different CM methods compare when applied to the same data.

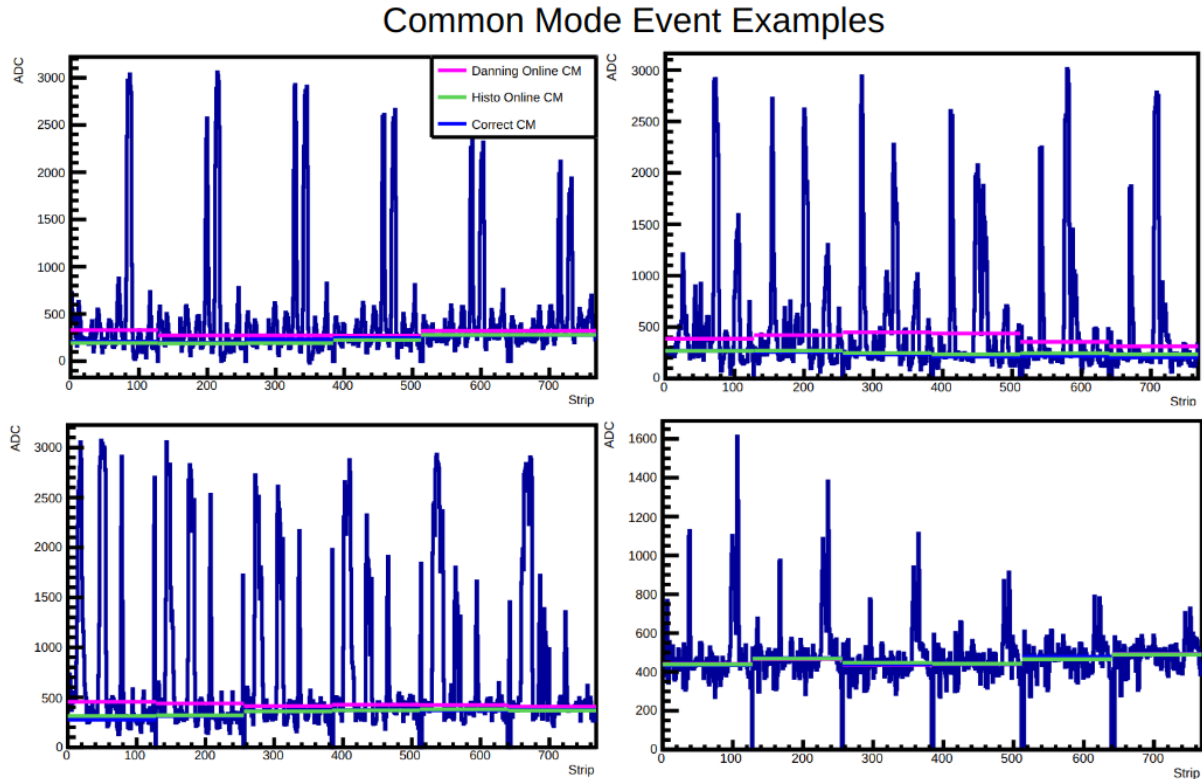


FIGURE 5.3: Example of different CM calculated for a few events. Note how high occupancy events cause the online Danning method to fail more often. Bottom right shows how all methods work well for low occupancy data.

Aggregating all events and calculating the difference between the each CM algorithm and the correct CM value shows how well the algorithm is working. For each method this is calculated $CM_{diff} = CM_{test} - CM_{correct}$. From all data the CM_{diff} average and standard deviation can be calculated. This is done for every APV and for every GEM module. The final results are seen in figure 5.4. The typical σ_{CM} is ~ 8 ADC which means the search window is 80 ADC wide for 5σ . For this three main methods are tested:

- **5σ Danning:** Danning method with a 5σ window cut.
- **30σ Danning:** Danning method with 30σ window cut.

- **30σ Histogramming:** Histogramming method with 30σ window cut.

The 5σ Danning window has typically been used in the past but it is found that at the highest luminosities it has large biases, up to 100 ADC, which is a significant portion of the signal ADC. By making the window larger we increase the chance of capturing the correct CM while also increasing the changes of high signal ADC biasing the CM result. It is shown that making the window much larger, 30σ , actually improves the results. This tells us that even this large window does not capture so much signal that it ruins the CM averaging. The Danning method still has some differences from the correct CM, up to 20 ADC, but is still much improved to the 5σ case. The search window for the histogramming method has different implications than the Danning method. Recall from section 4.5.6 that the search window has further binning inside of it in which strips are added for averaging. Therefore there is no obvious downside to increasing the histogramming search window, since it only increases the range of ADC channels checked for the correct CM. The histogramming search window should ideally be as large as possible. The histogramming method variation around the correct CM are < 5 ADC over all luminosities studied.

The luminosities during GEN-II were low compared to this study and so the 5σ Danning method was continued to be used. However for future experiments with higher luminosities new options must be deployed. VTP hardware experts have been informed and they are currently trying to recreate the histogramming method in the VTP. This would be essential to extracting accurate GEM APV signals in future experiments planned in hall A, namely GEp-V.

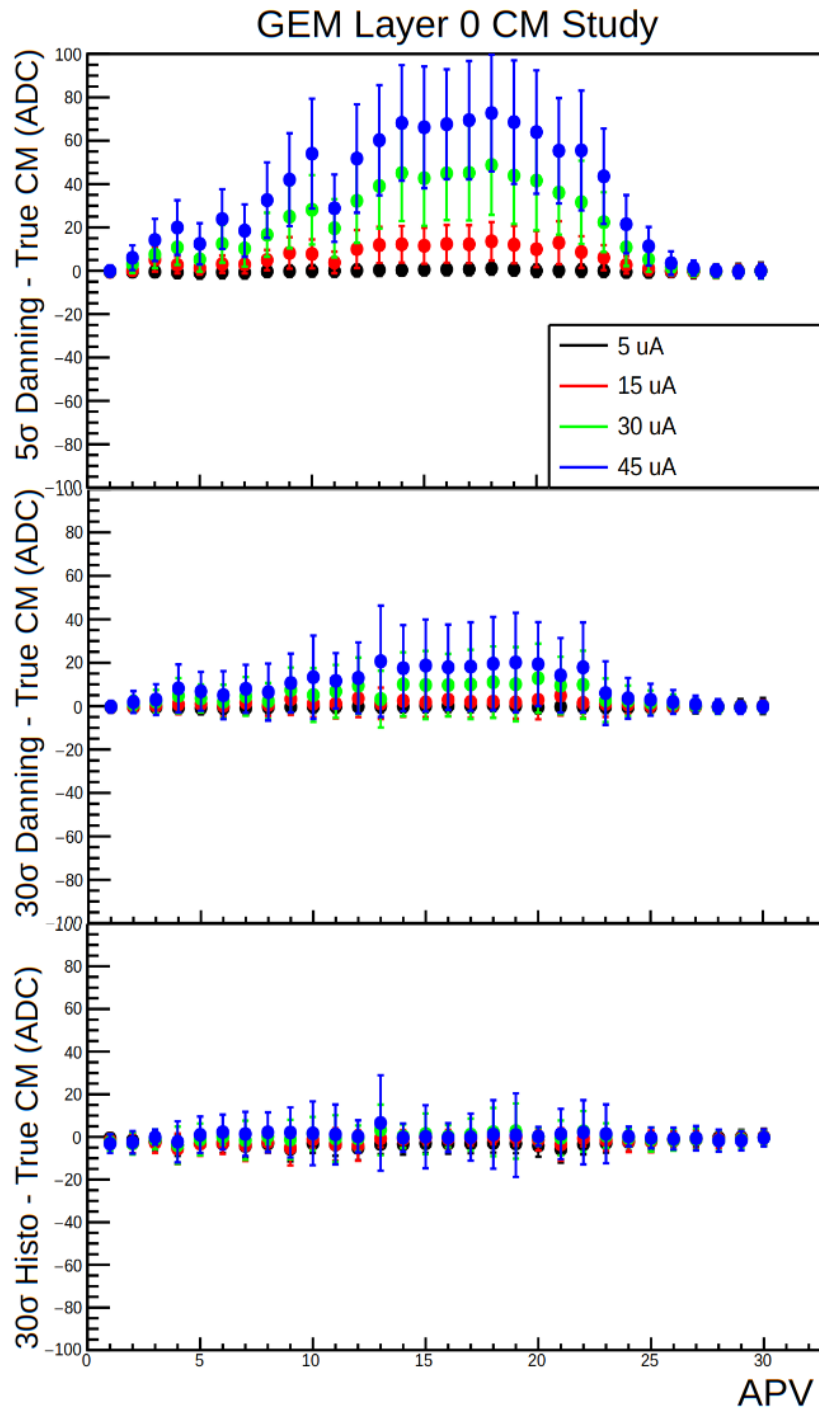


FIGURE 5.4: CM study results for GEM layer 0, which has the highest occupancies. The different beam currents are shown in the legend. Three methods are shown, with the 30σ histogramming window yielding the best results. The original method, 5σ Danning, yields large biases at high rates.

5.3 Shielding Results

It was discovered when the the GEM modules were moved from bench tests to the BB apparatus that the CM fluctuations significantly increased. Electromagnetic shielding was applied, as described in section 4.3.2, to reduce the outside effects causing this. The CM fluctuations were measured with the modules with no shielding inside the BB setup. It was then removed and shielding was applied and it was returned to BB. The resulting CM fluctuations are shown in figure 5.5. The standard deviation improves by a factor of 3. Also notably the fluctuations were checked again whenever changes were made to the experimental setup and the results remained unchanged after shielding.

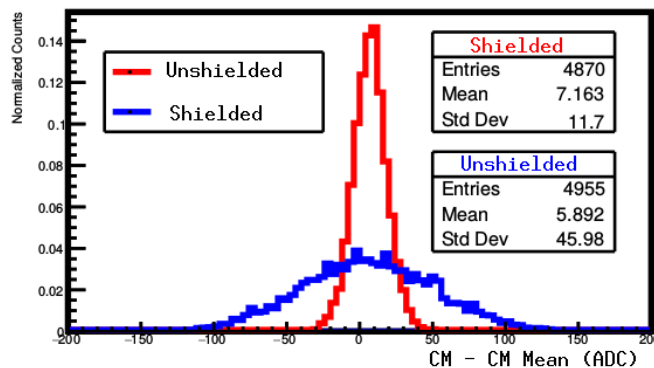


FIGURE 5.5: Shielding result for one GEM module. The CM resolution increases from 46 to 12 ADC. Similar improvements are found for all GEM modules after shielding.

5.4 Negative Signal Study

During GMn the CM algorithm used the Danning method with no lower bound on the search window. The logic was that all signal is positive, so any negative fluctuations around the baseline should be from noise. However during GMn it was discovered that under beam conditions the APVs do have some negative signal strips which throw off the CM result. Figure 5.6 shows an example of a negative spike which is found often in the beam data. After discovering this we ensured that the CM window had a cut on the negative and positive side so this bias was not introduced in the GEn running.

From the figure it is clear that the negative signal is a cluster from multiple strips combined and not random strips, spread throughout the APV. Therefore the immediate

worry is that this is a real hit that somehow gets flipped negative by the APV, and therefore is lost and would reduce the track reconstruction efficiency. We will save discussion for later as to what is causing this. First we investigate how much this affects our end result.

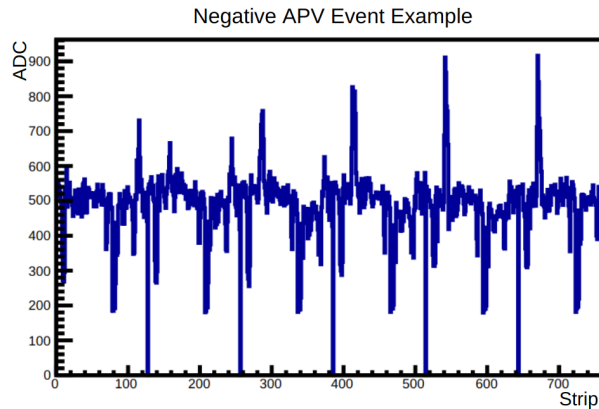


FIGURE 5.6: Negative event example from GMn data. Here a large spike can be seen in the negative direction, which is only found under beam conditions.

If a track passes through a layer and there is no hit found on that layer, we can search the region for a negative cluster. If there is a negative cluster on a track then we can conclude that real clusters are being flipped negative and decreasing our efficiency. Let us define the “negative occupancy” as the total fraction of strips that are negative. After all the tracks are formed, the GEMs missing hits on a track can be checked to see if the area around the track has a negative cluster. This can be evidence that the cluster was flipped negative and lost in the tracking algorithm. However the negative signals may also be random, and so we must also check if there are negative clusters nearby even if a normal positive hit is found near a cluster. This means that the negative cluster was nearby the track by coincidence. To make a fair comparison we must then compare negative clusters near missing hits to the negative clusters near found hits.

This study was done with three different beam currents of increasing luminosity. The results can be found in figure 5.7. As luminosity increases we find that the negative occupancy increase, which is to be expected. From figure 5.7a it is notable that as the occupancy increases the fraction of negative clusters on missing hits stays roughly the same over the range. If lower tracking efficiencies were caused by negative clusters then we would expect the fraction on missing hits to increase as the occupancy increased, but this is not seen. Figure 5.7c shows the result if we subtract from this

the random chance that a negative cluster is near a track (figure 5.7b). From the result, through all occupancies there is $< 5\%$ difference, meaning that no more than 5% of the missing hits could be due to the negative clusters. From this we determine that the negative strips are negligibly affecting our tracking results.

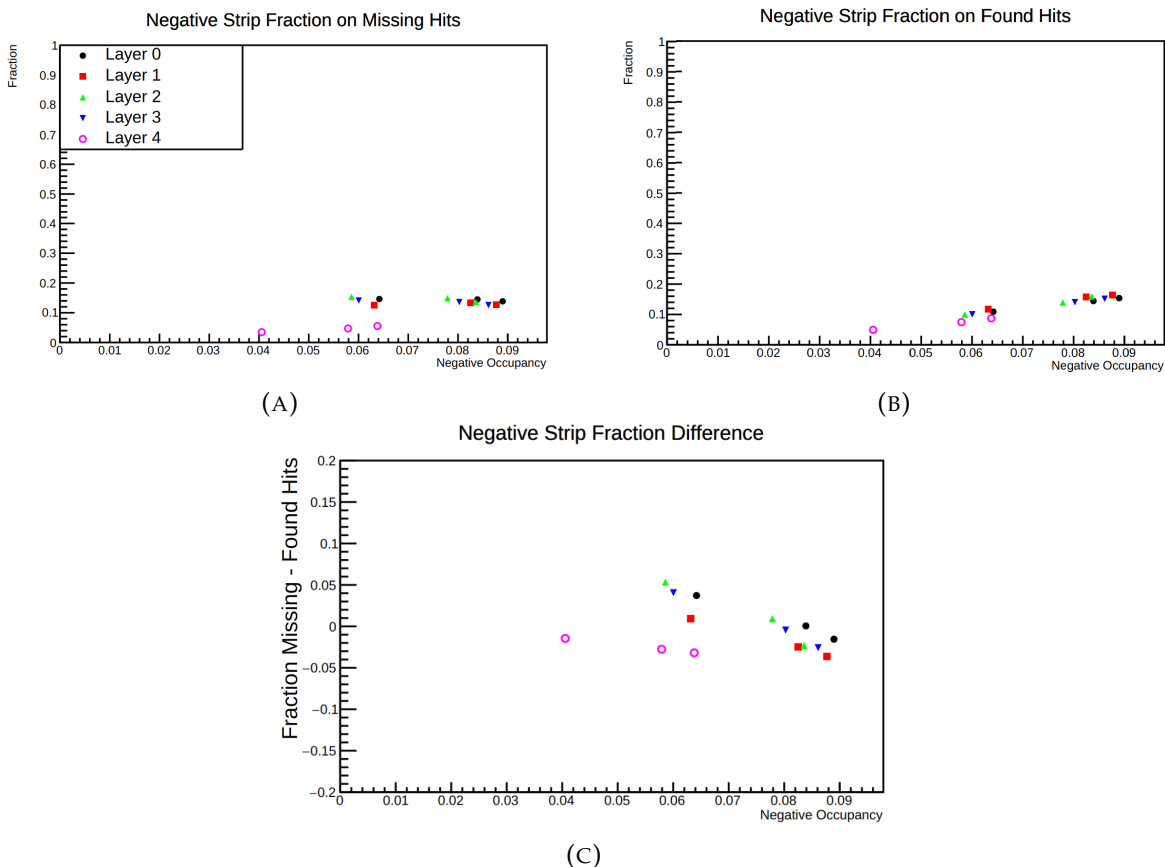


FIGURE 5.7: Results from the negative signal study. (A) The fraction of tracks with a missing hit that have a negative signal near the track. (B) The fraction of tracks with a hit that have a negative signal near the track. (C) Difference between the results from (A) and (B).

The question still remains, what is causing the negative signals? The negative signals are not seen at low rates ($< 5\%$ occupancy) and so are only seen under beam conditions. The root issue requires APV electronic experts to perform specific studies outside of the experiment, which has not yet happened. Therefore there is no conclusion yet about why this is happening, except that it is not largely affecting our data.

5.5 High Voltage Study

A major issue discovered during GMn was larger rates than expected causing the charge deposition on the GEM foils was larger, which change the current draw from the resistive voltage divider, and reduces the effective voltages provided by the divider and therefore the gain and tracking efficiency. This means the efficiency is greatly decreased as the luminosity increases.

The gain drop effect can be directly seen at the hardware level instead of having to rely on tracking results, which can be complicated by the algorithm. As the charge is deposited on the foils it creates some current which changes the current applied by the power supply. This reduces the effective voltage over the divider and so the power supply then increases the current in order to meet the proper voltage setting. We define the “excess current” as the current draw under beam conditions minus the current with no beam. By definition the excess current is at zero when the beam current is at zero. The current drawn by the GEM foils during operation is proportional to the rate of ionizing particles entering the GEM detector and the detector’s gain factor. If the detector gain remains constant, we expect the GEM foil current draw to be linear with the rate seen by the detector, and hence on the beam current with a given target. With the resistive divider the slope of the excess current versus beam current is proportional to the detector gain. Given this, the reduction of the slope gives the fractional reduction of the chamber gain at high beam currents. An example of this can be seen in figure 5.8.

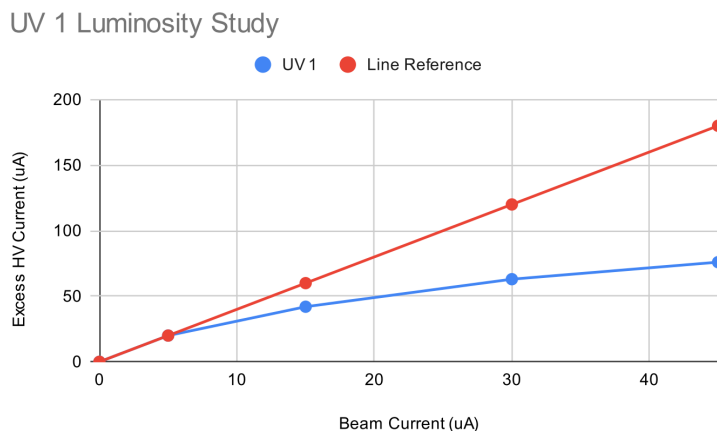


FIGURE 5.8: Example of the HV excess current versus beam current from GEN-II data. The excess current is proportional to the beam current at low beam currents, and then the slope of the plot goes down as the beam luminosity overwhelms the divider.

The parallel power supply (CAEN HiVolta DT1415ET) is used to remedy this issue. The voltage is then directly set by the power supply for each foil and so there is no drop from the resistors in the divider. However, as seen in figure 5.9, the protective resistors are still present and cause some voltage drop. There is a further benefit that the individual channels now measure the currents, which can be used to calculate the voltage drop over the protective resistor. The voltage can then be adjusted to match the desired value. The formula for this correction is found in equation 5.1. It is critical to remember here that the GEM foils are 60 sectors so the resistors are all in parallel. Therefore the values used in the equations 5.1 are $R_{0,1,2,3} = 10/60 \text{ M}\Omega$ and $R_{4,5} = 0.5/60 \text{ M}\Omega$.

A graduate student at UVa, Vimukthi Gamage, tested the parallel design at UVA using high rate x-ray exposure. He showed that the performance greatly improves the gain drop, as seen in figure 5.10. It was then decided to use on parallel HV supply for the first layer in the GEMs during GEN-II, which experiences the highest rates and would gain the most advantage. GEN-II is the lowest luminosity experiment in the SBS program and therefore is properly poised to test the design under real beam conditions. The GEN-II luminosities were low enough that there would be no significant drop in gain but a specific test on a carbon target was completed to measure how the new power supply performed.

Figure 5.11 shows the result of the HV study. Layer 0 clearly has much improved excess current compared to the other module that use the divider design. This result provided confidence that the new power supply setup improves the situation under beam conditions and all GEM modules will be switched over to parallel power supply's for future high luminosity experiments.

$$\begin{aligned}
 V'_0 &= V_0 - I_{B3}R_5 & I_{B3} &= I_1 - I_0 \\
 V'_1 &= V_1 + I_{B3}R_5 + I_{T3}R_4 & I_{T3} &= I_1 - I_2 \\
 V'_2 &= V_2 - I_{T3}R_4 - I_{B2}R_3 & I_{B2} &= I_3 - I_2 \\
 V'_3 &= V_3 + I_{B2}R_3 + I_{T2}R_2 & I_{T2} &= I_3 - I_4 \\
 V'_4 &= V_4 - I_{T2}R_2 + I_{B1}R_1 & I_{B1} &= I_4 - I_5 \\
 V'_5 &= V_5 - I_{B1}R_1 + I_{T1}R_0 & I_{T1} &= I_5 - I_6 \\
 V'_6 &= V_6 - I_{T1}R_0
 \end{aligned} \tag{5.1}$$

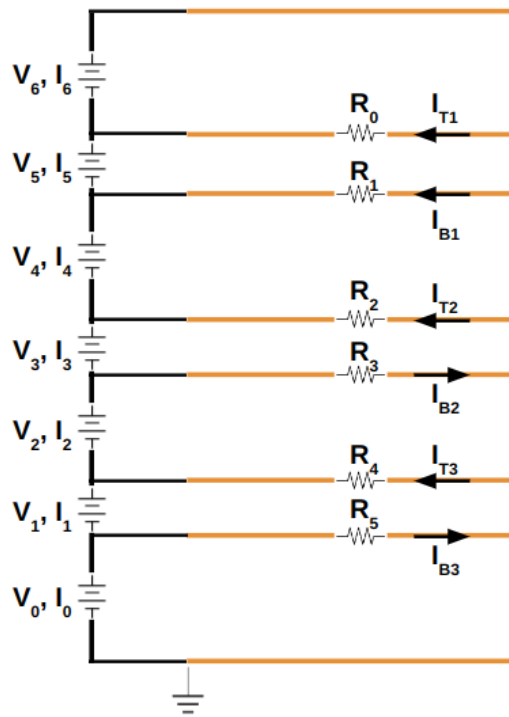


FIGURE 5.9: Schematic of the parallel divider with the HV current corrections. The power supply currents are listed on the left and all point downwards. The foil current (horizontal) directions are found from testing. The "T" and "B" subscripts refer to top and bottom of the foils, respectively.

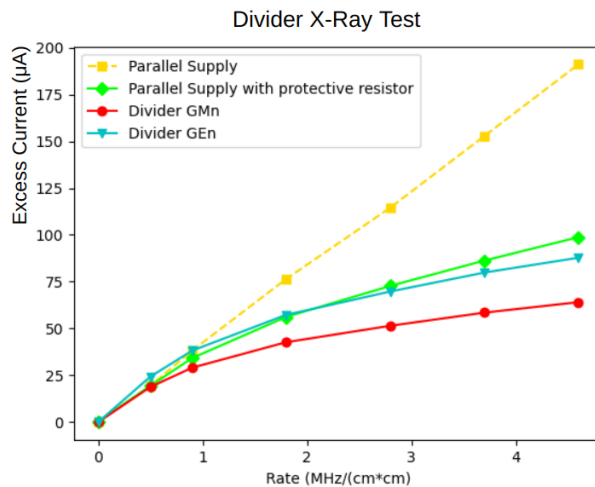


FIGURE 5.10: Divider x-ray study at UVA. A single XY GEM module with different HV schematics was study under different x-ray rates.

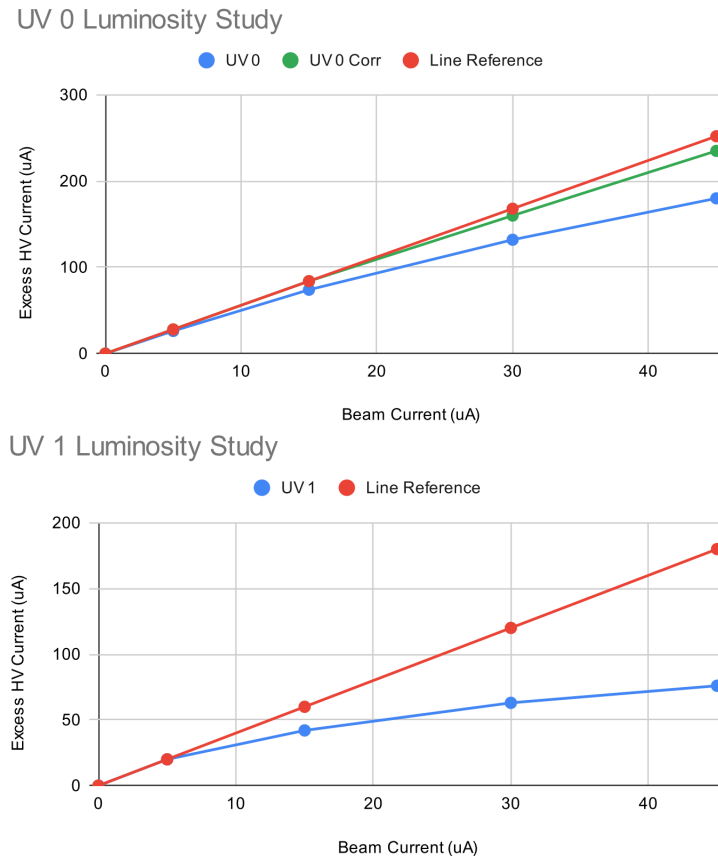


FIGURE 5.11: Results of the HV luminosity study. UV 0 has the parallel power supply while UV 1 has the resistive divider. Each module has a straight line drawn (red) between the first two data points to compare the data to a linear response. UV 0 also has the extra data from the corrections (green) applied from equations 5.1.

5.6 Spatial Resolution and Efficiency

The GEM residuals, as described in section 4.5.10, are calculated for the GEN-II data and plotted for all modules in figure 5.12. The resolution is then calculated by fitting Gaussians to each module and obtaining the σ . The resolution results are also presented in figure 5.12. Notable the UV modules have larger resolutions, with an average of $95 \mu\text{m}$, while the XY modules have average resolutions of $51 \mu\text{m}$. This is expected since the UV GEMs have higher occupancies in the front of the stack and the longer strips cause larger electrical noise fluctuations. Regardless the largest single module resolution was $106 \mu\text{m}$, which is more than good enough for the needs of the GEN-II experiment.

For the efficiency analysis there is an extra complication that the beam current from the CEBAF is often changing. The accelerator beam is liable to trip every five

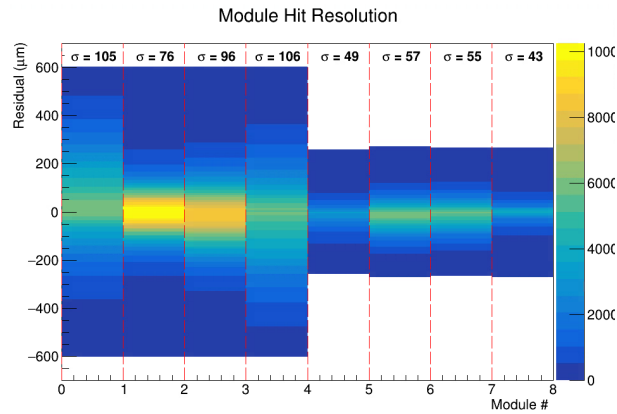


FIGURE 5.12: GEM resolution for GEN-II. The hits are plotted for each module. Each module is then fitted with a gaussian and the resolution is shown at the top of the plot. Recall from section 3.6.1 that modules 0 - 3 are UV and modules 4 - 7 are XY.

minutes or so. Even though it restarts almost immediately, a current ramp rate of $1 \mu\text{A/s}$ was used otherwise the glass target could be damaged. The operating current was usually $\sim 40 \mu\text{A}$, meaning the ramp would take almost a minute to stabilize. What all of this means is that often the average beam current was much less than the operating beam current. As discussed in section 5.5, the GEM efficiency is highly dependent on the beam current. Therefore an analysis of the GEM efficiency must also carefully account for the beam current at the time.

For the analysis here we will present the performance under the largest beam currents and then again with the overall data. The overall data will be representative of the experiment results, while the maximum beam current will be interesting to see how far the GEM performance was pushed. The results are seen in figure 5.13. The occupancy is always the highest for the first layer since it is directly facing the target with no material in between and so it sees the most particle rate. Meanwhile the rest of the front layers have a notably lower occupancy and the last layer is the lowest since it is further back behind other detectors and material. The first layer occupancy is $\sim 16\%$ at worst, but averages $\sim 14\%$ for all runs. Meanwhile all other layer occupancies are $\sim 12\%$ at worst, and averages $\sim 10\%$ for all runs. It is also notable that the occupancy lowers at higher kinematics slightly, but not significantly enough to affect the detector performance.

The module efficiency is always increased for layers further back because of the

different HV currents as explained in section 5.5. The efficiency does not change significantly for each kinematic since the rates are similar, just as found for the occupancy. With the highest beam current the first three layers' efficiency is $\sim 80\%$ and for all data averages $\sim 82\%$. For the last two layers the highest beam current yields an efficiency $\sim 90\%$ and for all data averages still $\sim 90\%$. Overall the conclusion is that the average run conditions are rather similar to the maximum beam current and therefore the time spent ramping up the beam was not a significant portion of the total recorded events.

These efficiencies are for a single module but for the experiment result the critical value is the track reconstruction efficiency. This means how often a true track is measured in the GEMs. A track is constructed from a minimum of three hits on the layers. The tracking efficiency can be calculated by using the individual layer efficiencies to combine the probability that at least three of the five GEM layers record a hit. The results are summarized in table 5.1. In the worst case during GEN-II the tracking efficiency was 96% and on average it was 97% showing that overall the track reconstruction was excellent in all conditions.

TABLE 5.1: Tracking efficiency results for GEN-II for the highest beam current setting and the overall data.

Kinematic	High Current Eff	Overall Eff
Kin2	97%	98%
Kin3	97%	97%
Kin4	98%	98%

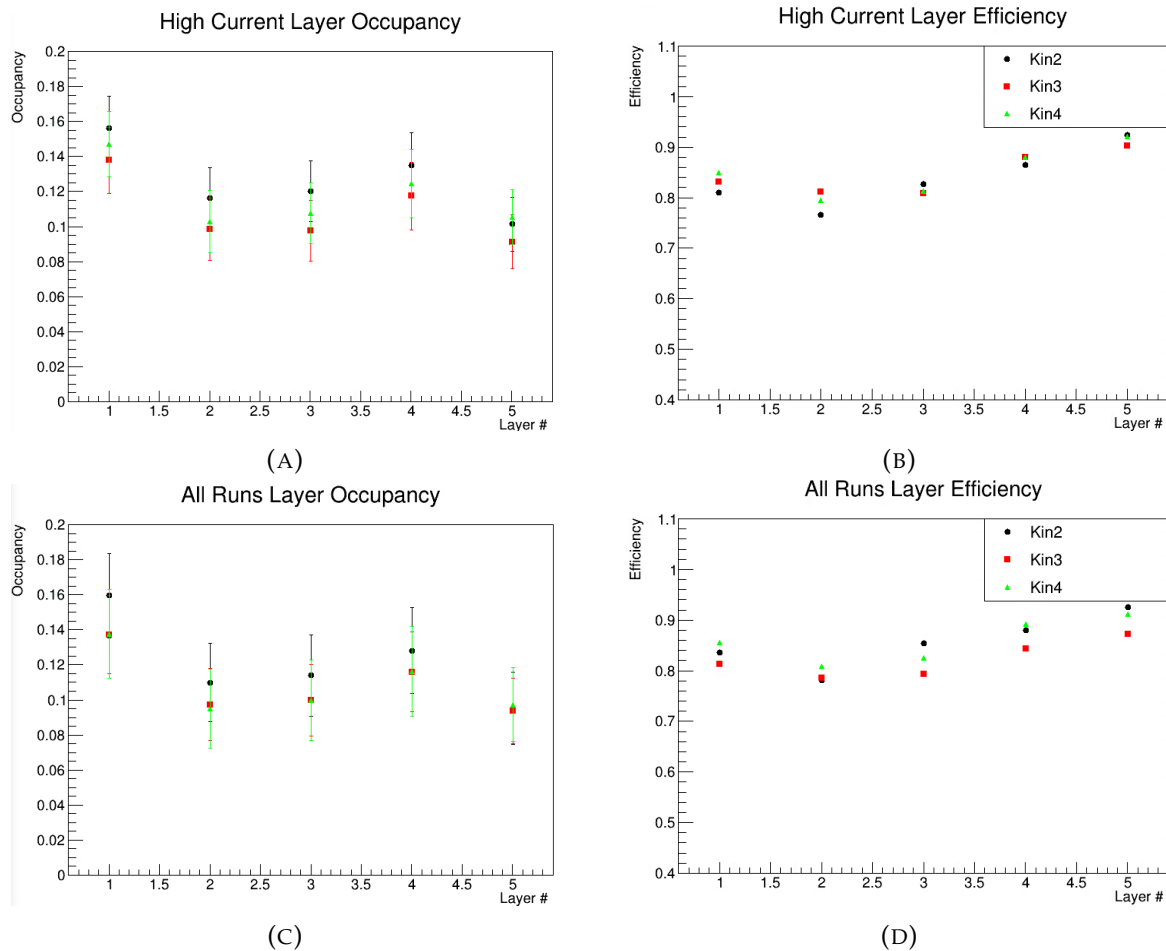


FIGURE 5.13: GEM results from all GEN-II data. High current data is analyzed for the (A) occupancy and (B) efficiency for each layer. Similarly all runs are combined to look at the overall (C) occupancy and (D) efficiency for each layer. Note that the occupancy plots show the average and standard deviation from all runs but the occupancy may actually vary widely for different beam currents. This is why the standard deviations are all larger in (C) compared to (A).

Chapter 6

Calibrations

All detector systems in the SBS program were newly built and therefore needed thorough calibrations to properly characterize the readout signals. The GMn experiment was the first to use the detectors and was critical in understanding the detector calibration before GEN-II. We owe a great thanks to the GMn students for developing the calibrations procedures which will be discussed here. Whenever possible we avoid using ^3He data for calibrations due to the Fermi motion which reduces the overall detector resolutions. The H_2 target (section 3.10.2) is often used here because the free proton target gives a very clean and well understood physics signal. The carbon target (section 3.10.1) is separately used for vertex position and angular calibrations.

6.1 Kinematic Notes

There are some nuances the calibrations data taken for this experiment which will be discussed here. There was no carbon target data taken for Kin2 and therefore the magnetic optics must rely on simulation models for this kinematic. This will be discussed in detail in section 6.4. To the best of my understanding, this data not being collected was an oversight during the experiment. Also there was no H_2 data collected for Kin4a and only 500k events collected for Kin4b. Therefore there is no hydrogen data to calibrate with for Kin4a, but there may be some future hope for Kin4b, although the statistics are low. This means that ^3He data must be used for calibration for Kin4, which may provide lower resolutions, which will be discussed in detail in chapter 6.6. This choice was made during experiment running because the high Q^2 settings would require a significant portion of beam time to be dedicated for collection of quasi-elastic events on

the H₂ target. Experts decided that the same calibrations could be done using ³He data instead.

6.2 GEM Trackers

For GEM detector data from a low beam current on H₂ target is used to get clean signals with low occupancy for calibration purposes. This means the tracking can be done with loose calibration settings and tracks can still be found, which are then used to calibrate the tracking algorithm parameters for a higher rate environment.

6.2.1 Alignment

TABLE 6.1: List of parameters used for GEM alignment.

Parameter	Description
x_0	Module x position center (m)
y_0	Module y position center (m)
z_0	Module z position center (m)
θ_x	Module x rotation (rad)
θ_y	Module y rotation (rad)
θ_z	Module z rotation (rad)

The analysis software must know, with sufficient accuracy, where each GEM module is positioned for tracks to be found with micrometer resolution. Each module has the parameters listed in table 6.1. For a given module position of the center is defined as

$$\vec{x}_{\text{mod}} = \begin{pmatrix} x_0 \\ y_0 \\ z_0 \end{pmatrix} \quad (6.1)$$

The rotations are then defined using the standard rotation matrices.

$$R_x = \begin{pmatrix} 1 & 0 & 0 \\ 0 & \cos(\theta_x) & -\sin(\theta_x) \\ 0 & \sin(\theta_x) & \cos(\theta_x) \end{pmatrix} \quad R_y = \begin{pmatrix} \cos(\theta_y) & 0 & \sin(\theta_y) \\ 0 & 1 & 0 \\ -\sin(\theta_y) & 0 & \cos(\theta_y) \end{pmatrix} \quad (6.2)$$

$$R_z = \begin{pmatrix} \cos(\theta_z) & -\sin(\theta_z) & 0 \\ \sin(\theta_z) & \cos(\theta_z) & 0 \\ 0 & 0 & 1 \end{pmatrix}$$

The absolute position for a single hit is then

$$\vec{x}_{\text{hit}} = \vec{x}_{\text{mod}} + R \vec{x}_{\text{hit,local}} \quad (6.3)$$

where \vec{x} is a 3D vector, $\vec{x}_{\text{hit,local}}$ is the local hit position inside the GEM, and \vec{x}_{hit} is the absolute position of the hit in space. The track position at each module is \vec{x}_{track} . From many hits a χ^2 can then be formed as

$$\chi^2 = \sum_{i=0}^{i=N \text{ hits}} (x_{\text{hit}} - x_{\text{track}})^2 + (y_{\text{hit}} - y_{\text{track}})^2 \quad (6.4)$$

The χ^2 can then be minimized to find the final module parameters. Figure 6.1 shows the result of the χ^2 minimization where all modules are nicely aligned at zero. The resolutions are all 100 μm or less.

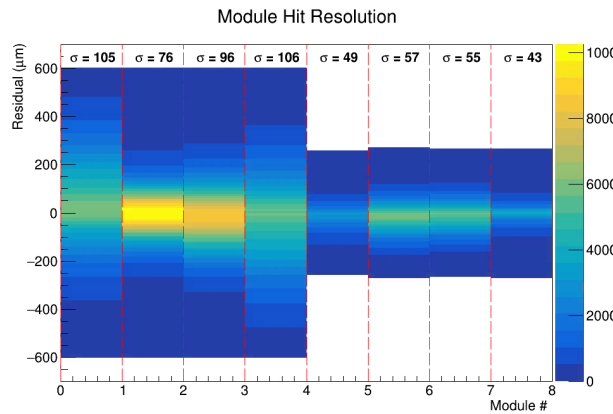


FIGURE 6.1: Result of the GEM alignment calibration. We see that each module is aligned to near zero.

6.2.2 Gain Matching

Due to gain variations, the ADC values returned by different GEM readout APV cards for similar energetic particle signals could vary by as much as 10%. As indicated in section 4.5.8, the asymmetry between ADC values from the two directions of the strip readout is used to identify 2D hit combinations in tracking. The gain variations affect this asymmetry variable and hence the ability identify the 2D hits. To ensure that any asymmetry cuts can properly compare strips from different APVs a gain coefficient is used for each APV and each module. The gain coefficients are defined as such

$$\text{ADC}_G = G_i G_j \text{ADC}_{\text{raw}} \quad (6.5)$$

where G_i is the gain for module i , G_j is the gain for APV j on that module, and ADC_{raw} is raw ADC recorded by the electronics. Recall that the ADC_{asym} has been previously defined in table 4.1. Over a statistically large sample the mean ADC_{asym} for each APV can be calculated along with the standard deviation. For convenience, for only this discussion, we will label the mean ADC asymmetry as A and the standard deviation as σ_A . Then for APV i along the U-axis we label the asymmetry as $A_{u,i}$ and for APV j along the V-axis we label the asymmetry $A_{v,j}$. $A_{u,i}$ and $A_{v,j}$ are calculated after the gain coefficients have been applied in equation 6.5, so the gains are accounted for. From this we further define

$$A_{u/v,\text{mod}} = \frac{\sum_{i=0}^{i=U/V \text{ APVs}} N_{u/v,i} A_{u/v,i}}{\sum_{i=0}^{i=U/V \text{ APVs}} N_{u/v,i}} \quad A_{ij} = \frac{A_{u,i} - A_{v,j}}{A_{u,i} + A_{v,j}} \quad (6.6)$$

$$A_{iv,\text{mod}} = \frac{A_{u,i} - A_{v,\text{mod}}}{A_{u,i} + A_{v,\text{mod}}} \quad A_{u,\text{mod},j} = \frac{A_{u,\text{mod}} - A_{v,j}}{A_{u,\text{mod}} + A_{v,j}} \quad (6.7)$$

where $A_{u/v,\text{mod}}$ is the U/V module weighted average, A_{ij} is the asymmetry combination between APV i on the U axis and APV j on the V axis, $A_{iv,\text{mod}}$ is the asymmetry combination between APV i on the U axis and the weighted average V axis asymmetry, and $A_{u,\text{mod},j}$ is vice versa with the V axis APV and the U axis weighted average. All of

these are then combined in the χ^2 used for minimization.

$$\chi^2 = \sum_{i=0}^{i=U \text{ APVs}} \sum_{j=0}^{j=V \text{ APVs}} \left(\frac{A_{ij,raw} - A_{ij}}{\sigma_{A_{ij,raw}}} \right)^2 + \sum_{i=0}^{i=U \text{ APVs}} \left(\frac{A_{u,i,raw} - A_{iv,mod}}{\sigma_{A_{i,raw}}} \right)^2 + \sum_{j=0}^{j=V \text{ APVs}} \left(\frac{A_{v,j,raw} - A_{u,mod,j}}{\sigma_{A_{j,raw}}} \right)^2 \quad (6.8)$$

This χ^2 is then minimized and the end result yields the gain parameters in equation 6.5 such that the ADC asymmetry between all U and V APVs is zero and the average module asymmetries is zero. Figure 6.2 shows an example of the gain calibration, where the asymmetries are all aligned around zero after the χ^2 minimization.

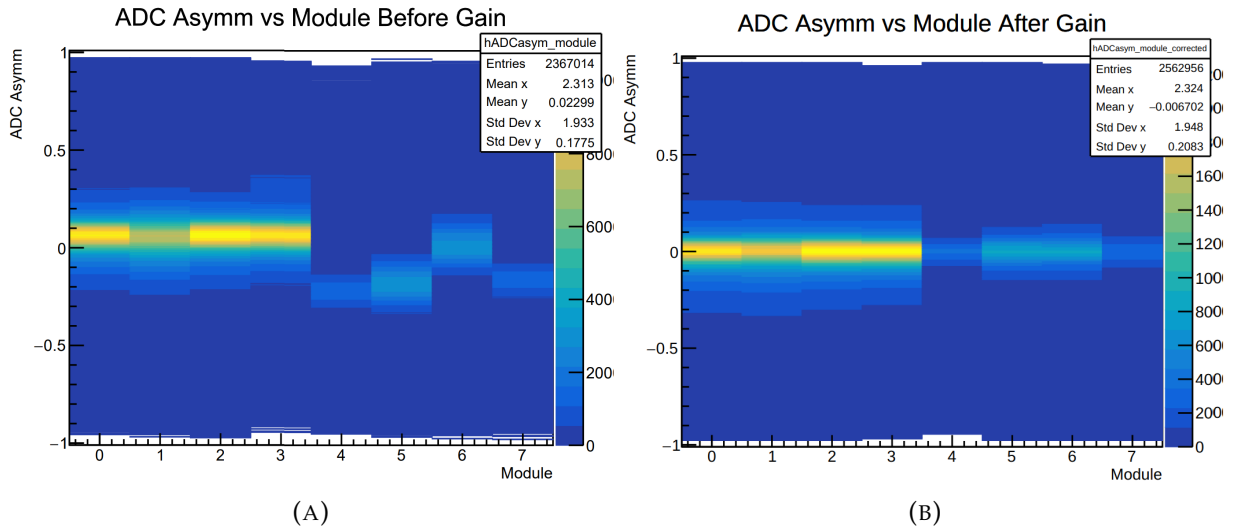


FIGURE 6.2: Results of the GEM gain calibrations. (A) Before gain calibrations the asymmetry values are not properly correlated. (B) After calibrations the gain values yield asymmetries around zero for all modules.

6.2.3 ADC Thresholds

ADC thresholds are used in individual strip samples, the strip sum values, and the cluster values as previously discussed in section 4.5.8. The ADC thresholds can be seen in figure 6.3. It is important to recall that this data passed all tracking cuts so most of the low ADC noise is already removed from the sample. Each of the three ADC thresholds are chosen such that the lowest 0.3% of ADC values are removed. This may

seem insignificant from the distributions but looking at raw ADC data before tracking in figure 6.4 it is clear that the threshold would remove a huge amount of noise in the tracking algorithm. Figure 6.3 shows the resulting threshold values for a subset of GEM data.

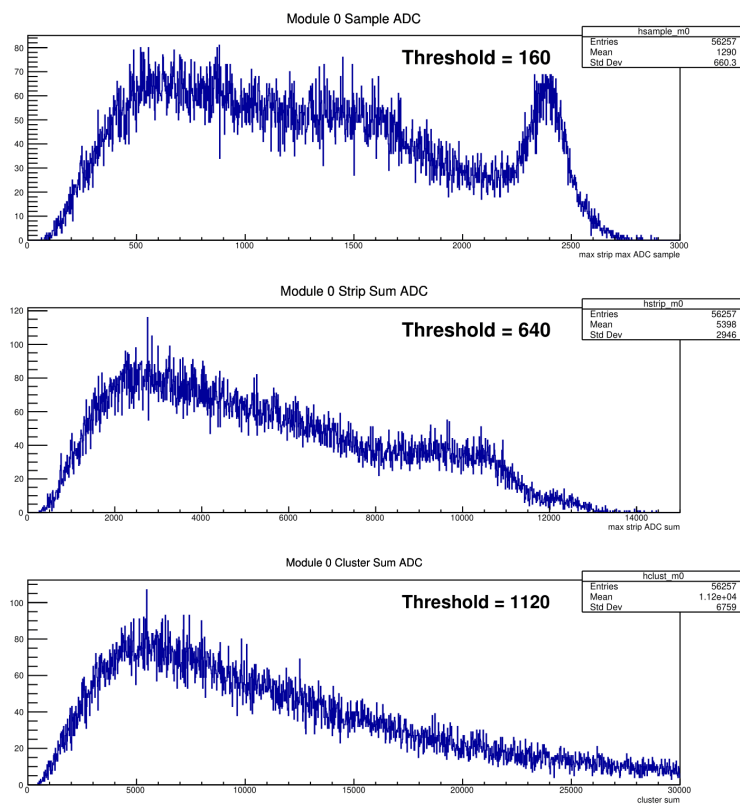


FIGURE 6.3: Results of the threshold calibration results. (Top) Max strip ADC, (middle) strip sum ADC, (bottom) cluster ADC. The value printed show what ADC value has 99.7% of events passing the cut.

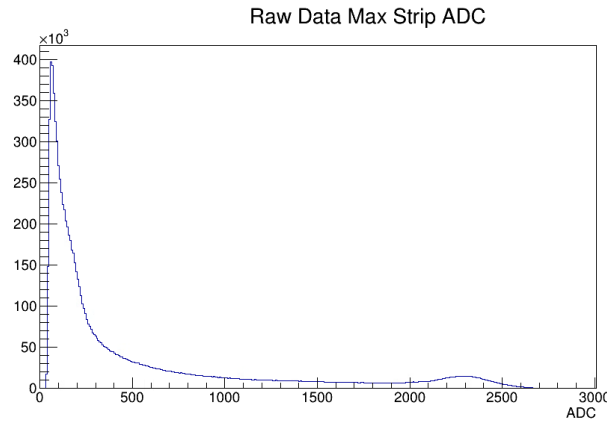


FIGURE 6.4: Example of raw ADC spectrum before any tracking analysis. Notice there is a huge amount of low ADC noise.

6.2.4 Timing

The cluster time, t_{clust} for an individual cluster on the U and V axis can be calculated. These times are all recorded in reference to the same start time from the main DAQ trigger. The time difference between a U and V cluster, Δt_{hit} , is also calculated. Due to slight latency differences between the U and V axis electronics, the average cluster times may be different between the U and V axes and need to be aligned. Many clusters are obtained from the calibration data and all are combined and fitted with a gaussian to obtain an average and standard deviation for the absolute times and the time differences. Figure 6.5 shows an example of the timing calibration results. For the U/V absolute strip time a cut is made at 4.5σ around the mean times. For the Δt a 5σ cut around zero is used. These values are calculated for every module and implemented in the clustering algorithm.

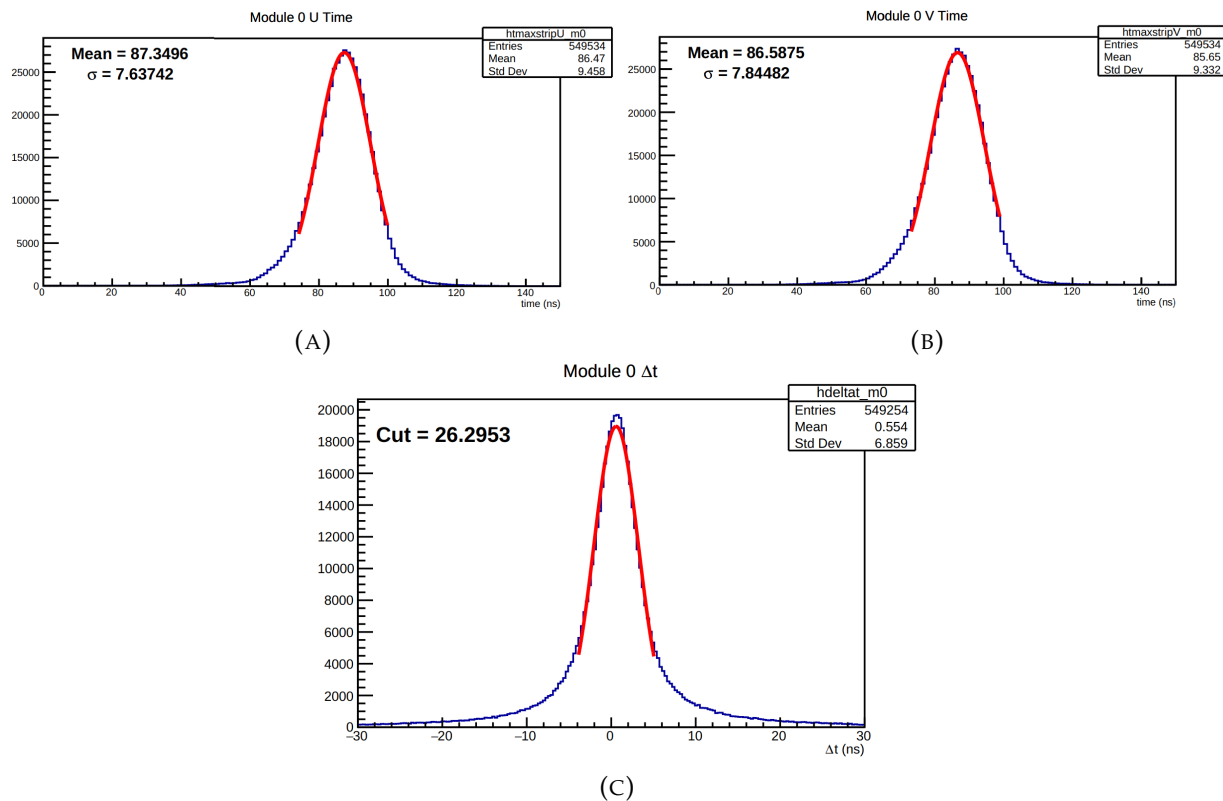


FIGURE 6.5: Results from the timing calibration. The upper row shows the gaussian fit to the timing for the (A) U and (B) V strips. (C) The Δt gaussian fit between the U and V strips. The cut printed out is 5σ from the fit.

6.3 Beam Position

The beam position reconstruction has been discussed in section 3.8.1. The carbon foil target with the two holes (figure 3.18) is used for calibration. As the raster currents change the beam position is moved and the result is seen in figure 6.6. The position reconstruction resolution is 1mm and therefore not fine enough to obtain a clear edge on the carbon holes, but the holes can be effectively seen. We know that the carbon hole is 2mm in diameter and so the radius of the hole and total raster radius can be compared in the figure to determine the raster size. It is clear that the total raster is near 5 mm from the figure and since the resolution is only 1 mm we take the raster diameter to be exactly $D_{\text{rast}} = 5.0$ mm.

The raster X and Y currents are then calibrated to determine the beam deviation from the center. The raster current values are compared to a 5 mm range, as seen in figure 6.6. The minimum X current then corresponds to -2.5 mm in the x-direction, the

maximum X current corresponds to +2.5 mm in the x-direction, and similarly for the Y current. Each kinematic has different accelerator settings which cause differences in the X and Y raster currents, and therefore each kinematic uses different raster minimum and maximum values. This means for each accelerator setting $Rast_{min}$ and $Rast_{max}$ is measured and used to convert from raster current units to mm, as has been described in section 3.8.1.

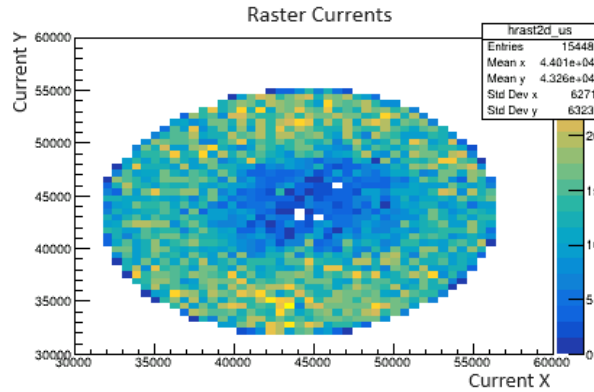


FIGURE 6.6: Raster x and y currents for data on the carbon hole target. The maximum and minimum values shown here are used to calibrate the conversion from raster current to position in meters.

6.4 Optics

Optics calibration is done using the carbon foil target (section 3.10.1) with a sieve plate in front of BB (section 3.9). The goal of the optics calibration is to calculate the expansion coefficients so the vertex position and the angles are reconstructed correctly. The carbon foil and the sieve hole positions are all surveyed so the “true” coordinates are known precisely. From the data, see figure 6.7, the vertex foil position and sieve hole position for a given track can be identified and the coordinates at the sieve plate that track should go through is known. The most downstream foil was damaged and removed before GEn-II started running and therefore only seven foils are found in the data even though the schematic drawing shows eight foils. The measured variable θ_{meas} , ϕ_{meas} , and y_{meas} from equation 3.19 can then be compared to the expected true values. The difference can be calculated, $\Delta y/\phi/\theta = y_{meas}/\phi_{meas}/\theta_{meas} - y_{exp}/\phi_{exp}/\theta_{exp}$, over a large sample of events and the result is minimized with final coefficients found for $C^{Y/T/P}$.

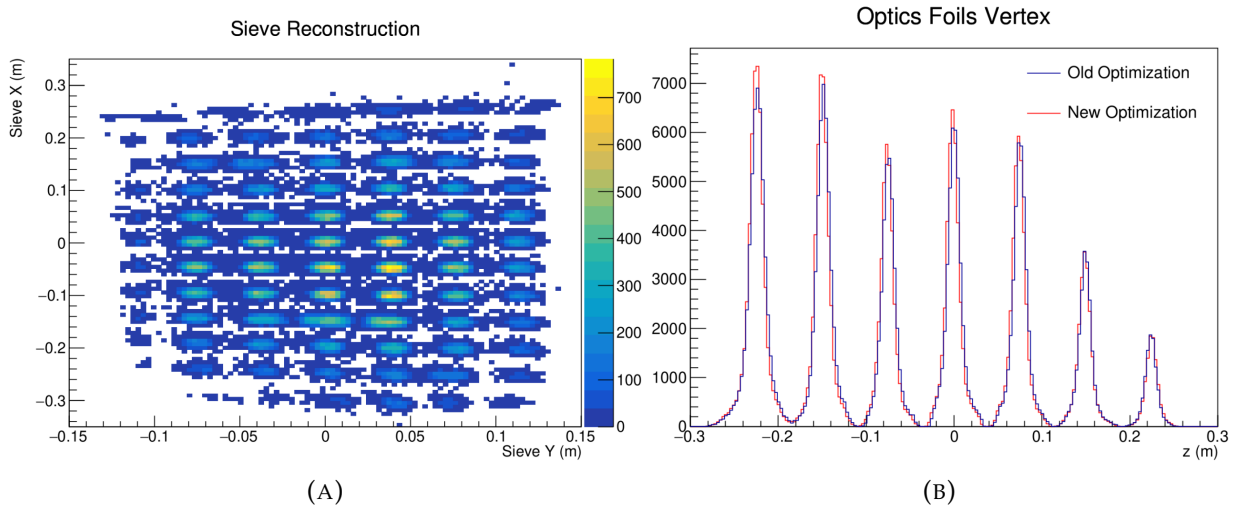


FIGURE 6.7: (A) Sieve X/Y position reconstruction using the expansion. (B) Carbon foil vertex z position reconstruction.

The maximum order of the expansion is set to $N = 2$ to reduce any overfitting issues since our magnet is only a dipole.

Since the raster is 5 mm in size and the target is 60 cm in length there are non-negligible variations in the reconstruction based on the beam $(x,y)_{\text{HCS}}$ position, and it should not be assumed to be $(0,0)$. Therefore every variable was checked as a function of the beam position with the results are shown in figure 6.8. It is clear that only the out of plane angle, θ_{tg} , has a correlation with the vertical beam position and all other variables have a negligible correlation. Recall that y_{beam} is in the HCS and so points vertically upwards towards the ceiling, see discussion in section 3.5. In the TCS, x_{tg} is the vertical direction, and therefore the correlation found with y_{beam} is equivalent to a correlation with x_{tg} . This point may seem unnecessary but it is more straightforward mathematically to correct the correlation using x_{tg} since it appears naturally in the θ_{tg} calculation in equation 3.19.

We conclude that the θ_{tg} expansion needs an extra term added which is dependent linearly on x_{tg} . Also note that the expansion, equation 3.19, has an x_{tg} term already included. However only the θ_{tg} term linear with x_{tg} should be nonzero and all other x_{tg} should be zero. This is done by forcing every coefficient, $C_{ijkl}^{Y/T/P}$, with $i \neq 0$ to zero **except** for C_{1000}^T . Also, as briefly discussed earlier, equation 3.20 shows that the z_{tg} and x_{tg} are dependent on each other. Therefore one will notice that the x_{tg} in equation 3.19 will change based on the result and minimization of the expansion. To handle this the x_{tg} is originally set to the negative of the beam y position, since the HCS and TCS are

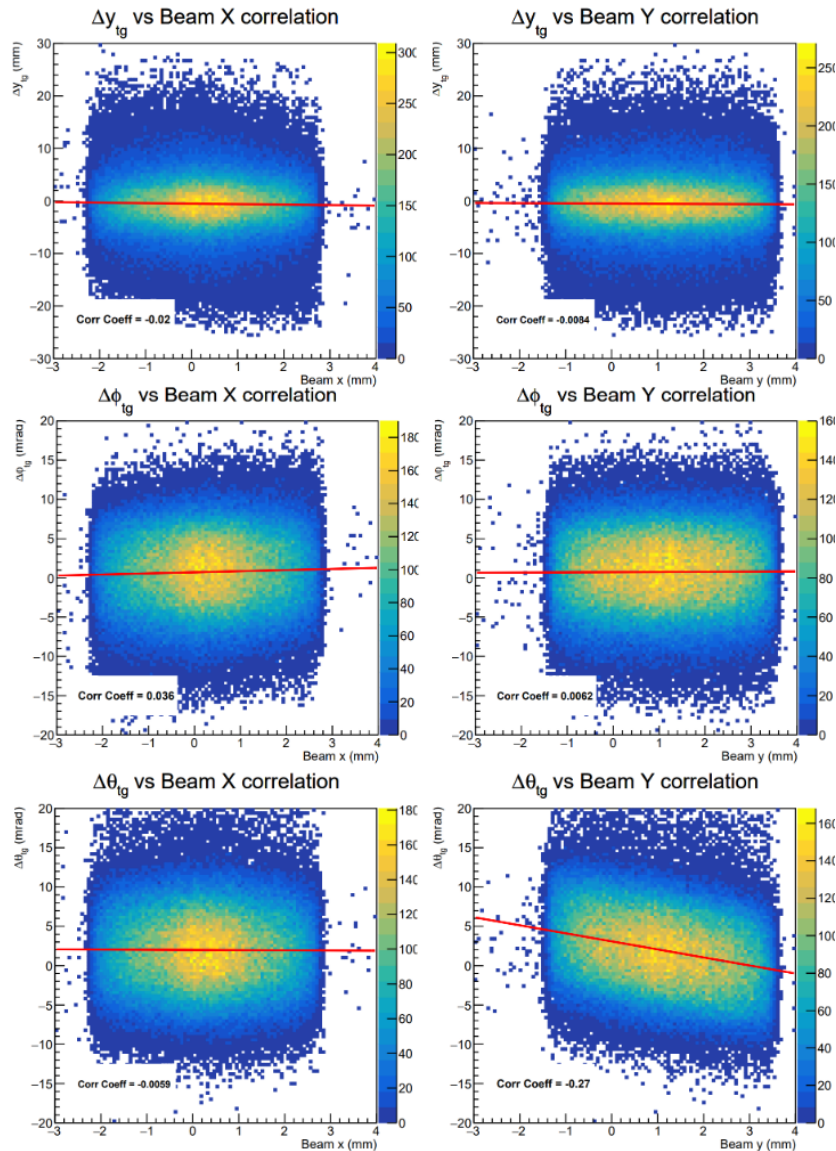


FIGURE 6.8: Correlations in target variables and the beam position. We note that only the θ_{tg} vs Beam y has a strong correlation.

in opposite directions vertically. With the x_{tg} set, the expansion and z_{tg} is calculated. Then x_{tg} is calculated from the result and the expansion is computed again with the new x_{tg} . This is done three times in total so that z_{tg} and x_{tg} settle on a final value. Only three iterations are needed since the $x_{tg} = -y_{beam}$ starting point is already an close approximation.

The result for Kin3 are found in figure 6.9 and Kin4 are found in figure 6.10. The “old optimizations” are the starting values from the simulation results. The final offsets and resolutions are good, so we are confident in the optics coefficients for use under

beam data. Unfortunately optics data was not taken during Kin2 so no optimization can be performed. Therefore we must use the simulation coefficients for the Kin2 production data. As seen in figure 6.9 and 6.10 the simulation gives reasonable results. Kin2 also requires less accurate calibrations since there is much less background data.

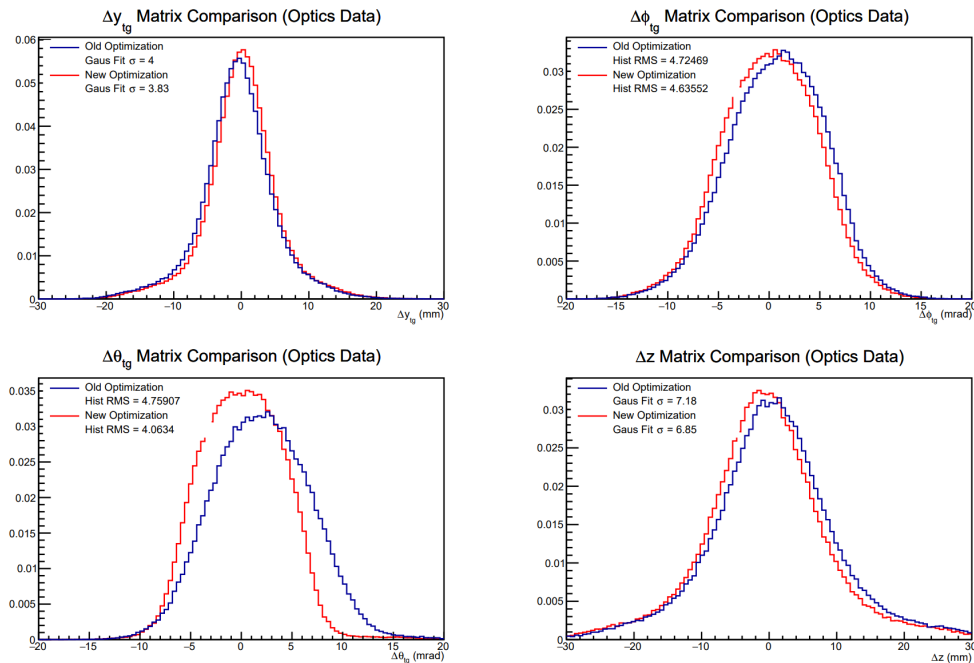


FIGURE 6.9: Optics calibration results for Kin3. After optimizations the distributions are all centered at zero with better resolutions.

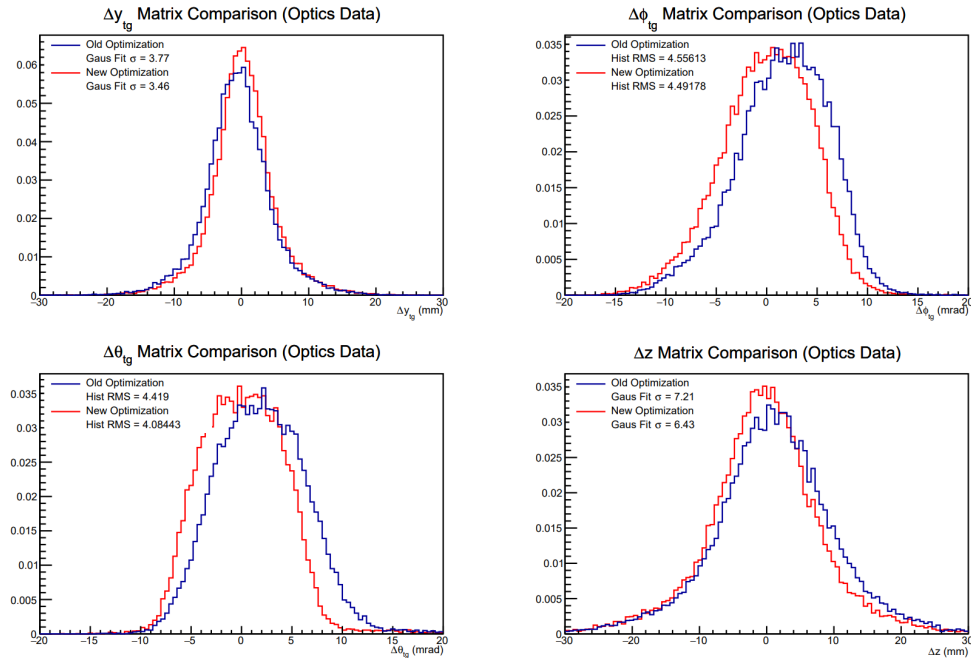


FIGURE 6.10: Optics calibration results for Kin4. After optimizations the distributions are all centered at zero with better resolutions.

6.5 Momentum

The momentum is calibrated using H₂ data, as discussed in section 3.9. Since hydrogen does not have Fermi smearing we can reliably calculate the momentum from the elastic scattering formula.

$$p_{\text{elastic}} = \frac{E_{\text{beam}}}{1 + \frac{E_{\text{beam}}}{M_p} (1 - \cos(\theta_e))} \quad (6.9)$$

As previously mentioned, equation 3.22, the momentum can be calculated directly from the magnetic momentum reconstruction of the scattered electron. This reconstructed momentum will be labeled p . A variable can then be defined, $\delta p = p/p_{\text{elastic}} - 1$, which is the percentage difference between the magnetic momentum reconstruction and the expected momentum. δp near zero tells us that the reconstruction momentum is close to the expected value from elastic scattering kinematics, and therefore the calibration is good. After following the formulation described in equation 3.22 the resulting momentum is plotted in figure 6.11. From the figure it is clear that the momentum has an extra linear dependence on the beam position. This must also be accounted for. The

momentum calculation is then modified to be

$$p = A(1 + B\theta_{tg})/\theta_{bend} - (C + Dy_{beam}) \quad (6.10)$$

where A, B, C and D are all fit parameters. Figure 6.11 shows momentum calibration result after using this formulation. It is clear that the correlation with the beam position has been removed, and therefore the overall resolution.

The final result of the momentum calibration is shown in figure 6.12. We find that the momentum reconstruction is greatly improved to 1.6% for Kin2 and 1.8% for Kin3 momentum resolution. Unfortunately there was no H_2 data taken during Kin4, so extra momentum calibrations cannot be performed. The Kin4b run group did have H_2 data taken and a future analysis will apply the extra corrections, but it is not done here.

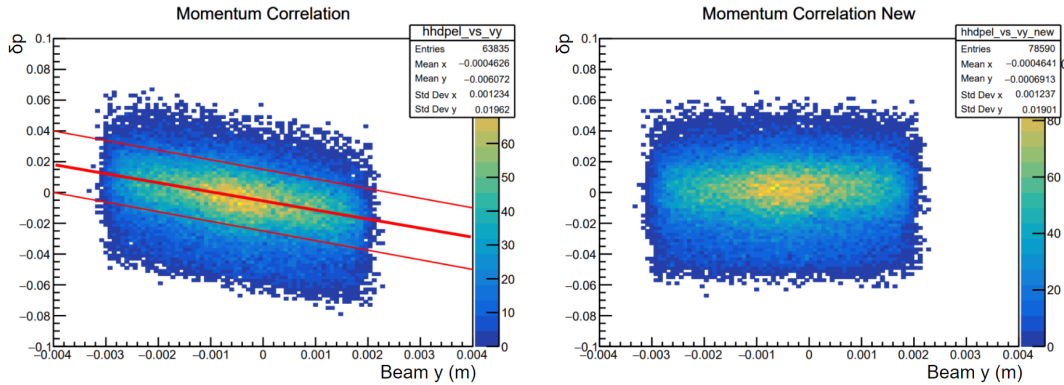


FIGURE 6.11: (left) The momentum clearly has a linear correlation with the beam y position after using equation 3.22. (right) this correlation can be removed as seen in this plot after using equation 6.10.

6.6 BigBite Calorimeter

The BigBite Calorimeter (BBCal) calibration here was performed by graduate student Kate Evans. BBCal provides the energy resolution for selecting the high energy elastically scattered electrons, at the trigger level, and therefore must have a thorough energy calibration. To achieve this H_2 data is used for a cleaner elastic event sample with which to calibrate from. A χ^2 can be formed for the calorimeter blocks

$$\chi^2 = \sum_{i=0}^N \left(p_e^i - \sum_{k=0}^M C_k A_k^i \right)^2 \quad (6.11)$$

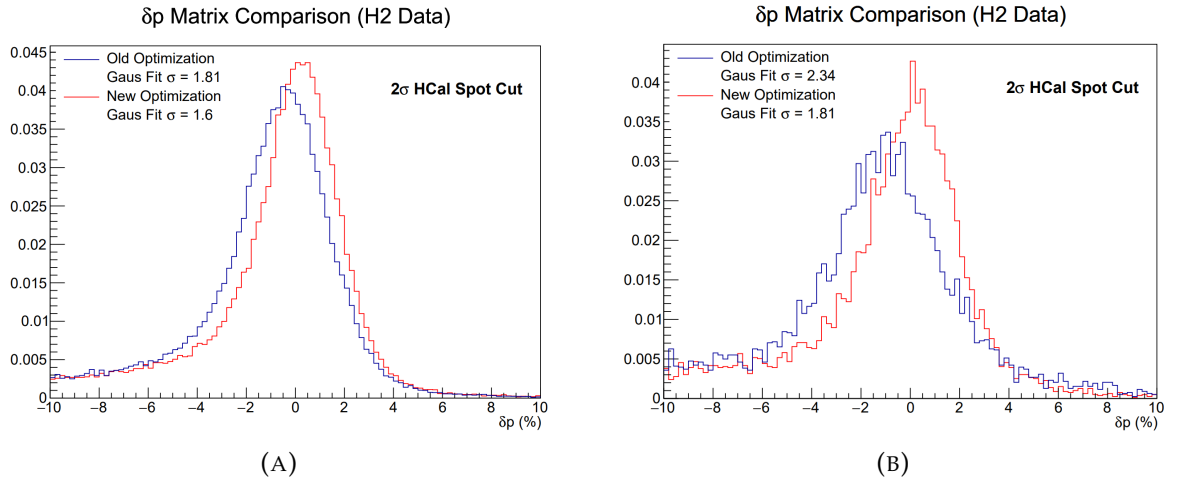


FIGURE 6.12: (A) Momentum calibration result for Kin2. (B) Momentum calibration result for Kin3.

where p_e^i is the track momentum of the event, i loops over the number of events, k loops over the number of blocks, C_k is the gain coefficient of block k , and A_k^i is the BBCal ADC reading from the block. p_e^i is calculated from the tracking and optics as explained in section 6.5. C_k is then chosen to minimize χ^2 . The goal is for the energy reconstruction as close to the momentum as possible, $E/p \approx 1$.

Figure 6.13 summarizes the results of the calibration procedure. We find that the energy resolution is $\sim 6.5\%$ after calibration for all kinematics. Also the energy reconstruction response is nearly flat for all momentum ranges. There are some slight differences but they are small. It is also notable that H₂ data was not taken during Kin4, as discussed in section 3.1, and therefore ³He data was used. This data is less clean but the results remain similar in resolution to other kinematics.

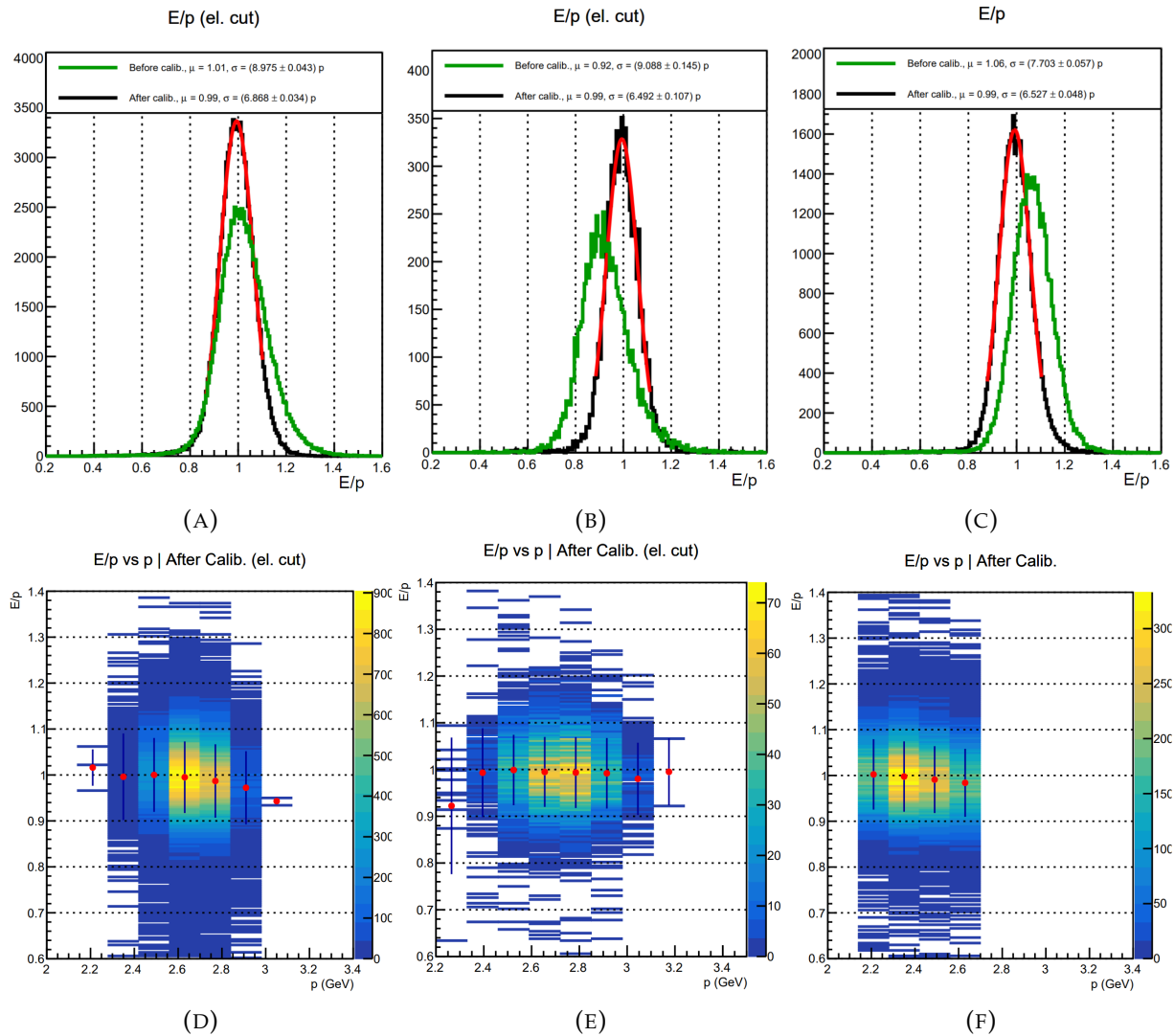


FIGURE 6.13: (A - C) E/p calibration result for (A) Kin2, (B) Kin3, and (C) Kin4. (D - F) E/p calibration vs momentum for (D) Kin2, (E) Kin3, and (F) Kin4.

6.7 Hodoscope

The hodoscope calibration presented here was performed by graduate student Gary Penman. As with BBCal, Kin2 and Kin3 utilized H₂ data while Kin4 utilized ³He data for this calibration. As mentioned in section 3.6.4 each hodoscope row has a left and right signal. Therefore the track position on the hodoscope can be used to better calibrate the signal time based on the left and right time difference. This is called track matching. Along with this there is also a “time walk” effect which must be accounted for. This effect is described by larger amplitude signals passing the ADC threshold

sooner, and therefore decreasing the recorded time. A simple linear fitting procedure can be done to remove the correlation between the amplitude and recorded time to return a uniform time for all signal heights. The calibrations discussed above will not be detailed here as Gary Penman will provide a thorough explanation of how everything was done in his thesis. Figure 6.14 summarizes the timing results of the hodoscope calibration. The bar mean times are used in the overall time calculation. We find that the timing resolution is then ~ 750 ps for all three kinematics.

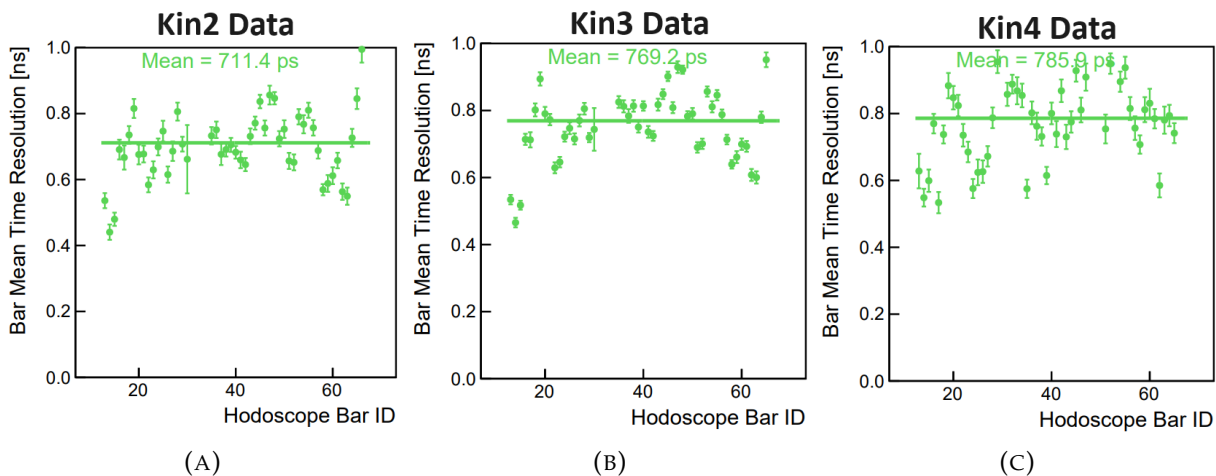


FIGURE 6.14: Hodoscope bar mean time resolution vs bar ID for Kin2 (A), Kin3 (B), and Kin4 (C). Note that some bars on the edges have low statistics and deviate from the mean. The mean value of all bars is printed at the top of each plot.

6.8 GRINCH

Unfortunately the GRINCH was uncalibrated for the data presented here. As previously discussed in section 3.6.2, the preshower can be used to remove a significant amount of pions, and so the GRINCH was put at a lower priority. Rough settings were used for a first look at the GRINCH response to get an idea of how well calibrated it currently is. Tracks can be projected to the GRINCH which can then be checked for PMT signals in the corresponding area. If a signal is found then then a cluster of at least three neighboring PMTs are also required to ensure this is not a random noise signal. Then this is identified as a electron.

The results of the GRINCH cuts can be seen in figure 6.15. The low energy peak in the preshower energy spectrum identifies pions, and can be used as a double check

of the GRINCH cuts. The data shows that the electron cuts on the GRINCH still has a large pion sample. Therefore more calibrations are needed and a future analysis may use the GRINCH to cleanly separate pions and electrons. For this analysis the GRINCH will not be used and instead the preshower is mainly utilized for removing pion events.

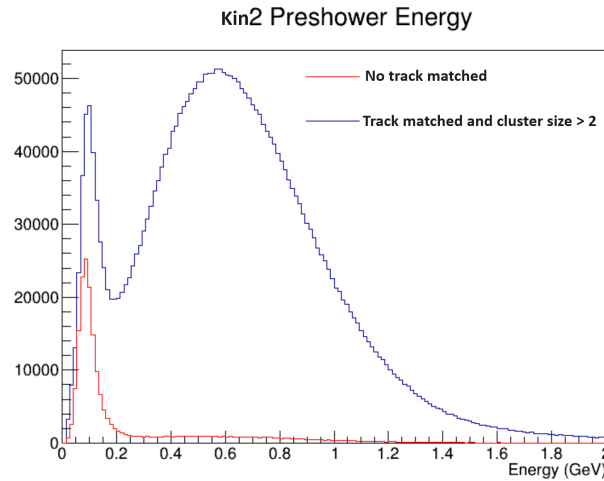


FIGURE 6.15: Particle identification check for the GRINCH from Kin2 preshower data. The red histogram shows the preshower spectrum for data passing the pion cuts in GRINCH while the blue histogram shows data passing the electron cuts in GRINCH.

6.9 Hadron Calorimeter

The Hadron calorimeter (HCal) calibration presented here was performed by graduate student Hunter Presley. The first step is to align the ADC time and TDC time. To do this the hodoscope time is used as a stable reference since it is the most accurate time in the experimental apparatus. For each channel on HCal the ADC and TDC times have offsets applied so that all channels are at the same value when subtracted from the hodoscope time.

More complicated than this is the procedure to calibrate the gain coefficients. The process we will follow here was created by Sebastian Seeds [62]. The gain calibration follows a similar form as described in section 6.6 with some minor but important difference.

$$\chi^2 = \sum_{i=0}^N \left(E_i - \sum_{k=0}^M C_k A_k^i \right)^2 / \sigma_E^2 \quad (6.12)$$

For a typical calorimeter with 100% sampling $\sigma_E^2 = E$ but HCal sampling fraction, S_f , can be 5% - 10%. For each kinematic S_f can be determined from monte carlo (MC) simulations. We then define a single factor R to account for any noise and constant effects that may also change the sampling fraction from the ideal MC. From this we can then define

$$S_f^* = RS_f \quad (6.13)$$

$$E_i = \nu_i S_f^* \quad (6.14)$$

$$\sigma_E^2 \approx \nu_i S_f^* \quad (6.15)$$

$$\chi^2 = \sum_{i=0}^N \frac{\left(E_i - \sum_{k=0}^M C_k A_k^i\right)^2}{\nu_i S_f^*} \quad (6.16)$$

where ν is the kinematic variable found in table 1.1. The C_k and R variables are then chosen such that χ^2 is minimized. This sets the gain coefficients such that the energy is reconstructed properly using the sampling fraction from MC.

H₂ data from Kin2 was used to calibrate HCal. The hardware was not changed for Kin2, Kin3, and Kin4, and so it is not necessary to change the calibration for each kinematics. Therefore the Kin2 calibration was applied to all three kinematics.

Chapter 7

Analysis

7.1 Analysis Software

Hall A has a standard analysis package known as the Hall A Analyzer [63] built upon CERN's ROOT library [64]. The Analyzer contains classes that are specific to the JLab setup and has a modular design that makes it simple to add detector channels to the analysis with a variety of functionality. On top of the Analyzer the SBS-offline package [65] was created specifically for the SBS program of experiments, since they all have a common setup which is reconfigured as needed for each experiment. SBS-offline has classes for all detectors in the SBS setup with specialized algorithms to handle the high luminosities anticipated in the experiments. For example, the entire tracking algorithm described in section 4.5 was written specifically for SBS-offline instead of using a much simpler tracking algorithm available in the Analyzer.

Using the raw CODA EVIO file as an input, SBS-offline then fully decodes and analyzes all detector channels and writes an output root file. This file has all calibrated detector outputs, like track position, calorimeter cluster energies, and beam helicity, but it has no physics analysis for each experiment. For GEN-II, I have produced a standalone analysis library [66] which then processes this into physics data. The detector ROOT files are used as input in this standalone program and physics ROOT files are produced. This file holds information like electron energy, momentum, invariant mass-squared (W^2), time, hadron energy, and more. From this file, the asymmetry analysis is performed and the final G_E^n value is extracted.

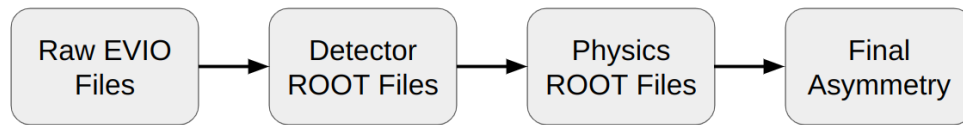


FIGURE 7.1: Flowchart of the analysis stages.

7.2 Monte Carlo Simulation

Monte Carlo (MC) simulations will be utilized for parts of this analysis. A realistic simulations setup called G4SBS [67] was created on top of the Geant4 framework [68]. All detectors and materials are included in G4SBS for accurate representations of detector responses to real life. Figure 7.2 shows the full experimental setup while figure 7.3 shows the target enclosure with all components in G4SBS.

G4SBS also includes full physics event generation capabilities. For quasielastic (QE) event simulation G4SBS can be given the beam properties and then uses the known cross section of a ${}^3\text{He}$ nucleus scattering to calculate the electron and struck nucleon scattering angles. Parameterizations for Fermi motion of the nucleons in the nucleus is also included for accuracy. The particles are then propagated through the materials and the energy depositions in each material is simulated.

We will also make use of single particle generators, which send particles at the detectors with kinematics settings input from the user. We will make specific use of generating pions at a range of energies and propagating them through the BB apparatus to simulate the response to pions.

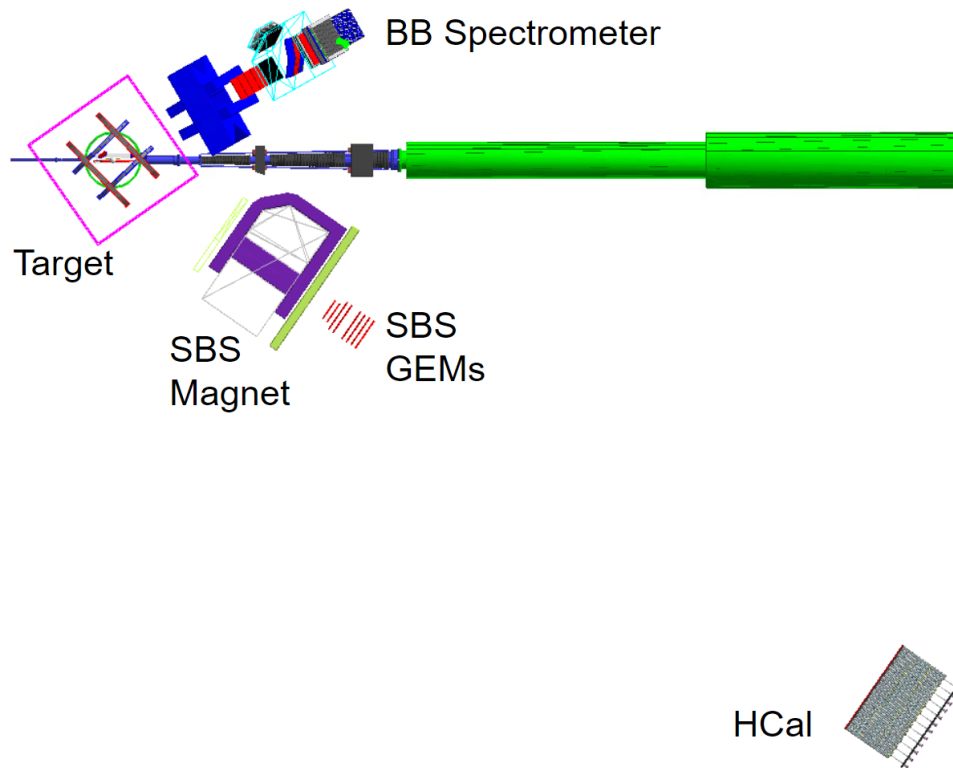


FIGURE 7.2: Picture of entire experimental setup in G4SBS.

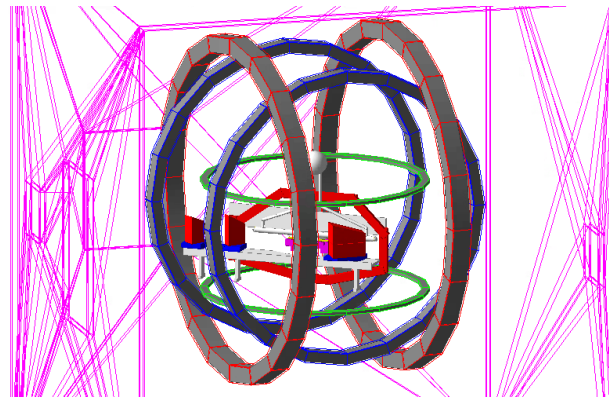


FIGURE 7.3: Closeup of the target enclosure in G4SBS.

7.3 Good Run Selection

There are some conditions that destroy the quality of an entire run and it must then be removed from the analysis. For GEN-II the helicity and Møller quality are the only values that would disqualify an entire run. If there are any errors then the entire run must be discarded because the asymmetry is completely unknown. As discussed in section 3.8.2, the beam helicity is expected to be unknown for 0.02% of all events during

the settle window. Therefore we check each run and if the helicity state is unknown for greater than 1% of the run, then that run is discarded. This has the largest affect on Kin2 due to issues in the helicity DAQ when the experiment first started. This resulted in 20% of the Kin2 data being lost due to unknown helicity recording. Discussions with experts suggest that this data may be recoverable [69], but that will be left for a future analysis. As for Kin3 and Kin4 less than 1% of the data was lost form bad helicity readback. The beam polarization is also unknown for some periods of time due to an accelerator change that did not have a corresponding Møller measurement. This will be detailed in section 7.6. If a run is during this time then it is also discarded. Overall this affected 13% of the Kin3 data, which is lost, while Kin2 and Kin4 have no losses. These are the only two cuts used to discard a full run. Further cuts on event by event basis will now be described in the following sections.

7.4 Quasielastic Event Selection

The goal of the physics analysis is to isolate quasielastic (QE) electron-neutron scattering from the ^3He target. At the high Q^2 values in this analysis the vast majority of the events recorded are not QE. Cuts must be applied to the data on all our physics handles to remove as much non-QE events as possible while keeping the majority of QE events. Here the physics variables used for QE event selection will be detailed.

7.4.1 Track Vertex

The track vertex position along the beamline, z_{tg} , is reconstructed for every event. This is useful for event selection since tracks must be originate physically within the length of the target. Figure 7.4 shows the vertex spectrum for Kin2, with some notable features. First, there is a beryllium window that separates the beamline vacuum from the open air before the target. This is reconstructed at its expected position, -40 cm, but is overall irrelevant to this analysis. The target extends from -30 cm to +30 cm as expected. The distribution shows the yield decreasing along the target length, due to the detector acceptance. The glass entrance window at -30 cm is difficult to see in ^3He data but still noticeable, but can clearly be seen in cleaner H_2 data. The H_2 data in figure 7.4a gives us confidence that the peak is also at the same location in ^3He data in figure 7.4b. The glass exit window at +30 cm is clearly seen in both data sets. The target end windows

are $150\ \mu\text{m}$ thick but from section 6.4 the vertex resolution is found to be $6.5\ \text{mm}$ so the widths of the window peaks are dominated by the resolution.

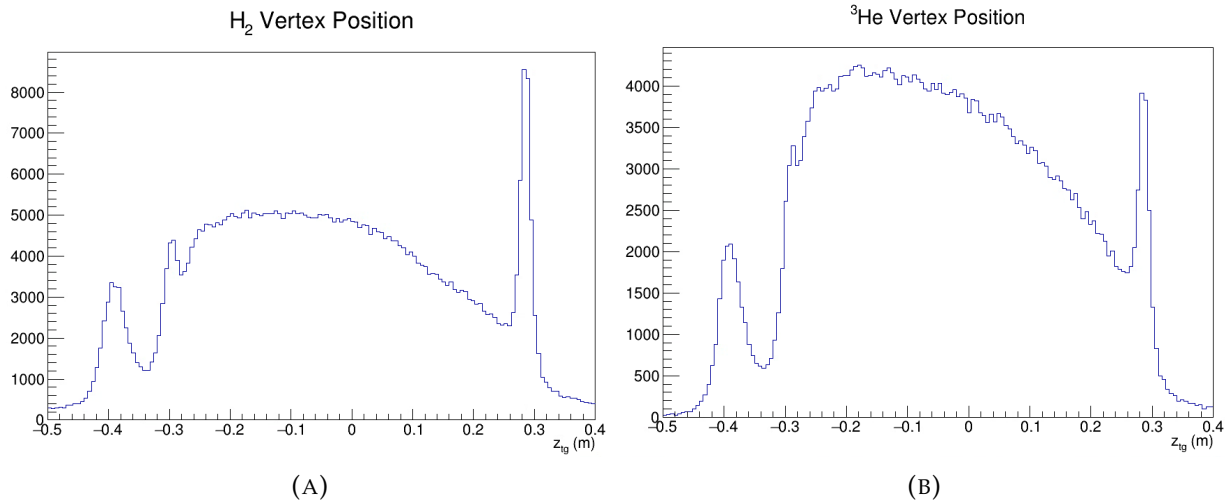


FIGURE 7.4: Target vertex for Kin2 for (A) H₂ and (B) ³He data.

7.4.2 Preshower Energy

The preshower energy is used to reject pion events. The preshower spectrum is checked for each kinematic, with the results seen in figure 7.5. It is found that as the Q^2 increases the pion to electron ratio also increases. All spectra have a majority of the pion events below $0.2\ \text{GeV}$. This is a good point for a cut that would greatly reduce pion contamination while minimally rejecting electrons. We will also note that all data shown is found from tracks which are bending upwards in the BB magnet, corresponding to a negative charge. This naturally removes the π^+ from the data so the preshower spectrum only has π^- events.

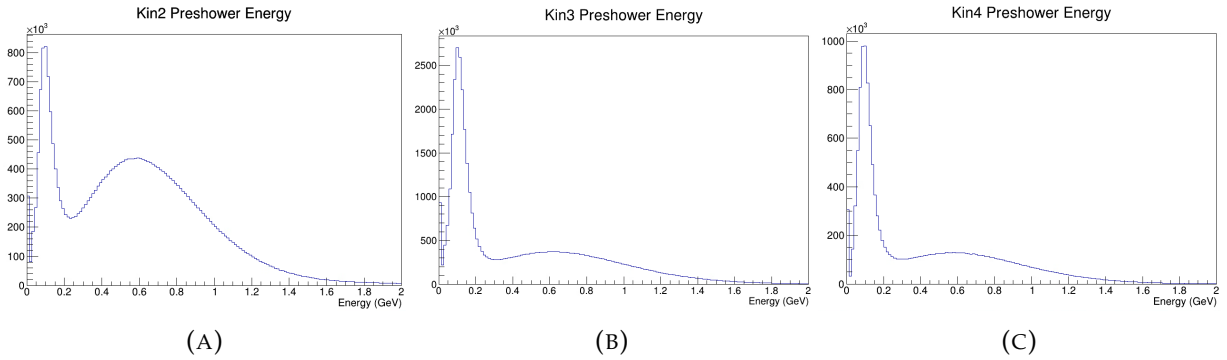


FIGURE 7.5: Preshower energy for all events for (A) Kin2, (B) Kin3, and (C) Kin4.

7.4.3 Invariant Mass

The nucleon mass, W^2 , reconstruction is a critical tool in determining quasielastic events. Recall that the W^2 calculation has been defined in table 1.1. We must note that this calculation assumes an elastically scattered nucleon with the initial nucleon at rest. This is not true for our experiment since there is Fermi motion, but it is not possible to measure the initial momentum. Therefore our W^2 is a pseudo-invariant mass, but we will continue call it “invariant mass” here for convenience. The invariant mass data from H_2 target, figure 7.6, is a nice example since the prominent proton resonances can be clearly seen. The proton and neutron targets should reconstruct a W of 0.938 GeV from QE scattering with some spread for Fermi motion and resolution effects. Inelastic data is expected to start at the pion production threshold, which is around $W^2 = 1.15 \text{ GeV}^2$.

One important property of the quasielastic data is the “kinematic broadening” at large Q^2 values. This can be seen in figure 7.7a, which shows a pure quasielastic simulation. Even this pure quasielastic data has significant spread at higher momentum transfers. This is due to uncertainties in the electron momentum smearing the energy and momentum transfer differences in the W^2 calculation. While the W^2 cut remains powerful for removing inelastic background, this simulation gives a reference for what fraction of QE data also may be lost in a certain W^2 cut. Figure 7.7b shows the W^2 spectrum for the data with the neutron particle identification applied. This particle identification will be explained in section 7.4.5, but for now we can take it on face value that this reduces the data to a region where quasi-elastic neutrons are expected. Without applying this cut a significantly larger amount of inelastic data would enter the distribution and it would be difficult to make any conclusions.

The differences between the data and pure QE simulation spectra tell us about how much inelastic events are in the data. As expected Kin3 and Kin4 show a significant amount of inelastic events, while Kin2 is rather close to the pure QE simulation. The W^2 cut must be chosen to balance between the two distributions so most of the QE simulation is inside the cut, while not too much of the high W^2 data is present.

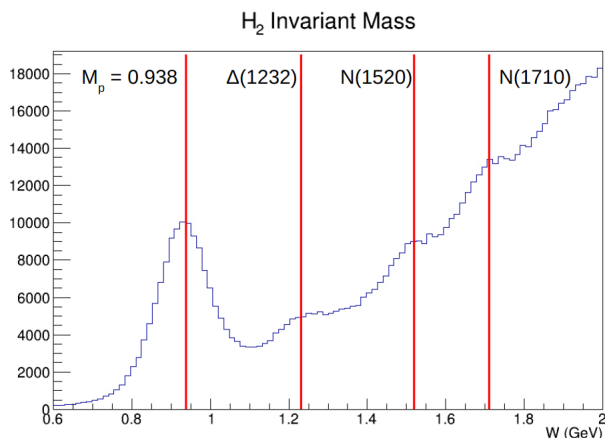


FIGURE 7.6: Invariant mass spectrum from H_2 data from Kin2. Numerous proton resonances can be seen.

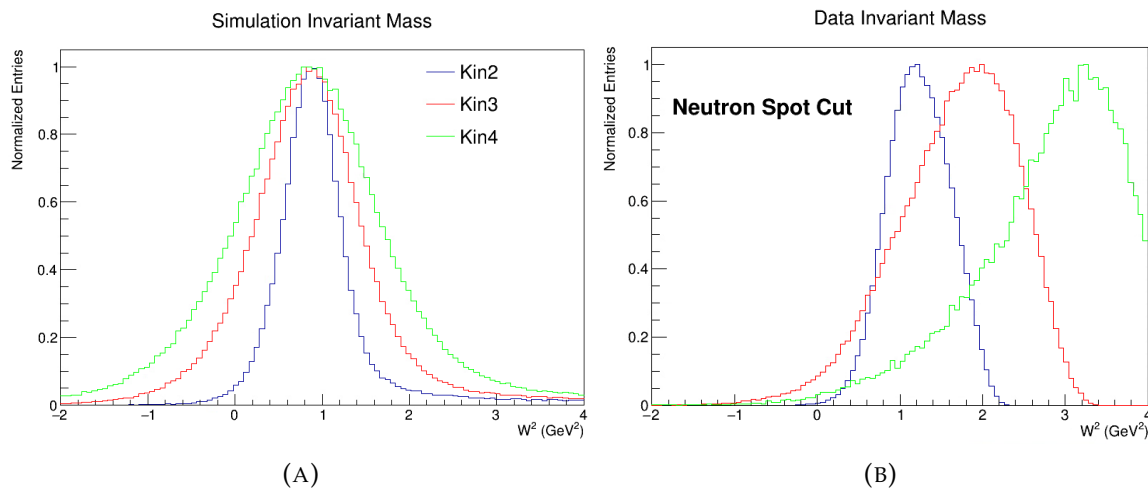


FIGURE 7.7: (A) Invariant mass spectrum from simulated ^3He data. Note that the kinematic smearing increases significantly for the higher Q^2 kinematics. (B) Invariant mass spectrum from real ^3He data. The neutron spot cut has also been applied to ensure the data is mostly QE sample.

7.4.4 Coincidence Time

The electron and hadron detector arms each record an arrival time for the detected particles. The hadron arm uses the HCal ADC cluster time as the overall arm time. As previously discussed, the hodoscope TDC time should be used for the electron arm time calculation, as it has the best timing resolution. However the BBCal ADC time could also be used for the electron arm time. The coincidence time, t_{coin} , is the time difference between the hadron arm and the electron arm. If the two arms trigger from the same scattered event there is only a small coincidence time overlap. Otherwise the arms are uncorrelated to the same event and are called “accidentals”.

We found that there are notable differences between using the hodoscope or the BBCal for the electron arm time. Figure 7.8 shows the coincidence times using both methods for the Kin2 data. We find that using the BBCal time gives a coincidence resolution of 1.9 ns while using the hodoscope time gives a resolution of 3.3 ns. It is currently unclear to us why the hodoscope time is much worse, as it’s internal calibration found in section 6.7 yields 750 ps resolutions. We suspect that some trigger time effects are not properly accounted for in the hodoscope time calculation, but unfortunately this issue still remains unresolved. For this analysis we must use the BBCal time but note that the hodoscope must be properly implemented in the future. It could increase timing resolution significantly.

Figure 7.9 shows the coincidence mean times and resolutions for all kinematics. Here it is useful to apply the W^2 cut and the neutron identification cut to clean up the timing sample. The neutron identification cut will be explained in the next section. Without these cuts the timing distributions would be wider. The distributions are fitted with a Gaussian and linear combination. However it is clear that the peak is slightly non Gaussian in figure 7.9. Therefore for accuracy the coincidence cut will be chosen such that the full peak is captured within it, which will not be the exact same number of σ 's for each kinematic. This cut is decided by looking at the coincidence results by eye. The result is in table 7.1.

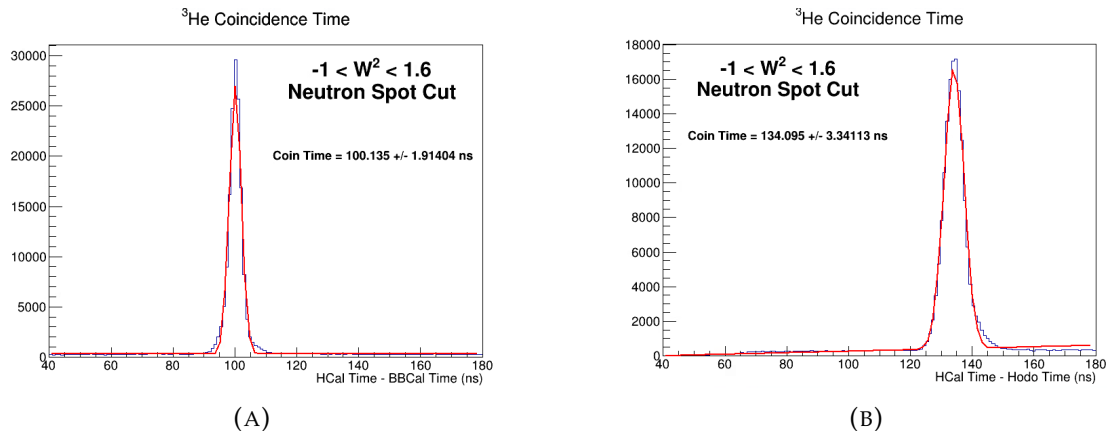


FIGURE 7.8: Coincidence time distributions for Kin2 using (A) BBCal for the electron arm time and (B) the hodoscope for the electron arm time. The fit resolutions are printed on the plots. (A) 1.9 ns using the BBCal ADC time and (B) 3.3 ns using the hodoscope time.

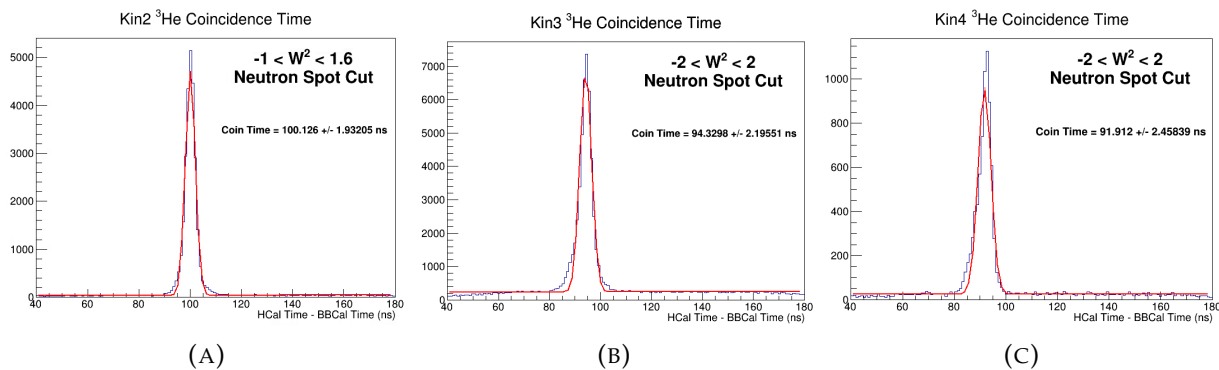


FIGURE 7.9: Coincidence time distributions for all three kinematics. A Gaussian + linear fit is used for the histogram. The resulting Gaussian fit is printed on each plot.

7.4.5 Hadron Particle Identification

The hadron arm can be used to separate proton and neutrons for identification. Figure 7.10a shows a simulation of a proton's deflection through the SBS magnet which separates their trajectory from the neutrons. We will now define important parameters used many times in this analysis called Δx and Δy . From the q vector the scattered QE nucleon trajectory can be calculated and projected forward to obtain the x_{expect} and y_{expect} position on the HCal. Again we must keep in mind that Fermi motion is not accounted for in this calculation and therefore the true trajectory is spread radially around our ideal, calculated trajectory. From the measured hits in the HCal clusters x_{meas} and

y_{meas} are calculated. Figure 7.10b shows the definition of the observables.

$$\begin{aligned}\Delta x &= x_{\text{meas}} - x_{\text{expect}} \\ \Delta y &= y_{\text{meas}} - y_{\text{expect}} \\ \Delta R &= \sqrt{\Delta x^2 + \Delta y^2}\end{aligned}\tag{7.1}$$

An example of ${}^3\text{He}$ data is shown in figure 7.10c. As expected there are two spots with the neutron spot in the center around $(0,0)$, because the neutron is not deflected and in the expected position, and the proton spot is vertically offset upwards as it is deflected. The size of the spots are analogous to the Fermi momentum since the x/y_{expect} positions are calculated assuming no initial momentum. Any spread is caused by the Fermi momentum. The proton and neutron events can then be identified by their separation in Δx . For this experiment only the neutron data is needed so a cut can be applied around the origin on the neutron spot to select on quasielastic neutron data.

In GEN-I [20] a perpendicular momentum, p_{\perp} , cut of 150 MeV was utilized. Measuring p_{\perp} requires accurately measuring the hadron energy. HCal energy resolution is 40%, as detailed in section 3.7.1, and therefore p_{\perp} can not be reconstructed in this analysis. Instead, the expected radial extent of the neutron position distribution, ΔR , corresponding to $p_{\perp} = 150$ MeV can be roughly estimated for our kinematics

$$\Delta R = D_{\text{HCal}} \frac{p_{\perp}}{|\vec{q}|}\tag{7.2}$$

where D_{HCal} is the distance from the target to HCal and $|\vec{q}|$ is the q-vector magnitude. Note that we are ignoring any possible missing momentum parallel to the q-vector here. D_{HCal} is 17 m for all kinematics and $|\vec{q}|$ can be calculated from the central kinematics in table. By using $p_{\perp} = 150$ MeV in equation 7.2 we calculate $\Delta R = 1.08$ m for Kin2, $\Delta R = 0.57$ m for Kin3, and $\Delta R = 0.42$ m for Kin4. However there is an extra complication that with a larger ΔR proton data begins to leak inside the neutron selection area. The radii calculated before are larger than the proton separation and so must be decreased enough so that only the proton tail remains inside the neutron spot. The Fermi smearing should be symmetric and so we keep Δx and Δy the same for this analysis. It would be helpful to justify the spot size using the simulation, however this analysis is not mature enough yet to test that and we leave it for a future analysis. Figure 7.11 shows the neutron spot identification for all kinematics and the resulting values are listed in table 7.1. Notice that all kinematics have a slight asymmetry where

more events are in the negative Δy region. This corresponds to smaller scattering angles, near the beamline, so more background is to be expected. Another important note is that the cuts are actually applied in a linear fashion as a square, as implied by table 7.1, but the figures below show circular spots to match the physical situation.

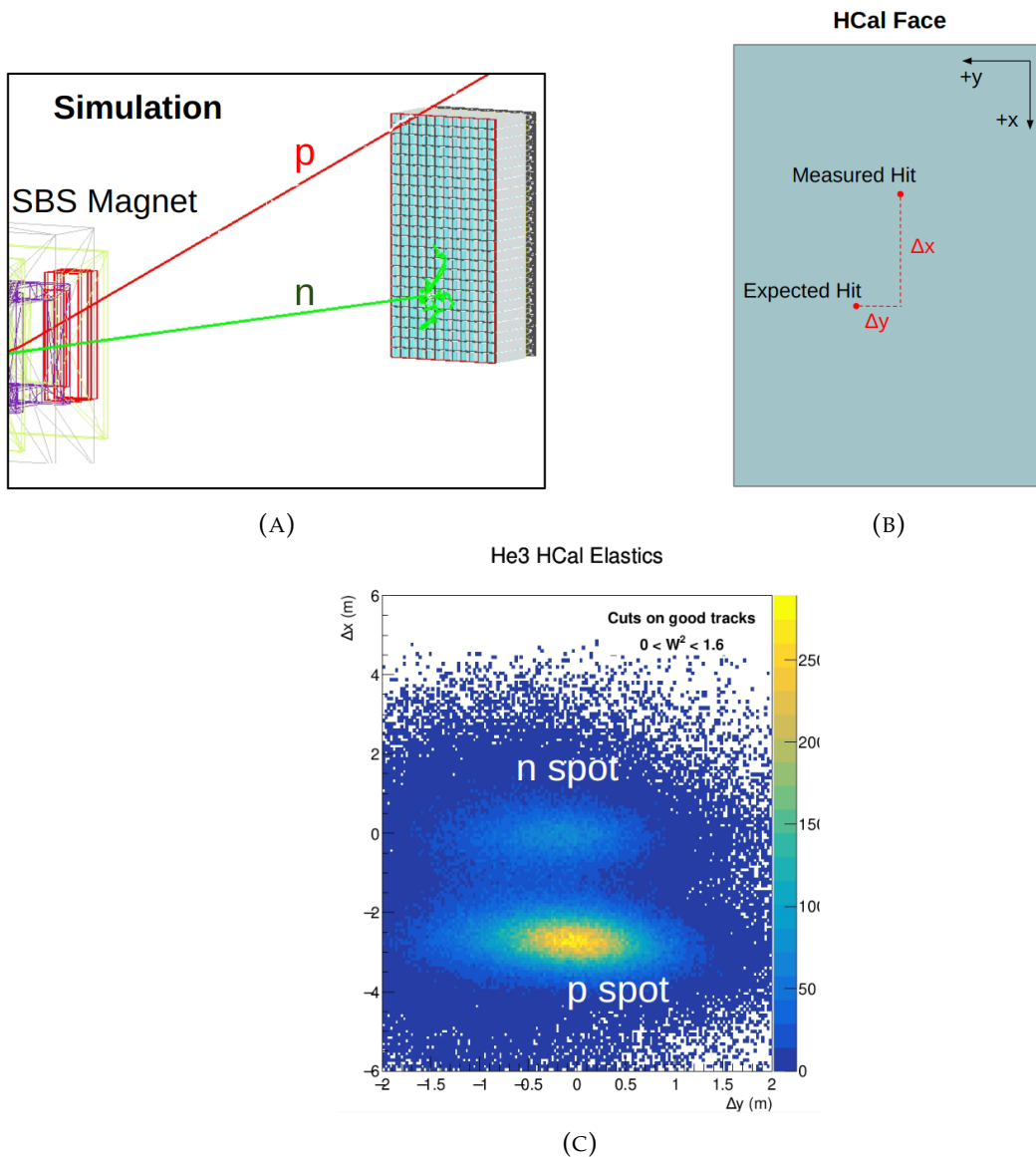


FIGURE 7.10: (A) G4SSBS simulation of proton and neutron with the same scattering angle and energy traversing the SBS magnet. Clearly the proton is bent away while the neutron continues straight. (B) The definition of the Δx and Δy are the difference between the measured and the expected position. (C) Kin2 data showing the Δx and Δy distribution, the neutron and proton spots are clearly seen.

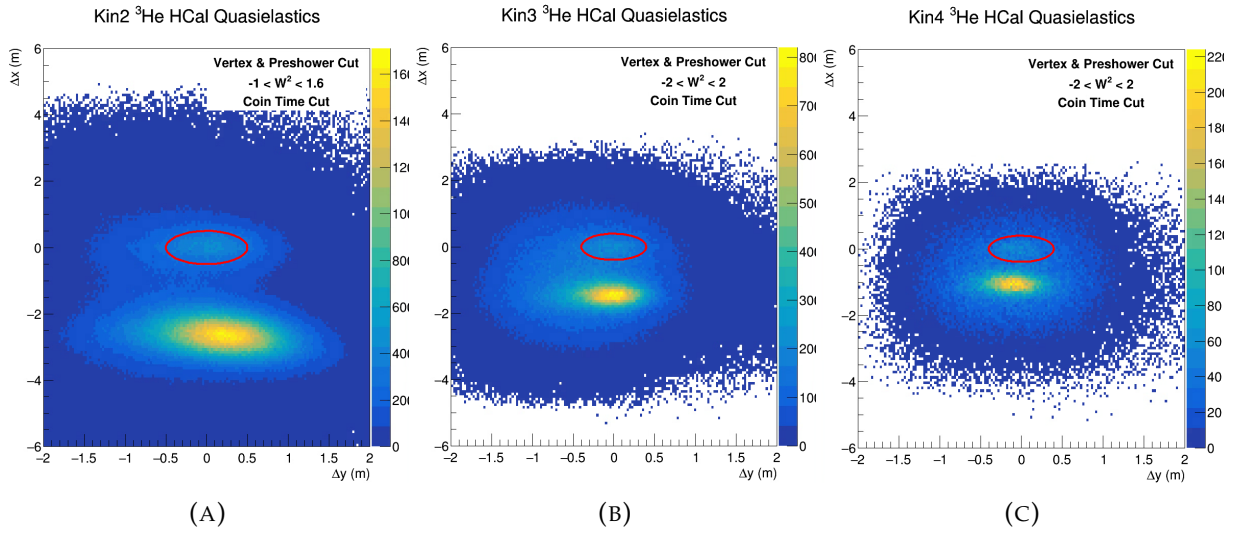


FIGURE 7.11: HCal data from all kinematics with the neutron identification radius displayed in red. Note that the x and y axes are not symmetric so the spot appears elliptical while it is actually circular.

7.4.6 Chosen Cuts

Quasielastic selections can now be made by applying cuts discussed in previous sections. Each event may have multiple tracks and the track which has the lowest χ^2 fit is taken as the best quasi-elastic track candidate. The vertex position of the end windows is found at ± 30 cm for each kinematic, with a position resolution of 6.5 mm. Therefore a cut selection of ± 27 cm is used to be $\sim 5\sigma$ outside of the glass window. The preshower energy cut was also set to 0.2 GeV setting for all kinematics in figure 7.5. The W^2 is now chosen based on the quasielastic simulation in figure 7.7. The coincidence time has also been shown for each kinematic in figure 7.9. The neutron spot selection has been discussed in section 7.4.5. All cuts applied are now summarized in table 7.1.

TABLE 7.1: Table of quasielastic cuts.

Cut	Kin2	Kin3	Kin4
Vertex	$ z_{tg} < 27$ cm	$ z_{tg} < 27$ cm	$ z_{tg} < 27$ cm
Preshower	$E_{PS} > 0.2$ GeV	$E_{PS} > 0.2$ GeV	$E_{PS} > 0.2$ GeV
W^2	$0 < W^2 < 1.6$ GeV	$-1.0 < W^2 < 2.0$ GeV	$-1.0 < W^2 < 2.0$ GeV
Timing	$90 < t_{\text{coin}} < 110$ ns	$85 < t_{\text{coin}} < 102$ ns	$83 < t_{\text{coin}} < 99$ ns
Δx	$ \Delta x < 0.5$	$ \Delta x < 0.4$	$ \Delta x < 0.4$
Δy	$ \Delta y < 0.5$	$ \Delta y < 0.4$	$ \Delta y < 0.4$

7.5 Simulation Fitting

The data can be deconstructed into individual components by comparing to a ^3He simulation with the same kinematic settings. The simulated events are pure QE scattering. From the QE simulation the scattered proton and neutron distributions are obtained. We then define everything in the data that does not match the simulated distributions as the "background". The proton and neutron are identified using the Δx separation, as explained in section 7.4.5, and therefore the Δx distribution from data is used for fitting.

The background is mostly from inelastic data so it would be natural to use an inelastic simulation to determine the shape. Unfortunately there is currently not an accurate inelastic simulation for this experiment, therefore some other method must be used. A polynomial distribution may be viable but it is important to use a low order fit to reduce any over fitting complications, and therefore we use a second order polynomial fit. Another idea is to use the data itself to obtain the shape of the background distribution. There is a wealth of background data in our sample and so some of it can be isolated separately from the QE data. Let us define the "background Δy " as the cut

$$\Delta y_{\text{bg,cut}} = \Delta y < y_{\text{bg,min}} \quad \text{or} \quad \Delta y > y_{\text{bg,max}} \quad (7.3)$$

where $y_{\text{bg,min}}$ and $y_{\text{bg,max}}$ cuts are chosen to be large values such that they are well outside the QE spot on the HCal. This is decided by looking at the plots in figure 7.10 and choosing values such that the cuts do not capture a significant amount of quasi-elastic proton and neutrons distributions. The concept for obtaining the background from data is shown outlined in figure 7.12. From the HCal plot the $\Delta y_{\text{bg,cut}}$ is used to select the regions from which the background Δx distribution is obtained. From the figure we see that the data passing the $\Delta y_{\text{bg,cut}}$ cut loses all features of the QE signal and this gives us confidence that this distribution can be used to portray the proper background shape.

We now have the neutron and proton shapes from simulation and the background shape. The polynomial background or the data background method may be used to obtain the background shape, but the next step remains the same for both. The three contributions can now be fitted to match the experimental data. The following fit is used

$$\text{sim} = N(p_{\text{sim}} + R * n_{\text{sim}} + N_{\text{bg}} * bg_{\text{dist}}) \quad (7.4)$$

where p_{sim} , n_{sim} , and bg_{dist} and the three distributions discussed while N , R , and N_{bg} are the fit parameters. Note that the fit parameters are all normalizations so the shapes are preserved. The fit parameters are set such that the *sim* result best matches the data.

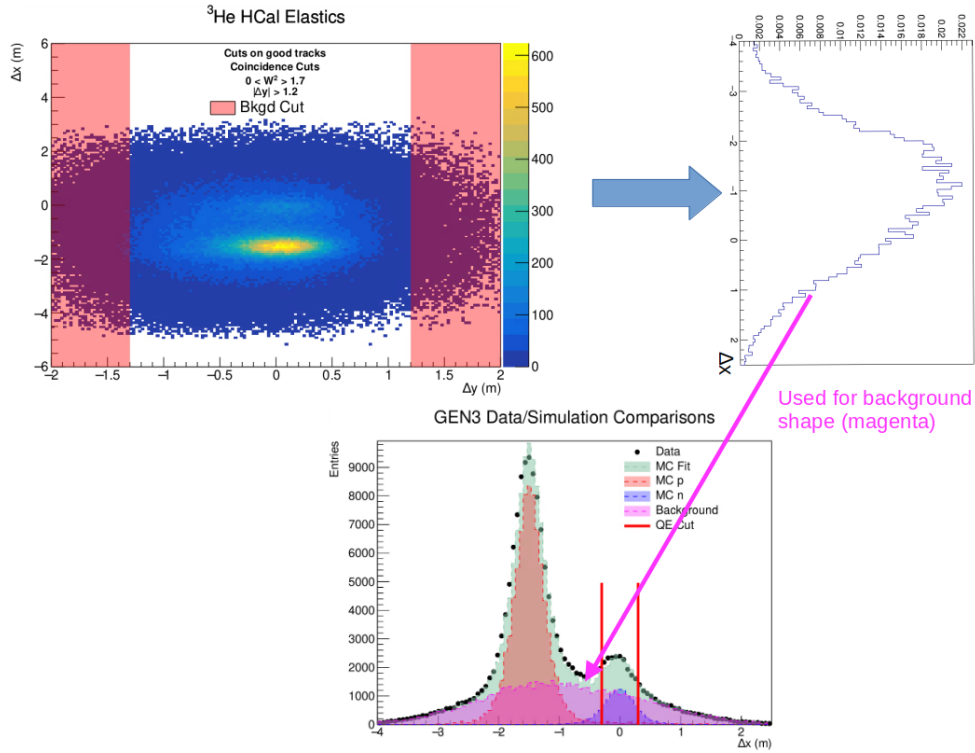


FIGURE 7.12: Procedure of obtaining background shape from data. (top left) HCal data with red regions for data considered to be background. (top right) Projection of Δx distribution of data from the red regions. (bottom) Data fitting using this distribution as the shape for the background fit.

An example of the fits for Kin2 and Kin3 are shown in figure 7.13. We note that the data background method is more accurate for higher Q^2 kinematics since polynomials fits with limited number of terms cannot capture the variations in the slope for this large background case. On the other hand, for Kin2 the large quasi-elastic footprint on HCal does not leave much area outside the quasi-elastic cut to extract the background shape from data, so the data method is not reasonable. Therefore the polynomial background is used for Kin2 only. For Kin3 and Kin4 the data background method is used.

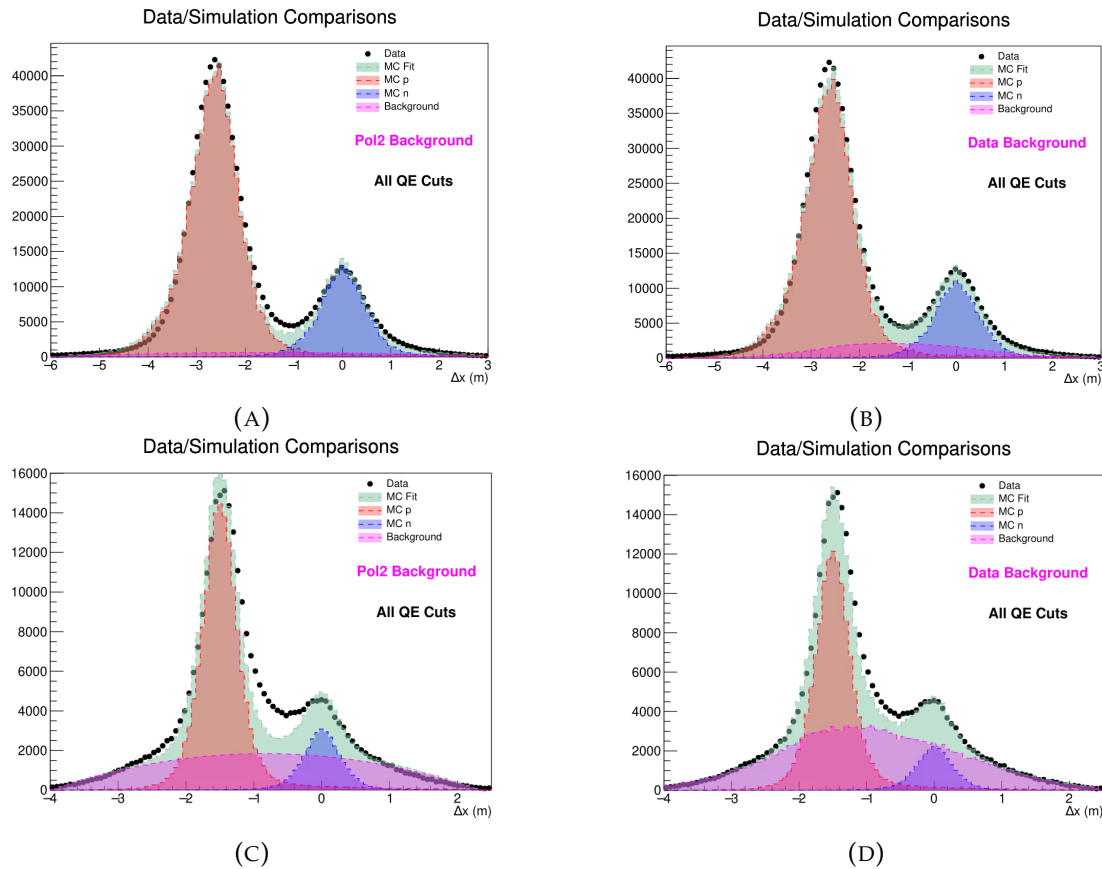


FIGURE 7.13: Examples of the fitting procedure shown here for different kinematics. (A) Kin2 data with the background shape taken from a second order polynomial. (B) Kin2 data with the background shape taken from the data. (C) Kin3 data with the background shape taken from a second order polynomial. (D) Kin3 data with the background shape taken from the data. Note that the polynomial background works better for Kin2 but the data background is better for Kin3.

7.6 Polarizations

The ^3He polarization analysis has been performed by another thesis student in the experiment, Hunter Presley. Here we will simply quote the results and not go into detail about how they were obtained. The polarization from every NMR measurement throughout the experiment is shown in figure 7.14. Since NMR measurements were taken every four hours and runs were one hour we must determine how to relate a specific polarization to an event. For this the NMR result can be linearly interpolated between each pair of measurements. The absolute time of every event is recorded by CODA. For a given event, the time can be combined with the linear interpolation of the

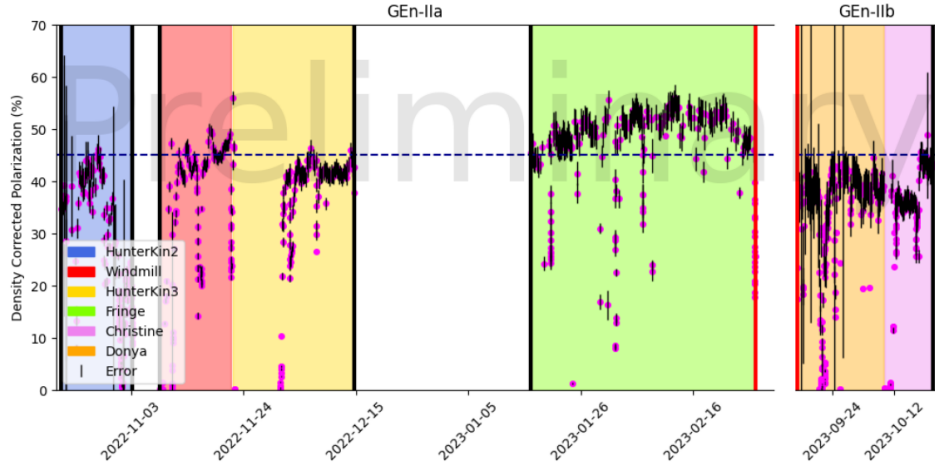


FIGURE 7.14: Result of every NMR measurement throughout GEN-II. Legend labels are the ^3He cell names. Figure provided by Hunter Presley

NMR measurements to obtain the polarization, $P_{^3\text{He},ev}$, and error, $\sigma_{P,ev}$, for that singular event. For all QE counts in a single run, the polarizations can then be averaged to yield the run polarization

$$P_{^3\text{He},i} = \frac{\sum_{\text{events}} P_{^3\text{He},ev}}{N_{\text{QE},i}} \quad \sigma_{P,i} = \frac{\sum_{\text{events}} \sigma_{P,ev}}{N_{\text{QE},i}} \quad (7.5)$$

where $P_{^3\text{He},i}$ and $\sigma_{P,i}$ is the polarization and error and $N_{\text{QE},i}$ is the total QE event count for run i . We will also make use of the average polarization for the entire kinematic. For this the weighted average of the polarization for every run is calculated with the number of quasielastic events as the weight. Similarly the average polarization error is the weighted average. To be explicit this is

$$\bar{P}_{^3\text{He}} = \frac{\sum_i N_{\text{QE},i} P_{^3\text{He},i}}{\sum_i N_{\text{QE},i}} \quad \bar{\sigma}_P = \frac{\sum_i N_{\text{QE},i} \sigma_{P,i}}{\sum_i N_{\text{QE},i}} \quad (7.6)$$

The beam polarization analysis was performed by graduate student Faraz Chahili. The beam polarization was measured through Møller measurements made once or twice for each kinematic, as described in section 3.8.3. The specific analysis will not be described here and we will quote the results. Figure 7.15 shows the beam polarization results throughout GEN-II. While the measurements are taken on one specific day, the result is applied to many weeks of beam, as shown in the plot. For a specific run the

beam polarization, $P_{\text{beam},i}$, and error, $\sigma_{P_{\text{beam},i}}$ is obtained from which Møller measurement matches it's time period. The average beam polarization for a single kinematic is then the statistically weighted average.

$$\bar{P}_{\text{beam}} = \frac{\sum_i N_{\text{QE},i} P_{\text{beam},i}}{\sum_i N_{\text{QE},i}} \quad \bar{\sigma}_{P_{\text{beam}}} = \frac{\sum_i N_{\text{QE},i} \sigma_{P_{\text{beam},i}}}{\sum_i N_{\text{QE},i}} \quad (7.7)$$

There is a period of time December 11 - 15 of 2022 where the a Møller measurement was not done at one specific accelerator setting. The result of this is that those 5 days of data have unknown beam polarizations. Therefore that data is discarded, and constitutes 13% of the total statistics for Kin3. More analysis is necessary to determine if the beam polarization is recoverable for this data.

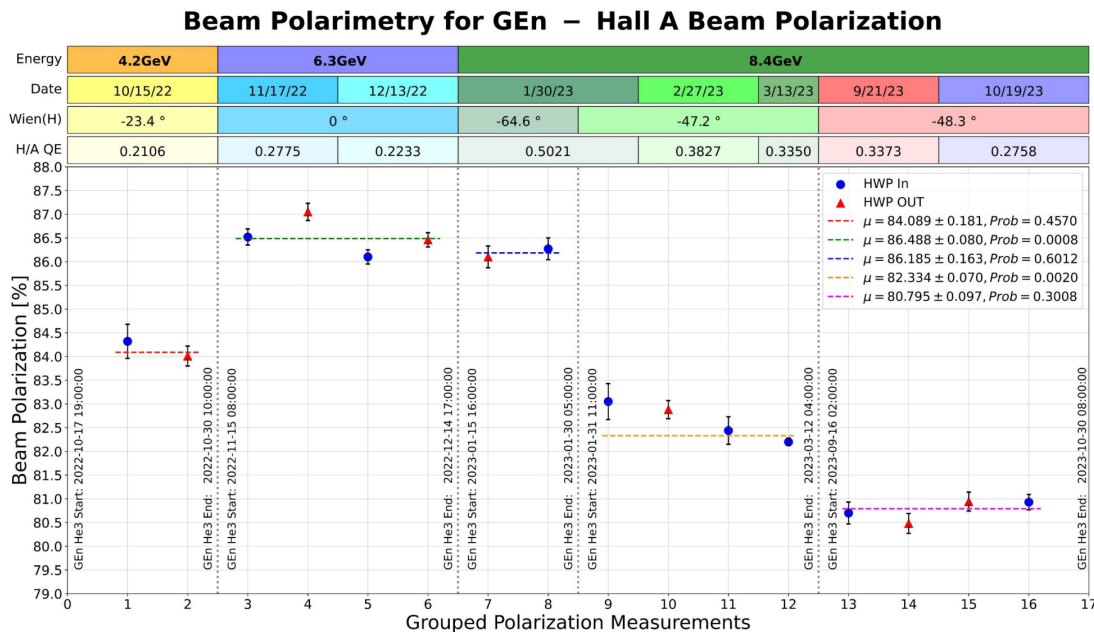


FIGURE 7.15: Results of all Møller measurements throughout GEN-II. The vertical lines and labels show the range of dates that each measurement applies to. Figure taken from [70].

The effective neutron polarization, P_n , describes the fraction of ^3He polarization that is carried by the neutron. P_n has been well known for decades to be 86% for the entire ^3He wavefunction [46]. However here we are making Δx and Δy cuts analogous to p_{\perp} cuts, as described in section 7.4.5. This means only part of the ^3He wavefunction is being investigated, and it turns out that this enhances the neutron effective polarization to be higher than 86%. For an accurate calculation a full nuclear wave function simulation must be performed. Unfortunately this is not currently available for this

analysis and instead we turn to the calculations done in GEN-I and assume the same effective polarization of $P_n = 96\%$ [20].

7.7 Helicity Calculation

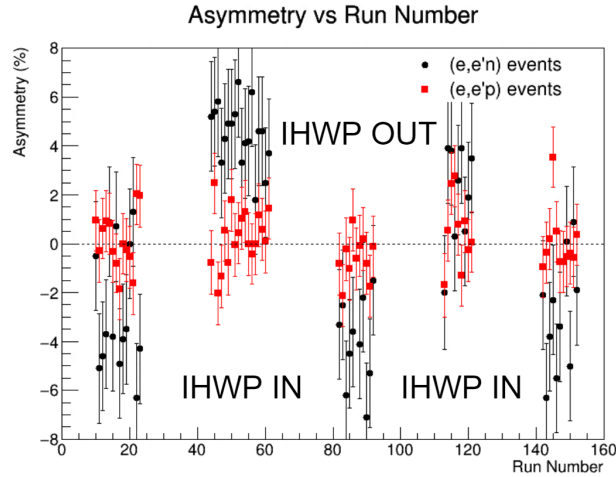


FIGURE 7.16: Raw helicity symmetry vs run number for a subset of data from Kin2. Proton and neutron events are separated to see nonzero asymmetries. The subset of runs with IHWP in and out are labeled.

Each event has a helicity recorded, $h_{\text{meas}} = \pm 1$. Recall that the helicity hardware has been overviewed in section 3.8.2. Figure 7.16 shows the raw measured asymmetry over a set of runs during Kin2 for neutron and proton events. The neutron events are identified to see the nonzero asymmetries. As the IHWP state switches the asymmetry also flips as expected. To recover the true helicity the IHWP must be accounted for. The corrected helicity is then

$$h_{\text{raw}} = P_{\text{IHWP}} P_{\text{kin}} h_{\text{meas}} \quad (7.8)$$

where P_{IHWP} is +1 or -1 if the IHWP is in or out respectively and P_{kin} is ± 1 determined by the accelerator settings. For each accelerating setting, meaning each kinematic, there are a number of beam spin flips which change the helicity at the target from the helicity at the injector. We know that for GEN-II the asymmetry measurement must physically be a positive value therefore P_{kin} is chosen for each kinematic such that the resulting asymmetry is positive. This result is summarized in table 7.2. With this info h_{raw} can now be determined for every event.

TABLE 7.2: Table of P_{kin} settings.

	Kin2	Kin3	Kin4
P_{kin}	-1	1	1

7.8 Asymmetry Formalism

The theoretical formalism has been laid out in section 1.5.2, with G_E^n/G_M^n found from A_{phys} . Now we will detail how the asymmetry is experimentally determined. A_{phys} is the physics asymmetry assuming a pure sample of 100% polarized neutron data and 100% polarized beam. The neutron asymmetry from real data will be

$$A_n = P_{\text{beam}} P_{3\text{He}} P_n A_{\text{phys}} \quad (7.9)$$

where P_{beam} is the beam polarization, $P_{3\text{He}}$ is the target polarization, and P_n is the effective polarization of the neutron in the target. These polarizations all lower the measured asymmetry value.

From all quasielastic cuts the number of events with + and - helicity can be calculated, N^+ and N^- . This will also be referred to as the "raw" counts. This includes everything passing the QE cuts, which has multiple contributions that are not pure quasielastic scattered neutrons. The main sources of contamination are:

1. Timing accidental background.
2. Nitrogen in the target cell.
3. Pion events within the electron selection cut.
4. Inelastic data inside the QE selection cuts.
5. Quasielastic proton events inside the neutron selection cut.
6. Nuclear effects.

The raw event counts can be broken up into individual contributions.

$$N^\pm = N_n^\pm + N_{\text{acc}}^\pm + N_{\text{N}_2}^\pm + N_\pi^\pm + N_{\text{in}}^\pm + N_{\text{p}}^\pm + N_{\text{FSI}}^\pm \quad (7.10)$$

It is important to note here that each correction is done in numerical order shown above. Therefore each subsequent correction must make sure to account for all previous corrections or else there will be double counting. This will be described in detail in the following sections. We now define some useful variables

$$\begin{aligned}
\Delta_x &= N_x^+ - N_x^- \\
\Sigma_x &= N_x^+ + N_x^- \\
A_x &= \Delta_x / \Sigma_x \\
\Sigma &= \sum_x \Sigma_x \\
f_x &= \Sigma_x / \Sigma \\
f_n &= 1 - \sum_{x \neq n} f_x
\end{aligned} \tag{7.11}$$

where N_x is the count for contribution type $x = n, \text{acc}, N_2, \text{etc}$, Σ is the total count of all events, f_x is the fractional amount of the contamination x in the sample, and A_x is the asymmetry of contamination x . Typical nuclear experiments in the past use dilution factors, which are defined as $D_x = 1 - \Sigma_x / \Sigma$. We find it more convenient for this analysis to use the fractional instead of the dilution formalism. One can conveniently convert between the two as $D_x = 1 - f_x$. The raw asymmetry can then be defined.

$$A_{\text{raw}} = \frac{N^+ - N^-}{N^+ + N^-} = \frac{\sum_x \Delta_x}{\sum_x \Sigma_x} = \sum_x \frac{\Delta_x}{\Sigma} = \sum_x f_x \frac{\Delta_x}{\Sigma_x} = \sum_x f_x A_x \tag{7.12}$$

$$A_{\text{raw}} = f_n A_n + \sum_{x \neq n} f_x A_x \tag{7.13}$$

$$A_n = \frac{A_{\text{raw}} - \sum_{x \neq n} f_x A_x}{f_n} \tag{7.14}$$

Equation 7.14 gives the neutron asymmetry in the sample, given the fractional asymmetries of all the various contaminations as defined in equation 7.11. This can be combined with equation 7.9 to calculate the physical asymmetry.

$$\begin{aligned}
A_{\text{phys}} &= \frac{A_{\text{raw}} - \sum_{x \neq n} f_x A_x}{P_{\text{beam}} P_{^3\text{He}} P_n f_n} \\
&= \frac{A_{\text{raw}} - f_{\text{acc}} A_{\text{acc}} - f_{\pi} A_{\pi} - f_{\text{in}} A_{\text{in}} - f_{\text{p}} A_{\text{p}} - f_{\text{FSI}} A_{\text{FSI}}}{P_{\text{beam}} P_{^3\text{He}} P_n (1 - f_{\text{acc}} - f_{N_2} - f_{\pi} - f_{\text{in}} - f_{\text{p}} - f_{\text{FSI}})}
\end{aligned} \tag{7.15}$$

In the above equation it is assumed that $A_{N_2} = 0$ since nitrogen is unpolarized.

Equation 7.15 calculates the physical asymmetry by subtracting out all the contributions of the other asymmetries that are not from the quasielastic neutron. It is important to note here that the asymmetry contributions, A_x , can be calculated separately from the quasielastic cuts if a good sample of contamination x can be identified. For example, the pion contamination, A_π , can be calculated using cuts to get a large pion sample instead of using the QE cuts. The QE cuts are then applied to calculate f_π , of the fraction of pions inside the QE sample. The combination of f_π and A_π then yields the overall asymmetry affect on our QE sample. This process will be described in detail in the upcoming sections. Table 7.3 summarizes all variables used in this analysis.

TABLE 7.3: Table of variables used throughout this analysis.

Variable	Description
Σ	All events passing the quasielastic cuts
N^\pm	All events passing the quasielastic cuts for ± 1 helicity
A_{raw}	Raw asymmetry from all quasielastic counts
A_{acc}	Asymmetry from a accidental background sample
A_π	Asymmetry from a pion sample
A_{in}	Asymmetry from an inelastic sample
A_{p}	Asymmetry associated with the proton scattering
A_{FSI}	Asymmetry associated with nuclear corrections
A_{phys}	Physical asymmetry related to G_E^n/G_M^n
f_{acc}	Accidental contamination fraction of Σ
f_{N_2}	N_2 contamination fraction of Σ .
f_π	pion contamination fraction of Σ
f_{in}	Inelastic contamination fraction of Σ
f_{p}	Proton contamination fraction of Σ
f_{FSI}	Nuclear corrections fraction of Σ
f_{n}	Neutron fraction of Σ
P_{beam}	Polarization of the electron beam
P_{He}	Polarization of the ^3He target
P_{n}	Effective polarization of the neutron inside ^3He

7.8.1 Accidental Contamination

The accidental contamination refers to out of time events that randomly fall into the QE timing window. For each kinematic the coincidence time is shown in figure 7.17. We find that the background is mostly flat, as expected because it is random, except for some difference near the very edge of the timing plots. This can be utilized to calculate the amount of accidentals in the peak.

First we calculate the asymmetry of the accidentals using the cuts in red shown in the plots. The purpose here is to obtain the largest sample of accidentals to calculate the asymmetry with low errors. This includes data outside of the timing peak but not the data where the background starts to slope down as this may have some edge effects that do not properly represent the accidental sample. It is also notable that the asymmetries in these regions all agree within the error, so there is no bias from sampling a particular part of the distribution. The asymmetry is then

$$A_{\text{acc}} = \frac{N_{\text{acc}}^+ - N_{\text{acc}}^-}{N_{\text{acc}}^+ + N_{\text{acc}}^-} \quad (7.16)$$

where N_{acc}^+ and N_{acc}^- are the helicity counts from the data in the accidental cuts.

Now the fraction of accidentals inside the QE cuts can be calculated. The width of the QE timing cut can be shifted to the right of the peak and applied to the out of time events. This the blue cut in figure 7.17. Since the background is flat this sample can be assumed to be the same as under the peak. The fraction can then be calculated as $f_{\text{acc}} = N_{\text{acc,QE}}/\Sigma$, where $N_{\text{acc,QE}}$ is the total number of counts inside this cut and Σ is the total number of QE events, as previously defined in table 7.3.

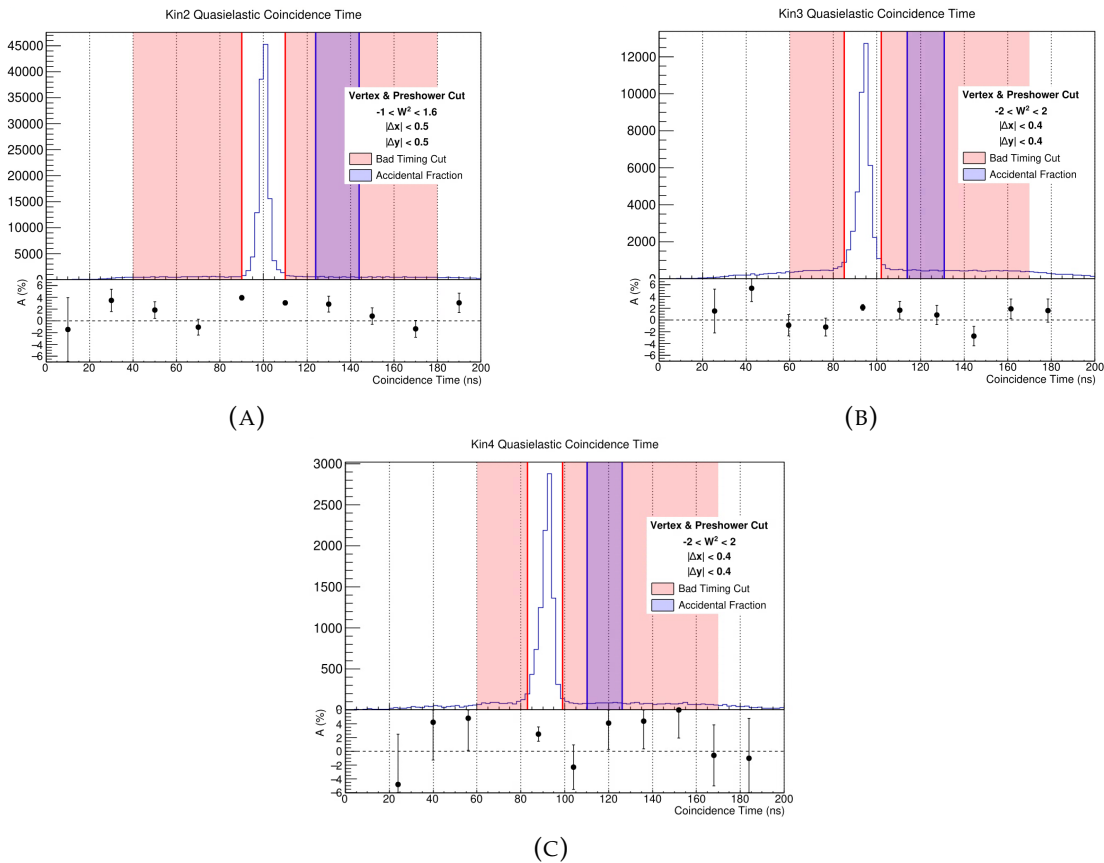


FIGURE 7.17: Coincidence timing distributions for all kinematics. The red bands show the data used calculate the accidental asymmetry. The blue bands show the data used to calculate the accidental fraction. The peak in the middle shows the QE data cut. For each figure the asymmetry in 20 ns intervals is shown below.

7.8.2 Nitrogen Contamination

The ^3He target contains a small amount of N_2 which may cause some fraction of events to scatter off them. Data could be taken on a N_2 target to estimate the N_2 contamination. This target was not used during GEn-II and so other methods are needed. Carbon and nitrogen have similar nucleon numbers, and therefore carbon can be used as a good approximation to nitrogen. The carbon data set used for optics calibration is utilized for this analysis.

Nitrogen is unpolarized and so A_{N_2} is set to zero and only f_{N_2} must be calculated. This can be calculated as

$$f_{N_2} = \frac{Q(^3\text{He})}{Q(C)} \frac{m_{N_2} (^3\text{He})}{m_C(C)} \frac{\Sigma(C) - \Sigma_{\text{acc}}(C)}{\Sigma(^3\text{He}) - \Sigma_{\text{acc}}(^3\text{He})} \quad (7.17)$$

where $Q(t)$ is the beam charge accumulated on target t , $m(t)$ is the mass thickness of target t , $\Sigma(C)$ is the total events passing QE cuts on the carbon target, $\Sigma_{\text{acc}}(C)$ is the accidental estimation in the carbon sample, and $\Sigma(^3\text{He})$ and $\Sigma_{\text{acc}}(^3\text{He})$ are the previously defined counts from the ^3He data, with the added cuts to match the acceptance of the carbon data.

The carbon data must have the air between the foils removed, since it is irrelevant for our estimation. Even though the carbon foil is 0.01 inch thick there is significant spread due to the optics resolution (section 6.4), and so a cut of ± 2.1 cm around each foil is used as seen in figure 7.18a. Similarly the data outside of the sieve holes must be removed as shown in figure 7.18b. These cuts are also applied to the ^3He data to match the acceptances exactly.

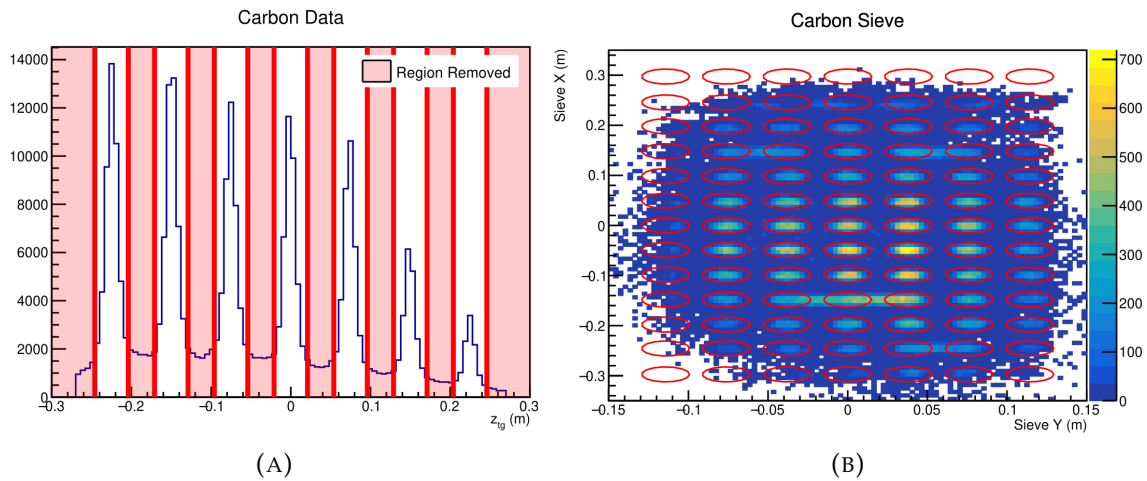


FIGURE 7.18: (A) Vertex cuts applied to carbon data. (B) Sieve hole cuts applied to carbon data.

The vertex cut of ± 2.1 cm for each foil means that $\Delta z = 4.2$ cm of air is captured in each cut. Therefore when $m_C(C)$ is calculated the air must also be accounted for.

Meanwhile the ${}^3\text{He}$ target is continuous so $m_{\text{N}_2}({}^3\text{He})$ needs no further correction.

$$l_{\text{air}} = n_{\text{foils}}\Delta z \quad (7.18)$$

$$m_{\text{N}_2}({}^3\text{He}) = \rho_{\text{N}_2} l_{\text{air}} \quad (7.19)$$

$$m_{\text{C}}(\text{C}) = \rho_{\text{C}} l_{\text{C}} + \rho_{\text{air}} l_{\text{air}} \quad (7.20)$$

where n_{foils} is the number of foils, Δz is the size of the foil cut, l_{air} is the length of the air cut on the carbon target, ρ_{N_2} is the density of the N_2 in the ${}^3\text{He}$ cell, ρ_{C} is the density of the carbon target, and l_{C} is the length of all the carbon thicknesses.

7.8.3 Pion Contamination

Some amount of π^- events may pass all the QE cuts and this contribution must be estimated. As previously discussed in section 6.8, the GRINCH signal should be used to cleanly identify pion and electron events but it is not properly calibrated yet and therefore BBCal preshower data must be used. In the future this analysis should be repeated using GRINCH analysis. For this analysis a clean sample of pion and electron preshower distributions are obtained through simulations. For electrons, a QE ${}^3\text{He}$ simulation is used, with the scattered QE electron simulated in BB. For pions, π^- particles are simulated with momentum range and acceptance matching the data and are propagated through the BB spectrometer.

The accidental fraction must be counted and removed from this sample since it has already been calculated in section 7.8.1. The same timing cut method is applied here. Figure 7.19 shows data from Kin3 with no preshower cuts applied so the effect on the pion peak can be clearly seen. Note in figure 7.19b that the preshower distribution with the accidental timing cut has a large peak < 0.2 GeV corresponding with the expected pion signal. This demonstrates that the accidental fraction is mostly pion instead of electron. However it is difficult to disentangle the pion and electron mix from the total distributions and so we will assume the accidental fraction affects the whole distribution equally but note here that this assumption leads to an overestimating the final pion fraction. From figure 7.19a the number of accidentals in the data with no preshower cut can be obtained and we will denote it as $\Sigma_{\text{acc,PS}}$. Similarly we will denote the number of events inside the coincidence peak, but with no preshower cut to be Σ_{PS} .

The nitrogen correction should be applied as well since it has already been calculated. Unfortunately the carbon data statistics used for N_2 estimation was too small a sample to get good statistics for the fitting procedure done here. Therefore the N_2 contamination could not be calculated in this analysis. However this would be a single % level correction on a single % level correction and the overall effect on the final A_{phys} would be negligible.

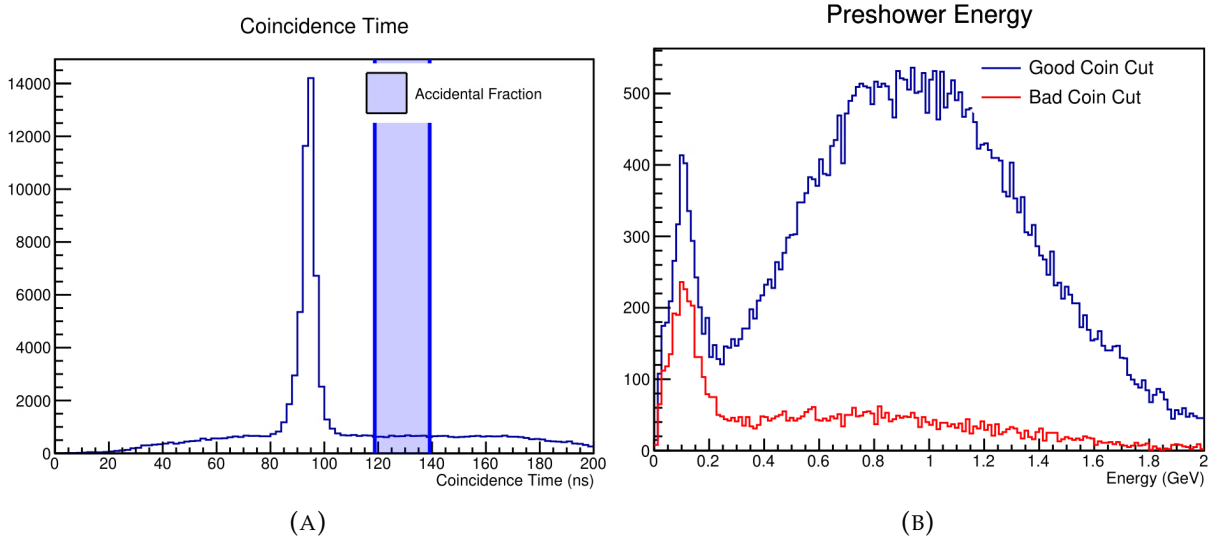


FIGURE 7.19: Data from Kin3 with no preshower cut applied. (A) the timing cut is applied to obtain the accidental fraction just as before. (B) The preshower energy is plotted for the good QE time cut and the accidental timing cut. Notably we find that the accidentals timing cut is a majority of pions.

The individual distributions of pions and electrons from simulation are weighted by the cross section and so the results are distributions and not counts like the experimental data. Therefore instead of the typical N_π notation we have been using we will instead use $S_{\pi,e}$ to denote the pion and electron yields from simulation. The simulation results can then be fitted to the data to obtain scaling factors

$$N_{\text{data}} = C_\pi S_\pi + C_e S_e \quad (7.21)$$

where N_{data} is the data distribution, S_π is the simulated pion distribution, S_e is the simulated electron distribution, and C_π and C_e are parameters to be decided by the fit. For the simulations and the data, the preshower cut in table 7.1 is **not** applied; otherwise this would remove the pions. The simulation does not have helicity calculations but the helicity can still be determined by looking at the +1 or -1 helicity data individually. The

simulations can be fitted to a specific helicity distribution

$$N_{\text{data}}^{\pm} = C_{\pi}^{\pm} S_{\pi} + C_e^{\pm} S_e \quad (7.22)$$

where C_{π}^{\pm} and C_e^{\pm} are parameters decided by the fit and can be used to calculate the individual helicity contributions. The S_{π} distribution can be integrated over to get the raw simulation yield. For the asymmetry calculation we want to maximize pion statistics and so the entire S_{π} distribution is integrated over to obtain $S_{\pi,\text{all}}$. Then the total pion helicity counts is $N_{\pi}^{+} = C_{\pi}^{+} S_{\pi,\text{all}}$ and $N_{\pi}^{-} = C_{\pi}^{-} S_{\pi,\text{all}}$, but recall that none of these variables are integers.

For asymmetry calculation only the single arm BB data is used for the fit to increase statistics of pions for better error estimation of the asymmetry. This means that only the vertex and the W^2 cuts are applied to this data set. Figure 7.20 shows the fit results for each kinematic. The asymmetry can then be formed.

$$A_{\pi} = \frac{N_{\pi}^{+} - N_{\pi}^{-}}{N_{\pi}^{+} + N_{\pi}^{-}} = \frac{C_{\pi}^{+} - C_{\pi}^{-}}{C_{\pi}^{+} + C_{\pi}^{-}} \quad (7.23)$$

The accidental fraction correction does not appear here since the fraction is applied equally to all distributions and therefore would be canceled in the ratio.

For pion fraction calculation all QE cuts except the preshower cut must now be applied to the data and then the same fitting procedure is applied. To calculate the pions inside the QE cuts S_{π} is then integrated above 0.2 GeV to obtain $S_{\pi,\text{PS}}$. Here we look to obtain the total pion counts $\Sigma_{\pi} = C_{\pi} S_{\pi,\text{PS}}$ in the QE sample. The results of the fitting for each kinematic is found in figure 7.21. However, since the C_{π} parameter was calculated by fitting to the total data, which includes accidentals, this would be double counting the accidentals. As already discussed, the accidentals are assumed to affect all the data equally and so the Σ_{π} must be scaled by the accidentals.

$$\Sigma_{\pi} = C_{\pi} S_{\pi,\text{PS}} (1 - f_{\text{acc,PS}}) = C_{\pi} S_{\pi,\text{PS}} \left(1 - \frac{\Sigma_{\text{acc,PS}}}{\Sigma_{\text{PS}}} \right) \quad (7.24)$$

The resulting fraction for just the pions is then

$$f_{\pi} = \frac{\Sigma_{\pi}}{\Sigma} = \frac{C_{\pi} S_{\pi,\text{PS}} \left(1 - \frac{\Sigma_{\text{acc,PS}}}{\Sigma_{\text{PS}}} \right)}{\Sigma} \quad (7.25)$$

where Σ is the total events passing QE cuts. For each kinematic three distributions

must be fitted, the +1 helicity, -1 helicity, and total distribution. For each kinematic the parameters C_π , C_π^\pm , C_e , C_e^\pm are obtained.

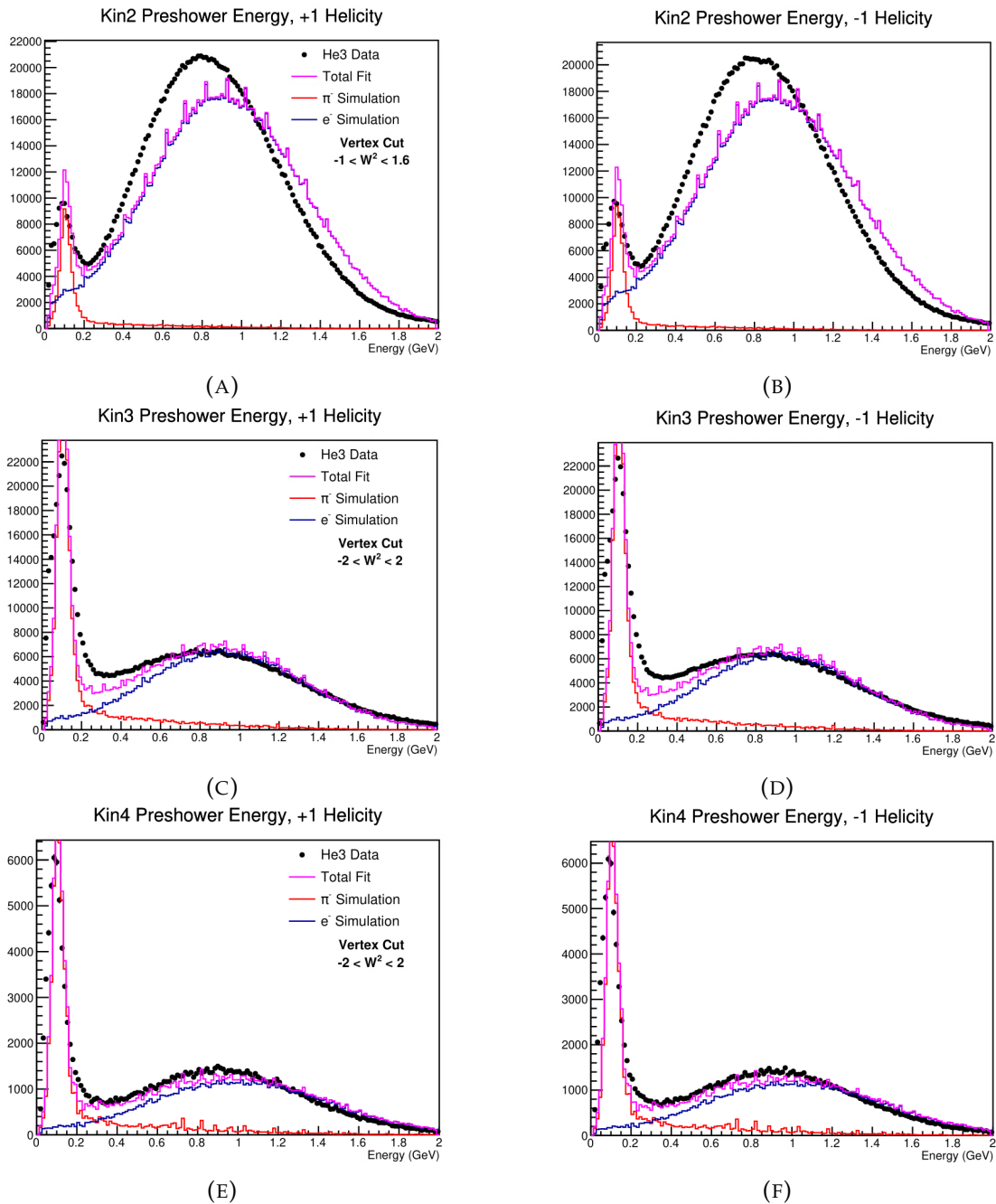


FIGURE 7.20: Results of fitting the preshower distribution from a π^- and ${}^3\text{He}$ QE simulation to real data for each kinematic. The helicity +1 data is shown in figures (A), (C), and (E) while the -1 data is shown in figures (B), (D), and (F). From these fits the parameters C_π^\pm and C_e^\pm are obtained.

future analysis should attempt to simulate this background for a more thorough comparison.

For this estimation a clean sample of inelastic data must be obtained. From the quasielastic particle identification in figure 7.22 we can determine a method of identifying inelastic events. the $\Delta y_{\text{bg,cut}}$ cut will be used here, as defined in equation 7.3. This value is determined by looking at the data and selecting $\Delta y_{\text{bg,cut}}$ such that it is not near the QE spots and therefore not correlated with a elastically scattered event. This idea is outlined in figure 7.22. By changing only the Δy cut to be outside the QE spots we identify high W^2 events which must be inelastic while Δy cut within the QE spot is associated with W^2 around the expected elastic peak.

While we obtain the inelastic data from the $\Delta y_{\text{bg,cut}}$ we must ascertain it's effects inside the Δy elastic cut. Therefore it must be shown that the results from the inelastic region can be extrapolated to the elastic region. To confirm this we look at figure 7.22 and 7.23 for all kinematics. This shows the asymmetry as a function of W^2 for both elastic and inelastic cuts. It is clear for all kinematics that the asymmetry for the inelastic data is constant for all W^2 bins, within the error. We remain confident that that the asymmetry obtained in this region will then be the same asymmetry underneath the elastic region. The inelastic background cuts applied in this analysis is summarized in table 7.4. The only difference between this and the QE cuts is the Δy cut applied and there is no W^2 cut applied.

TABLE 7.4: Table of inelastic background cuts.

Cut	Kin2	Kin3	Kin4
$\Delta y_{\text{bg,cut}}$	$\Delta y < -3.0 \text{ m}$ or $\Delta y > 2.5 \text{ m}$	$\Delta y < -1.3 \text{ m}$ or $\Delta y > 1.0 \text{ m}$	$\Delta y < -1.1 \text{ m}$ or $\Delta y > 1.0 \text{ m}$
W^2	none	none	none
other	same as QE	same as QE	same as QE

The asymmetry can then be calculated

$$A_{\text{in}} = \frac{N_{\text{in}}^+ - N_{\text{in}}^-}{N_{\text{in}}^+ + N_{\text{in}}^-} \quad (7.26)$$

where N_{in}^{\pm} are the helicity counts passing the inelastic cuts in table 7.4. As before there are no accidental or other fractions applied because they cancel out in the asymmetry ratio.

The inelastic fraction must then be determined using a different method. The fitting procedure described in section 7.5 is now applied to determine the amount of background compared to simulation. The QE simulation can be compared to data to determine how much background is in the data. The resulting distributions for each kinematic can be seen in figure 7.24. All QE cuts have been applied to these plots except the Δx cut, naturally. The background distribution can now be integrated inside the Δx cut to obtain the background counts, Σ_{bg} .

There is a critical subtlety here. Since the simulation fit, equation 7.4, only includes the proton, neutron, and background it does not comment on what the background is. Therefore the background must also include everything that is **not** proton or neutron QE scattering. This means the background includes all previous corrections discussed here except for the proton. The inelastic fraction can then be disentangled as follows

$$f_{\text{in}} = \frac{\Sigma_{\text{in}}}{\Sigma} = \frac{\Sigma_{\text{bg}} - \Sigma_{\text{acc}} - \Sigma_{\text{N}_2} - \Sigma_{\pi}}{\Sigma} \quad (7.27)$$

where the inelastic counts, Σ_{in} , are calculated by subtracting out all previous corrections from the background counts, Σ_{bg} .

At this point one may look at the plots in figure 7.24 and consider, since the neutron distribution is obtained from this fit can we simply apply this method to +1 and -1 helicity data separately to directly obtain the neutron distribution and form an asymmetry? This would bypass detailing each contribution individually as we have done in the last few sections. But unfortunately this does not work because it assumes the polarizations are stable throughout the kinematic setting. This may be true for the beam polarization but the ^3He polarization is varying significantly as seen in figure 7.14 and the asymmetry may be much different for different time periods. Therefore this fitting method can only be used to look at counts for the entire kinematic and the run by run effects must be taken into account separately.

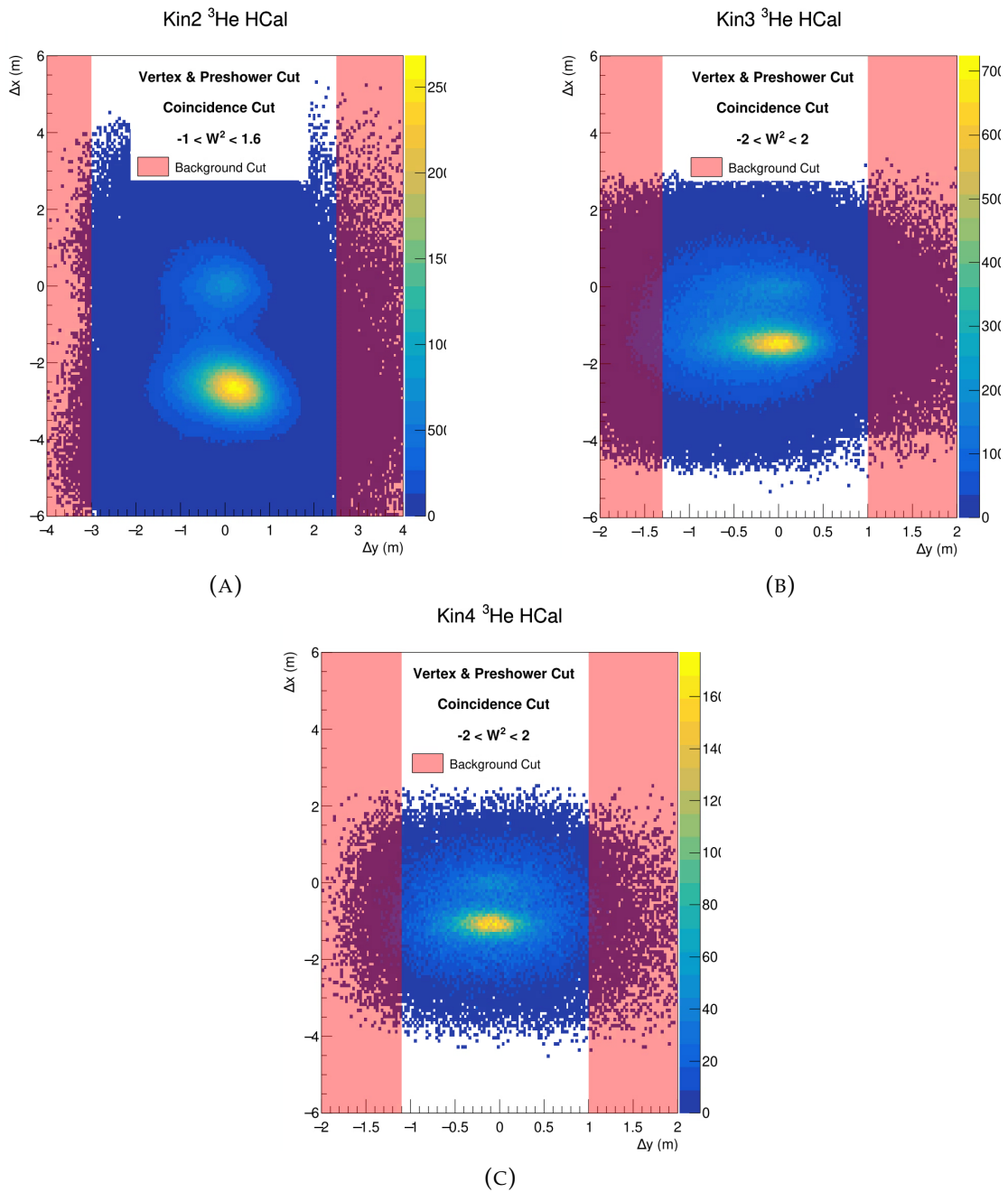


FIGURE 7.22: Δx vs Δy plot for all kinematics with the $\Delta y_{\text{bg,cut}}$ regions highlighted in red. This region is labeled as the “background cut”.

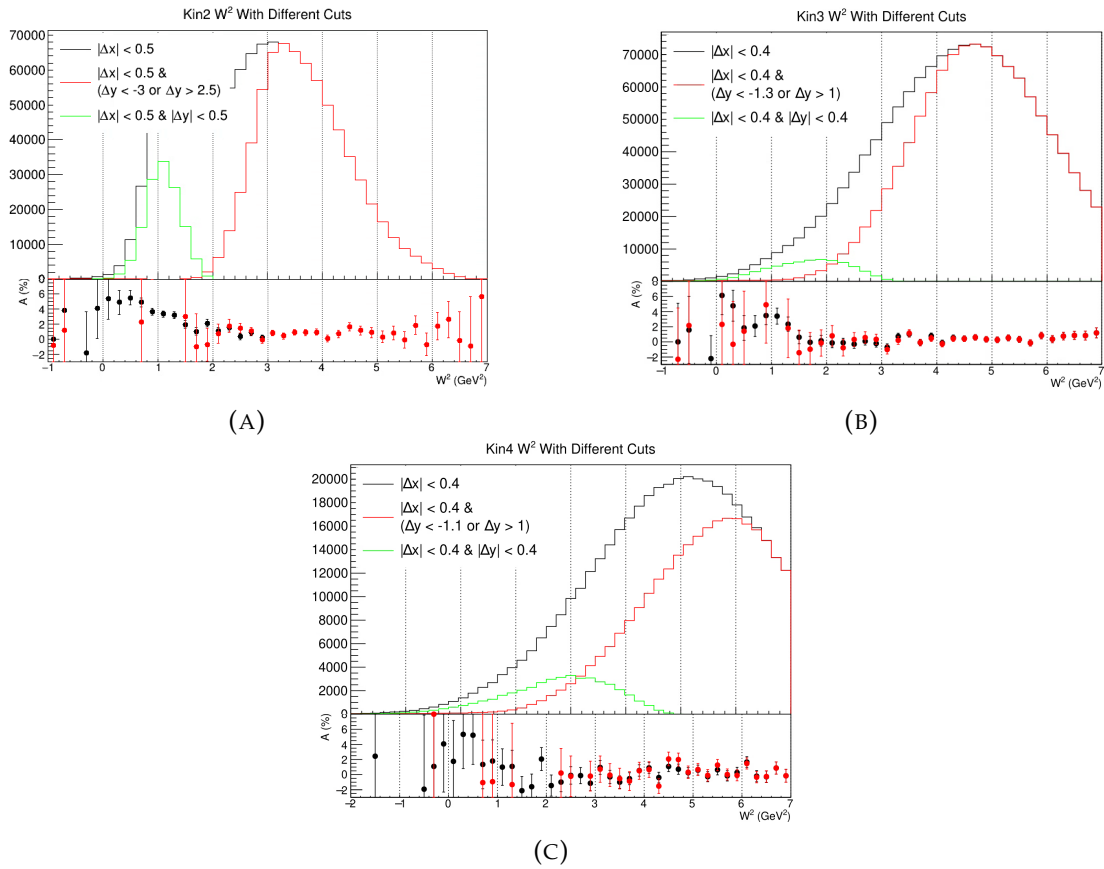


FIGURE 7.23: W^2 distributions for all kinematics with different Δy cuts. Below each plot is the asymmetry for each W^2 bin of 0.2 GeV. Black data points are for the black histogram and red data points are for the red histogram.

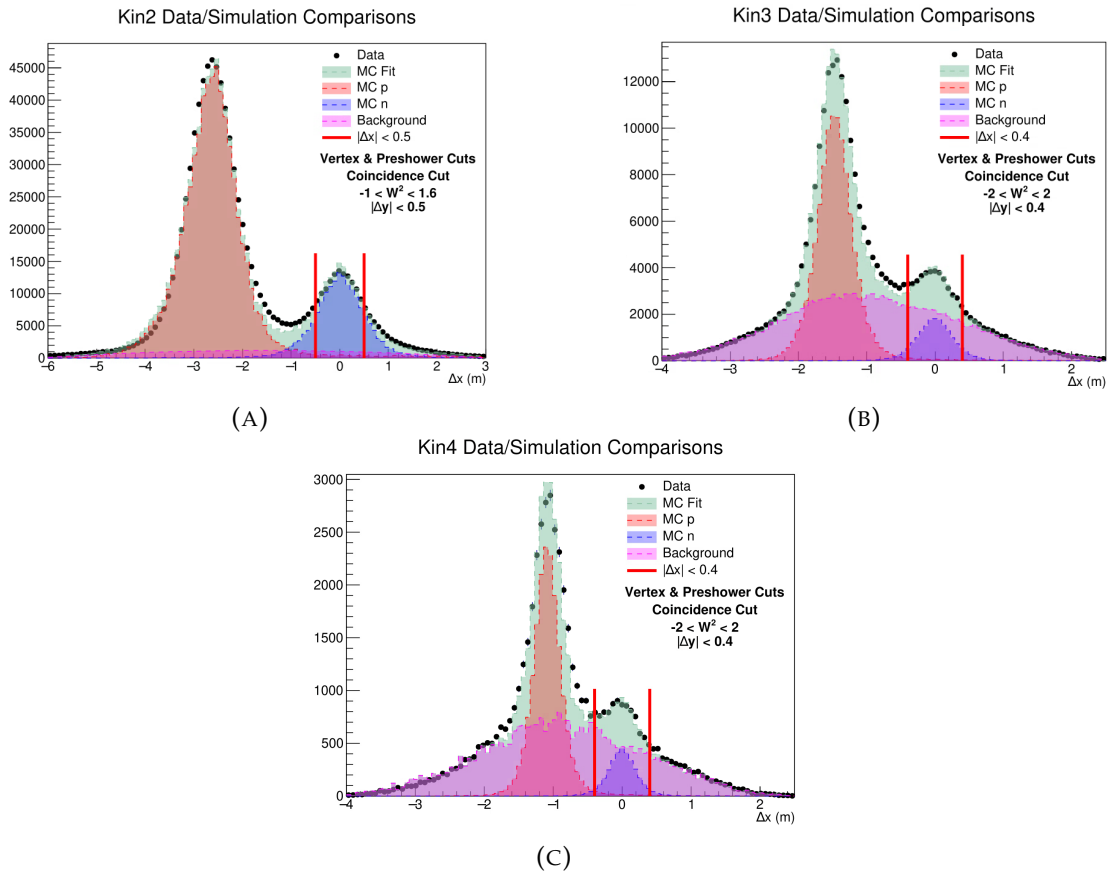


FIGURE 7.24: Results of the simulation fitting for each kinematic with different contributions colored. The Δx cut in vertical red lines shows the region where QE events are selected. The different contributions inside the QE cut gives an idea of how much contamination there is.

7.8.5 Proton Contamination

The neutron Δx cut has some small fraction of proton events passing the cut. Determining this fraction follows a similar process as described in section 7.8.4 except now the proton fit is of interest instead of the background fit. The proton distribution underneath the QE Δx cut can be integrated to obtain the total proton counts, Σ_p . The proton fraction is then simply $f_p = \Sigma_p / \Sigma$.

The proton asymmetry was calculated from the parameterizations (section 1.7.4). This parameterization gives a G_E^p / G_M^p value for the Q^2 range in our analysis. From the experimental kinematics, the average Q^2 , ϵ , τ , P_x , and P_z can be used in equation 3.10 to obtain the physical asymmetry from the proton

$$A_{p,\text{phys}} = -\frac{1}{1 + \frac{\bar{\epsilon}}{\bar{\tau}} \Lambda^p(Q^2)^2} \left[\Lambda^p(Q^2) \sqrt{\frac{2\bar{\epsilon}(1-\bar{\epsilon})}{\bar{\tau}}} \bar{P}_x + \sqrt{1 - \bar{\epsilon}^2} \bar{P}_z \right] \quad (7.28)$$

where all the kinematic variables have been averaged and $\Lambda^p(Q^2) = G_E^p / G_M^p$ is the global parameterization for the proton, section 1.7.4. The averaging of the kinematic variables will be explained in detail in section 7.10.

Just as for the neutron, the polarizations for the proton must be accounted for

$$A_p = P_{\text{beam}} P_{^3\text{He}} P_p A_{p,\text{phys}} \quad (7.29)$$

where P_p is the effective polarization of the proton in ^3He . This value is taken to be -0.03. Although $A_{p,\text{phys}}$ is large compared to the neutron asymmetry, the small value of P_p leaves the raw asymmetry contribution due to the proton, A_p , rather small. Overall, combined with the small proton overlap with the neutron spot, the proton correction is small.

7.8.6 Nuclear Effects and Final State Interactions

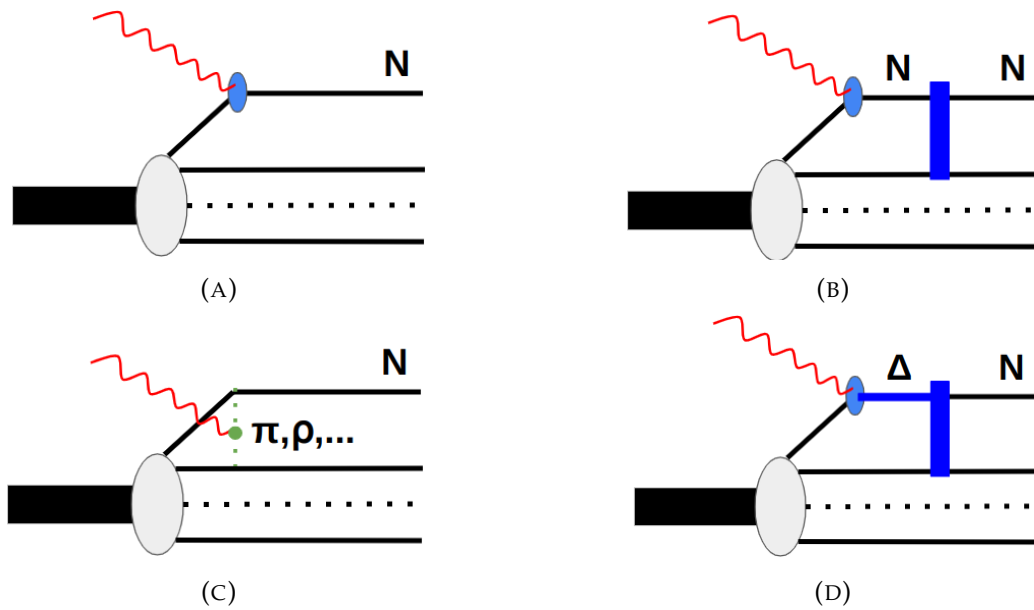


FIGURE 7.25: Feynman diagrams of nuclear processes in this scattering. (A) impulse approximation, (B) final state interactions, (C) meson exchange currents, and (D) isobar currents.

The neutron is part of a nuclei system and therefore there are other nuclear effects that may contribute to the neutron scattering process. The four main contributing diagrams are shown in figure 7.25 and are listed as follows

1. Impulse approximation (IA) where a single nucleon is scattered out of the nucleus without any other interaction.
2. Final state interactions (FSI) where the scattered nucleon rescatters with the residual nuclei.
3. Meson exchange currents (MEC) where the exchanged virtual photon interacts with a meson exchanged between the nucleons.
4. Isobar currents (IC) where the exchanged virtual photon excites a nucleon into a Δ isobar which interacts with the residual nucleus to produce the scattered nucleon.

It has been shown that the FSI, MEC, and IC contributions are significant at low Q^2 and large missing momentum [71]. Large perpendicular missing momenta is removed during our HCal spot cuts as described in section 7.4.5. Moreover, the MEC and IC

contributions become suppressed at $Q^2 > 1 \text{ GeV}^2$ since they have an extra factor of $1/Q^4$ compared to IA and FSI, and so MEC and IC can be ignored at the Q^2 values of this analysis.

The FSI contribution can be computationally calculated utilizing the generalized eikonal approximation (GEA) [72], which allows a nucleon with non-zero initial nucleon momentum. The GEA calculates the possible single and double scattering of each residual nucleon with the scattered nucleon. This GEA analysis and a simulation was created by Misak Sargsian to estimate the IA and FSI cross sections for the GEN-I analysis. The estimated accuracy of the GEA calculation for GEN-I was estimated to be 2% [20].

Notably the GEA method was only calculated for $1 < Q^2 < 4 \text{ GeV}^2$. Unfortunately this author is not currently aware of any extension of this analysis to $Q^2 = 10$, which is needed for GEN-II. Therefore we must make some assumptions based on the GEN-I results and future work must be done for accuracy of the GEA. This will be detailed in section 8.2.6.

7.9 Run Summation

The experimental conditions change slightly over time and so each run must be treated independently. For example, depending on the target polarization the asymmetry could change by 10 % or more over time. The physical asymmetry from equation 7.15 can be modified for a single run

$$A_{\text{phys},i} = \frac{A_{\text{raw},i} - f_{\text{acc}}A_{\text{acc}} - f_{\pi}A_{\pi} - f_{\text{in}}A_{\text{in}} - f_{\text{p}}A_{\text{p}} - f_{\text{FSI}}A_{\text{FSI}}}{P_{\text{beam},i}P_{3\text{He},i}P_{\text{n}}(1 - f_{\text{acc}} - f_{\text{N}_2} - f_{\pi} - f_{\text{in}} - f_{\text{p}} - f_{\text{FSI}})} \quad (7.30)$$

where i index is the run number. Note that only $A_{\text{raw},i}$, $P_{\text{beam},i}$, and $P_{3\text{He},i}$ are changed for each run. All correction fractions and asymmetries are taken to be constant throughout the kinematic. For a single run the statistical error can then be calculated as

$$\sigma_{\text{stat},i} = \frac{\sigma_{A_{\text{raw},i}}}{P_{\text{beam},i}P_{3\text{He},i}P_{\text{n}}f_n} \quad (7.31)$$

Runs can then be statistically combined to obtain the total asymmetry for a kinematic.

$$A_{\text{phys}} = \frac{\sum \frac{A_{\text{phys},i}}{\sigma_{\text{stat},i}^2}}{\sum \frac{1}{\sigma_{\text{stat},i}^2}} \quad (7.32)$$

It is important here to mention how the single run values are calculated. $A_{\text{raw},i}$ is simply calculated from the counts in a run as shown in equation 7.12. Meanwhile the ^3He polarization per run is calculated from interpolation of the NMR measurements, as detailed in section 7.6. The beam polarization is treated slightly differently since it is only measured a few times in the entire kinematic. The beam polarization is measured for each accelerator configuration as discussed in section 7.6. Therefore $P_{\text{beam},i}$ is selected based on the accelerator configuration for that run i in question. Technically $P_{\text{beam},i}$ is the same for value hundreds of runs, but for consistency it is easier to use the i index per run.

7.10 Finite Acceptance

The asymmetry calculation in equation 3.4 is for a fixed value of θ and ϕ .

$$A_{\text{phys}} = \frac{\Delta(\theta, \phi)}{\Sigma(\theta, \phi)} \quad (7.33)$$

However the large acceptance of detector apparatus allows for a range of scattering angles for a single kinematic. A way to average all the values for the kinematic must be determined. Here we will follow the method used by Seamus Riordan [73]. The measured asymmetry, ignoring constant factors like polarizations, is given by

$$A_{\text{meas}} = \frac{\int \Delta(\theta, \phi) \epsilon(\theta, \phi) d\Omega}{\int \Sigma(\theta, \phi) \epsilon(\theta, \phi) d\Omega} \quad (7.34)$$

where $\epsilon(\theta, \phi)$ is the acceptance as a function of the kinematics. $\epsilon(\theta, \phi)$ can be calculated by measuring the counts in the each bin and comparint to the elastic scattering cross section.

$$\epsilon(\theta, \phi) = \frac{dN^+(\theta, \phi) + dN^-(\theta, \phi)}{\Sigma(\theta, \phi)} \quad (7.35)$$

This can then be substituted into equation 7.34.

$$A_{\text{meas}} = \frac{\int \frac{\Delta(\theta, \phi)}{\Sigma(\theta, \phi)} [dN^+(\theta, \phi) + dN^-(\theta, \phi)] d\Omega}{\int [dN^+(\theta, \phi) + dN^-(\theta, \phi)] d\Omega} \quad (7.36)$$

$$A_{\text{meas}} = \frac{1}{N^+ + N^-} \sum_{\text{QE Events}} \frac{\Delta(\theta, \phi)}{\Sigma(\theta, \phi)}$$

Equation 7.36 tells us that the measured asymmetry is the weighted average of the asymmetry in each bin. This means that asymmetry is the measurement of the average values of the kinematics.

Therefore equation 3.4 can be adjusted to the following,

$$A_{\text{phys}} = -\frac{1}{1 + \frac{\bar{\epsilon}}{\bar{\tau}} \Lambda^2} \left[\Lambda \sqrt{\frac{2\bar{\epsilon}(1 - \bar{\epsilon})}{\bar{\tau}}} \bar{P}_x + \sqrt{1 - \bar{\epsilon}^2} \bar{P}_z \right] \quad (7.37)$$

where $\bar{\epsilon}$, $\bar{\tau}$, \bar{P}_x , \bar{P}_z are the weighted average values of the kinematic variables for all QE events. Also note that there is a range of Q^2 values for each kinematic. For a single kinematic the quoted Q^2 value will be the weighted average from the QE events, just as done for the other kinematic variables.

7.11 G_E^n Extraction

At this point we have calculated A_{phys} and the averaged kinematic variables. This information can now be used to extract the form factor ratio, Λ . It will be convenient to define the temporary variables.

$$A = \frac{\bar{\epsilon}}{\bar{\tau}} A_{\text{phys}}$$

$$B = \sqrt{\frac{2\bar{\epsilon}(1 - \bar{\epsilon})}{\bar{\tau}}} \bar{P}_x \quad (7.38)$$

$$C = A_{\text{phys}} + \sqrt{1 - \bar{\epsilon}^2} \bar{P}_z$$

Equation 7.37 can then be rearranged.

$$\begin{aligned}
 -A_{\text{phys}} - \frac{\bar{\epsilon}}{\bar{\tau}} A_{\text{phys}} \Lambda^2 &= \Lambda \sqrt{\frac{2\bar{\epsilon}(1-\bar{\epsilon})}{\bar{\tau}}} \bar{P}_x + \sqrt{1-\bar{\epsilon}^2} \bar{P}_z \\
 0 &= \left(\frac{\bar{\epsilon}}{\bar{\tau}} A_{\text{phys}} \right) \Lambda^2 + \left(\sqrt{\frac{2\bar{\epsilon}(1-\bar{\epsilon})}{\bar{\tau}}} \bar{P}_x \right) \Lambda + \left(A_{\text{phys}} + \sqrt{1-\bar{\epsilon}^2} \bar{P}_z \right) \\
 0 &= A\Lambda^2 + B\Lambda + C
 \end{aligned} \tag{7.39}$$

From this the quadratic formula can be solved to obtain Λ .

$$\Lambda = \frac{-B + \sqrt{B^2 - 4AC}}{2A} \tag{7.40}$$

From $\Lambda = G_E^n / G_M^n$, the G_E^n value itself can be extracted. This requires combining it with a separate G_M^n measurement. From the world data parameterization in section 1.7.4 the G_M^n value can be extracted at each Q^2 value. The G_M^n parameterization uncertainties will also improve as the recent GMn experiment, mentioned in section 2.1, will finalize its analysis and extend the world data accuracy in the next couple years.

Chapter 8

Results and Outlook

8.1 Error Calculations

Here the resulting values from the individual contributions mentioned in section 7.8 will be presented. Also the error calculation for each process will be outlined. Almost all of the analysis deals with counting number of events. Therefore we will make constant use of Poisson statistics which determines that the error on N counts is $\sigma_N = \sqrt{N}$. Also we assume that each contribution to the total uncertainty is independent and so error propagation on variable y dependent on several x_i variables is calculated as

$$(\sigma_y)^2 = \sum_i \left(\frac{\delta y}{\delta x_i} \sigma_{x_i} \right)^2 \quad (8.1)$$

8.1.1 Asymmetry and Fractional Errors

Most asymmetries presented in this analysis follows the A_x formula, defined in equation 7.11, where x is the contribution type. Since most data types follow this formula the error can also follow the same process. The error propagation on this value is

$$\sigma_{A_x} = \frac{\sqrt{\Sigma_x^2 - \Delta_x^2}}{\Sigma_x^{3/2}} \quad (8.2)$$

where definitions of all variables have been previously provided in equation 7.11. Similar to the asymmetry, the fractional errors also follow a common f_x formula, defined

in equation 7.11. The error propagation on this value is

$$\sigma_{f_x} = \frac{\Sigma_x}{\Sigma^2} + \frac{\Sigma_x^2}{\Sigma^3} \quad (8.3)$$

These two equations, 8.2 and 8.3, will be reused repeatedly in this analysis for different contamination results.

In particular the **Raw, Accidental, and Inelastic** contributions all follow the asymmetry error formula 8.2. This means that the only change is the counts for each event type. Meanwhile the **Pion and Proton** asymmetry errors are calculated differently. For the fractions the **Raw, Accidental, and Proton** contributions all follow the fractional error formula 8.3. Again the only change in the formula is the counts for each event type. Meanwhile the **Nitrogen, Pion, and Inelastic** fractional error is calculated differently.

8.1.2 Pion Errors

The pion asymmetry is described in equation 7.23. The errors then only come from the fit parameters C_{π}^+ and C_{π}^- . The asymmetry error is

$$\sigma_{A_{\pi}}^2 = \frac{4 \left((C_{\pi}^+ \sigma_{C_{\pi}^-})^2 + (C_{\pi}^- \sigma_{C_{\pi}^+})^2 \right)}{(C_{\pi}^+ + C_{\pi}^-)^4} \quad (8.4)$$

where $\sigma_{C_{\pi}^+}$ and $\sigma_{C_{\pi}^-}$ are errors from the fit parameters.

The pion fraction is described in equation 7.25. The pion signal from simulation, S_{π} is assumed to be negligible. The total error on the fraction is then

$$\sigma_{f_{\pi}}^2 = \left(\frac{f_{\pi}}{C_{\pi}} \right)^2 \sigma_{C_{\pi}}^2 + \left(\frac{C_{\pi} S_{\pi,PS}}{\Sigma \Sigma_{PS}} \right)^2 \Sigma_{acc,PS} + \left(\frac{C_{\pi} S_{\pi,PS} \Sigma_{acc,PS}}{\Sigma \Sigma_{PS}^2} \right)^2 \Sigma_{PS} + \frac{f_{\pi}^2}{\Sigma} \quad (8.5)$$

8.1.3 Proton Asymmetry

The proton asymmetry has been described in equation 7.29, which clearly does not fit the generic formula 8.2. We must propagate error on P_{beam} , P_{3He} , and $A_{p,phys}$. For $A_{p,phys}$ error propagation must be performed on equation 7.28. The situation can be simplified by assuming that all the kinematic variables have negligible errors and so

can be simplified to

$$A_{p,\text{phys}} = -\frac{1}{1+a\Lambda^2} (b\Lambda + c) \quad (8.6)$$

where a , b , and c are all constants. Error propagation on this then leads to

$$\begin{aligned} \sigma_{\Lambda}^2 &= \Lambda^2 \left(\left(\frac{\sigma_{G_E^p}}{G_E^p} \right)^2 + \left(\frac{\sigma_{G_M^p}}{G_M^p} \right)^2 \right) \\ \sigma_{A_{p,\text{phys}}}^2 &= \left(\frac{2a\Lambda A_{p,\text{phys}} + b}{1+a\Lambda^2} \right)^2 \sigma_{\Lambda}^2 \end{aligned} \quad (8.7)$$

where $G_{E/M}^p$ and the associated errors are taken from the global fits in section 1.7.4. This can then be combined into the full error propagation for A_p .

$$\sigma_{A_p}^2 = A_p^2 \left[\left(\frac{\sigma_{A_{p,\text{phys}}}}{A_{p,\text{phys}}} \right)^2 + \left(\frac{\sigma_{P_{^3\text{He}}}}{P_{^3\text{He}}} \right)^2 + \left(\frac{\sigma_{P_{\text{beam}}}}{P_{\text{beam}}} \right)^2 \right] \quad (8.8)$$

The polarization results and errors have been defined in section 7.6.

8.1.4 Nitrogen Fraction

The nitrogen fraction has been described in equation 7.17, which does not fit the generic formula 8.3. The beam charges, Q , and the mass density, m , errors can be assumed to have negligible error. The error propagation is then performed on the counts to yield

$$\begin{aligned} \sigma_{f_{N_2}}^2 &= \left(\frac{Q(^3\text{He})}{Q(C)} \frac{m_{N_2}(^3\text{He})}{m_C(C)} \right)^2 \left[\frac{\Sigma(C) + \Sigma_{\text{acc}}(C)}{(\Sigma(^3\text{He}) - \Sigma_{\text{acc}}(^3\text{He}))^2} \right. \\ &\quad \left. + \frac{(\Sigma(C) - \Sigma_{\text{acc}}(C))^2 (\Sigma(^3\text{He}) + \Sigma_{\text{acc}}(^3\text{He}))}{(\Sigma(^3\text{He}) - \Sigma_{\text{acc}}(^3\text{He}))^4} \right] \end{aligned} \quad (8.9)$$

8.1.5 Inelastic Fraction

The inelastic fraction in equation 7.27, which does not fit the generic formula 8.3. However equation 7.27 can be rewritten.

$$f_{\text{in}} = \frac{\Sigma_{\text{bg}}}{\Sigma} - \frac{\Sigma_{\text{acc}}}{\Sigma} - \frac{\Sigma_{N_2}}{\Sigma} - \frac{\Sigma_{\pi}}{\Sigma} = f_{\text{bg}} - f_{\text{acc}} - f_{N_2} - f_{\pi} \quad (8.10)$$

Error propagation on this is then

$$\sigma_{f_{\text{in}}}^2 = \sigma_{f_{\text{bg}}}^2 + \sigma_{f_{\text{acc}}}^2 + \sigma_{f_{\text{N}_2}}^2 + \sigma_{f_{\pi}}^2 \quad (8.11)$$

where the individual fractional errors in equation 8.11 added in quadrature are all calculated using the general formula 8.3.

8.1.6 Physical Asymmetry Error

The measured physical asymmetry for a single run has already been presented in equation 7.30, but we will repeat it here to be explicit.

$$\begin{aligned} A_{\text{phys},i} &= \frac{A_{\text{raw},i} - f_{\text{acc}}A_{\text{acc}} - f_{\pi}A_{\pi} - f_{\text{in}}A_{\text{in}} - f_{\text{p}}A_{\text{p}} - f_{\text{FSI}}A_{\text{FSI}}}{P_{\text{beam},i}P_{\text{He},i}P_{\text{n}}(1 - f_{\text{acc}} - f_{\text{N}_2} - f_{\pi} - f_{\text{in}} - f_{\text{p}} - f_{\text{FSI}})} \\ &= \frac{A_{\text{raw},i} - f_{\text{acc}}A_{\text{acc}} - f_{\pi}A_{\pi} - f_{\text{in}}A_{\text{in}} - f_{\text{p}}A_{\text{p}} - f_{\text{FSI}}A_{\text{FSI}}}{P_{\text{beam},i}P_{\text{He},i}P_{\text{n}}f_{\text{n}}} \end{aligned} \quad (8.12)$$

The error propagation on this can be broken up into three components

$$\sigma_{A_{\text{phys},i}}^2 = \sigma_{A_{\text{all}}}^2 + \sigma_{f_{\text{all}}}^2 + \sigma_{P_{\text{all}}}^2 \quad (8.13)$$

where $\sigma_{A_{\text{all}}}^2$ is the error of all the asymmetries, $\sigma_{f_{\text{all}}}^2$ is the error of all the fractions, and $\sigma_{P_{\text{all}}}^2$ is the error of all the polarizations. It will be convenient to define

$$P_i = P_{\text{beam},i}P_{\text{He},i}P_{\text{n}} \quad (8.14)$$

which will simplify the following calculations. The errors associated from the asymmetry are

$$\sigma_{A_{\text{all}}}^2 = \frac{\sigma_{A_{\text{raw},i}}^2 + f_{\text{acc}}^2\sigma_{A_{\text{acc}}}^2 + f_{\pi}^2\sigma_{A_{\pi}}^2 + f_{\text{in}}^2\sigma_{A_{\text{in}}}^2 + f_{\text{p}}^2\sigma_{A_{\text{p}}}^2 + f_{\text{FSI}}^2\sigma_{A_{\text{FSI}}}^2}{(P_i f_{\text{n}})^2} \quad (8.15)$$

The fractional errors are then

$$\begin{aligned} \sigma_{f_{\text{all}}}^2 &= \left(\frac{A_{\text{phys},i}}{f_{\text{n}}}\right)^2 \sigma_{f_{\text{N}_2}}^2 + \left(\frac{P_i A_{\text{phys},i} - A_{\text{acc}}}{P_i f_{\text{n}}}\right)^2 \sigma_{f_{\text{acc}}}^2 + \left(\frac{P_i A_{\text{phys},i} - A_{\pi}}{P_i f_{\text{n}}}\right)^2 \sigma_{f_{\pi}}^2 \\ &+ \left(\frac{P_i A_{\text{phys},i} - A_{\text{in}}}{P_i f_{\text{n}}}\right)^2 \sigma_{f_{\text{in}}}^2 + \left(\frac{P_i A_{\text{phys},i} - A_{\text{p}}}{P_i f_{\text{n}}}\right)^2 \sigma_{f_{\text{p}}}^2 + \left(\frac{P_i A_{\text{phys},i} - A_{\text{FSI}}}{P_i f_{\text{n}}}\right)^2 \sigma_{f_{\text{FSI}}}^2 \end{aligned} \quad (8.16)$$

The polarization errors are then

$$\sigma_{P_{\text{all}}}^2 = A_{\text{phys},i}^2 \left[\left(\frac{\sigma_{P_{3\text{He}}}}{P_{3\text{He}}} \right)^2 + \left(\frac{\sigma_{P_{\text{n}}}}{P_{\text{n}}} \right)^2 + \left(\frac{\sigma_{P_{\text{beam}}}}{P_{\text{beam}}} \right)^2 \right] \quad (8.17)$$

To be explicit we can now substitute equation 8.15, 8.16, and 8.17 into equation 8.13 to get the full error calculation.

$$\begin{aligned} \sigma_{A_{\text{phys},i}}^2 = & \frac{\sigma_{A_{\text{raw},i}}^2 + f_{\text{acc}}^2 \sigma_{A_{\text{acc}}}^2 + f_{\pi}^2 \sigma_{A_{\pi}}^2 + f_{\text{in}}^2 \sigma_{A_{\text{in}}}^2 + f_{\text{p}}^2 \sigma_{A_{\text{p}}}^2 + f_{\text{FSI}}^2 \sigma_{A_{\text{FSI}}}^2}{(P_i f_n)^2} \\ & + \left(\frac{A_{\text{phys},i}}{f_n} \right)^2 \sigma_{f_{\text{N}_2}}^2 + \left(\frac{P_i A_{\text{phys},i} - A_{\text{acc}}}{P_i f_n} \right)^2 \sigma_{f_{\text{acc}}}^2 + \left(\frac{P_i A_{\text{phys},i} - A_{\pi}}{P_i f_n} \right)^2 \sigma_{f_{\pi}}^2 \\ & + \left(\frac{P_i A_{\text{phys},i} - A_{\text{in}}}{P_i f_n} \right)^2 \sigma_{f_{\text{in}}}^2 + \left(\frac{P_i A_{\text{phys},i} - A_{\text{p}}}{P_i f_n} \right)^2 \sigma_{f_{\text{p}}}^2 + \left(\frac{P_i A_{\text{phys},i} - A_{\text{FSI}}}{P_i f_n} \right)^2 \sigma_{f_{\text{FSI}}}^2 \\ & + A_{\text{phys},i}^2 \left[\left(\frac{\sigma_{P_{3\text{He}}}}{P_{3\text{He}}} \right)^2 + \left(\frac{\sigma_{P_{\text{n}}}}{P_{\text{n}}} \right)^2 + \left(\frac{\sigma_{P_{\text{beam}}}}{P_{\text{beam}}} \right)^2 \right] \end{aligned} \quad (8.18)$$

The statistical error comes from the raw counts, which are used to calculate A_{raw} and so the total statistical error is on $A_{\text{phys},i}$ is

$$\sigma_{\text{stat},i} = \frac{\sigma_{A_{\text{raw},i}}}{P_{\text{beam},i} P_{3\text{He},i} P_{\text{n}} f_n} \quad (8.19)$$

Again recall that statistical error is for a single run, i , as has been previously detailed in section 7.9. The total statistical error for the all runs in a kinematic can be calculated.

$$\sigma_{\text{stat}} = \frac{1}{\sqrt{\sum_i \frac{1}{\sigma_{\text{stat},i}^2}}} \quad (8.20)$$

Simply put, the systematic error is then everything else in equation 8.18 with equation 8.19 removed. Again, to be explicit this is

$$\begin{aligned}
\sigma_{\text{sys}}^2 = & \frac{f_{\text{acc}}^2 \sigma_{A_{\text{acc}}}^2 + f_{\pi}^2 \sigma_{A_{\pi}}^2 + f_{\text{in}}^2 \sigma_{A_{\text{in}}}^2 + f_{\text{p}}^2 \sigma_{A_{\text{p}}}^2 + f_{\text{FSI}}^2 \sigma_{A_{\text{FSI}}}^2}{(P f_n)^2} \\
& + \left(\frac{A_{\text{phys}}}{f_n} \right)^2 \sigma_{f_{\text{N}_2}}^2 + \left(\frac{P A_{\text{phys}} - A_{\text{acc}}}{P f_n} \right)^2 \sigma_{f_{\text{acc}}}^2 + \left(\frac{P A_{\text{phys}} - A_{\pi}}{P f_n} \right)^2 \sigma_{f_{\pi}}^2 \\
& + \left(\frac{P A_{\text{phys}} - A_{\text{in}}}{P f_n} \right)^2 \sigma_{f_{\text{in}}}^2 + \left(\frac{P A_{\text{phys}} - A_{\text{p}}}{P f_n} \right)^2 \sigma_{f_{\text{p}}}^2 + \left(\frac{P A_{\text{phys}} - A_{\text{FSI}}}{P f_n} \right)^2 \sigma_{f_{\text{FSI}}}^2 \\
& + A_{\text{phys}}^2 \left[\left(\frac{\sigma_{P_{\text{He}}}}{P_{\text{He}}} \right)^2 + \left(\frac{\sigma_{P_{\text{n}}}}{P_{\text{n}}} \right)^2 + \left(\frac{\sigma_{P_{\text{beam}}}}{P_{\text{beam}}} \right)^2 \right]
\end{aligned} \tag{8.21}$$

Notice how equation 8.21 does not have any i run indices. The systematic error is assumed to affect all runs equally and so A_{phys} and P are the statistically weighted average of the run by run values. The total error is then simply the statistical and systematic added in quadrature.

$$\sigma_{\text{tot}}^2 = \sigma_{\text{stat}}^2 + \sigma_{\text{sys}}^2 \tag{8.22}$$

8.1.7 G_E^n Error

The Λ calculation has already been described in section 7.11. As before we assume that all kinematic variables have negligible errors except for A_{phys} . For simplification of this calculation the same quadratic variables defined in equation 7.38 will be used here.

$$\sigma_{\Lambda}^2 = \left(\frac{C}{A \sqrt{B^2 - 4AC}} + \frac{\Lambda}{A} \right)^2 \sigma_A^2 + \frac{\sigma_C^2}{B^2 - 4AC} \tag{8.23}$$

Errors can also be calculated on A and C .

$$\sigma_A = \frac{\bar{\epsilon}}{\bar{\tau}} \sigma_{A_{\text{phys}}} \qquad \sigma_C = \sigma_{A_{\text{phys}}} \tag{8.24}$$

This can be plugged into equation 8.23 to yield the final error.

$$\begin{aligned}
 \sigma_{\Lambda}^2 &= \left[\left(\frac{C}{A\sqrt{B^2 - 4AC}} + \frac{\Lambda}{A} \right)^2 \left(\frac{\epsilon}{\tau} \right)^2 + \frac{1}{B^2 - 4AC} \right] \sigma_{A_{\text{phys}}}^2 \\
 \sigma_{\Lambda, \text{stat}}^2 &= \left[\left(\frac{C}{A\sqrt{B^2 - 4AC}} + \frac{\Lambda}{A} \right)^2 \left(\frac{\epsilon}{\tau} \right)^2 + \frac{1}{B^2 - 4AC} \right] \sigma_{\text{stat}}^2 \\
 \sigma_{\Lambda, \text{sys}}^2 &= \left[\left(\frac{C}{A\sqrt{B^2 - 4AC}} + \frac{\Lambda}{A} \right)^2 \left(\frac{\epsilon}{\tau} \right)^2 + \frac{1}{B^2 - 4AC} \right] \sigma_{\text{sys}}^2
 \end{aligned} \tag{8.25}$$

From here it is straight forward to calculate $G_E^n = G_M^n \Lambda$. The error is

$$\sigma_{G_E^n}^2 = (\Lambda \sigma_{G_M^n})^2 + (G_M^n \sigma_{\Lambda})^2 \tag{8.26}$$

Recall that G_M^n and $\sigma_{G_M^n}$ are calculated from the uncertainty bands of the parameterizations of the world data in section 1.7.4.

8.2 Contamination Values

All the tools have now been presented to calculate all parts of G_E^n and the associated errors. Here the numbers used in the analysis will be quoted with the final calculations for each contribution. **An important note:** this is a preliminary work with more students still working on this analysis and results will be refined in the future.

8.2.1 Accidentals

The accidental contamination analysis has been presented in section 7.8.1. The counts are taken from figure 7.17 for each kinematic to calculate the accidental contamination results. The results are then summarized in table 8.1. The asymmetry is low, at $< 1\%$ for all kinematics. The fractional value increases at higher Q^2 but still remains at a manageable level of 7% at most.

TABLE 8.1: Accidental results for each kinematic.

Variable	Kin2	Kin3	Kin4
N_{acc}^+	19583	14786	2677
N_{acc}^-	19245	14644	2620
Σ_{acc}	5332	3827	683
A_{acc}	0.0087 ± 0.0051	0.0048 ± 0.0048	0.0108 ± 0.0137
$\sigma_{A_{\text{acc}}} / A_{\text{acc}}$	0.59	1.00	1.27
f_{acc}	0.0422 ± 0.0006	0.0921 ± 0.0016	0.0729 ± 0.0029
$\sigma_{f_{\text{acc}}} / f_{\text{acc}}$	0.01	0.02	0.04

8.2.2 Nitrogen

The nitrogen contamination analysis has been presented in section 7.8.2. The density of nitrogen in the ^3He cell, ρ_{N_2} , has been provided by target experts. The density in different target cells are all within 2% of each other and so one value of ρ_{N_2} is used here for all targets. The air density, ρ_{air} , can be calculated from barometric pressure from the JLab weather information [74]. The carbon foils are known to be 0.01 inch thick and the carbon density of graphite is known. The parameter values are detailed in table 8.2.

The beam charge is recorded for each run and can be totaled to obtain the beam charge for the kinematic. It is also extremely important recall from section 3.1 that there is no carbon data for Kin2 and so the nitrogen analysis cannot be performed. From the results below Kin3 and Kin4 are very similar and therefore we assume that the Kin2 are the same results as Kin3. Also notably all nitrogen corrections are very small so difference in this assumption from reality should have a negligible result in the final calculation. The final values are listed in table 8.3. For all kinematics the fractional contribution is $< 2\%$. This is overall a small contribution on the final asymmetry.

TABLE 8.2: Nitrogen and carbon target parameters. The targets parameters are the same for all kinematics.

Variable	Value
l_{air} (cm)	29.4
l_{C} (cm)	0.0254
ρ_{N_2} (mg/cm ³)	5.513
ρ_{C} (mg/cm ³)	2266
ρ_{air} (mg/cm ³)	1.17
m_{N_2} (^3He) (mg/cm ²)	5.51
m_{C} (C) (mg/cm ²)	438

TABLE 8.3: Nitrogen results for each kinematic.

Variable	Kin2	Kin3	Kin4
$Q(^3\text{He})$		48.52 C	51.59 C
$Q(\text{C})$		0.40 C	0.25 C
$\Sigma(\text{C})$		138	14
$\Sigma_{\text{acc}}(\text{C})$		37	1
$\Sigma(^3\text{He})$		9939	2395
$\Sigma_{\text{acc}}(^3\text{He})$		908	157
f_{N_2}	0.0178 ± 0.0018	0.0178 ± 0.0018	0.0151 ± 0.0041
$\sigma_{f_{\text{N}_2}} / f_{\text{N}_2}$	0.10	0.10	0.27

8.2.3 Pion

The pion contamination analysis has been presented in section 7.8.3. The final values are taken from the plots in figure 7.20 and 7.21. The results are detailed in table 8.4. The final asymmetries and fractions are all $< 1\%$ for each kinematics. Therefore this contribution is a rather small effect on the final result.

TABLE 8.4: Pion results for each kinematic.

Variable	Kin2	Kin3	Kin4
$S_{\pi,\text{all}}$	1.000	1.000	1.001
$S_{\pi,\text{PS}}$	0.2627	0.2578	0.2762
C_{π}^+	69260 ± 369.3	230375 ± 552.5	55252 ± 270.8
C_{π}^-	70630 ± 370.8	230791 ± 552.8	55225 ± 270.7
C_{π}	11.85 ± 0.9895	2531 ± 71.61	710.48 ± 36.73
N_{π}^+	69270	230425	55303
N_{π}^-	70640	230842	55276
$\Sigma_{\text{acc,PS}}$	5480	5552	1076
Σ_{PS}	123272	47216	11536
Σ_{π}	3.114	652.4	196.2
A_{π}	-0.0098 ± 0.0037	-0.0009 ± 0.0017	0.0002 ± 0.0035
$\sigma_{A_{\pi}} / A_{\pi}$	0.32	1.88	17.5
f_{π}	0 ± 0	0.0077 ± 0.0002	0.0107 ± 0.0006
$\sigma_{f_{\pi}} / f_{\pi}$	0	0.03	0.06

8.2.4 Inelastic

The inelastic contamination analysis has been presented in section 7.8.4. The final values are taken from figure 7.24 and results are detailed in table 8.6. The asymmetry

results are rather small, at $< 1\%$ for all kinematics. However the fractional results increase as Q^2 increases, up to 50% and 60% for Kin3 and Kin4, respectively, while Kin2 remains quite low at 4%. Therefore this contribution is by far the largest effect for Kin3 and Kin4 while Kin2 remains similar size to the other contributions.

TABLE 8.5: Inelastic results for each kinematic.

Variable	Kin2	Kin3	Kin4
N_{in}^+	348861	562368	134238
N_{in}^-	343304	558242	133387
Σ_{bg}	12361	27006	6418
Σ_{in}	4876	22124	5493
A_{in}	0.0080 ± 0.0012	0.0037 ± 0.0009	0.0032 ± 0.0019
$\sigma_{A_{\text{in}}} / A_{\text{in}}$	0.15	0.24	0.59
f_{in}	0.0386 ± 0.0006	0.5330 ± 0.0044	$0.5868 \pm .0010$
$\sigma_{f_{\text{in}}} / f_{\text{in}}$	0.02	0.01	0.02

8.2.5 Proton

The proton contamination analysis has been presented in section 7.8.5. The final values are taken from figure 7.24 and equation 7.29. The asymmetry is $< 1\%$ and the fraction is $< 4\%$ for all kinematics. Overall this is a small but noticeable contribution.

TABLE 8.6: Proton results for each kinematic.

Variable	Kin2	Kin3	Kin4
Q^2	2.90	6.50	9.46
$\bar{\tau}$	0.8245	1.8462	2.6852
$\bar{\epsilon}$	0.8002	0.6278	0.5838
\bar{P}_x	0.9908	0.9914	0.9917
\bar{P}_z	-0.0391	-0.0267	-0.0197
Λ^p	0.2297 ± 0.0045	0.1094 ± 0.0147	0.0389 ± 0.0343
P_{beam}	0.8409 ± 0.0018	0.8649 ± 0.0008	0.8384 ± 0.0011
P_{3He}	0.3788 ± 0.0189	0.4206 ± 0.0210	0.4925 ± 0.0246
P_{p}	-0.03	-0.03	-0.03
Σ_{p}	4912	879	241
$A_{\text{p,phys}}$	-0.1125 ± 0.0024	-0.0337 ± 0.0072	-0.0004 ± 0.0145
A_{p}	0.0011 ± 0.0001	0.0004 ± 0.0001	0.0000 ± 0.0002
f_{p}	0.0389 ± 0.0006	0.0212 ± 0.0007	0.0257 ± 0.0017

8.2.6 FSI

It was already detailed in section 7.8.6 that FSI calculations have not yet been done for GEN-II. As previously discussed, the FSI contamination is expected to decrease as Q^2 increase. For this analysis we choose to use the GEN-I result [75] but note that this is overestimating the contamination since the GEN-I Q^2 values were all lower. For all the kinematics in GEN-I the FSI asymmetry was near zero and the FSI fraction is around 3%. The average of the FSI values for all GEN-I kinematics are $A_{\text{FSI}} = 0.0003 \pm 0.0005$ and $f_{\text{FSI}} = 0.0287 \pm 0.0026$. These values will be used for this analysis.

8.3 Exploratory G_E^n Result

A_{phys} must now be obtained using the formalism in section 7.9. The only parameter that has not yet been calculated is the raw asymmetry, A_{raw} . The raw asymmetry, defined in equation 7.12, is calculated from all counts passing the QE cuts. Λ can then be calculated using the formalism in section 7.11. Here we will reference the same A , B , and C parameters defined in equation 7.38 for extracting G_E^n from A_{phys} . Once Λ is known then G_E^n can be calculated as well by combining Λ with G_M^n parameterization from section 1.7.4. World data for G_M^n has been measured to higher precision than G_E^n and so the parameterization of G_M^n contributes less than 2% error. The results are seen in table 8.7.

Now all variables have been calculated for GEN-II. For convenience, table 8.8 summarizes the results from the most important parameters for each kinematic. Kin2 obtained significantly more QE statistics and therefore the statistical and systematic errors are comparable while Kin3 and Kin4 are much more statistically limited and therefore dominated by statistical errors. All contaminations on Kin2, except for the pions, have small and similar size contributions. Overall the final error on Kin2 is relatively small at 12%. This is to be expected since Kin2's low Q^2 value causes much less inelastic background compared to Kin3 and Kin4. As for Kin3 and Kin4 the inelastic background dominates the error. Since the contaminations are a multiplicative factors on the error (equation 8.19) this contributes significantly to the large errors for Kin3 and Kin4. The final error on Kin3 is 30% and on Kin4 is 52%. Also the lower statistics obtained for Kin3 and Kin4 make the statistical errors much larger, which causes the relative error on A_{raw} is much larger for Kin3 and Kin4 than Kin2. The other contamination's are

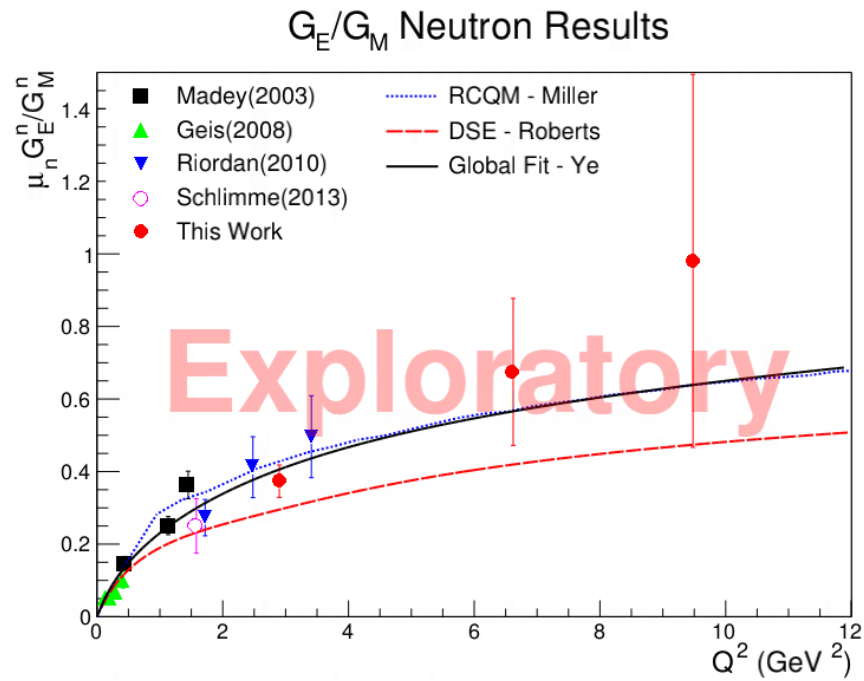
similar in size to Kin2 and do not significantly contribute to this final error. The results are plotted along with current world data and notable theories in figure 8.1.

TABLE 8.7: Exploratory G_E^n results for each kinematic. Values with two errors are of the form Result \pm Statistical \pm Systematic.

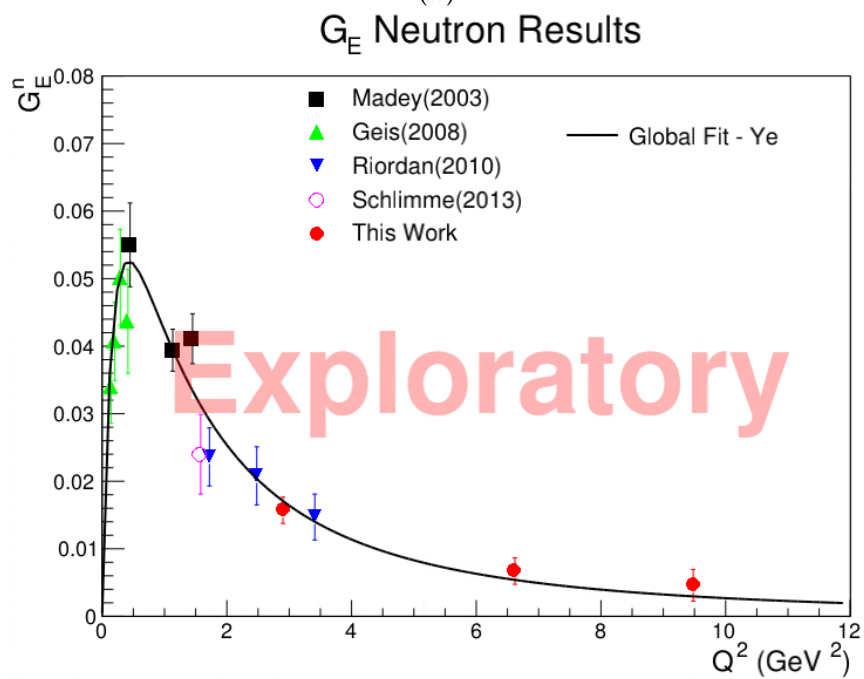
Variable	Kin2	Kin3	Kin4
$\bar{\tau}$	0.8245	1.8462	2.6852
$\bar{\epsilon}$	0.8002	0.6278	0.5838
\bar{P}_x	0.9908	0.9914	0.9917
\bar{P}_z	-0.0391	-0.0267	-0.0197
A	0.1347	0.0716	0.0478
B	0.6170	0.4988	0.4219
C	0.1153	0.1899	0.2037
N^+	65411	21224	4786
N^-	60805	20336	4577
A_{raw}	0.0365 ± 0.0028	0.0214 ± 0.0049	0.0223 ± 0.0103
A_{phys}	0.1387 ± 0.0110 ± 0.0073	0.1887 ± 0.0465 ± 0.0119	0.2197 ± 0.0979 ± 0.0206
Λ	-0.1952 ± 0.0194 ± 0.0130	-0.3527 ± 0.1026 ± 0.0262	-0.5127 ± 0.2629 ± 0.0552
G_M^n	-0.0803 ± 0.0009	-0.0189 ± 0.0002	-0.0089 ± 0.0001
G_E^n	0.0157 ± 0.0016 ± 0.0011	0.0067 ± 0.0019 ± 0.0005	0.0046 ± 0.0023 ± 0.0005

TABLE 8.8: Summary of exploratory GEN-II results for all kinematics. Values with two errors are of the form Result \pm Statistical \pm Systematic.

Variable	Kin2	Kin3	Kin4
Q^2	2.90	6.50	9.46
Σ	126216	41560	9363
P_{beam}	0.8409 ± 0.0018	0.8649 ± 0.0008	0.8384 ± 0.0011
$P_{3\text{He}}$	0.3788 ± 0.0189	0.4206 ± 0.0210	0.4925 ± 0.0246
P_n	0.96	0.96	0.96
P_p	-0.03	-0.03	-0.03
A_{acc}	0.0087 ± 0.0051	0.0048 ± 0.0048	0.0108 ± 0.0137
A_π	-0.0098 ± 0.0037	-0.0009 ± 0.0017	0.0002 ± 0.0035
A_{in}	0.0080 ± 0.0012	0.0037 ± 0.0009	0.0032 ± 0.0019
A_p	0.0011 ± 0.0001	0.0004 ± 0.0001	0.0000 ± 0.0002
A_{FSI}	0.0003 ± 0.0005	0.0003 ± 0.0005	0.0003 ± 0.0005
f_{acc}	0.0422 ± 0.0006	0.0921 ± 0.0016	0.0729 ± 0.0029
f_{N_2}	0.0178 ± 0.0018	0.0178 ± 0.0018	0.0151 ± 0.0041
f_π	0.0000 ± 0.0000	0.0077 ± 0.0002	0.0107 ± 0.0006
f_{in}	0.0386 ± 0.0006	0.5330 ± 0.0044	$0.5868 \pm .0010$
f_p	0.0389 ± 0.0006	0.0212 ± 0.0007	0.0257 ± 0.0017
f_{FSI}	0.0287 ± 0.0026	0.0287 ± 0.0026	0.0287 ± 0.0026
f_n	0.8338	0.2995	0.2601
A_{raw}	0.0365 ± 0.0028	0.0214 ± 0.0049	0.0223 ± 0.0103
A_{phys}	0.1387 ± 0.0110 ± 0.0073	0.1887 ± 0.0465 ± 0.0119	0.2197 ± 0.0979 ± 0.0206
Λ	-0.1952 ± 0.0194 ± 0.0130	-0.3527 ± 0.1026 ± 0.0262	-0.5127 ± 0.2629 ± 0.0552
G_M^n	-0.0803 ± 0.0009	-0.0189 ± 0.0002	-0.0089 ± 0.0001
G_E^n	0.0157 ± 0.0016 ± 0.0011	0.0067 ± 0.0019 ± 0.0005	0.0046 ± 0.0023 ± 0.0005



(A)



(B)

FIGURE 8.1: Exploratory result of this analysis plotted along with selected previous G_E^n measurements and theory curves.

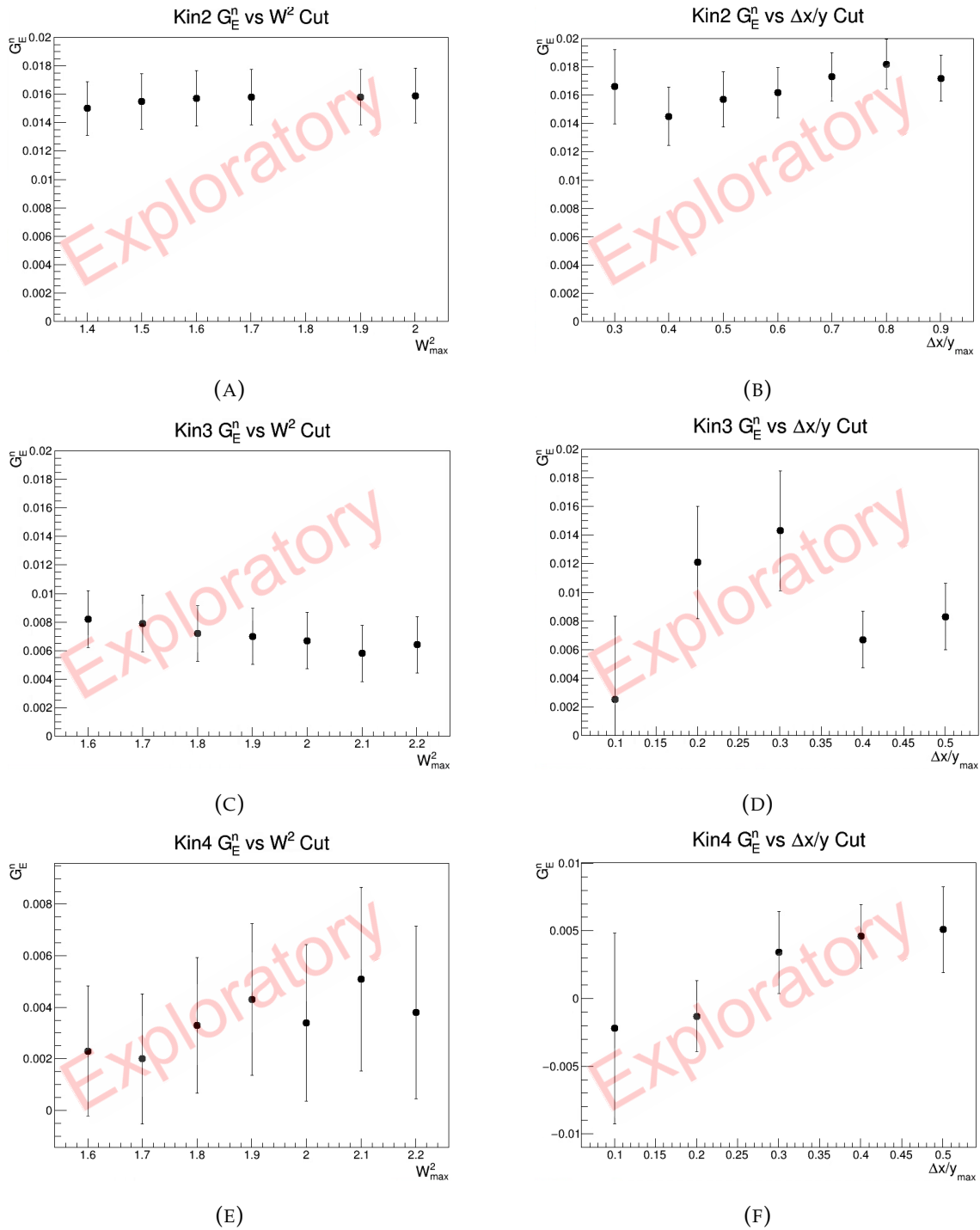


FIGURE 8.2: Exploratory results of G_E^n for different cut values. (A), (C), and (E) show G_E^n with different W_{\max}^2 values while all other cuts remain the same as in table 7.1. (B), (D), and (F) show G_E^n with different $\Delta x/y_{\max}$ values while all other cuts remain the same as in table 7.1.

8.4 Variable Cuts

The full analysis can be redone using different cuts to check their impact on the result. With stringent cuts the background contributions can be minimized but the statistics will also be very small, leading to large statistical errors. As cuts are loosened then the statistical error decreases but the systematic error increases as the background inside the data increases. Our goal is then to find an optimal cut where the error is minimized between these two extremes.

Recall that the selection of cuts are listed in table 7.1. The most important cuts used are the Δx , Δy , and W^2 since they greatly affect the backgrounds in the analysis while the other cuts, like timing, have a significantly smaller impact on the final result. Therefore we will only investigate varying the Δx , Δy , W^2 cuts and the results. Recall from section 7.4.5 that the same cut is applied to Δx and Δy since the distributions are symmetric. For this purpose we define $|\Delta x/y| < \Delta x/y_{\max}$, where $\Delta x/y_{\max}$ is our cut which will be varied. Here the / symbol is used as on "or" and not a fraction. For W^2 the cut is applied as $W_{\min}^2 < W^2 < W_{\max}^2$, where the W_{\min}^2 and W_{\max}^2 values are shown in table 7.1. The W_{\min}^2 value has little effect on the result since there is almost no background at the lower end of the W^2 spectrum, see figure 7.7, and so we only investigate varying the W_{\max}^2 value and its resulting effects.

Figure 8.2 shows the resulting G_E^n values as a function of the cuts. For Kin2, the G_E^n value and error remains very similar for all cuts. The error is dominated by systematics, which do not change significantly with different cuts. For Kin3, the W_{\max}^2 cut results are all similar in value and within error of each other. The $\Delta x/y_{\max}$ cut has a significant impact on G_E^n for Kin3. At small values the statistics are low and the error bars are much larger. For Kin4, the W_{\max}^2 cut results are all within error, but the error grows slightly larger as W^2 increases as more background is included in the data. Small Δ cuts also cause large errors for Kin4 due to small statistics. As the cut value increases the G_E^n value stabilizes and is within error of each other. The cuts we have applied in our final results are therefore shown to have minimized errors on the final result.

8.5 Conclusions and Future

GEN-II has measured G_E^n by colliding a polarized electron beam onto a polarized ^3He target at $Q^2 = 2.90, 6.50, \text{ and } 9.47 \text{ GeV}^2$, and the exploratory analysis has been presented. This experiment has tripled the current Q^2 range of world data. Kin2 purposefully overlaps with previous world data for a straight forward check of the consistency of this analysis. Kin2 matches well with previous data and theory expectations, which gives us confidence in our analysis procedure. The error on Kin4 is currently much too large to make any comment on and must be left for future analysis improvements. From Kin3 this analysis is more consistent with the RCQM theory by Miller and Cloët than the DSE theory by Roberts. However both theories are still within the error of this result. The result agrees with theoretical predictions that there is no foreseeable zero crossing of $\mu_n G_E^n / G_M^n$.

This is the first analysis of GEN-II data and a first pass of detector calibrations was performed before this analysis. Further calibrations must be performed to improved detector performance. Based on student experience from the GMn experiment, notable detector energy and timing resolutions can be made. After another pass of calibrations, tighter QE cuts can be applied in this analysis with better resolutions which will improve the background reduction. Specifically, this can reduce the inelastic background, which has been the largest contributor of error. Students are currently working on moving this analysis forward with better calibrations. Furthermore, the statistics presented here for Kin3 and Kin4 will be improved in future analysis. For Kin3 13% of the data was removed from this analysis due to issues with the beam polarization measurement, which will be added back into the total statistics as that polarization is recalculated. Also the Kin4b data set must be fully analyzed, which will double the statistics of Kin4 presented here. Both of these factors should notably improve the final errors on Kin3 and Kin4.

References

- [1] E. E. Chambers and R. Hofstadter. Phys. Rev. 103.1454 (1956).
- [2] F. Halzen and D. Martin. *Quarks and Leptons: An Introductory Course in Modern Particle Physics*. John Wiley and Sons, Inc., 1984.
- [3] M. N. Rosenbluth. Phys. Rev. 79.615 (1950).
- [4] A. Accardi et al. Eur. Phys. J. A 52.9 (2016).
- [5] R. G. Sachs. Phys. Rev. 126.2256 (1962).
- [6] G. D. Cates, C. W. de Jager, S. Riordan, and B. Wojtsekhowski. Phys. Rev. Lett. 106.252003 (2011).
- [7] C.D. Roberts et al. Eur. Phys. J. ST 140 (2007).
- [8] D. Benaksas, D. Drikey, D. Frerejacque. Phys. Rev. 148.1327 (1966).
- [9] B. Grossetete, S. Julian, P. Lehmann. Phys. Rev. 141.1435 (1966).
- [10] S. Galster, H. Klein, J. Moritz, K. H. Schmidt, D. Wegener, and J. Bleckwenn. Nucl. Phys. B 32.221 (1971).
- [11] Raymond G. Arnold, Carl E. Carlson, and Franz Gross. Phys. Rev. C 23.363 (1981).
- [12] R. Madey et al. Phys. Rev. Lett. 91.122002 (2003).
- [13] D.I. Glazier et al. Eur. Phys. J. A 24.101 (2005).
- [14] G. Warren et al. Phys. Rev. Lett. 92.042301 (2004).
- [15] E. Geis et al. Phys. Rev. Lett. 101.042501 (2008).
- [16] B. Blankleider and R.M. Woloshyn. Phys. Rev. C 29.538 (1984).
- [17] N. Dombey. Rev. Mod. Phys. 41.236 (1969).
- [18] M. Meyerhoff et al. Phys. Lett. B 327.201 (1994).
- [19] J. Bermuth et al. Phys. Lett. B 564.199 (2003).
- [20] S. Riordan, et al. Phys. Rev. Lett. 105.262302 (2010).

- [21] B. S. Schlimme et al. Phys. Rev. Lett. 111.132504 (2013).
- [22] A. V. Belitsky, Xiandong Ji, and Feng Yuan. Phys. Rev. Lett. 91.092003 (2003).
- [23] Ian C. Cloet and Gerald A. Miller. Phys. Rev. C 86.015208 (2012).
- [24] L. Schlessinger and C. Schwartz. Phys. Rev. Lett. 16.1173 (1966).
- [25] Z.n Yao, D. Binosi, Z.Cui, and C. D. Roberts. arXiv preprint. (2024). URL: <https://arxiv.org/abs/2403.08088>.
- [26] V. Punjabi et al. Eur. Phys. J. B 51.79 (2015).
- [27] M. Diehl and P. Kroll. 73.2397 (2013).
- [28] J. J. Kelly. Phys. Rev. C 70.068202 (2004).
- [29] Z. Ye, et al. Phys. Lett. B 777.210 (2018), pp. 8–15.
- [30] R. Gilman, B. Quinn, and B. Wojtsekhowski. *GMn Experiment Proposal*. JLab Document Server. (2010). URL: https://www.jlab.org/exp_prog/proposals/10/PR12-10-005.pdf.
- [31] G. Cates, S. Riordan, and B. Wojtsekhowski. *GEN-II Experiment Proposal*. JLab Document Server. (2010). URL: https://www.jlab.org/exp_prog/proposals/09/PR12-09-016.pdf.
- [32] G. Cates, S. Riordan, and B. Wojtsekhowski. *GEN-II Experiment Proposal Update*. JLab Document Server. (2010). URL: https://www.jlab.org/exp_prog/proposals/proposal_updates/PR12-09-016_pac35.pdf.
- [33] E.J. Brash, M.K. Jones, V. Punjabi, and C.F. Perdrisat. *GEp-V Experiment Proposal*. JLab Document Server. (2010). URL: https://www.jlab.org/exp_prog/proposals/09/PR12-09-001.pdf.
- [34] E.J. Brash, M.K. Jones, V. Punjabi, and C.F. Perdrisat. *GEp-V Experiment Proposal Update*. JLab Document Server. (2010). URL: https://www.jlab.org/exp_prog/PACpage/PAC37/proposals/Proposals/Conditionally%20Approved/C12-09-001.pdf.
- [35] T.W. Donnelly and A. S. Raskin. Ann. of Physics 169 (1986).
- [36] Leigh Harwood, unpublished. “The JLab 12 GEV Energy Upgrade Of CEBAF”. Proceedings of PAC2013 (2013).
- [37] Hall A Collaboration. Nucl. Instr. and Meth. A 552.294 (2004).

- [38] Arun Tadepalli. *Bigbite Calorimeter*. February 2022. URL: https://indico.jlab.org/event/503/contributions/9183/attachments/7516/10459/halla_collaboration_meeting_feb10.pdf.
- [39] Provakar Datta. *The BigBite Calorimeter*. June 2022. URL: https://indico.jlab.org/event/546/contributions/9961/attachments/7914/15183/SBS_BBCAL.pdf.
- [40] Maria Satnik. *SBS GRINCH Gas Cherenkov Detector*. August 2022. URL: https://www.jlab.org/sites/default/files/user-liaison/jluo2022/poster_2022_JLUO_SATNIK.pdf.
- [41] David Hamilton. *BigBite Timing Hodoscope Performance Update*. June 2023. URL: <https://sbs.jlab.org/cgi-bin/DocDB/private/ShowDocument?docid=399>.
- [42] P.A. Adderley et al. *Nucl. Instr. and Meth. A* 1046.167710 (2023).
- [43] D. E. King et al. *Nucl. Instr. and Meth. A* 1045.167506 (2023).
- [44] M. Mihovilovic et al. *Nucl. Instr. and Meth. A* 686 (2012), pp. 20–30.
- [45] Arun Tadepalli. *Carbon foil information for GEN-II target*. October 2022. URL: <https://sbs.jlab.org/cgi-bin/DocDB/private/ShowDocument?docid=323>.
- [46] J. L. Friar et al. *Phys. Rev. C* 42.2310 (1990).
- [47] A. Ben-Amar Baranga, S. Appelt, M. V. Romalis, C. J. Erickson, A. R. Young, G. D. Cates, and W. Happer. *Phys. Rev. Lett.* 80.2801 (1999).
- [48] Earl Babcock, Ian Nelson, Steve Kadlecsek, Bastiaan Driehuys, L. W. Anderson, F. W. Hersman, and Thad G. Walker. *Phys. Rev. Lett.* 91.123003 (2003).
- [49] M. V. Romalis and G. D. Cates. *Phys. Rev. A* 58.3004 (1998).
- [50] CODA Homepage. URL: <https://coda.jlab.org/>.
- [51] EPICS Homepage. URL: <https://epics.anl.gov/>.
- [52] Fabio Sauli. *Nucl. Instr. and Meth. A* 805 (2016), pp. 2–24.
- [53] Particle Data Group. *Passage of Particles Through Matter*.
- [54] I. Lehraus, R. Matthewson, and W. Tejessy. *Nucl. Instr. and Meth.* 200 (1982), pp. 199–210.
- [55] W.S. Wong et al. *Radiation Measurements* 131.106230 (2020).
- [56] K. Gnanvo et al. *Nucl. Instr. and Meth. A* 782 (2015), pp. 77–86.

- [57] J. A. Boyd. *PhD Thesis, University of Virginia*. 2024. URL: https://libraetd.lib.virginia.edu/public_view/tb09j7238.
- [58] Lawrence Jones. *Apv25-s1 user guide version 2.2*. CERN document server. 2001.
- [59] Paolo Musico. *MPD Specifications*. 2001. URL: https://coda.jlab.org/drupal/system/files/pdfs/HardwareManual/MPD/MPD4_UserManual_r2.5.pdf.
- [60] Benjamin Raydo. *VTP Manual*. JLab Documents. 2016.
- [61] Benjamin Raydo, Private communication.
- [62] Sebastian Seeds. *HCal Calibrations*. September 2023. URL: <https://sbs.jlab.org/cgi-bin/DocDB/private/ShowDocument?docid=441>.
- [63] Analyzer Homepage. URL: <https://redmine.jlab.org/projects/podd/wiki>.
- [64] ROOT Homepage. URL: <https://root.cern/>.
- [65] SBS-offline github. URL: <https://github.com/JeffersonLab/SBS-offline>.
- [66] GEN Analysis Github. URL: https://github.com/seanjeffas/GEN_analysis.
- [67] G4SBS Homepage. URL: https://hallaweb.jlab.org/wiki/index.php/Documentation_of_g4sbs.
- [68] S. Agostinelli, J. Allison, et al. *Nucl. Instr. and Meth. A* 506 (2003), p. 250.
- [69] Paul King, Private communication.
- [70] Faraz Chahili. *GEN-II Moller Polarimetry*. February 2024. URL: <https://sbs.jlab.org/cgi-bin/DocDB/private/ShowDocument?docid=532>.
- [71] M. M. Sargsian. *Int. J. Mod. Phys. E* 10.06 (2001), pp. 405–457.
- [72] M. M. Sargsian, T. V. Abrahamyan, M. I. Strikman, and L. L. Frankfurt. *Phys. Rev. C* 71.044614 (2005).
- [73] S. Riordan. *PhD Thesis, Carnegie Mellon University*. 2008. URL: https://misportal.jlab.org/ul/publications/view_pub.cfm?pub_id=11818.
- [74] URL: <https://www.jlab.org/fm/wx/index.html>.
- [75] F. Obrecht. *PhD Thesis, University of Connecticut*. 2019. URL: <https://inspirehep.net/files/03fe72dd8545c3b7f381a8f2fe4ed55d>.